Università degli Studi di Torino
Scuola di Dottorato

Dottorato in Fisica ed Astrofisica

Quarkonium polarization in Pb–Pb collisions with the ALICE experiment at the LHC

Luca Micheletti

Tutor: Dr. Enrico Scomparin
Co-tutor: Dr. Livio Bianchi

Examination committee:
Prof. Anton Andronic, Westfälischen Wilhelms-Universität, Münster
Dr. Javier Castillo Castellanos, Irfu, CEA Saclay
Prof. Massimo Masera, Università degli studi di Torino

Abstract

The study of the formation and the properties of the strongly interacting medium produced in ultrarelativistic heavy-ion collisions, named Quark-Gluon Plasma (QGP), is the main research goal of the ALICE experiment at the CERN Large Hadron Collider (LHC). Quarkonia, bound states of two heavy quarks (charm or bottom), represent a valuable tool in the investigation of the color deconfinement, since their binding can be strongly affected by the presence of the QGP, which may lead to their dissociation and subsequent re-generation, depending on the initial density of the heavy quarks that constitute them. Among the various observables typically studied in hadronic collisions, quarkonium polarization, which measures the spin alignment of a particle with respect to a chosen axis, plays an important role. On one side, the relatively small value measured at the LHC in proton-proton collisions has represented a serious challenge for the commonly-used theoretical models. On the other, in heavy-ion collisions quarkonium polarization could also be sensitive to the formation of the QGP.

The work discussed in this thesis represents the first measurement of J/ψ and Υ(1S) polarization in heavy-ion collisions at the LHC. The present analysis, performed in the dimuon decay channel at forward rapidity ($2.5 < y < 4$), exploits the full Run 2 data sample collected by the ALICE experiment in Pb–Pb collisions at $\sqrt{s_{\mathrm{NN}}} = 5.02$ TeV.

In the first part of the thesis, an overview of the main theoretical and experimental aspects related to quarkonium production and polarization is presented, together with a description of the ALICE experiment apparatus.
In the second part the measurement of the J/ψ polarization is discussed. This analysis is performed as a function of the transverse momentum, in three p_{T} ranges from 2 to 10 GeV/c, and in four centrality classes. The results will be compared with the existing measurements in pp collisions, in order to evaluate the potential modification of the polarization moving from small to large collision systems. Moreover, the possibility to use polarization to investigate the formation of an intense magnetic field in heavy-ion collisions will be also discussed, presenting a feasibility study of J/ψ polarization with respect to the event plane. Finally the measurement of Υ(1S) polarization is shown. This result is obtained for $p_{\mathrm{T}} < 15$ GeV/c, integrating over centrality from 0 to 90%.

Beyond the quarkonium polarization analysis, which represents the main topic of this thesis, a part of the research activity carried out during my PhD was dedicated to the study of

ψ(2S) production in p–Pb collisions at $\sqrt{s_{\rm NN}} = 8.16$ TeV. The results of this analysis show that the strongly interacting system created in p–Pb collisions at LHC energy can dissociate this state, contrary to what happens for the more strongly bound J/ψ. This analysis is performed as a function of transverse momentum, rapidity and collision centrality and is discussed in a dedicated appendix.

The results presented in this thesis have been approved by the ALICE collaboration. The measurements of J/ψ and Υ(1S) polarization in Pb–Pb collisions as a function of the transverse momentum are reported in Ref. [1] and submitted to Physics Letters B, while the study of ψ(2S) production in p–Pb collisions was published in Refs. [2, 3]. Finally the analysis of J/ψ polarization as a function of the collision centrality was approved by ALICE as a preliminary result.

Table of Contents

Chapter 1

Quark-Gluon plasma and heavy-ion collisions

The standard Model (SM) is the theory which provides the most detailed description of the fundamental interactions among elementary particles in our Universe. In this model, formally a quantum field theory, the basic building blocks of matter are semi-integer spin particles, the *fermions*, interacting through the exchange of spin-integer particles, the *bosons*. Fermions are classified in three generations of quarks (u,d), (c,s), (t,b) and three generations of leptons (e,ν_e), (μ,ν_μ), (τ,ν_τ), each of them with their corresponding anti-particles. The bosons are mediators of the three fundamental forces and each of them is associated to a specific interaction. The *electromagnetic* force is carried by the *photon* (γ), the weak force is carried by the $W^\pm$ and Z bosons, while the strong force is carried by *gluons* (g). The latter is responsible for binding the quarks inside the *hadrons*, condition which is known as *confinement*, since quarks can be observed only as bound states and not as free particles. This assumption can be considered as valid up to few microseconds after the Big Bang, because before the temperature and the energy density were so high that no bound state existed. The state of matter where quarks and gluons are no more confined inside hadrons is named Quark-Gluon plasma and is an important research topic of high-energy physics.

1.1 Quantum Chromodynamics

Quantum Chromodynamics (QCD) is a gauge field theory which mathematically describes the interaction between quarks and gluons. Based on the non-Abelian symmetry group

$SU(3)$, the lagrangian of QCD [4] can be written as

$$\mathcal{L}_{\rm QCD} = -\frac{1}{4}G_a^{\mu\nu}G^a_{\mu\nu} + \sum_f \bar{q}_f(i\gamma_\mu D_\mu - m_f)q_f, \tag{1.1}$$

where $G_a^{\mu\nu}$ is the gluon field tensor, q_f represents the quark field, γ_μ the Dirac matrices and m_f the quark mass, while a and f are the gluon color and the flavor indexes. As for QED, the invariance under local gauge transformation is required introducing the covariant derivative $D_\mu \equiv \partial^\mu + ig_S\frac{\lambda^a}{2}G_a^\mu$, which contains λ^a, the generators of the fundamental representation of $SU(3)$. The gluon tensor can be decomposed as follows:

$$G_a^{\mu\nu} = \partial^\mu G_a^\nu - \partial\nu G_a^\mu - g_{\rm S}\sum_{b,c=1}^{8} f_{abc}G^{\mu b}G^{\nu c} \tag{1.2}$$

with G_a^ν the gluon field and f_{abc} the structure constants of $SU(3)$. With this formalism all interactions between quarks and gluons are given in terms of $g_{\rm S}$, which is the *strong coupling constant* and it is normally written as $\alpha_{\rm S} = g_{\rm S}^2/4\pi$. The first term of eq. 1.1 plays a crucial role because introduces one of the properties deriving from the non-Abelian character of the color group, the *gluon self-interaction*, which is a different feature with respect to QED. In fact, in QED the coupling constant α(S) decreases at large distances, effect which can be intuitively explained considering the charge screening generated by a virtual fermion pair. Differently, in QCD gluons have color charge, and this property determines an increase of the field at large distance, the so called *anti-screening*. The dependence of the strong coupling constant on the momentum transferred in the interaction can be written as:

$$\alpha_{\rm S}(Q^2) = \frac{\alpha_0}{1+\alpha_0\frac{33-2n_f}{12\pi}ln\frac{Q^2}{\mu^2}} \tag{1.3}$$

where n_f is the number of quark flavors and α_0 the coupling constant for a given momentum transferred μ. From this expression it is easy to observe that the strength of the coupling constant decreases for short distances ($Q \to \infty$), allowing quarks to behave as quasi-free particles. This particular property is called *asymptotic freedom* and it allows to treat QCD as a perturbative theory when $\alpha_{\rm S} \to 0$. On the contrary, for large distances ($Q \to 0$) the coupling constant becomes large and color charges are bound inside hadrons, in the so called *confinement* regime. In Fig. 1.1 a summary of the QCD coupling constant measurements performed considering different systems is shown as a function of Q.

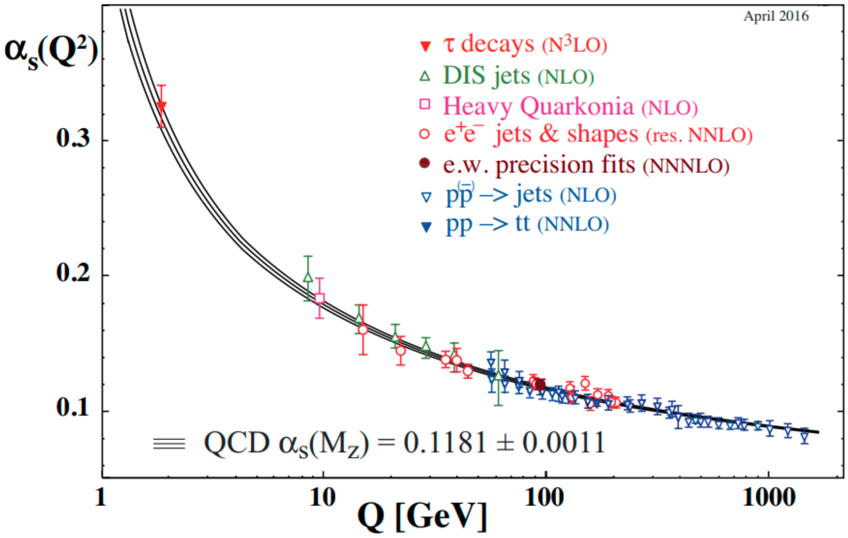

Figure 1.1: Summary of the measurements of α_S as a function of the energy scale Q [5].

1.2 The QCD phase diagram

When dealing with an extended system of quarks and gluons, the regimes of confinement and asymptotic freedom can be connected by means of a phase transition. The transition can be illustrated in a phase diagram, in terms of temperature (T) and baryochemical potential (μ_B). The latter represents the variation of energy (E) in the system associated to the variation of the net number of baryons (N_B) of a certain species ($\mu = \partial E/\partial N_B$). In Fig. 1.2 the QCD phase diagram is shown with ordinary nuclear matter approximately around $T \approx 0$ and $\mu_B \approx 1$ GeV. When the temperature of the system increases, strongly interacting matter moves to a state of hadron gas [6], where quarks and gluons are still bound inside colorless objects. The transition to a deconfined phase is expected to occur via a *first order transition*, which then becomes a continuous *crossover* [7] for low baryochemical potential and high temperature. For high values of μ_B and low temperature the nuclear matter behaves as a color superconductor, a situation which could be present inside neutron stars [8].

An approximative estimate of the pressure and the energy density necessary for the QGP formation can be provided by the the *bag model* [9]. In this phenomenological model, hadrons are formed by massless quarks confined into a bag of finite dimension and the confinement derives from the balancing of the pressure exerted by quarks into the bag and an external pressure B, which parametrizes the non-perturbative effects of QCD.

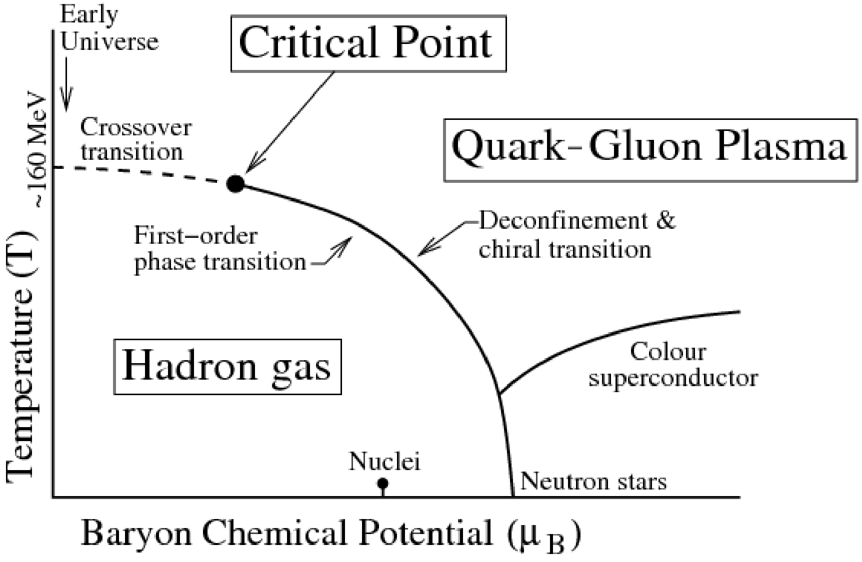

Figure 1.2: The QCD phase diagram as a function of the temperature (T) and the baryon chemical potential (μ_{B}). Figure taken from [10].

Parton deconfinement is achieved when the internal pressure exceeds the value of B. This situation can occur in two different ways:

- increase of temperature and as a consequence increase of the kinetic energy of quarks inside the bag. This is the situation of the "hot" QGP.
- increase of baryon density via compression. This scenario is possible in extremely dense objects like neutron stars and is defined as "cold" QGP.

Numerically, the bag pressure is estimated in the model to be around 200 MeV. The pressure of an ideal QGP can be computed as

$$P = g_{\mathrm{DOF}} \cdot \frac{\pi^2}{90} \cdot T^4, \tag{1.4}$$

where g_{DOF} corresponds to the total number of degrees of freedom for quarks, anti-quarks and gluons. From these vales one gets $T_{\mathrm{c}} \sim 145 - 150$ MeV for the critical temperature. The corresponding energy density is $\varepsilon = 3P \sim 1$ GeV/fm^3.

A rigorous estimate of the temperature and the energy density at the phase transition can be obtained in the framework of the Lattice QCD. The estimate of the pressure, energy density and entropy density as a function of the temperature of the system, for $\mu_\mathrm{B} = 0$, are presented in Fig. 1.3. The strong increase in all the thermodynamic variables is related to the increase in the degrees of freedom of the system occurring at $T \sim 150$ MeV. For smaller temperatures, the observables are in agreement with the predictions of the Hadron Resonance Gas (HRG) model [11], which is based on the assumption of thermal equilibrium for a system composed of free hadrons and resonances and is expected to well describe all the thermodynamic quantities at low temperature.
A relative precise evaluation of the critical temperature T_c can be obtained by the analysis of the temperature dependence of the *chiral susceptibility* (see Fig. 1.3, right panel), a quantity related to the chiral symmetry of QCD and that is expected to change rapidly in the vicinity of T_c. These studies give the value

$$T_c = (154 \pm 9)\ \mathrm{MeV}. \tag{1.5}$$

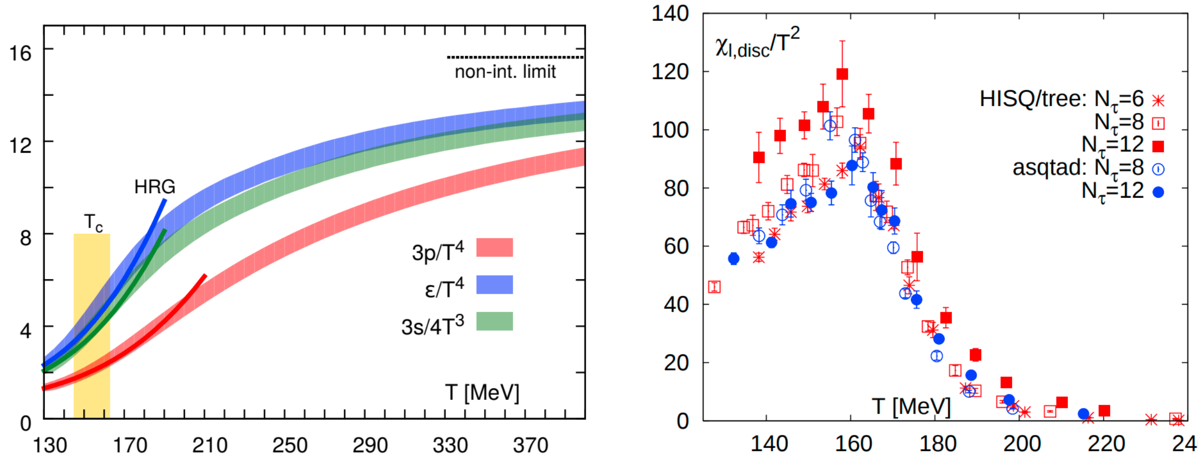

Figure 1.3: Left panel: normalized pressure, energy density and entropy density as a function of the temperature [12]. The dark lines represent the prediction of the hadron gas resonance (HRG) model [11]. Right panel: disconnected part of the chiral susceptibility as a function of temperature for different choices of the temporal extent (N_τ) (for more details see Ref. [13]).

1.3 Heavy-ion collisions

Heavy-ion collisions represent the experimental tool through which it is possible to study the Quark-Gluon plasma. With such collisions, it is possible to obtain a strongly interacting medium with large spatial extension, greater than the scale of the strong interaction (~ 1 fm), and a long lifetime. In this way the system can reach the thermal equilibrium and can be described with the language of the thermodynamics ($t \gg 1$ fm$/c$). These features are necessary but not sufficient to the QGP formation.

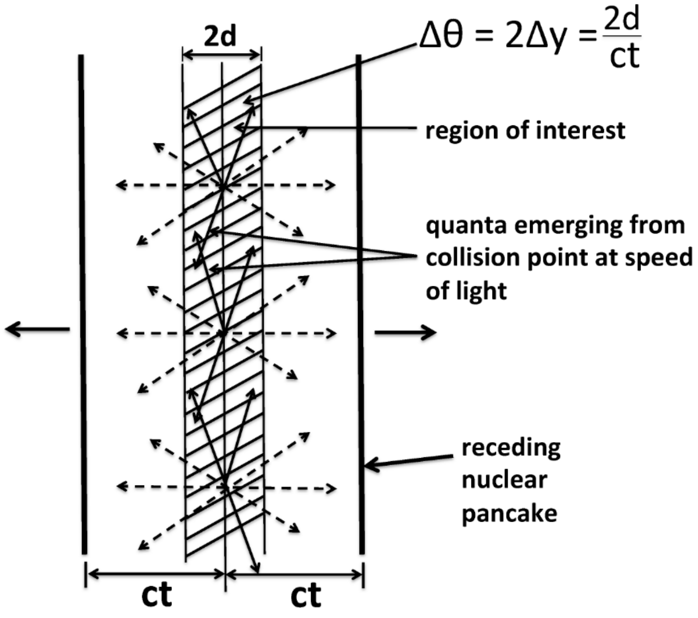

Figure 1.4: Geometry of the initial state of the produced plasma in AA collisions [14].

As discussed previously, a critical energy density of ~ 1 GeV/fm^3 has to be reached. A simple estimate of this quantity in the frame of the heavy-ion collisions was given by J.D. Bjorken [14] starting with the following assumptions:

- the crossing time of the colliding nuclei is smaller than the characteristic time of the strong interaction, which can be estimated as $\tau_{\text{strong}} \sim 1/\Lambda_{\text{QCD}} \sim 1$ fm$/c$. Since in ultra-relativistic heavy-ion collisions the nuclei are Lorentz-contracted (defined as "pancakes" in Ref. [14] and shown in Fig. 1.4), the crossing time is calculated as $\tau_{\text{cross}} = 2R/\gamma$, with γ the Lorentz factor and R the nuclear radius, obtaining that

$\tau_{\mathrm{cross}} \ll \tau_{\mathrm{strong}}$ for $\gamma > 12$. The latter is valid for a center-of-mass energy larger than $\sqrt{s_{\mathrm{NN}}} \sim 25$ GeV, meaning that at the LHC this condition is fully respected since $\sqrt{s_{\mathrm{NN}}} = 5.02$ TeV. Under this hypothesis, the particles which are generated in the collision process, are created once the nuclei have crossed each other.

- a plateau in the particle distribution at mid-rapidity. This assumption ensures the rapidity symmetry of the system, simplifying significantly its hydrodynamical description.

Under these two assumptions, the energy density can be estimated as

$$\varepsilon_{\mathrm{Bj}}(y,\tau) = \left|\frac{dE_{\mathrm{T}}}{dy}\right| \times \frac{1}{\pi R^2 \tau}, \tag{1.6}$$

where τ is the formation time, R the nuclear radius ($R \sim 1.124\ A^{-1/3}$) and E_{T}[1] the transverse energy.

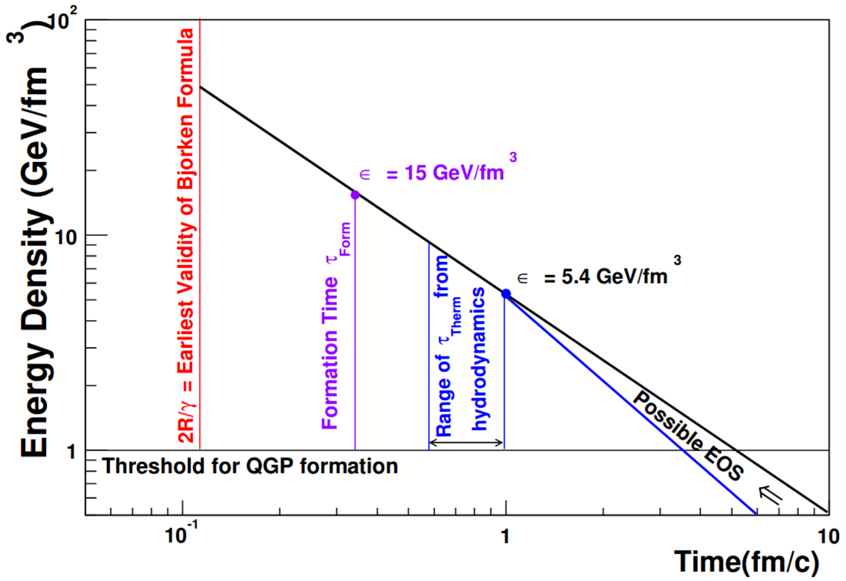

Figure 1.5: Energy density as a function of time derived using the Bjorken formula [15].

---

[1] $E_{\mathrm{T}} = E\frac{\vec{p_{\mathrm{T}}}}{|\vec{p}|} = \frac{E}{\sqrt{E^2-m^2}}\vec{p_{\mathrm{T}}}$

At RHIC, where the center-of-mass energy per nucleon is $\sqrt{s_{\mathrm{NN}}} = 200$ GeV, the particle formation time is evaluated to be $\tau_{\mathrm{Form}} \sim 0.35$ fm/c. As shown in Fig. 1.5 the corresponding energy density is $\varepsilon_{\mathrm{Bj}} \sim 15$ GeV/fm^3, well above the approximate threshold of 1 GeV/fm^3. After particle formation, the system expands and cools down. Still at RHIC energy, the thermalization time (τ_{Therm}) of the system is assumed to range around 1 fm/c. At that moment the energy density is $\varepsilon \sim 5.4$ GeV/c^2, still much larger than the critical energy density. More generally, in a scenario in which Bjorken assumptions are valid, the space-time evolution of heavy-ion collisions can be summarized through the following stages (see Fig. 1.6):

1. $0 < t \lesssim 1$ fm/c → **pre-equilibrium**: this phase starts after the collision ($t = 0$) and it is characterized by particle production mainly via hard scatterings. Since this implies processes with the exchange of large Q^2, perturbative QCD can be applied for theoretical calculations. The thermal equilibrium is then achieved through multiple interactions among the partons produced in the collision.

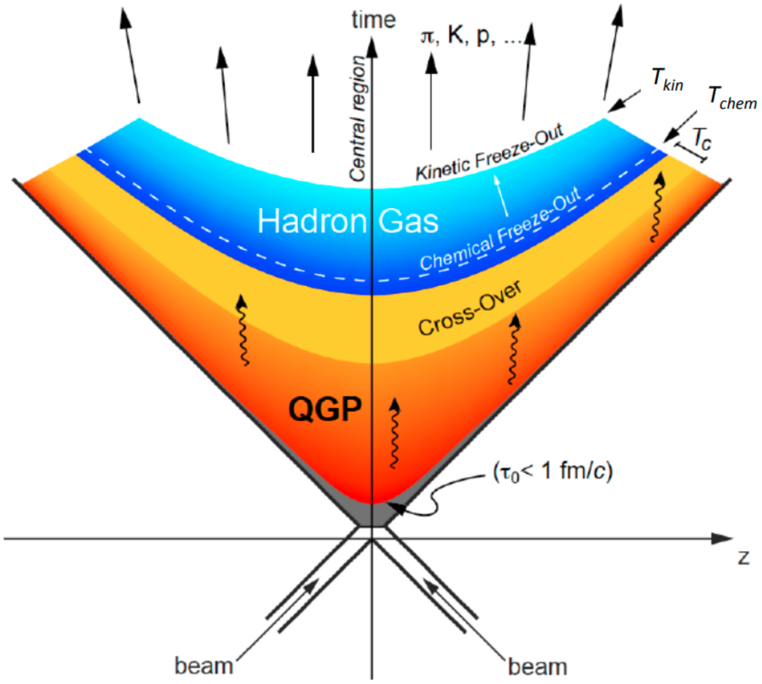

Figure 1.6: Space-time evolution of the medium produced in a heavy-ion collision [16].

2. $1 < t \lesssim 10$ fm/c → **thermalization and QGP**: after having reached the thermal equilibrium, the strongly interacting system expands due to the pressure gradient between the surrounding vacuum and the dense medium. This phase can be described in the picture of the *relativistic viscous hydrodynamics* [17].

3. $t \gtrsim 10$ fm/c → **hadronization**: during the expansion, the system cools down and when the critical temperature is reached, the hadronization starts. In general the formation of new hadrons may occur via two different processes: *fragmentation*, when high-p_{T} partons produce high-p_{T} hadrons, and *coalescence*, when hadrons are formed through the combination of low-p_{T} partons. The relative abundances of the various particle changes as long as the inelastic interactions continue and when they stop there is the so called *chemical freeze-out* (T_{chem}). A second freeze-out, namely *kinetic* (T_{kin}), occurs when also the elastic interactions between hadrons cease and the particles produced in the collision stream freely towards the detectors.

From an experimental point of view, the exploration of the QCD phase diagram has been performed by various heavy-ion collision experiments. More in detail, the large center-of-mass energy reached by the LHC and RHIC colliders, $\sqrt{s_{\mathrm{NN}}} = 5.02$ and 0.2 TeV respectively, allows to investigate the regime of $\mu_{\mathrm{B}} \to 0$ and high temperature. This is mainly pursued by dedicated experiments, as the ALICE experiment at the LHC and the STAR and PHENIX experiments at RHIC. On the opposite, the domain of large baryon chemical potential is studied in both collider and fixed target experiments, characterized by center-of-mass energies around $\lesssim 20$ GeV. Among them is important to mention the Beam Energy Scan (BES) [18] program at RHIC, scheduled from 2019 to 2021. In this campaign of measurements data will be taken from $\sqrt{s_{\mathrm{NN}}} = 7$ to 19 GeV in collider mode and from $\sqrt{s_{\mathrm{NN}}} = 3$ to 7 GeV in fixed target mode, exploring μ_{B} with steps of ∼50 MeV. The CBM collaboration [19] at the FAIR facility at GSI will measure various observables in fixed target collisions at beam energies between $\sqrt{s_{\mathrm{NN}}} = 10$ and 45 GeV, with emphasis on very high interaction rates. Finally, at the CERN-SPS the NA61/SHINE experiment [20] focuses on light nuclei collisions, varying the beam momentum from 13 to 158 GeV/c per nucleon. In the future, another experiment at CERN-SPS, named NA60+ [21], might be able to study the leptonic observables in the full SPS energy range.

1.4 Heavy-ion collision geometry

The geometry of a collision between heavy nuclei has in the centrality one of its key parameters. The definition of this observable depends on the impact parameter b, which represents the distance between the centers of the colliding nuclei for nucleus-nucleus collisions, and the distance between the proton and the center of the nucleus in proton-nucleus collisions. Centrality allows to classify collisions as:

- *peripheral* when the impact parameter b is large and few nucleons are involved in the process. In this case there is a reduced overlap region between the two colliding nuclei, which means that a small interaction volume and few particles are produced.
- *central* when the impact parameter b is small and many nucleons are involved in the process. In this case there is an extended overlap region between the two colliding nuclei, which means that a large interaction volume and many particles are produced.

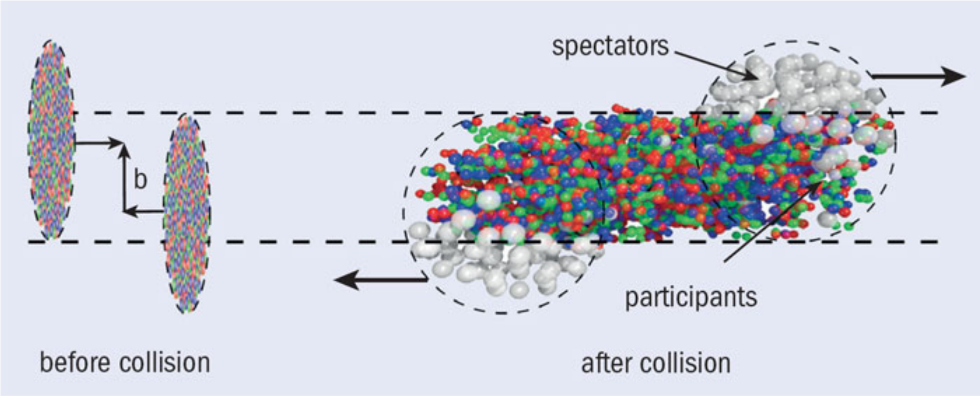

Figure 1.7: Schematic picture of the initial and the final stages of a heavy-ion collision.

As shown in Fig. 1.7, once the impact parameter is defined, nucleons can be divided among those which have at least one interaction, namely *participants*, and those traveling without interacting, namely *spectators*. As a consequence it is possible to define two other parameters which are often used to quantify the collision centrality, the number of binary collisions between nucleons (N_{coll}) or the number of nucleons participating to the collision (N_{part}). These quantities cannot be directly measured, but they can be estimated using a phenomenological model describing the geometrical features of a heavy-ion collision, the *Glauber model* [22]. In this model the interaction among nuclei is treated as an incoherent superposition of binary collisions between point-like objects. Moreover, colliding nucleons travel along straight lines, while the elementary nucleon-nucleon cross section is assumed to be independent on the number of collisions they undergo. These assumptions are very important because they allow to derive an analytical expression for the N_{part}, N_{coll} and many other observables widely used in heavy-ion collisions.

1.5 QGP: experimental probes

Given the short time scale associated to the formation and the existence of the Quark-Gluon Plasma, a direct observation of this state of matter is not feasible. Nevertheless there is a wide set of observables which are sensitive to the production of this strongly interacting medium, hence allowing to understand if the medium is effectively formed in the collision and to study its properties. Since the list of observables is rather large, in general they are classified in *soft* and *hard probes*. In the following sections some of the results relative to the main observables studied will be reviewed, focusing on experiments carried out at RHIC ($\sqrt{s_{\mathrm{NN}}} = 0.2$ TeV) and LHC ($\sqrt{s_{\mathrm{NN}}} = 2.76$ and 5.02 TeV).

1.5.1 Soft probes

Most particles produced in heavy-ion collisions are produced via soft interactions ($\sim$99.5% with $p_{\mathrm{T}} < 1$ GeV/c in Au-Au collision at RHIC). Typically, their production yields increase linearly with the number of nucleons participating to the collision. In the following some results on direct photon production, particle spectra, anisotropic flow and strangeness enhancement are reported.

Direct photons

Direct photons represent an important tool to study the evolution of the medium in heavy-ion collisions. Defined as those photons not originating from hadron decays, they are produced in all the stages of the collision, escaping from the nuclear matter basically unaffected and carrying with them different kind of information. In particular, the study of *thermal* radiation emitted by the QGP and nuclear matter created in the collision provides information about the temperature and space-time evolution of the medium. These photons mainly contribute to the low-p_{T} range ($p_{\mathrm{T}} \leq 4$ GeV/c).

The PHENIX experiment measured the direct photon spectrum in Au-Au collisions at $\sqrt{s_{\mathrm{NN}}}$ =200 GeV [23], observing that it is compatible for $5 \leq p_{\mathrm{T}} \leq 21$ GeV/c with the proton-proton one scaled with the number of binary nucleon-nucleon collisions. Such high-p_{T} photons (prompt production) are produced in the hard scattering of incoming partons. This result was then confirmed by the ATLAS [24] and CMS [25] collaborations in their measurements of isolated photons. At low p_{T} ($p_{\mathrm{T}} \leq 3$ GeV/c), the PHENIX experiment observed a clear excess of direct photons with respect to scaled pp collisions [26]. By parameterizing the excess with an exponential function ($f(p_{\mathrm{T}}) \propto e^{-p_{\mathrm{T}}/T_{\mathrm{eff}}}$), it is possible to extract the slope parameter, which can be interpreted as the effective temperature of the system. The same measurement was performed by the ALICE collaboration [27]. In Fig. 1.8 the two results are compared. It can be noticed that the T_{eff} measured by ALICE ($T_{\mathrm{eff}} = 304 \pm 11 \pm 40$ MeV) is larger than the one by PHENIX ($T_{\mathrm{eff}} = 239 \pm 25 \pm 7$ MeV), which indicates that a hotter medium with average temperature much higher than T_{c} is produced moving from RHIC to LHC energies. In addition these results are in agreement with models including high radial flow velocities and QGP formation [28].

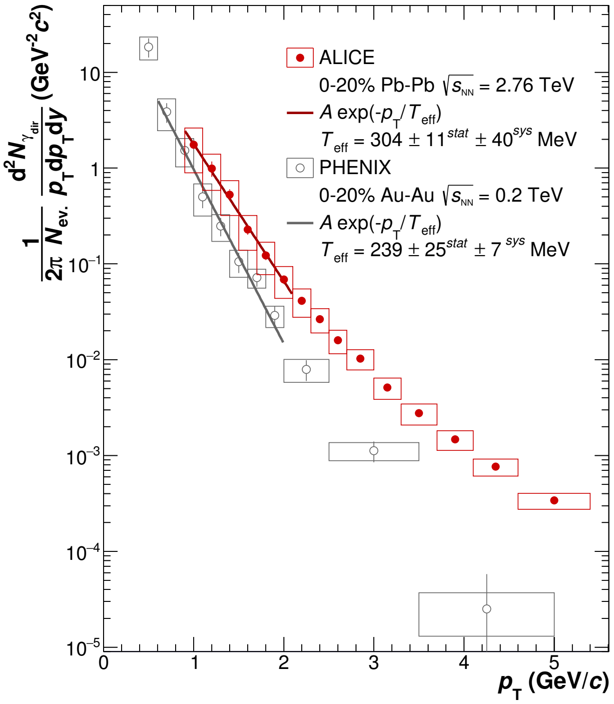

Figure 1.8: Direct photon spectra measured by the ALICE collaboration [27] in Pb–Pb collisions at $\sqrt{s_{\mathrm{NN}}}$ =2.76 TeV and by the PHENIX collaboration [29] in Au–Au collisions at $\sqrt{s_{\mathrm{NN}}}$ =200 GeV. Both results are obtained for the 0-20% centrality class and the pQCD contribution is not subtracted.

Particle spectra

The *momentum spectra* and *yields of identified particles* represent an important tool to investigate the collective and thermal properties of the medium. Assuming a Boltzmann-

Gibbs distribution, the particle spectra at the kinetic freeze-out can be written as

$$\frac{1}{m_{\mathrm{T}}}\frac{\mathrm{d}N}{\mathrm{d}m_{\mathrm{T}}} \propto e^{-\frac{m_{\mathrm{T}}}{T_{\mathrm{slope}}}}, \tag{1.7}$$

where m_{T} is the transverse mass[2]. The temperature T_{slope} is a free parameter and can be studied for various particles and different collision systems.

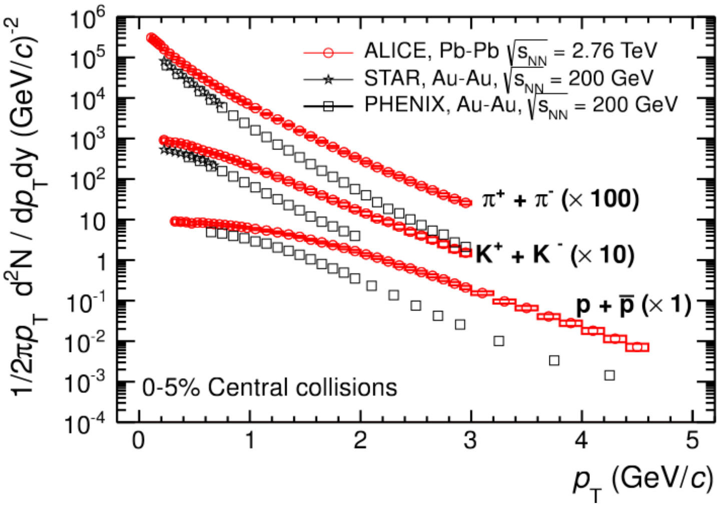

Figure 1.9: Distributions of proton(anti-proton), pions and kaons as a function on p_{T} in central (0-5%) Au–Au collisions at $\sqrt{s_{\mathrm{NN}}}$ = 200 GeV at RHIC [30, 31] and in Pb–Pb collisions at $\sqrt{s_{\mathrm{NN}}}$ = 2.76 TeV at the LHC [32].

Measurements of the STAR collaboration in pp collisions at $\sqrt{s_{\mathrm{NN}}}$ = 200 GeV [33] have shown that the slope of proton, pion and kaon spectra for $m_{\mathrm{T}} < 2$ GeV/c^2 are in fair agreement, an observation indicated as m_{T}*-scaling*. If T_{slope} represents the emission temperature of the light hadrons produced in the collision, it should correspond, in a simple Boltzmann's scenario, to the kinetic freeze-out temperature. The STAR collaboration measured $T_{\mathrm{slope}} = 127 \pm 13$ MeV [30]. The scaling with the transverse mass is broken in nucleus-nucleus collisions, where a different slope for the various light hadron spectra is observed both at RHIC [30, 31] and at the LHC[32]. As shown in Fig. 1.9, the slopes for protons, kaons and pions are inversely proportional to the particle mass, with a shift

---

[2] $m_{\mathrm{T}} = \sqrt{m^2 + p_{\mathrm{T}}^2}$

to higher p_{T} values for the heaviest ones. This behavior indicates the superposition of a collective motion to the thermal agitation, which can be expressed by rewriting T_{slope} as

$$T_{\mathrm{slope}} = T_{\mathrm{kin}} + \frac{1}{2} m \langle v_{\mathrm{T}} \rangle^2, \tag{1.8}$$

where v_{T} is the velocity in the transverse plane and T_{kin} is the temperature at the kinetic freeze-out. This collective motion, named *radial flow*, is due to the pressure gradients generated by the compression and the heating of the nuclear matter in the collision and it is responsible of pushing the mean transverse momentum of the particles proportionally to their mass. In addition, the softer spectrum measured at RHIC with respect to LHC (Fig. 1.9) suggests the presence of stronger pressure gradients when the center-of-mass energy increases.

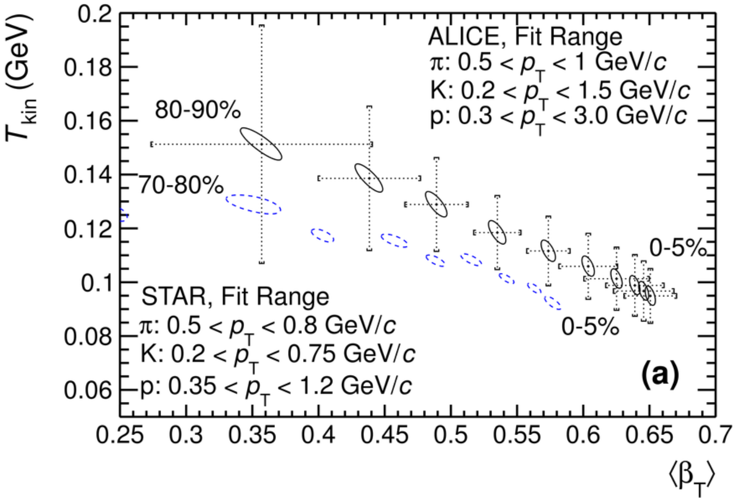

Figure 1.10: T_{kin} as a function of the mean radial velocity $\langle \beta_{\mathrm{T}} \rangle$ measured by the ALICE experiment in Pb–Pb collisions at $\sqrt{s_{\mathrm{NN}}} = 2.76$ TeV and by the STAR collaboration Au–Au collisions at $\sqrt{s_{\mathrm{NN}}} = 200$ GeV. Figure taken from Ref. [34].

The hydrodynamic expansion along the transverse plane can be studied with the Blast-Wave model [35], which allows to extract both the kinetic freeze-out temperature T_{kin} and the mean radial transverse velocity $\langle \beta_{\mathrm{T}} \rangle$. In Fig. 1.10, the results of a Blast-Wave fit obtained by ALICE at $\sqrt{s_{\mathrm{NN}}} = 2.76$ TeV and by the STAR collaboration at $\sqrt{s_{\mathrm{NN}}} = 200$ GeV are compared, showing a stronger radial flow and a higher T_{kin} at LHC with respect to RHIC.

Anisotropic transverse flow

Azimuthal anisotropies in the particle production represent another important signature of the collective motion of the particles produced in heavy-ion collisions, which is a consequence of the thermalization of the system. As shown in Fig. 1.11, the partial overlap of the colliding nuclei for non-central collisions creates an asymmetric interaction volume, typically represented with an *almond shape*. For each collision it is also possible to single out a reaction plane, defined by the impact parameter and the beam axis, rotated by an angle Ψ_{RP} with respect to the laboratory frame.

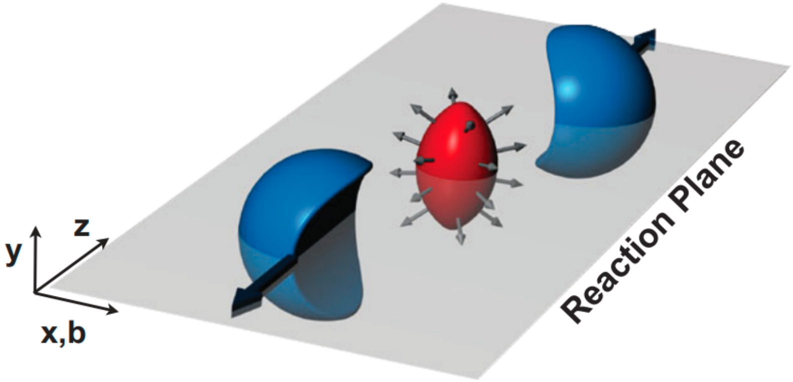

Figure 1.11: Schematic view of a non-central collision between two heavy nuclei. In the figure the reaction plane, containing the impact parameter b, is shown in gray, while the almond shape in red represents the interaction volume. The figure is taken from [36].

The correlation among the azimuthal angle and the impact parameter, named *anisotropic flow*, is generated when the momentum of the particles in the final state does not depend only on the local conditions of the production, but also on the global geometry of the event. From a macroscopic point of view, the azimuthal distribution of detected particles will be anisotropic, since the pressure gradients will be larger in the $x-z$ plane with respect to the y axis. On a microscopic scale, the initial spatial anisotropy can be converted through the interaction among the produced particles into an anisotropy in the particle momenta. The latter can be measured via the Fourier expansion of the azimuthal distribution of particles with respect to Ψ_{RP}:

$$\frac{\mathrm{d}N}{\mathrm{d}(\varphi-\Psi_{\mathrm{RP}})}=\frac{N_0}{2\pi}(1+2v_1\cos(\varphi-\Psi_{\mathrm{RP}})+2v_2\cos[2(\varphi-\Psi_{\mathrm{RP}})]+...), \tag{1.9}$$

where $v_1, v_2, ...$ are the flow coefficients, describing the difference with respect to an isotropic distribution, N_0 is a normalization constant and φ is the azimuthal angle measured in the laboratory frame. The terms containing the sine are not present in Eq. 1.5.1 as a consequence of the reflection symmetry with respect to the reaction plane. The coefficients of the Fourier expansion can be calculated as

$$v_n = \langle \cos[n(\varphi - \Psi_{\mathrm{RP}}) \rangle, \tag{1.10}$$

where the $\langle\ \rangle$ indicate the average over all the particles, summed over all the events. According to the value of v_n it is possible to distinguish between different cases:

- when $v_1 \neq 0$ a *directed flow* is observed. The non-zero value assumed by the first coefficient of the Fourier expansion implies that there is a preferred direction in the emission of the particles, in particular there is a difference among the number of particles produced parallel and anti-parallel to the impact parameter.
- when $v_2 \neq 0$ an *elliptic flow* is observed. Differently from directed flow, a non-zero v_2 means that there is a difference in the number of particles produced parallel and orthogonally with respect to the impact parameter. As mentioned above, the elliptic flow represents a deformation of the particle distribution in the transverse plane, and it can be explained considering the effect of the different pressure gradients with respect to the reaction plane. If $v_2 < 0$ the emission is mainly out-of-plane, otherwise if $v_2 > 0$ it is mainly in-plane.
- values of $v_3 \neq 0$ and $v_4 \neq 0$, namely *triangular* and *quadriangular flow*, are related to the initial inhomogeneities of the system. Their measurement is particularly important to study the properties of the medium and the dynamics of the thermalization.

An example of the information which can be extracted measuring the flow coefficients is shown in Fig. 1.12, where the elliptic flow for different light hadron species as a function of p_{T} [37] is reported. It is interesting to observe that the v_2 magnitude increases with centrality up to $40-50\%$ for all the species. This behavior is expected since the eccentricity of the overlap volume increase with centrality, causing an almost linear increase of the v_2. For more peripheral collisions (i.e. $50-60\%$ and $60-70\%$) the v_2 is smaller than for previous centralities, suggesting that system formed has short life time, not allowing the formation of a large elliptic flow.

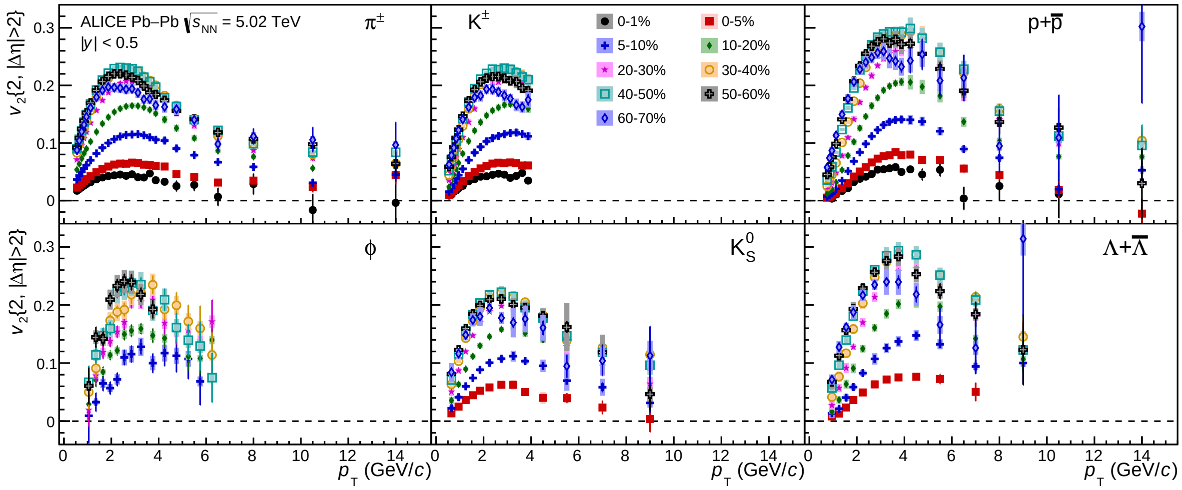

Figure 1.12: Elliptic flow (v_2) $p_{\rm T}$ dependence for $\pi^{\pm}$, $K^{\pm}$, $p+\bar{p}$, ϕ, $K^0_{\rm S}$ and $\Lambda+\bar{\Lambda}$ in different centrality classes [37].

Strangeness enhancement

The strangeness enhancement was one of the early signatures proposed for the QGP formation [38]. The original idea of studying strange hadrons in nucleus-nucleus collisions was that strange quarks are not present in the colliding nuclei but can be abundantly produced in the plasma, due to the fact that at the critical temperature the mass of the strange quark is expected to decrease from its constituent value to its current value of about $\sim$ 100 MeV/c^2. Therefore, their enhanced production could represent a signature of the deconfinement phase. In fact the high density of strange quarks in the medium is a natural source of strange hadrons like K^+/K^- $(u\bar{s}/\bar{u}s)$ and $\Lambda(uds)$, named *primary strange*. The enhancement should be particularly large for baryons containing more than one strange quark, like $\Xi^-(dss)$ and $\Omega^-(sss)$, which are also called *multi-strange*. Such an enhancement was already observed at SPS energies ($\sqrt{s_{\rm NN}} \sim 20$ GeV) by the NA57 experiment [39]. Further measurements of the abundances of strange hadrons relative to pions at RHIC and at the LHC did not show a significant dependence on the center-of-mass energy and on the collision centrality. In particular it was realized that particle ratios in central collisions are in agreement with the predictions for a hadron gas in thermal and chemical equilibrium, while in peripheral collisions, particle ratios start to decrease and become similar to the ones observed in pp collisions. This different behavior was explained considering that in central collisions, given the size of the system and the high particle multiplicity, the grand canonical ensemble limit [40] is valid and the strangeness conservation is satisfied globally. On the contrary in peripheral collisions, where the interaction volume is smaller, the canonical ensemble must be applied, hence the strangeness conservation is valid only locally. As a consequence the enhancement seen in nuclear collisions is in reality due to the so-called *canonical suppression* [41] occurring in collisions of small systems, that disappears in nucleus-nucleus collisions.

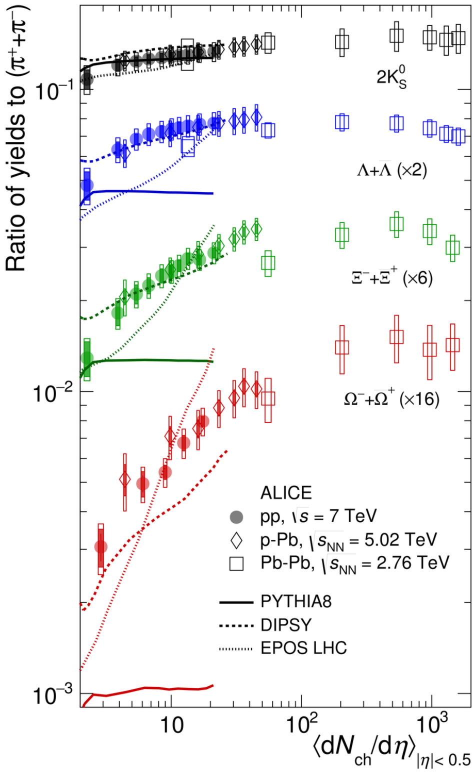

Figure 1.13: p_{T}-integrated yield ratios to pions $(\pi^{+}+\pi^{-})$ as a function of $\langle dN_{ch}/d\eta\rangle$ for $|y| < 0.5$ in pp, p–Pb and Pb–Pb collisions. Results are compared with Monte-Carlo models [42],[43] and [44].

One of the most interesting recent results in this field of research is shown in Fig. 1.13, where the particle ratio for K^0_S, $\Lambda(\bar{\Lambda})$, $\Xi^{-}(\Xi^{+})$ and $\Omega^{-}(\Omega^{+})$ relative to pions is shown as a function of the mean pseudorapidity densities of primary charged particles $\langle dN_{ch}/d\eta\rangle$ at midrapidity ($|\eta| < 0.5$) [45]. The measurements are obtained for different colliding systems and at slightly different center-of-mass energies, but is important to notice that there is a continuous increasing trend for the particle ratios as a function of the multiplicity in pp and p–Pb collisions, while in Pb–Pb ones no further significant dependence on the multiplicity is observed. This suggests that there is a common physical mechanism for all the three colliding systems. As evident considering the comparison with Monte Carlo models, the overall mechanism is not fully understood and more extended and precise measurements might be necessary to reach a firm conclusion.

1.5.2 Hard probes

Hard probes are produced in processes with high momentum transfer and therefore on a short time scale. They are characterized by relatively small cross sections and in general perturbative calculations are feasible for their production studies, since α_{S} is small. Typically, their production cross section scales with the number of nucleon-nucleon collisions in the interaction.

Jet quenching

The production of high p_{T}-hadrons occurs in the first stages of the collision, in processes with high transferred momentum Q^2. The time scale associated to the production of these particles ($\tau \ll 1$ fm/c) makes them a perfect probe to study the properties of the QGP, in particular the mechanisms responsible for their propagation and energy loss. High momentum partons, produced via hard scattering, propagate through the expanding hot and dense medium and fragment into "sprays" of hadrons, which are measured as jets. Jets are an important observable for QCD studies already in pp collisions, and in nucleus-nucleus ones their fragmentation is expected to be modified due to the parton-medium interaction. The latter is usually parametrized as the combination of two effects, the elastic scattering with the partons in the medium (*collisional energy loss*) and the gluon radiation (*radiative energy loss*) [46, 47]. One of the consequences of this mechanism is the reduction of the high-p_{T} particle yields, especially for central collisions. This effect can be observed considering two back-to-back jets; since one of them crosses a longer path in the nuclear medium, it becomes softer and broader, and a quenching of the leading hadron p_{T} can be observed.

The angular dependence of the jet suppression was studied by the STAR collaboration in d–Au and Au–Au collisions [48], as shown in in Fig. 1.14. It was observed that the away-side peak, shifted by 180 degrees with respect to near-side one and clearly visible in pp collisions, is strongly suppressed for central Au–Au collisions. while it is not significantly modified in d–Au ones.

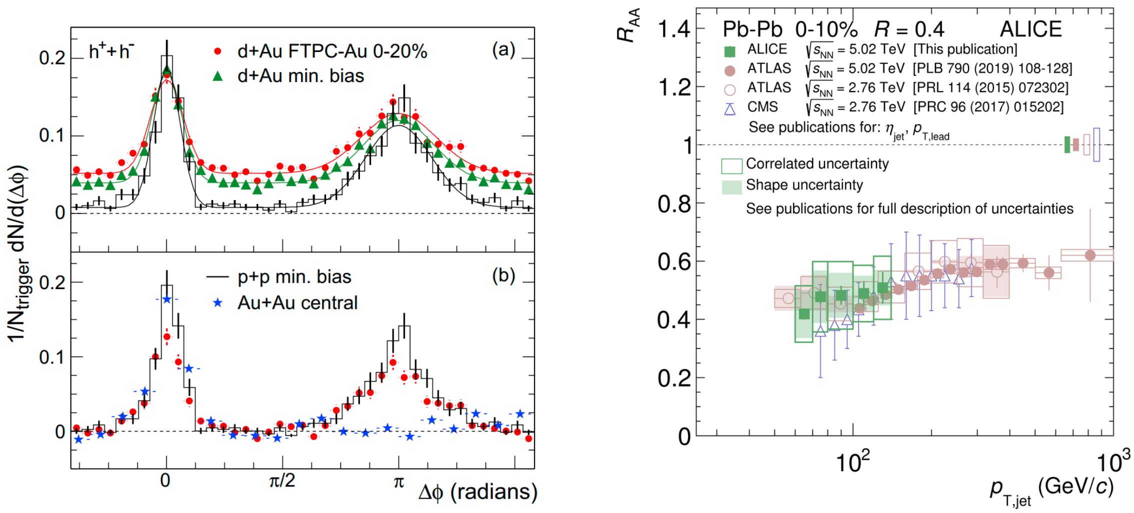

Figure 1.14: Left panel: two-particle azimuthal distributions measured by the STAR collaboration at $\sqrt{s_{\mathrm{NN}}} = 200$ GeV [48] (a) for minimum bias and central d–Au collisions, and for pp collisions; (b) for central d–Au collisions compared with those seen in pp and central Au–Au collisions. Right panel: jet R_{AA} in 0–10% central Pb–Pb collisions for all currently published experimental results [49]. Closed markers denote $\sqrt{s_{\mathrm{NN}}} = 5.02$ TeV and open markers denote $\sqrt{s_{\mathrm{NN}}} = 2.76$ TeV.

Typically the *jet quenching* is quantified via the *nuclear modification factor* R_{AA} defined as

$$R_{\mathrm{AA}} = \frac{1}{\langle N_{\mathrm{coll}} \rangle} \cdot \frac{\mathrm{d}N_{\mathrm{AA}}/\mathrm{d}p_{\mathrm{T}}}{\mathrm{d}N_{\mathrm{pp}}/\mathrm{d}p_{\mathrm{T}}}, \tag{1.11}$$

which is basically the ratio of the jet p_{T} spectrum in Pb–Pb divided by the spectrum in pp collisions scaled by the mean number of binary collisions ($\langle N_{\mathrm{coll}} \rangle$). If the full jet energy remains contained inside the jet-cone defined in the $\eta - \phi$ plane and there are no initial state effects, R_{AA} should be equal to one. In Fig. 1.14, the comparison among the jet nuclear modification factor measured by the ALICE [49], ATLAS [50, 51] and CMS [52] collaborations at $\sqrt{s_{\mathrm{NN}}} = 2.76$ and 5.02 TeV is shown for more central collisions (0–10%). The measured jet spectrum in Pb–Pb collisions exhibits a strong suppression with respect to pp ones, with a slight p_{T}-dependence. Results from different experiments agree within the uncertainties, without indicating a clear dependence on the center-of-mass energy of the collision.

Open heavy flavors

Mesons and baryons which contain a single heavy quark, c or b, are usually indicated as *open heavy flavors*. Due to their large masses, their production time ($\tau \sim 0.1$ and 0.02 fm/c for quarks c and b, respectively [53]) is shorter than the QGP formation time ($\tau \sim 0.3-1.5$ fm/c at the LHC [54]), hence heavy quarks experience the evolution of the hot and dense QCD medium. Analogously to jets, the interaction with the QGP induces mechanisms of radiative and collisional energy loss [46, 47], while the hadronization process may occur via fragmentation or via recombination with light quarks (namely *coalescence* [55]). This last mechanism is particularly interesting because it allows to study how the energy loss affects hadrons with different quark composition and to evaluate the modification of the hadronization process.
In proton-proton collisions, hard processes can usually be studied with pQCD calculations, factorizing the cross section for the production of a generic high-p_{T} particle as

$$\sigma_{hh\rightarrow Hx} = PDF(x_a, Q^2)PDF(x_b, Q^2) \times \sigma_{ab\rightarrow q\bar{q}}(x_a, x_b) \times D_{q\rightarrow H}(z_q, Q^2), \tag{1.12}$$

where PDF is the parton distribution function, $x_{a,b}$ the nucleon momentum fraction carried by the a, b parton, $\sigma_{ab\rightarrow q\bar{q}}$ the partonic cross section and $D_{q\rightarrow H}(z_q, Q^2)$ the fragmentation function, expressing the probability that a parton q forms a hadron H with a fraction z_q of the parton momentum [56]. In nucleus-nucleus collisions the cross section as a function of p_{T} is expected to scale with the mean number of elementary collisions. Therefore, the nuclear modification factor is a typical quantity used also in open heavy flavor studies.

In Fig. 1.15, two measurements of heavy flavors and charged particles nuclear modification factors carried out by ALICE and CMS are shown. A clear suppression is present, reaching a factor ∼5 at $p_{\mathrm{T}} \sim 10$ GeV/c. In the left panel the average of D^0, D^+ and D^{*+} is presented. A fair agreement with various models that implement different mixtures of collisional and radiative energy loss effects can be observed. In the right panel, the R_{AA} of D mesons ($D^0 + \bar{D}^0$) is compared with the one of B mesons ($B^{\pm}$) and charged hadrons, which are all in fair agreement for $p_{\mathrm{T}} > 10 - 15$ GeV/c, pointing to a similar suppression at high transverse momentum. At lower p_{T} there is a hint of a smaller suppression for particles containing a b quark. Such a mass dependence of the energy loss is a specific QCD prediction related to the suppression of low-angle gluon emission for heavy quarks (*dead cone effect* [65]).

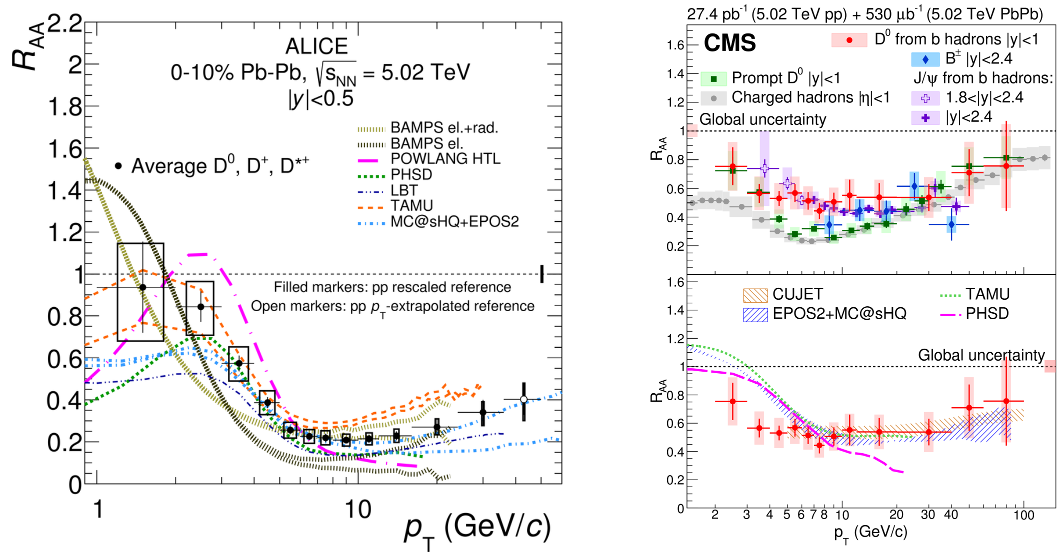

Figure 1.15: Left panel: D mesons R_{AA} as a function of p_{T} in the 0–10% centrality class measured by ALICE [57]. Data are compared with models including heavy quark transport. More details can be found in [58, 59, 60, 61, 62, 63]. Right panel: nuclear modification factor of D mesons, B mesons and charged particles as a function of p_{T} in the 0–100% centrality class measured by CMS [64] and compared with theoretical predictions.

Quarkonia

The study of quarkonia, bound states of a heavy quark and anti-quark, represents an excellent tool to investigate the QGP properties. The possibility of using quarkonia as probe for the Quark-Gluon Plasma, was discussed for the first time by Matsui and Satz in Ref. [66]. The binding energy of the heavy quark pair in the vacuum can be expressed with a Cornell potential

$$V^{\text{VAC}}(r) = -\frac{\alpha}{r} + k \cdot r, \tag{1.13}$$

where α is the Coulombic interaction coupling and k the string tension. When the pair is inside a deconfined medium the potential can be rewritten as

$$V^{\text{QGP}}(r) = -\frac{\alpha}{r} \cdot e^{-r/\lambda_D}, \tag{1.14}$$

where the term $k \cdot r$ disappears, since color charges are free in the QGP, while the negative exponential is the so called Debye screening term, in analogy with the screening of electric charges inside a plasma of electrons and ions. The latter depends on the parameter λ_D, namely the *Debye length*, which is a function of the temperature of the system and is related to the maximum distance between two quarks at which the bound state can be formed. It decreases with increasing temperature leading to a suppression of the quarkonium states once λ_D becomes smaller than their size.

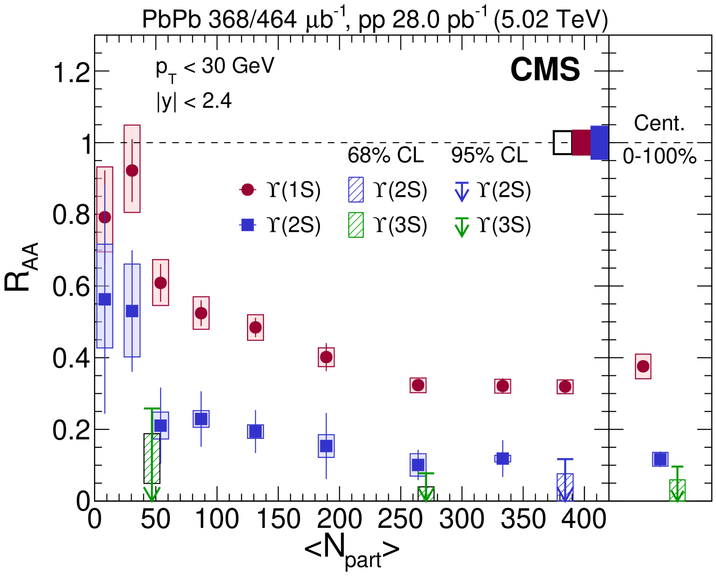

Figure 1.16: J/ψ nuclear modification factor as a function of the mean number of participants ($\langle N_{\text{part}}\rangle$) at $\sqrt{s_{\text{NN}}} = 5.02$ TeV measured by the ALICE experiment [67]. Right panel: Υ(1S), Υ(2S) and Υ(3S) R_{AA} as a function of centrality measured by the CMS collaboration [68].

Thanks to the existence of a large number of quarkonium states which differ in binding energy between a few tens of MeV (ψ(2S)) and more than 1 GeV (Υ(1S)), one could detect a process of *sequential suppression*, which consists in the progressive disappearance of the various quarkonium resonances for increasing values of the temperature of the system. For this reason quarkonia can be considered as a thermometer and comparing their nuclear modification factor with the theoretical predictions it could be possible to give an estimation of the QGP temperature. In Fig. 1.16, the nuclear modification for different bottomonium ($\text{b}\bar{\text{b}}$) states measured by the CMS collaboration is shown [68]. This result is particularly important because the sequential melting is clearly visible. The ground state (Υ(1S)) exhibits a R_{AA} lower than unity for more central collisions, while the excited states

(Υ(2S) and Υ(3S)) are even more suppressed, given their smaller binding energy.

This last part is meant to provide a very brief introduction to quarkonia in heavy ion collisions, in the following chapter we will focus on this topic entering in more details.

Chapter 2

Heavy quarkonia

Quarkonia, bound states of a heavy quark and anti-quark, represent an important tool for the understanding of the Quantum ChromoDynamics (QCD). Their production involves both perturbative and non-perturbative aspects and therefore has to be treated with approaches that includes both regimes. In nuclear collisions, since they are produced in the early stages, they can be used to investigate the properties of the Quark-Gluon Plasma (as briefly anticipated at the end of Chapter 1). For these reasons, heavy quarkonium represents a very versatile probe and a still open field in high energy physiscs, with some aspects related to its production that are not completely settled. In this chapter, a historical introduction to charmonium ($c\bar{c}$) and bottomonium ($b\bar{b}$) will be given, providing the background which can be useful for the understanding of the following sections. A selection of the most recent experimental results will also be discussed.

2.1 The November revolution

The history of heavy quarkonia can be considered to start in November 1974. For particle physics, that period was so crucial and fruitful in terms of scientific discoveries to deserve the name of "*November revolution*".

The team leaded by S. Ting, colliding a 30 GeV/c proton beam on a fixed target at BNL, observed for the first time a sharp peak in the e^+e^- invariant mass spectrum for $m \sim 3.1$ GeV/c^2 [69] and gave it the name "J". Nearly in the same period the group under the supervision of B. Richter announced the observation of a new resonance in the same mass range at the SPEAR storage ring, colliding electron and positron beams [70]. The corresponding papers were submitted to *Physical Review Letters* journal with only one day of difference and because of the simultaneous discovery the new particle was then named J/ψ. Few weeks later another resonant state with a slightly larger mass ($m \sim 3.7$ GeV/c^2) was discovered by the SLAC group, representing the first of many new particles discovered in the following years.

Further studies focused on characterization of the J/ψ, which was found to have the same quantum numbers of the photon ($J^{\mathrm{PC}} = 1^{--}$).

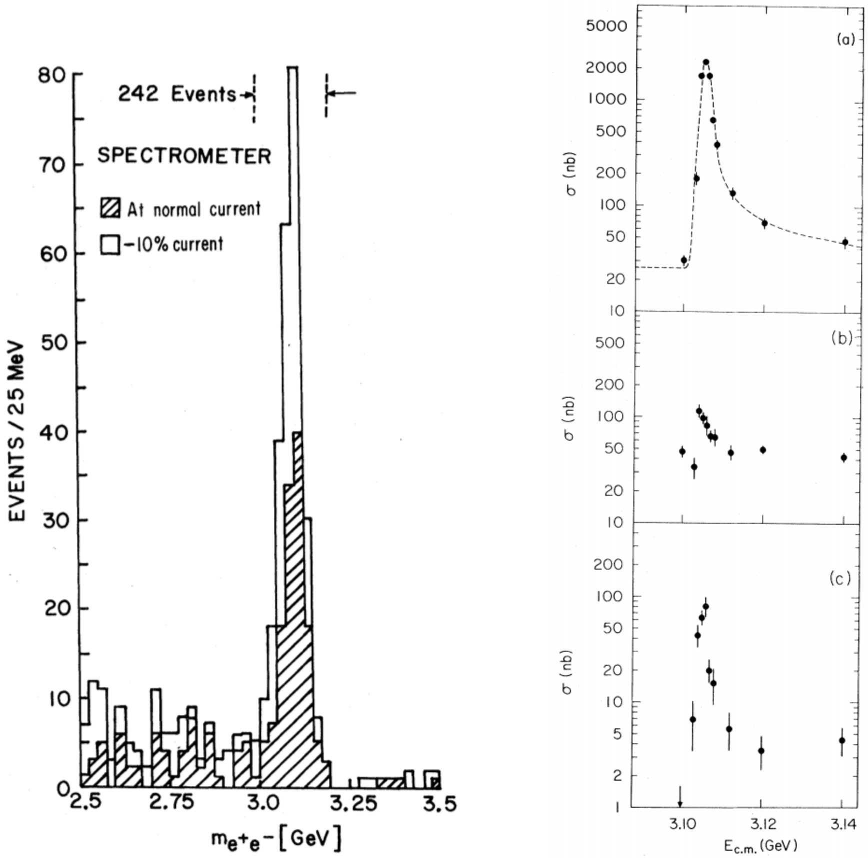

Figure 2.1: Left panel: e^+e^- invariant mass distribution showing the existence of the J/ψ. The results correspond to two different settings of the spectrometer, showing that the peak is independent of the spectrometer currents [69]. Right panel: Cross section as a function of energy for multi-hadron final states (top), e^+e^- (middle) and $\mu^+\mu^-$, $\pi^+\pi^-$ and K^+K^- (bottom). The curve in (a) is the expected shape of the δ-function folded with the Gaussian energy spread of the beams and including radiative processes [70].

Since the cross section ratio R, defined as:

$$R = \frac{\sigma(e^+e^- \to hadrons)}{\sigma(e^+e^- \to \mu^+\mu^-)} \tag{2.1}$$

was larger on-resonance than off, meaning that the particle had a direct hadronic decay channel, the J/ψ was classified as hadron. Many theoretical efforts were performed to integrate this state with the current particle theory, which predicted the existence of three quarks (u, d, s) and four leptons (e, ν_e, μ, ν_μ). Before the first observation of the J/ψ, Glashow and Bjorken had proposed the existence of a fourth quark [71], named *charm*, which was necessary to understand the anomalies in the kaon decay rates [72]. This quark was predicted to have a mass larger than the proton and to be characterized by an electric charge of 2/3. In this context, the J/ψ appeared to be a bound state of a charm and an anti-charm quark, representing a first proof of the validity of many theoretical developments performed until there.

Indeed, the "*November revolution*" was just the first step towards a more complete definition of the Standard Model. In fact, in 1977 the team led by L. M. Lederman observed a narrow peak in the dimuon invariant mass spectrum around 9.5 GeV/c^2 [73]. The new particle, named Υ, was considered as the first bound state of two quarks heavier than charm, named *bottom* or *beauty*. Similarly to the J/ψ, many excited states were soon observed (Υ(2S) and Υ(3S) [74, 75]).

Since it was observed that $c\bar{c}$ and $b\bar{b}$ systems were characterized by an energy level spectrum similar to the *positronium*, in complete analogy they were defined as *charmonium* (term introduced for the first time in 1975) and *bottomonium*. The sixth quark, named *top*, was discovered in 1994 at Tevatron by the CDF collaboration [76], but given its very short lifetime it cannot form a bound state.

2.2 Charmonium and Bottomonium spectroscopy

Charmonium and bottomonium bound states are classified using the quantum numbers L (orbital angular momentum), S (spin), J (total angular momentum) and n (principal quantum number), using the spectroscopic notation ($n^{2S+1}L_J$). Moreover, as shown in Figs. 2.2 and 2.3, they can also be characterized with the J^{PC} notation, with the parity $\mathrm{P} = (-1)^{L+1}$ and the charge conjugation $\mathrm{C} = (-1)^{L+S}$. The most commonly produced states are S-wave ($L = 0$) and P-wave states. If they are a singlet of the total angular momentum ($J = 0$) they are called η_{c} or η_{b}, if they are triplet ($J = 1$) they are called ψ ($c\bar{c}$) or Υ ($b\bar{b}$), while in case of P-wave triplet they are named χ_{c} or χ_{b}.

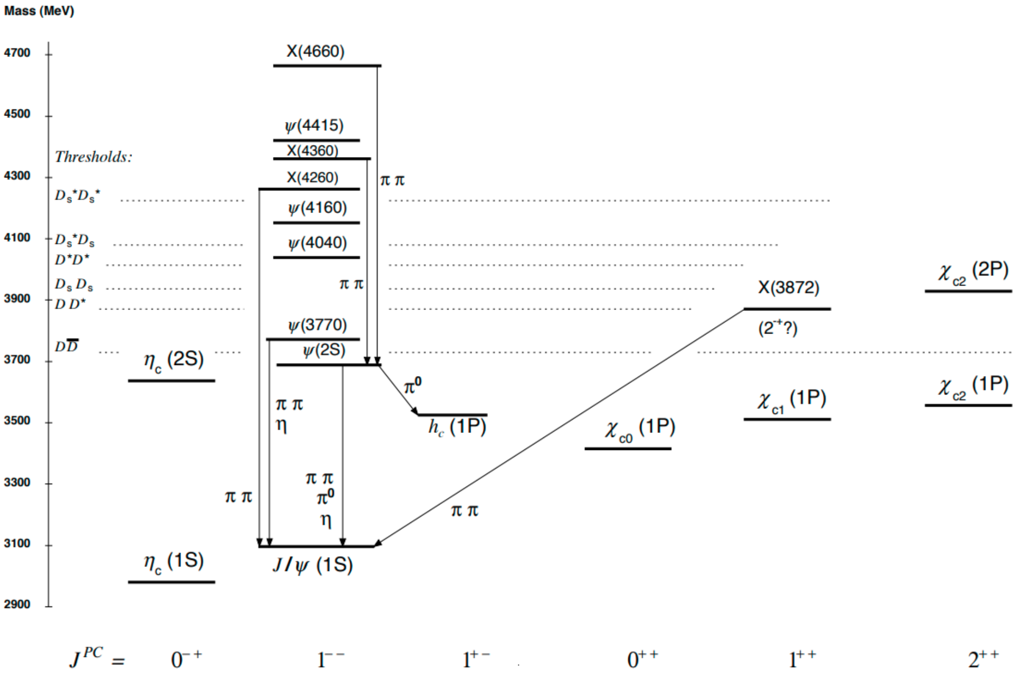

Figure 2.2: The level scheme of $c\bar{c}$ states showing experimentally established states with solid lines. Singlet states are called η_c and h_c, while triplet states χ_{cJ} and ψ, and unassigned charmonium-like states X. Figure taken from [5].

Moreover both J/ψ and Υ(1S) are below the mass threshold for the decay into open heavy flavors ($m_{\mathrm{J}/\psi} < 2m_D$ and $m_{\Upsilon(1\mathrm{S})} < 2m_B$). The vector states ($J^{\mathrm{PC}} = 1^{--}$) are very narrow ($\Gamma(\mathrm{J}/\psi) = 93$ KeV, $\Gamma(\Upsilon(1\mathrm{S})) = 54$ KeV) and decay to lepton pairs. This decay represents a fundamental feature which eases their reconstruction in a high hadron multiplicity environment (as heavy-ion collisions). In particular decay muon pairs can be reconstructed by dedicated spectrometers, allowing to reach a good signal-to-background ratio. The charmonium and bottomonium states shown in Figs. 2.2 and 2.3 possess decay channels leading from excited to ground states. This aspect implies that the inclusive sample of J/ψ and Υ(1S) experimentally measured is composed by different contributions, usually summarized as follows:

- **Direct**
- **Feed down**

which represent the "*prompt*" production. In the first case $q\bar{q}$ pair produced in the parton hard scattering from colliding hadrons, directly hadronizes into the bound states J/ψ and Υ(1S). The second case includes all J/ψ and Υ(1S) which are produced in the decay of the excited states (ψ(2S), Υ(2S), χ_c, ecc...). In addition to the prompt production, for charmonium a "*non-prompt*" component is present, related to the decay of hadrons containing a b valence quark (B-hadrons).

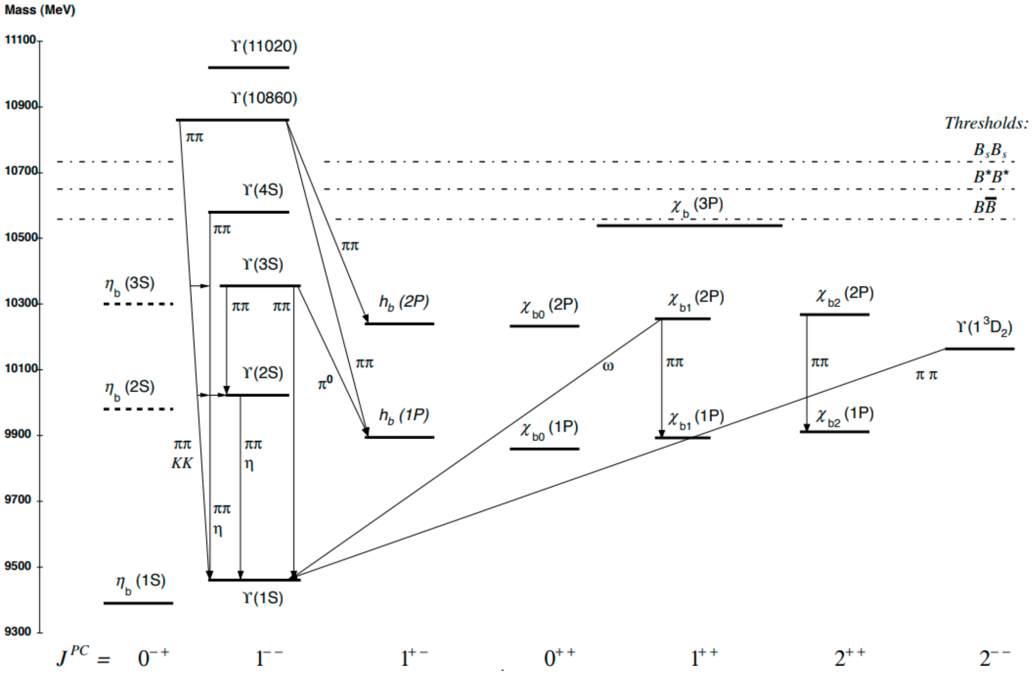

Figure 2.3: The level scheme of b$\bar{\text{b}}$ states showing experimentally established states with solid lines. Singlet states are called η_b and h_b, while triplet states $\chi_{\text{b}J}$ and Υ. Figure taken from [5].

Originating from a weak decay process, the non-prompt part can be separated, since the primary vertex of the B-hadron is displaced of $c\tau \sim 0.5$ mm with respect to the secondary vertex (e.g. $B \to \text{J}/\psi + X$). This is achieved following a procedure used for the first time at CDF for the measurement of the B-hadron lifetime [77]. It consists in the simultaneous fit of the invariant mass and the pseudoproper decay length (x) [1] distributions with:

$$F(x,m) = f_\text{Sig} \cdot F_\text{Sig}(x) \cdot M_\text{Sig}(m) + (1 - f_\text{Sig}) \cdot F_\text{Bkg}(x) \cdot M_\text{Bkg}(m)$$
$$F_\text{Sig}(x) = f_\text{B} \cdot F_\text{B}(x) + (1 - f_\text{B}) \cdot F_\text{prompt}(x)$$

---

[1] $x = c \cdot L_{xy} \cdot m_{\text{J}/\psi}/p_\text{T}^{\text{J}/\psi}$, where L_{xy} is the scalar product between the J/ψ p_T and the vector connecting the primary and the secondary vertexes.

where $F_{\rm Sig}$, $F_{\rm Bkg}$, $M_{\rm Sig}$ and $M_{\rm Bkg}$ are probability density functions, while $f_{\rm Sig}$, $f_{\rm Bkg}$ and $f_{\rm B}$ are the signal, background and non-prompt fractions. The fit to the pseudoproper decay length allows to separate the three components, as shown in the left panel of Fig. 2.4, and to extract the fraction of J/ψ coming from B-hadron decays.

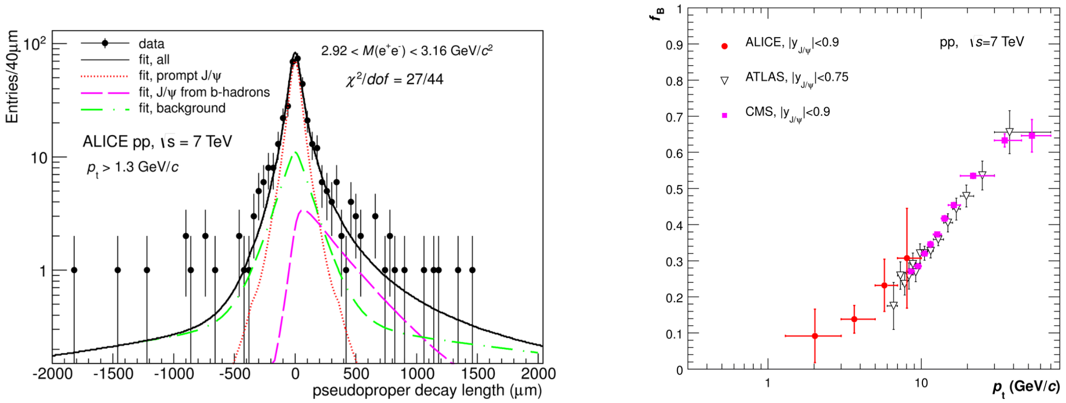

Figure 2.4: Left panel: fit to the J/ψ pseudoproper decay length distribution [78]. Right panel: The fraction of J/ψ from the decay of B-hadrons as a function of $p_{\rm T}$ compared with results from ATLAS [79] and CMS [80] in pp collisions at $\sqrt{s} = 7$ TeV.

All the LHC experiments measured the J/ψ non-prompt fraction, as shown in the right panel of Fig. 2.4, and a clear $p_{\rm T}$ dependence was observed. In particular $f_{\rm B}$ increases with the transverse momentum, passing from $\sim 10\%$ at low $p_{\rm T}$ to $\gtrsim 30\%$ for $p_{\rm T} > 10$ GeV/c and without a strong dependence on the rapidity. For what concerns the evaluation of the feed-down fractions from the P-wave states, this can be achieved through the study of the radiative decays $\chi_{\rm c} \rightarrow {\rm J}/\psi + \gamma$ and $\chi_{\rm b} \rightarrow \Upsilon(1{\rm S}) + \gamma$. For J/$\psi$ this contribution increases with $p_{\rm T}$ form $\sim 12\%$ to $\sim 30\%$ ($2 < p_{\rm T} < 14$ GeV/c) [81], while for Υ(1S) it amounts to $\sim 20\%$ [82], without a clear $p_{\rm T}$ dependence. Finally the estimate of the prompt ψ(2S) and Υ(2S) production with the precise branching ratio measurements allows to also estimate their feed-down contribution, which goes from $\sim 10\%$ ($p_{\rm T} \approx 0$) to $\sim 30\%$ ($p_{\rm T} \approx 14$ GeV/c) for J/ψ [83] and from $\sim 20\%$ ($p_{\rm T} \approx 0$) to $\sim 35\%$ ($p_{\rm T} \approx 12$ GeV/c) for the Υ(1S) [84].

2.3 Quarkonium production in hadronic collisions

2.3.1 Production models

From a theoretical point of view the description of quarkonium production is a complex challenge. Given the heavy quark mass, the relative velocity of the $\mathrm{Q\bar{Q}}$ pair is rather small, $v^2 \sim 0.3$ and $v^2 \sim 0.1$ for $c\bar{c}$ and $b\bar{b}$ respectively, so that quarkonium can be treated as a non-relativistic system. In this case it is possible to identify a hierarchy of the energy scales, in particular the *hard scale* for the heavy quark mass m_{Q}, a *soft scale* for the relative momentum ($p \sim mv$) among the quark/antiquark pair and an *ultra-soft scale* for the binding energy ($E \sim mv^2$) among the $\mathrm{Q\bar{Q}}$ pair. For these reasons the quarkonium production mechanisms can be separated into two steps, the formation of the pre-resonant state ($c\bar{c}$ or $b\bar{b}$) and the hadronization into the bound state.
On the one hand the creation of the $\mathrm{Q\bar{Q}}$ pair is a process involving a transferred momentum at least of the order of the heavy quark mass ($m_{\mathrm{c}} = 1.27$ GeV/c, $m_{\mathrm{b}} = 4.18$ GeV/c), hence it can be treated perturbatively because $m_{\mathrm{Q}} \gg \Lambda_{\mathrm{QCD}}$ and $\alpha_{\mathrm{S}} \ll 1$. On the other hand, since $p \sim mv \sim 1/r$, the corresponding coupling constant becomes larger, $\alpha_{\mathrm{S}} \sim 0.7$ for J/ψ ($r_{\mathrm{J}/\psi} \sim 0.25$ fm) and $\alpha_{\mathrm{S}} \sim 0.4$ for $\Upsilon(1\mathrm{S})$ ($r_{\Upsilon(1\mathrm{S})} \sim 0.15$ fm). This implies that for the soft scale the perturbative approach can not be performed. This coexistence of *shot-distance* and *long distance* processes makes the theoretical treatment of the quarkonium production particularly complex, requiring the use of complementary approaches to the perturbative QCD, as Non-Relativistic Effective Field Theories (e.g. NRQCD [85]) and purely phenomenological models, some of which are discussed below.

Color-Singlet model

The Color-Singlet model (CSM) is one of the earliest approaches used in the description of the quarkonium production and it was proposed for the first time shortly after the discovery of the J/ψ. It was rather succesfully used until 1995, when the comparison with the measurements at Tevatron showed that it under-predicted the cross section by more than one order of magnitude [86]. Nevertheless, it has revived in the last years, since the computation at next-to-leading order [87] has improved the agreement with experimental data. Formally, the model can be obtained from the NRQCD factorization formula in Eq. 2.2 dropping all the color-octet terms, retaining the color-singlet term whose quantum numbers are the same of the quarkonium state. The main assumptions of the model are that the $\mathrm{Q\bar{Q}}$ pair do not change its color and spin during the hadronization and it is produced in the hard scattering as a color-singlet state. What makes the CSM model highly predictive is that the only required input is the absolute value of the $\mathrm{Q\bar{Q}}$ wave function and its derivatives. The latter can be determined experimentally measuring the decay widths of the quarkonium into a lepton pair or phenomenologically applying potential models. Once given, CSM has no free paramenters.

Non-Relativistic QCD (NRQCD)

Non-Relativistic QCD [88] is a framework used to compute decay rates and production cross sections for heavy quarkonia. In this effective field theory, based on the factorization among hard and soft scales, the production cross section for a generic quarkonium state $\mathcal{Q}$ can be expressed as the cross section for the production of a $\mathrm{Q\bar{Q}}$ pair in a $A+B$ collision, multiplied by the probability that the $\mathrm{Q\bar{Q}}$ pair evolves into a certain $\mathcal{Q}$ state, expressed in terms of *long-distance matrix elements* (LDMEs). The production cross section for $\mathcal{Q}$ can be written as

$$\sigma_{A+B\to\mathcal{Q}+X} = \sum_{i,j,n} \int dx_i dx_j f_i^A(x_i,\mu_F) f_j^B(x_j,\mu_F) \hat{\sigma}_{i,j\to Q\bar{Q}}(\mu_F,\mu_R) \times \mathcal{L}(Q\bar{Q}\to\mathcal{Q}), \tag{2.2}$$

where the sum is over spin, orbital angular momentum and colors of the i,j partons, f_i^A and f_j^B are the parton distribution functions in the A and B hadrons, μ_F and μ_R the factorization and renormalization scales respectively and finally $\hat{\sigma}$ the partonic cross section to produce a $\mathrm{Q\bar{Q}}$ pair. $\mathcal{L}$ represents the LDMEs, which are assumed to be universal and constant, e.g. independent on the $\mathrm{Q\bar{Q}}$ kinematics and on the collision system, and are obtained through a fitting procedure to the measured cross section [89]. Since the pre-resonant state can be produced in a color-singlet or color-octet state, as shown in Fig. 2.5, the matrix elements correspond to the probability that these states evolve into a color-singlet quarkonium. At leading order, the color-octet production proceeds via the emission of a nearly collinear gluon to the $\mathrm{Q\bar{Q}}$ pair during the hadronization process, in order the neutralize the color charge. In principle an infinite number of matrix elements are required, nevertheless Eq. 2.2 can be organized as an expansion in powers of the relative heavy quark velocity (v) and, truncating at a given order of v, only a finite set of matrix elements contributes. The NRQCD predictive power holds if this truncation is valid and the LDMEs are effectively universal. Despite this approach succeeded in the description of many observables and it is currently used for the evaluation of the quarkonium cross sections, there are still some open issues, as the *quarkonium polarization puzzle*, which will be described in details in the following.

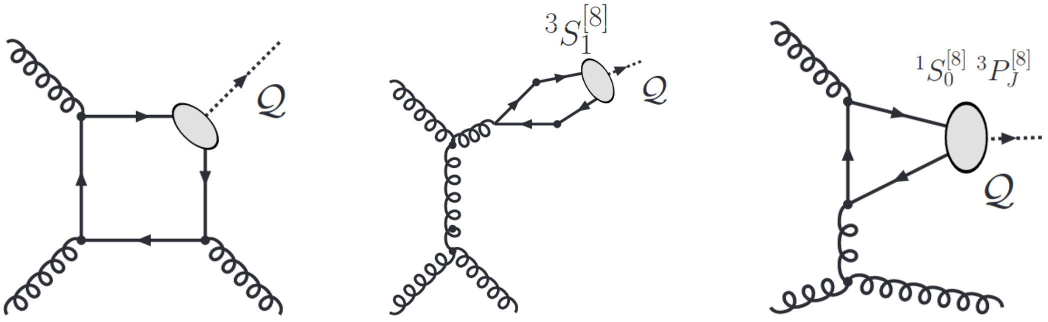

(a) (b) (c)

Figure 2.5: Feynman diagrams contributing to hadroproduction via the color-singlet channel (a), and the color-octet channels (b,c). Figures taken from [90].

2.3.2 Experimental results

In the following sections some remarkable experimental results on the quarkonium production will be presented. Heavy-ion collisions measurements will be discussed in a dedicated section.

Tevatron

Charmonium and bottomonium production has been investigated in different high-energy hadron colliders and among them the experiments at Tevatron have performed some of the earliest and most precise measurements. Tevatron, operating at Fermilab, was a $p\bar{p}$ collider designed to achieve the maximum center-of-mass energy of $\sqrt{s} = 1.96$ TeV.
A particularly interesting result is the cross section measurement for direct J/ψ and inclusive Υ(1S) production performed by the CDF collaboration during Run I [86]. As shown in the left panel of Fig. 2.6, the prediction of the CSM at the leading order in α_{S} is not able to describe experimental the data. Even when including higher order corrections, which involve gluon fragmentation, the prediction is smaller by an order of magnitude. On the other hand the NRQCD factorization approach, which contains both color-singlet and color-octet matrix elements, shows an improved agreement with data.
Similarly, the comparison with the Υ(1S) returns a similar outcome (right panel of Fig. 2.6), with the difference that NRQCD matches accurately data only for $p_{\mathrm{T}} > 8$ GeV/c. This set of results was particularly important because it determined the crisis of the CSM and in parallel the first success of the new NRQCD approach. As previously mentioned in

Section 2.3.1, NRQCD encountered problems in the description of the quarkonium polarization and also for that reason new theoretical developments were introduced on the side of the CSM with higher order calculations in α_S.

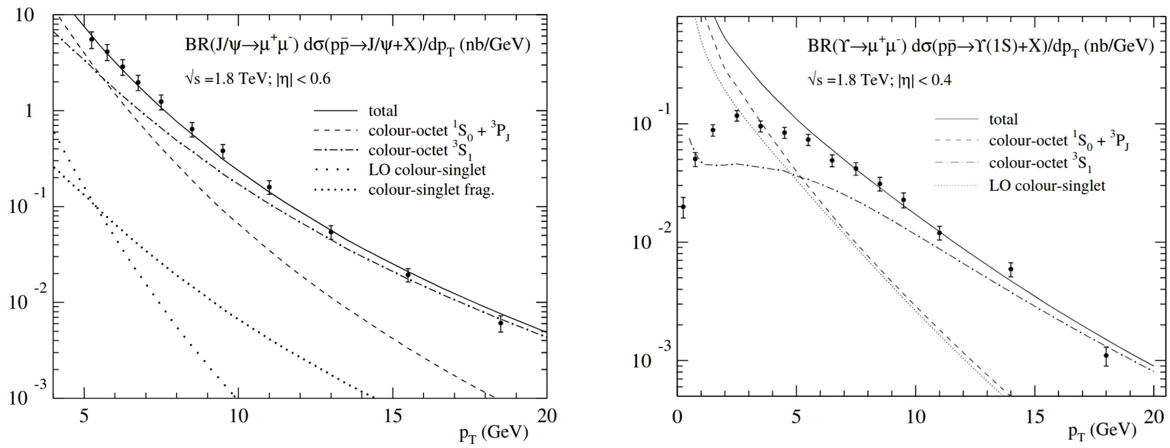

Figure 2.6: p_{T}-differential cross section for direct J/ψ (left panel) and inclusive Υ(1S) (right panel) production measured by the CDF collaboration [86].

LHC

Quarkonium production has been widely investigated by all the LHC experiments, ALICE, CMS, ATLAS and LHCb. Their complementarity in therm of kinematics and the unprecedented measurement precision reached in hadronic collisions allowed the addition of stringent constraints to the theoretical predictions.

The ALICE experiment, which will be discussed in detail in Chapter 4, can explore charmonium and bottomonium production both in the mid ($|y| < 0.9$) and forward ($2.5 < y < 4$) rapidity regions, down to $p_{\mathrm{T}} \sim 0$. This feature is extremely important for the theoretical models, since they are in general able to describe the high p_{T} region, but fail at low p_{T}. As shown in the left panel of Fig. 2.7, the measurement of inclusive J/ψ cross section at $\sqrt{s} = 13$ TeV is in fair agreement with the NRQCD predictions, even if for $p_{\mathrm{T}} < 8$ GeV/c quarkonium production has to be treated in a specific framework, named *Color-Glass Condensate* (CGC, for more details see Ref. [91]) to successfully describe the trend observed in data. The ALICE detector allows to study quarkonia decaying to $\mu^+\mu^-$ and e^+e^- pairs. The two decay channels are complementary, and in the dielectron one quarkonium, in particular J/ψ, is studied at mid-rapidity ($|y| < 0.9$) separating the prompt and non-prompt components. The dimuon decay channel is studied by means of a dedicated spectrometer, covering the forward rapidity region ($2.5 < y < 4$). In this case higher precision is reached allowing to study the low cross section resonances, as the $\Upsilon(1S)$. In the right panel of Fig. 2.7, the J/ψ cross section is shown at $\sqrt{s} = 7$ TeV in all the available rapidity ranges covered by ALICE. It is important to notice that the measurements are in good agreement with the LHCb ones, which are obtained in a similar rapidity window.

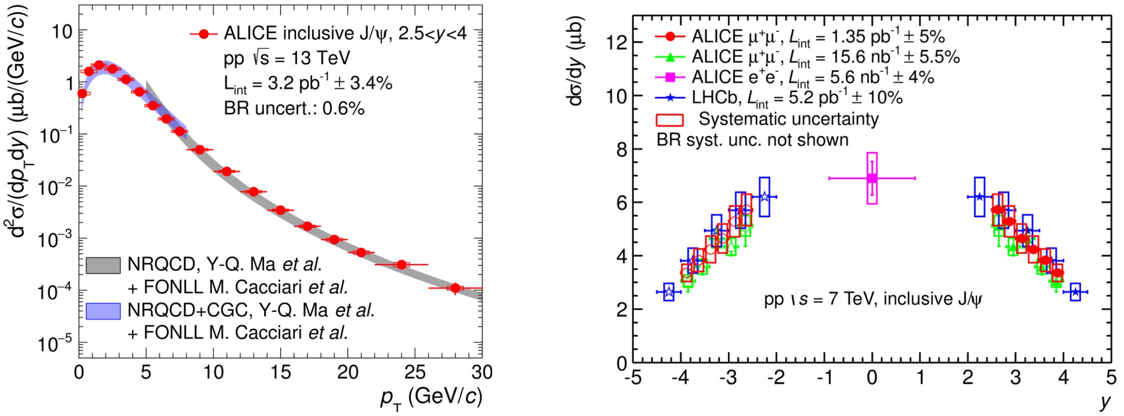

Figure 2.7: Left panel: p_T-differential cross section for inclusive J/ψ at $\sqrt{s} = 13$ TeV [92] compared with theoretical predictions for prompt J/ψ from NLO NRQCD (gray) [93] and LO NRQCD coupled with CGC [91]. Right panel: J/ψ cross section as a function of rapidity measured by the ALICE experiment in the $\mu^+\mu^-$ and e^+e^- decay channels at $\sqrt{s} = 7$ TeV [94] compared with LHCb results at the same center-of-mass energy [95].

The CMS collaboration has widely investigated quarkonium production, focusing on the mid-rapidity region ($|y| < 1.2$). Thanks to a dedicated detector for muon tracking, the drift tube (DT) system, charmonium, bottomonium and many other resonances can be studied reaching a very high precision, as shown in the left panel of Fig. 2.8. The CMS collaboration published results on both prompt [96] and non-prompt [97] charmonium production, while bottomonia have been deeply studied, observing that NLO NRQCD describes very accurately the $\Upsilon(1S)$, $\Upsilon(2S)$ and $\Upsilon(3S)$ [98]. In addition, results on both J/ψ [99] and $\Upsilon(1S)$ [100] pair production were published. These analyses are particularly interesting from a theoretical point of view because they could help to shed light on the production mechanism via multiparton scattering, which is difficult to address within the framework of the perturbative QCD. Finally, it is worth mentioning one of the most recent results, which is the study of J/ψ production inside jets in pp collisions [101]. In fact, by measuring the fraction of the jet energy carried by the J/ψ (see Fig. 2.8), it is possible to test different sets of LDME, constraining the NRQCD factorization approach.

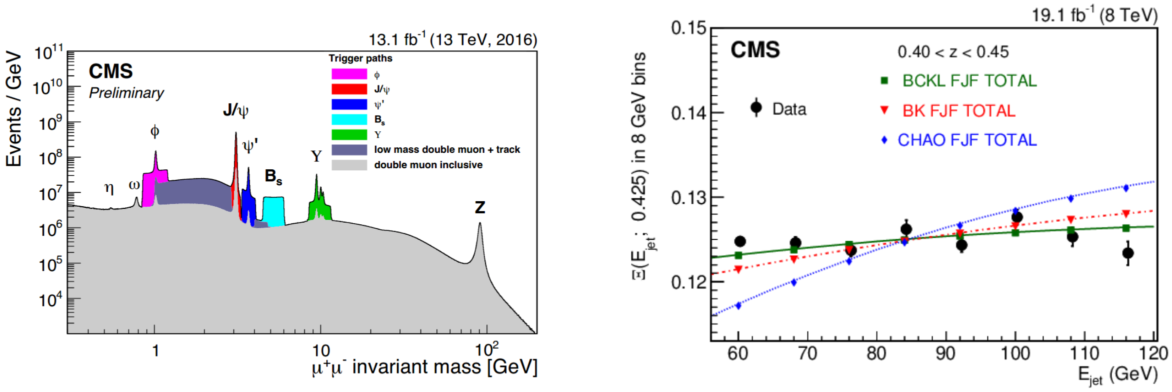

Figure 2.8: Left panel: dimuon invariant mass distribution at $\sqrt{s} = 13$ TeV for the CMS experiment [102]. Right panel: Ξ as a function of jet energy compared with the fragmentation jet function model [103] with different set of LDME (BCKL, BK, CHAO). Ξ is the fraction of events having a J/ψ meson contained in a jet.

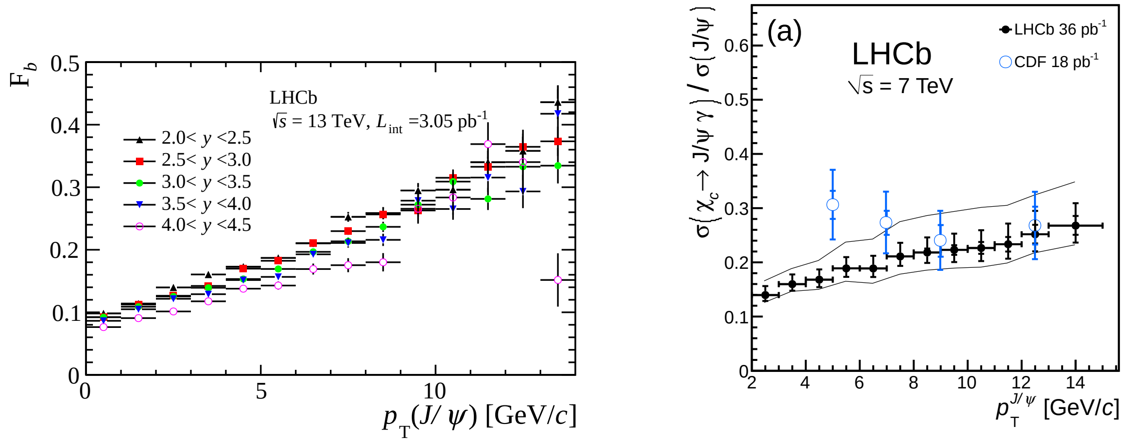

Figure 2.9: Left panel: fraction J/ψ-from-b mesons as a function of the J/ψ p_T at $\sqrt{s} = 13$ TeV [104]. Right panel: $\sigma(\chi_c \to J/\psi)/J/\psi$ as a function of J/ψ p_T at $\sqrt{s} = 7$ TeV [81].

The LHCb collaboration has measured quarkonium production in the forward rapidity region ($2 < y < 4.5$) down to $p_T \sim 0$. The sizable data sample collected during Run 2 at different center-of-mass energies and the wide rapidity coverage allowed many multi-differential studies of both charmonium [104, 83] and bottomonium [84]. The fraction of J/ψ coming from b-hadrons, obtained as a function of the transverse momentum for different y intervals at $\sqrt{s} = 13$ TeV, represents the most precise measurement of this quantity at the LHC and is shown in Fig. 2.9. The study of χ_c production [81] also deserves to be mentioned. In particular the ratio $\sigma(\chi_c \to J/\psi)/J/\psi$, shown in the right panel of Fig. 2.9, can be used to constrain many theoretical models and yields an important improvement in the estimation of the J/ψ feed-down fractions.

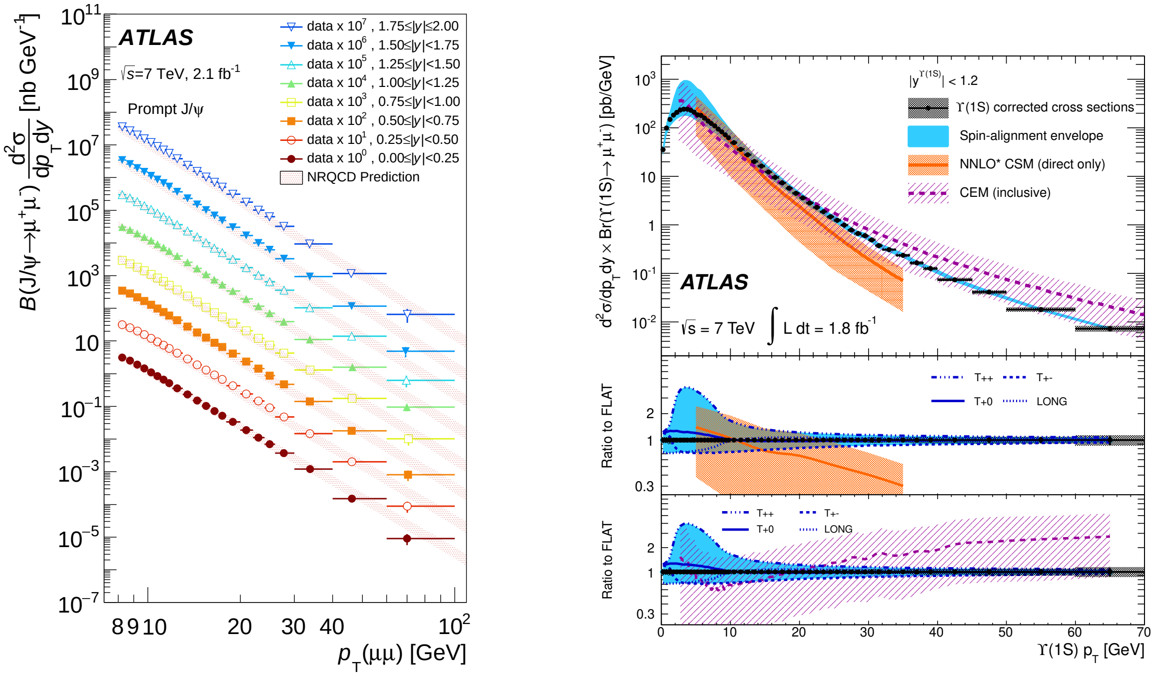

Figure 2.10: Left panel: cross section of prompt J/ψ and ψ(2S) production as a function of p_T in 8 different rapidity ranges [105]. Right panel: Υ(1S) cross section as a function of p_T compared with NNLO CSM [106] and with the Color Evaporation Model [107].

The ATLAS collaboration measured J/ψ and ψ(2S) production up to $p_T \sim 100$ GeV/c [105] at mid-rapidity ($|y| < 2$). The measurements are compared in Fig. 2.10 with the theoretical predictions of the NRQCD, which are able to describe accurately the data. Υ(1S), Υ(2S) and Υ(3S) cross sections were measured as a function of the transverse momentum at $\sqrt{s} =$ 7 TeV [108, 109] and the results show a significant disagreement both in the shape and in the normalization with the predictions of the CSM, even including the next-to-next-to-leading order correction [106]. Finally the ATLAS collaboration measured the cross section for prompt and non-prompt χ_{c1} and χ_{c2} [110]. Combining the measurement with the existing results of prompt J/ψ allowed to derive the fraction of J/ψ coming from feed-down decays, which is estimated to range between 20 and 30% for $10 < p_{\mathrm{T}} < 30$ GeV/c.

2.4 Quarkonium production in heavy-ion collisions

As anticipated in Section 1.5.2, the study of quarkonium production represents an important benchmark for the current understanding of QCD. In nucleus-nucleus collisions at LHC energies, the process that goes from the collision to the hadronization of the heavy quark pairs can be roughly divided into a defined series of steps. Assuming that the QGP is produced in the collision, this strongly interacting medium is expected to reach the thermal equilibrium (τ_{Therm}) between 0.1 and 1 fm/c, while its lifetime is estimated to range between 5-10 fm/c (τ_{QGP}). For heavy quarks the thermalization time is expected to be smaller than τ_{QGP}, therefore:

$$\tau_{\mathrm{crossing}} \ll \tau_{\mathrm{Therm}} < \tau_{\mathrm{QGP}} \tag{2.3}$$

This implies that the $\mathrm{Q\bar{Q}}$ pair experiences the evolution of the hot and dense medium produced in the collision, making it a perfect probe to investigate the formation and the properties of the quark-gluon plasma.
In the following quarkonium production will be discussed referring to two different classes of collisions, proton-nucleus and nucleus-nucleus collisions.

2.4.1 Proton-Nucleus collisions

One of the fundamental aspects in the study of the quark-gluon plasma is to disentangle the effects related to the presence of a deconfined phase to those due to the interaction with standard cold nuclear matter or more in general to effects non-related to the produced medium. Normally this is achieved studying particle production in proton-nucleus collisions, where in principle the energy density is not large enough to to allow the formation of the QGP. In the literature these effects are normally defined as *cold nuclear matter effects*, to distinguish them from those which indicate the interaction with the hot and dense medium produced in the collision. Among them *nuclear absorption*, *nuclear shadowing* and *energy loss* are the most recurrent in the theoretical treatment of the mechanisms at work in proton-nucleus collisions.

- **Nuclear absorption**: it indicates the interaction between the $\mathrm{Q\bar{Q}}$ pair and the nucleons of the colliding nuclei. Observed both in proton-nucleus and nucleus-nucleus collisions [111], it is a mechanism which can lead to a dissociation of the state and a consequent suppression of quarkonium production. This effect depends on the amount of nuclear matter traversed by the heavy quark pair and it is relevant when the formation time of the resonance (τ_{form}) is shorter than the crossing time of a proton through the nucleus (τ_{crossing}). As a consequence, since τ_{crossing} decreases for rising $\sqrt{s}$, when $\tau_{\text{form}} \gg \tau_{\text{crossing}}$ as at the LHC energies, the nuclear absorption becomes negligible.

- **Nuclear shadowing**: under this definition effects related to the modification of the partonic structure of the nucleon inside a nucleus compared to a free proton [112] are included. Quantitatively it is evaluated with the ratio

  $$R_i^A(x, Q^2) = \frac{f_i^A(x, Q^2)}{f_i(x, Q^2)}, \tag{2.4}$$

  where f_i^A and f_i are the PDFs for a nucleon inside a nucleus and a free nucleon respectively, which are functions of the transferred momentum Q^2 and of the nucleon momentum fraction carried by the parton x. If there are no nuclear effects $R_i^A(x, Q^2)$ should be 1, while a deviation from unity indicates a modification of parton distribution. In general it is possible to roughly distinguish among various effects according to the fraction x of the nucleon momentum carried by the parton:

  - ($x \lesssim 0.1$) *shadowing*: is observed when the partonic probability density for the nucleon is smaller when it is inside a nucleus than when it is free ($R_i^A(x, Q^2) < 1$). This effect is related to the fact that at small x values there can be a spatial overlap of the partons of different nucleons.
  - ($0.1 \lesssim x \lesssim 0.3$) *anti-shadowing*: is directly related to shadowing. In fact, because of momentum conservation, the reduction of partons at low-x values implies an enhancement at larger x.
  - ($0.3 \lesssim x \lesssim 0.8$) *EMC effect*: consists in a depletion of the quark distributions at high x values.
  - for $x \to 1$ $R_i^A(x, Q^2)$ is larger than 1 and the effect is due to the *Fermi motion* of the bound nucleons inside the nucleus.

Nowadays these effects are mostly treated via fits of extended set of data and making use of the DGLAP [113] evolution of the PDF at next-to-leading order in collinear factorization [114]. At low-x the PDFs suffer large uncertainties due to lack of precise experimental measurements. Alternatively, the behavior of low-x parton production can be described in the framework of the *Color Glass Condensate* (CGC) [115], an effective theory which describes the properties of saturated gluons. At low-x the gluon density increases until their separation becomes smaller, with a maximum occupation of the phase space proportional to $\sim 1/\alpha_{\mathrm{S}}$. When the saturation limit is reached, the system can be seen as a color *condensate*, where the strength of the color field depends on the saturation scale $Q_s^2(x)$. The latter can be estimated with the "pocket" formula:

$$Q_s^2(x) \sim A^{1/3} \cdot x^{-0.3}. \tag{2.5}$$

The CGC framework is applicable in a wide range of processes (from $e+p$ to A–A collisions) and provides an approach to study the initial conditions for the evolution of the QGP.

- **Coherent energy loss**: this mechanism was introduced and studied, for quarkonium production in p–A collisions, by Arleo and Peigné [116]. They showed that the energy lost by partons via small-angle gluon emission determines a modification of the charmonium p_{T} spectrum in p–A collisions and a consequent modification of the nuclear modification factor (R_{pA}). This model assumes that the $\mathrm{Q\bar{Q}}$ pair is produced in a color octet state in a time scale $\tau_{\mathrm{Q\bar{Q}}}$, remaining in this state for $\tau_{\mathrm{octet}} \gg \tau_{\mathrm{Q\bar{Q}}}$. In the nucleus rest frame quarkonium hadroproduction looks like small angle scattering of a color charge. The effect of the associated gluon radiation is similar to what happens to a color octet receiving an effective transverse momentum kick $q_\perp$. The amount of medium induced gluon radiation, and the strength of quarkonium suppression, depends on the transverse momentum nuclear broadening $\Delta q_\perp^2$. This quantity is expressed in terms of the path length (L) traveled across the target:

$$\Delta q_\perp^2(L) = \hat{q}_A \cdot L_A - \hat{q}_p \cdot L_p \tag{2.6}$$

  where $\hat{q}_A$ and $\hat{q}_p$ are the transport coefficients in the nucleus and in the proton, respectively.

Quarkonium production in proton-nucleus collisions has been widely investigated at the LHC. As in nucleus-nucleus collisions, the nuclear modification factor (R_{pA}) is the tool used to quantify the various effects and to compare data with theoretical predictions. The ALICE collaboration measured R_{pA} for both J/ψ and ψ(2S) at $\sqrt{s_{\mathrm{NN}}} = 8.16$ TeV [2] (see Fig. 2.11). It can be noticed that for J/ψ $R_{\mathrm{pA}} \sim 1$ at backward rapidity ($-4.46 < y <$

-2.96), while at forward rapidity ($2.03 < y < 3.53$) there is a significant suppression. This behavior can be properly described within the set of initial-state effects previously mentioned, in particular with the nuclear shadowing [117, 118] and the energy loss [116, 117] in a cold nuclear medium. A similar trend of the nuclear modification factor is expected for the ψ(2S), since both shadowing and energy loss exhibit a limited sensitivity to the quantum numbers of the bound state. Nevertheless, contrary to the predictions, the ψ(2S) is found to be more suppressed than J/ψ at backward rapidity. One possibility to explain this observation is the presence of a final-state mechanism affecting the excited state. This hypothesis seems to be confirmed by the comparison with models implementing the interaction with particles produced in the collision and which travel together with the charmonium state. These particles are usually defined as *comovers*, but it is still unclear if they interact as light hadrons or at a partonic level with the forming $c\bar{c}$ pair [119, 120].

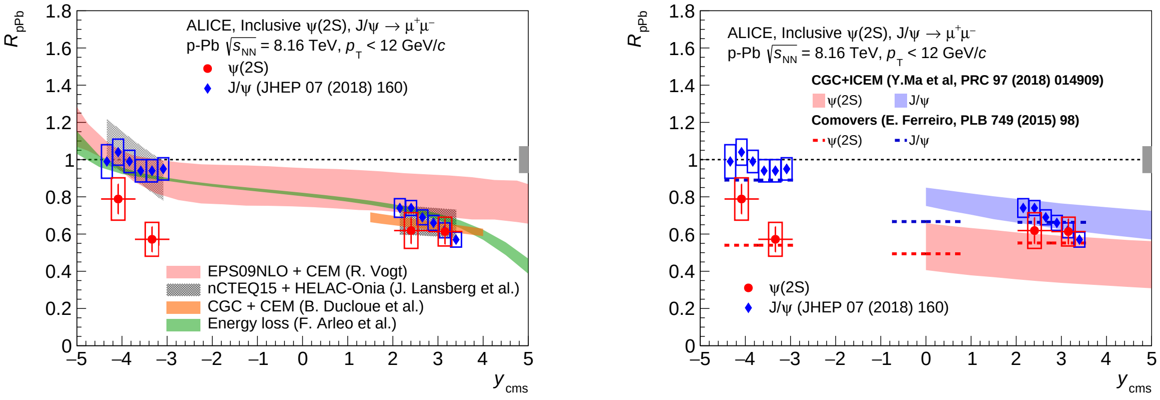

Figure 2.11: Rapidity dependence of the R_{pA} for ψ(2S) and J/ψ in p–Pb collisions at $\sqrt{s_{\mathrm{NN}}} = 8.16$ TeV [2]. Results are compared with models including initial-state effects [121, 117, 118] and coherent energy loss [116, 117] (left panel), and to models which also implement final-state effects [119, 120] (right panel).

Similarly to charmonia, also bottomonia have been studied at the LHC. Both the ALICE and LHCb collaborations have published several results exploiting the full Run 2 data sample at $\sqrt{s_{\mathrm{NN}}} = 5.02$ and 8.16 TeV and obtaining a remarkable precision in the measurement of these states. In Fig. 2.12 the Υ(1S) nuclear modification factor as a function of rapidity is reported, showing a good agreement among the two experiments. Both in the forward and in the backward regions the Υ(1S) production appears to be more suppressed with respect to pp collisions, with a slightly stronger effect for positive y values. The measurements are compared with models including different shadowing implementations [122, 123, 124] and parton energy loss [116], which describe rather accurately the observed trend, slightly overestimating the R_{pA} at backward rapidity. The result is also compared with a model implementing a combination of shadowing and comovers interaction [125], which shows a general behavior similar to the other models indicating that final state dissociation probably plays a minor role for the tightly bound $\Upsilon(1\mathrm{S})$.

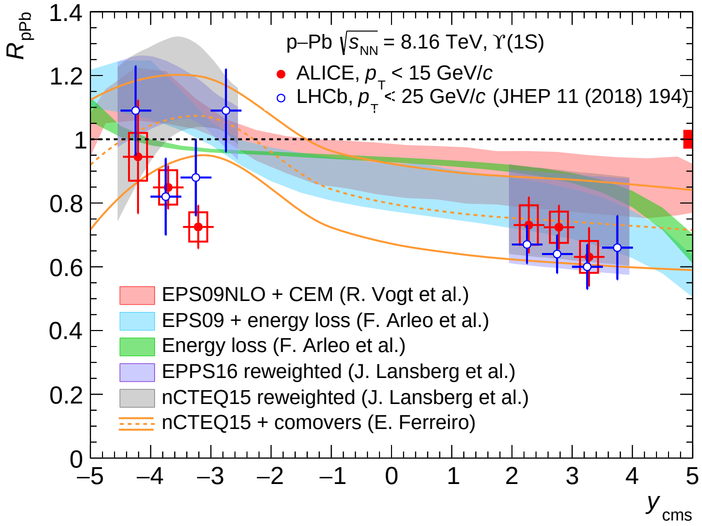

Figure 2.12: $\Upsilon(1\mathrm{S})$ nuclear modification factor as a function of rapidity at $\sqrt{s_{\mathrm{NN}}} = 8.16$ TeV measured by the ALICE [126] and LHCb [127] collaborations. Results are compared with different implementations of the nuclear shadowing (EPS09 [122], EPPS16 [123], nCTEQ15 [124]), coherent energy loss [116] and models including contributions of shadowing and comovers interaction [125].

2.4.2 Nucleus-Nucleus collisions

Quarkonium production is expected to be suppressed in presence of a strongly interacting medium. A bound state of two heavy quarks can indeed be dissociated via a screening mechanism analogous to the one observed in a plasma of electrons and ions. Since the binding potential between the $\mathrm{Q\bar{Q}}$ pair is smaller for the excited state (ψ(2S), Υ(2S), Υ(3S)) with respect to the ground state (J/ψ, Υ(1S)), the sequential suppression of the various quarkonium resonances according to their binding is expected to be observed when the system is close or exceeds the critical temperature T_{c}. This feature is particularly important because it can be used to obtain an estimation of the temperature of the medium according to the disappearance of a specific state, as shown in Table 2.4.2. One should anyway note that the values of the dissociation temperature exhibit a rather strong dependence on the theory approach.

State	J/ψ	χ_c	ψ(2S)	Υ(1S)	Υ(2S)	Υ(3S)
T_d/T_c	2.10	1.16	1.12	>4.0	1.60	1.17

Table 2.1: Quarkonium dissociation temperature in units of the critical temperature [128].

Recent developments, based on the combination of state-of-the-art lattice QCD simulations and NRQCD factorization approach [129], allows one to perform a detailed spectral analysis of the various resonances for different temperatures of the system. In Fig. 2.13 the evolution of the charmonium and bottomonium spectral functions is clearly visible.

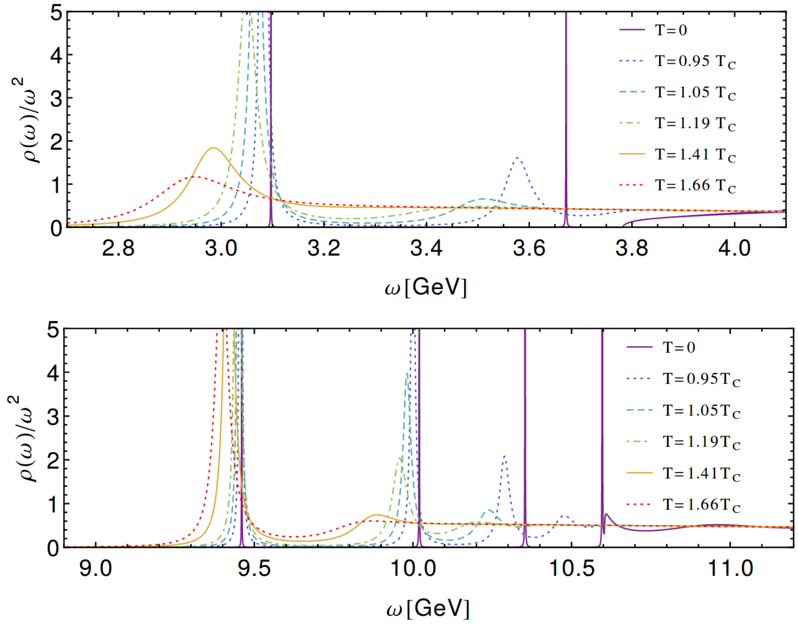

Figure 2.13: S-wave charmonium (top panel) and bottomonium in medium spectral function for different temperatures expressed in units of the critical temperature T_c [129]

A logical consequence of the sequential melting is that for sufficiently high temperature all quarkonium states should be melt by the medium and, from an experimental point of view, this can in principle be achieved increasing the center-of-mass energy of the collisions up to a value for which $R_{AA} \to 0$. Indeed, in this optics, at LHC energies a much stronger suppression with respect to RHIC could have been expected given the order of magnitude difference in center-of-mass energy per nucleon pair among the two colliders. Nevertheless, the results at $\sqrt{s_{\rm NN}} = 2.76$ TeV [130] pointed to a different behavior, since J/ψ was found to be less suppressed than at RHIC, as shown in Fig. 2.14. The accepted explanation for this effect is the *quarkonium regeneration*, which partially counterbalances the QGP suppression via the statistical recombination of uncorrelated $c\bar{c}$ pairs. The larger effect observed at the LHC can be justified considering that the number of $c\bar{c}$ pairs per event is ∼10 times larger than at RHIC, hence a large regeneration can be expected. Finally, comparing the $R_{\rm AA}$ as a function of $p_{\rm T}$ between LHC and RHIC energy one finds that ALICE shows $R_{\rm AA}$ values 4 times larger than the ones of PHENIX, suggesting that the recombination contribution is much more significant for J/ψ of low transverse momentum.

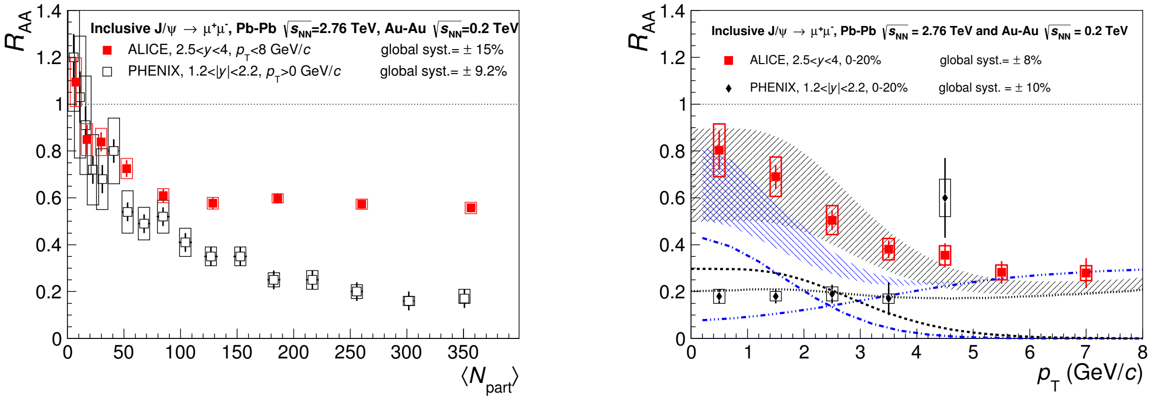

Figure 2.14: Left panel: J/ψ nuclear modification factor as a function of the collision centrality measured by the ALICE [131] and PHENIX [132] collaborations at $\sqrt{s_{\rm NN}} = 2.76$ TeV and 200 GeV respectively. Right panel: J/ψ nuclear modification factor as a function of $p_{\rm T}$ compared with the predictions of the transport models TM1 (black) [133] and TM2 (blue) [134]. Dashed and dotted lines represent the separate contributions of primordial and regenerted J/ψ, while then colored bands correspond to their sum.

For bottomonia the sequential suppression appears to be the dominant mechanism. Even if in principle it could also be affected by regeneration as the J/ψ, the small number of $b\bar{b}$ pairs produced per event at the LHC prevents for the moment the observation of this effect.

The charmonium enhancement production due the recombination has been included in the main theoretical models, and in particular the *Statistical Hadronization Model* (SHM) [135] and the *Transport Model* [136]. Within the SHM scenario, bound states don't exist during the lifetime of the QGP and they are all created at the phase boundary, assuming chemical equilibrium. In the transport models, where only a partial thermalization is reached, a significant fraction (∼50% for J/ψ depending on the kinematics and the centrality of the collision) is produced via recombination, while the rest comes from primordial production. In the transport model approach, in addition to the nuclear modification factor, also the elliptic flow of the J/ψ is estimated. It is directly inherited from the velocity field of the individual heavy quarks, resulting in a positive v_2 coefficient, mainly at low-p_{T}. The transport models give a good description of the data at low p_{T} but are not able to describe properly the full p_{T}-dependence of the v_2, as shown in Fig. 2.15.

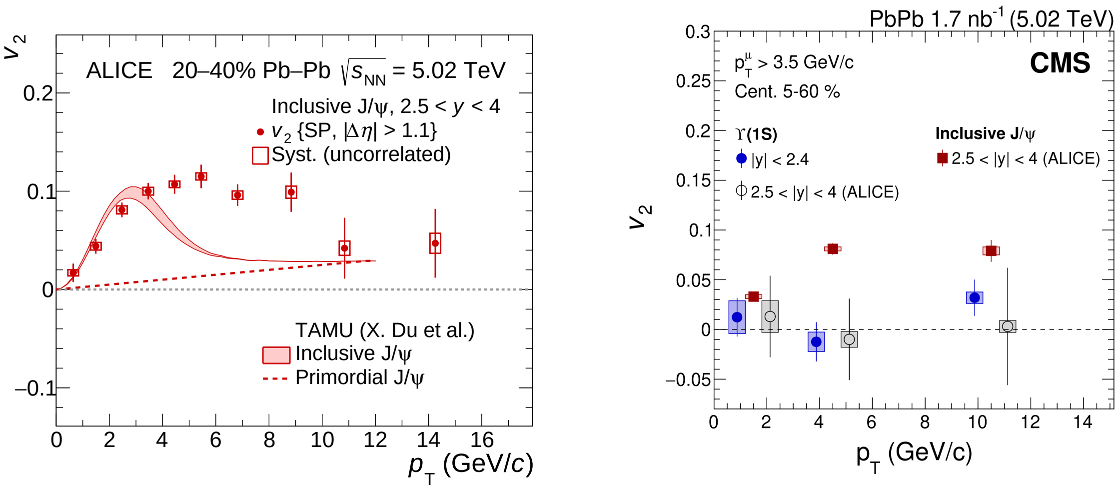

Figure 2.15: Left panel: inclusive J/ψ v_2 as a function of p_{T} at $\sqrt{s_{\mathrm{NN}}} = 5.02$ TeV measured by the ALICE collaboration for semi-central collisions (20-40%) [137]. Results are compared with the predictions of a transport model [136]. Right panel: comparison between the Υ(1S) v_2 as a function of p_{T} at $\sqrt{s_{\mathrm{NN}}} = 5.02$ TeV measured by the ALICE [138] and CMS collaborations [111].

For bottomonia the flow coefficients are expected to be much smaller than the J/ψ ones. The reason is that, given the larger binding energy, the dissociation occurs at higher temperature and it is limited to the earlier stages of the collisions where the path length difference between in-plane and out-of-plane emission, relevant for the v_2 at high p_{T}, is small. In addition the regeneration contribution which would contribute mainly at low p_{T}, is expected to be negligible since the multiplicity of bottom quarks is much smaller than the charm ones. The measurement performed by ALICE [138] and CMS [111] seem to confirm the expectations, with a v_2 compatible with zero within the uncertainties.

Chapter 3

Quarkonium polarization: an overview

Among the various observables used in the study of quarkonia, polarization plays a special role. On one hand, theoretical predictions depict it as the perfect probe to shed light on the long lasting question of the quarkonium production mechanism in elementary collisions. On the other, since it may be sensitive to the environment where the particle production occurs, it represents a potential tool to investigate the effects of a deconfined medium on the formation of a bound state of two heavy quarks.

This versatility is partially balanced by the difficulties in the theoretical description of the experimental results, which date back to the first measurements performed at Tevatron. Also, thanks to the recent improvements in the NRQCD factorization approach performed in the framework of the Color Glass Condensate [139], a satisfactory agreement with the LHC measurements in proton-proton collisions was recently reached.

In this chapter a general introduction to the main polarization concepts will be given, with a focus on the theoretical aspects underlying this observable and on the main experimental results achieved across the years.

3.1 Vector meson polarization

Polarization is an observable that measures the total angular momentum of a particle with respect to a certain direction, defined as the polarization or quantization axis. The latter can be chosen arbitrarily, even if in the following the most used choices will be described.

The total angular momentum $\vec{J}$ is calculated as

$$\vec{J} = \vec{S} + \vec{L}, \tag{3.1}$$

where $\vec{S}$ and $\vec{L}$ are the particle spin and the total angular momentum operators. Considering $\vec{S}$ and $\vec{L}$ as ordinary vectors of the 3D space, the maximum allowed value for the module will be $|\vec{S}| + |\vec{L}|$, while the minimum is $||\vec{S}| - |\vec{L}||$. If the module of the vectors is identified with the corresponding eigenvalues s and l, the $\vec{J}$ eigenvalues can range in

$$|l - s| < j < l + s. \tag{3.2}$$

The total angular momentum is also specified through its component j_z, which corresponds to the projection of j along the z-axis, therefore, for a given particle, the total angular momentum state is expressed with the ket $|j, j_z\rangle$. Vector mesons ground states, as J/ψ or Υ(1S), are characterized by $s = 1$ and $l = 0$, therefore $j = 1$, meaning that their third component can assume the values $j_z = 0, \pm 1$. As a consequence for a generic vector meson $\mathcal{V}$ the total angular angular momentum state can be expressed as the linear combination

$$|\mathcal{V}\rangle = b_{+1}|1, +1\rangle + b_0|1, 0\rangle + b_{-1}|1, -1\rangle. \tag{3.3}$$

The coefficients of this linear combination, namely the eigenvalues of each sub-state, define the polarization of the particle. In particular if $b_0 = 0$ and $|b_{+1} + b_{-1}| = 1$ the particle is *transversely polarized*, while if $b_0 = 1$ and the other two coefficients are null it is *longitudinally polarized*.

It is not possible to determine the values of b_{+1}, b_0 and b_{-1} via experimental measurements, nevertheless the study of the anisotropies in the angular distributions of the particle decay products provides an indirect approach to extract its degree of polarization. In fact in a two body decay, as in the J/ψ and Υ(1S) dilepton channels, the geometrical shape of the angular distribution reflects its polarization, in particular a spherical symmetric distribution indicates that the state under study is unpolarized, while an anisotropic one signals the presence of polarization. The correlation among the coefficients b_{+1}, b_0 and b_{-1} and the angular distribution of the decay products can be demonstrated from first principles, as done in Ref. [140] from which the calculations in the following are taken and adapted.

Let's consider a situation as the one represented in Fig. 3.1. A quarkonium state (in the picture a J/ψ) flying in the z-direction, decays into a lepton pair $\ell^+\ell^-$ which is emitted back-to-back in the quarkonium rest frame and defines the z'-axis.

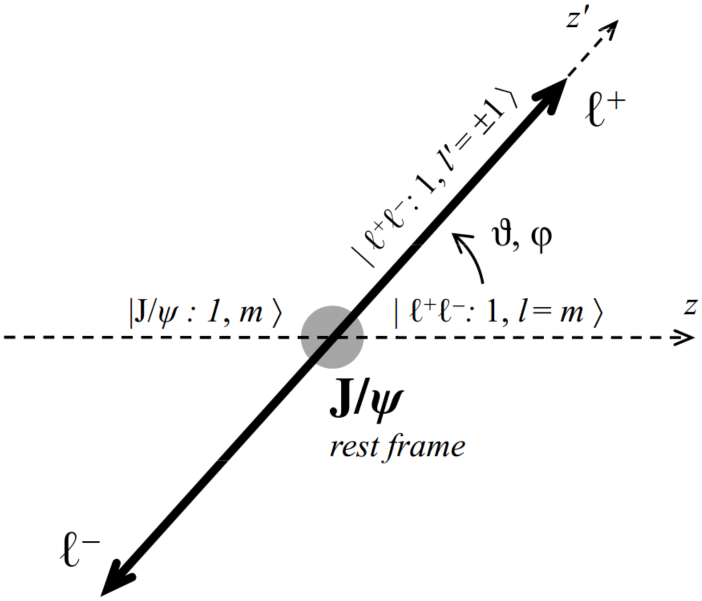

Figure 3.1: Sketch of the decay $J/\psi \rightarrow \ell^+\ell^-$. Figure taken from [140].

1. before the decay, the quarkonium total angular momentum and its third component along the z-direction can be written as $|Q\bar{Q} = J/\psi : 1, m\rangle$.
2. after the decay the dilepton state is written as $|\ell^+\ell^- : 1, l = m\rangle$ with respect to the z-axis, with $l = m$ because of the angular momentum conservation.
3. with respect to the z'-axis the dilepton state is written as $|\ell^+\ell^- : 1, l' = \pm 1\rangle$. The condition $l' = \pm 1$ is due to the helicity conservation for massless fermions in the decay process $Q\bar{Q} \rightarrow \gamma^* \rightarrow \ell^+\ell^-$ and for this reason the dilepton system has the same projection of the angular momentum along the z'-axis as the virtual photon. It is important to notice that the decay leptons are clearly not massless, nevertheless this assumption is approximately valid because their masses are negligible ($m_e \approx 0.51$ MeV/c^2, $m_\mu \approx 105$ MeV/c^2) with respect to the lightest quarkonium state ($m_{J/\psi} \approx$ 3.096 GeV/c^2).

The purpose of the demonstration is to express $|\ell^+\ell^- : 1, l' = \pm 1\rangle$ as a superposition of $J_{z'}$ eigenstates, $|\ell^+\ell^- : 1, l\rangle$ with $l = 0, \pm 1$. This change of quantization axis is performed using the rotation operator which is commonly used in the angular momentum theory. A rotation from a generic set of axis (x, y, z) to the set (x', y', z') is indicated with $R(\alpha, \beta, \gamma)$, where α, β and γ are the Euler angles. A $J_{z'}$ eigenstate $|J, M'\rangle$ can be expressed as a superposition of J_z eigenstates $|J, M\rangle$ via the transformation:

$$|J, M'\rangle = \sum_{M=-J}^{+J} \mathcal{D}^J_{MM'}(R)|J, M\rangle, \tag{3.4}$$

where $\mathcal{D}^J_{MM'}$ is the complex rotation matrix and it can be expressed in terms of reduced matrix elements $d^J_{MM'}(\beta)$:

$$\begin{aligned}\mathcal{D}^J_{MM'}(\alpha, \beta, \gamma) &= \langle J, M|e^{-i\alpha J_z} e^{-i\beta J_y} e^{-i\gamma J_z}|J, M'\rangle \\ &= \; e^{-iM\alpha}\langle J, M|e^{-i\beta J_y}|J, M'\rangle e^{-iM'\gamma} \\ &= \; e^{-iM\alpha} d^J_{MM'}(\beta) e^{-iM'\gamma}.\end{aligned} \tag{3.5}$$

Using Condon and Shortley choice of phase [141] the reduced rotation matrices are real and can be explicitly expressed as:

$$d^J_{MM'}(\beta) = \sum_{t=max(0,M-M')}^{min(J+M,J-M')} (-1)^t \times \mathcal{K}(t) \times \left(\cos\frac{\beta}{2}\right)^{2J+M-M'-2t} \left(\sin\frac{\beta}{2}\right)^{2t-M+M'} \tag{3.6}$$

$$\mathcal{K}(t) = \frac{\sqrt{(J+M)!(J-M)!(J+M')!(J-M')!}}{(J+M-t)!(J-M'-t)!t!(t-M+M')} \tag{3.7}$$

Since the purpose is to bring the z-axis to coincide with the z'-axis, the most general rotation is obtained using the parametrization $\beta = \theta$ and $\alpha = -\gamma = \varphi$. As a consequence Eq. 3.4 can be re-written as:

$$|\ell^+\ell^- : 1, l'\rangle = \sum_{l=0,\pm1}, \mathcal{D}^1_{ll'}(\varphi, \theta, -\varphi)|\ell^+\ell^- : 1, l\rangle. \tag{3.8}$$

To compute the amplitude for the process $\mathrm{J}/\psi(m) \to \ell^+\ell^-(l')$, it is necessary to calculate the bracket among the final and the initial state, applying the transition operator $\mathcal{B}$:

$$B_{ml'} = \sum_{l=0,\pm1} \mathcal{D}^{1*}_{ll'}(\varphi, \theta, -\varphi)\langle\ell^+\ell^- : 1, l|\mathcal{B}|\mathrm{J}/\psi : 1, m\rangle, \tag{3.9}$$

since the third component of the angular momentum has to be conserved in the transition, the action of the operator $\mathcal{B}$ is imposed to be:

$$\langle \ell^+\ell^- : 1, l|\mathcal{B}|\mathrm{J}/\psi : 1, m\rangle = B\delta_{ml} \tag{3.10}$$

hence, Eq. 3.9 can be rewritten as:

$$B_{ml'} = B\mathcal{D}^{1*}_{ml'}(\varphi, \theta, -\varphi). \tag{3.11}$$

The amplitude for $\mathrm{J}/\psi \to \ell^+\ell^-(l')$ considering all the possible m values in the initial states is obtained substituting $|\mathrm{J}/\psi : 1, m\rangle$ with Eq. 3.3

$$B_{l'} = \sum_{m=\pm1} b_m B\mathcal{D}^{1*}_{ml'}(\varphi, \theta, -\varphi) = \sum_{m=\pm1} a_m \mathcal{D}^{1*}_{ml'}(\varphi, \theta, -\varphi) \tag{3.12}$$

The transition probability is obtained squaring $B_{l'}$ and summing over all the unobserved spin alignments ($l' = \pm1$) of the dilepton system:

$$W(\cos\theta, \varphi) \propto \sum_{l'=\pm1} |B_{l'}|^2 \tag{3.13}$$

and using Eq. 3.6 in Eq. 3.12 the d elements are written as:

$$d^1_{0,\pm1} = \pm\frac{\sin\theta}{\sqrt{2}} \quad d^1_{\pm1,\pm1} = \frac{(1+\cos\theta)}{2} \quad d^1_{\pm1,\mp1} = \frac{(1-\cos\theta)}{2} \tag{3.14}$$

hence the Eq. 3.13 is written so that the angular distribution is explicitly obtained:

$$\begin{aligned} W(\cos\theta, \varphi) \propto \frac{\mathcal{N}}{3+\lambda_\theta} \cdot (1 &+ \lambda_\theta \cos^2\theta \\ &+ \lambda_\varphi \sin^2\theta \cos 2\varphi + \lambda_{\theta\varphi} \sin 2\theta \cos\varphi \\ &+ \lambda^\perp_\varphi \sin^2\theta \sin 2\varphi + \lambda^\perp_{\theta\phi} \sin 2\theta \sin\varphi) \end{aligned} \tag{3.15}$$

where $\mathcal{N} = |a_0|^2 + |a_1|^2 + |a_2|^2$.

The λ values are the *polarization parameters* and are directly dependent on the amplitudes a_m:

$$\begin{aligned}
\lambda_\theta &= \frac{\mathcal{N} - 3|a_0|^2}{\mathcal{N} + |a_0|^2} \\
\lambda_\varphi &= \frac{2\mathrm{Re}[a_{+1}^{(i)*} a_{-1}]}{\mathcal{N} + |a_0|^2} \\
\lambda_{\theta\varphi} &= \frac{\sqrt{2}\mathrm{Re}[a_0^{(i)*}(a_{+1} - a_{-1})]}{\mathcal{N} + |a_0|^2} \\
\lambda_\varphi^\perp &= \frac{-2\mathrm{Im}[a_{+1}^* a_{-1}]}{\mathcal{N} + |a_0|^2} \\
\lambda_{\theta\phi}^\perp &= \frac{-\sqrt{2}\mathrm{Im}[a_0^*(a_{+1} + a_{-1})]}{\mathcal{N} + |a_0|^2}.
\end{aligned} \tag{3.16}$$

In Eq. 3.15 the last two terms ($\lambda_\varphi^\perp \sin^2\theta \sin 2\varphi$ and $\lambda_{\theta\phi}^\perp \sin 2\theta \sin\varphi$) introduce an asymmetry by reflection with respect to the (x, z) plane. The latter coincides, from an experimental point of view, with the production plane, which is defined by the direction of the colliding hadrons and the momentum of the decaying particle. Nevertheless in hadronic collisions the asymmetry can be observed only considering as z-axis the parton momentum and not the hadron one. This means that the last two terms in Eq. 3.15 are unobservable because they vanish averaging over multiple parton collisions. After this further simplification the experimental accessible angular distribution is:

$$\begin{aligned}
W(\cos\theta, \varphi) \propto \frac{\mathcal{N}}{3 + \lambda_\theta} \cdot (1 &+ \lambda_\theta \cos^2\theta \\
&+ \lambda_\varphi \sin^2\theta \cos 2\varphi + \lambda_{\theta\varphi} \sin 2\theta \cos\varphi).
\end{aligned} \tag{3.17}$$

Alternatively to this expression, which is function of both $\cos\theta$ and φ, is is possible to obtain the one-dimensional distribution integrating over the angular variables:

$$W(\cos\theta) \propto \frac{\mathcal{N}}{3 + \lambda_\theta}(1 + \lambda_\theta \cos^2\theta), \tag{3.18}$$

$$W(\varphi) \propto 1 + \frac{2\lambda_\varphi}{3 + \lambda_\theta} \cos 2\varphi, \tag{3.19}$$

From these angular shapes, λ_θ and λ_φ parameters can be determined in two separate steps, improving the fit stability for low-statistics analyses. The $\lambda_{\theta\varphi}$ term, which vanishes in both the integrations, can be extracted defining the extra angular variable $\tilde{\varphi}$:

$$\tilde{\varphi} = \begin{cases} \varphi - \frac{3}{4}\pi & \text{for } \cos\theta < 0 \\ \varphi - \frac{\pi}{4} & \text{for } \cos\theta > 0 \end{cases} \tag{3.20}$$

As reported in Eq. 3.16, the polarization parameters directly depend on the coefficients of Eq. 3.3 ($b_m B = a_m$, see Eq. 3.12), therefore it is possible to extract the degree of spin alignment directly by fitting the observable angular distribution. For instance, considering two opposite scenarios of pure longitudinal and transverse polarization, the parameters are:

- $\lambda_\theta = -1$ and $\lambda_\varphi, \lambda_{\theta\varphi} = 0$ for pure longitudinal polarization, obtained substituting $a_0 = 1$ and $a_{\pm1} = 0$ in Eq. 3.16
- $\lambda_\theta = +1$ and $\lambda_\varphi, \lambda_{\theta\varphi} = 0$ for pure transverse polarization, obtained substituting $a_{0,-1} = 0$ and $a_{+1} = 1$ (or $a_{0,+1} = 0$ and $a_{-1} = 1$) in Eq. 3.16

From Eq. 3.16 and imposing the condition that $|\lambda_\theta| \leq 1$, the following relations among the polarization parameters can be deduced:

$$|\lambda_\varphi| \leq \frac{1}{2}(1+\lambda_\theta) \qquad |\lambda_{\theta\varphi}| \leq \frac{1}{2}(1-\lambda_\varphi) \tag{3.21}$$

$$(1+2\lambda_\varphi)^2 + 2\lambda_{\theta\varphi}^2 \leq 1 \quad \text{for} \quad \lambda_\varphi < -1/3 \tag{3.22}$$

These relations imply that $|\lambda_\varphi| \leq 1$ and $|\lambda_{\theta\varphi}| \leq 1/\sqrt{2}$, while λ_φ should vanish for $\lambda_\theta \to -1$. In Fig. 3.2 the projection of the 3D parameters space is shown for the $(\lambda_\theta, \lambda_\varphi)$, $(\lambda_\theta, \lambda_{\theta\varphi})$ and $(\lambda_\varphi, \lambda_{\theta\varphi})$ planes.

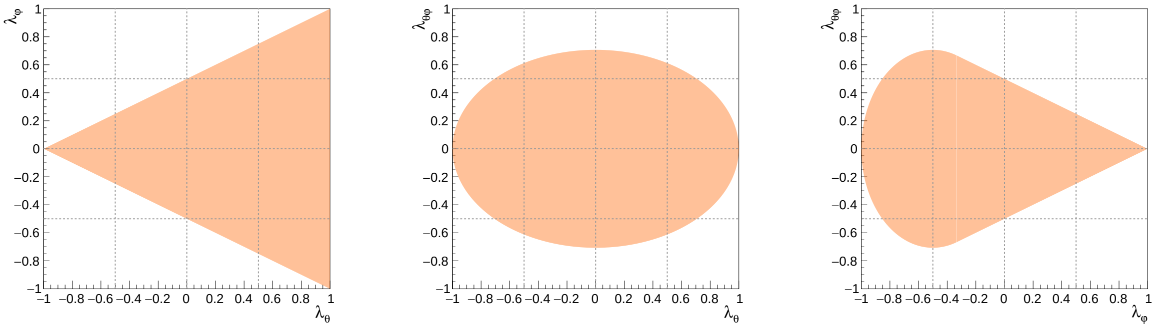

Figure 3.2: Allowed regions for the polarization parameters. Left panel: $(\lambda_\theta, \lambda_\varphi)$ plane. Central panel: $(\lambda_\theta, \lambda_{\theta\varphi})$ plane. Right panel: $(\lambda_\varphi, \lambda_{\theta\varphi})$ plane.

3.1.1 Reference frames

From an experimental point of view, the measurement of the angular distributions requires the choice of a reference frame, with respect to which the momentum direction of the decay products is expressed in spherical coordinates. Once the plane containing the momenta of the colliding beams (*production plane*) is fixed, as shown in Fig. 3.3, in the quarkonium rest frame the polar angle θ is determined as the direction of the positive lepton with respect to the quantization axis, while the azimuthal angle φ is measured with respect to the production plane. Since for an inclusive measurement the final result depends on the average of all the single production processes, each of them can favor a specific spin-alignment configuration. As a consequence it can be expected that different definitions of the quantization axis provide different values for λ_θ, λ_φ and $\lambda_{\theta\varphi}$. For this reason the evaluation of the polarization parameters using different reference systems can be important to study the various mechanisms involved in the production process. Moreover the comparison among the different results can also be helpful to investigate possible sources of systematic uncertainties.

In standard quarkonium polarization analyses and in most of the publications related to this topic, the main reference systems used are three:

- **helicity**: the z-axis is chosen as the quarkonium momentum direction in the collision center-of-mass frame.
- **Collins-Soper**: the z-axis is the bisector of the angle formed by the directions of one

beam and the opposite of the other beam, in the quarkonium center of mass frame [142].

- **Gottfried-Jackson**: the z-axis is the momentum direction of one of the two colliding beams. It is mainly used for fixed target experiments where the definition is unambiguous [143].

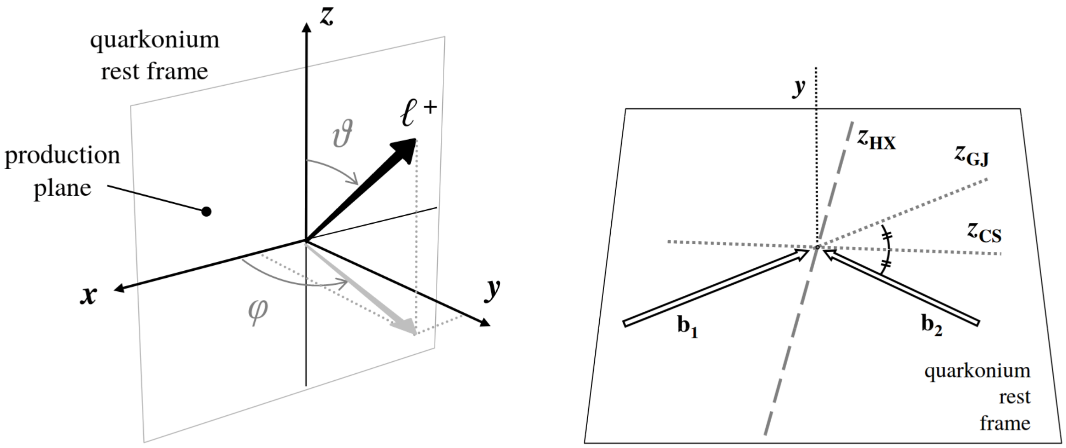

Figure 3.3: Left panel: illustration of the coordinate system used for the measurement of the angular variables for a two body decay. Right panel: representation of the z-axis for different reference frames definitions: heliciy (HX), Collins-Soper (CS) and Gottfries-Jackson (GJ). Both the figures are taken from [140].

Since the experimentally definable quantization axes lay on the production plane, it is possible to parametrize the transformation from one reference frame to the other as a rotation around the y-axis. Therefore, instead of rotating all the angular momentum state vectors, a purely geometrical transformation can be applied to the observable angular distribution using the rotation matrix:

$$R_y(\delta) = \begin{pmatrix} \cos\delta & 0 & -\sin\delta \\ 0 & 1 & 0 \\ \sin\delta & 0 & \cos\delta \end{pmatrix} \tag{3.23}$$

indicating with δ the angle between the two different reference frames. In spheric coordinates the unit vector which indicates the lepton direction is $\hat{r} = (\sin\theta\cos\varphi, \sin\theta\sin\varphi, \cos\theta)$, hence the change of coordinates is achieved expressing the direction in the old frame as a function of the coordinates in the new frame ($\hat{r}'$):

$$\hat{r} = R_y(\delta)^{-1}\hat{r}'. \tag{3.24}$$

Solving the system of equations the angular distribution in the rotated frame is:

$$\begin{aligned} W'(\cos\theta', \varphi') \propto \frac{1}{3+\lambda'_\theta} \cdot (1 + \lambda'_\theta \cos^2\theta' \\ + \lambda'_\varphi \sin^2\theta' \cos 2\varphi' + \lambda'_{\theta\varphi} \sin 2\theta' \cos\varphi'), \end{aligned} \tag{3.25}$$

where:

$$\begin{aligned} \lambda'_\theta &= \frac{\lambda_\theta - 3\Lambda}{1+\Lambda} \\ \lambda'_\varphi &= \frac{\lambda_\varphi + \Lambda}{1+\Lambda} \\ \lambda'_{\theta\varphi} &= \frac{\lambda_{\theta\varphi}\cos 2\delta - \frac{1}{2}(\lambda_\theta - \lambda_\varphi \sin 2\delta)}{1+\Lambda} \\ \text{with} \quad \Lambda &= \frac{1}{2}(\lambda_\theta - \lambda_\varphi)\sin^2\delta - \frac{1}{2}\lambda_{\theta\varphi}\sin 2\delta. \end{aligned}$$

These relations implies the existence of the frame invariant quantity:

$$\mathcal{F}_{c_1,c_2,c_3} = \frac{(3+\lambda_\theta) + c_1(1-\lambda_\varphi)}{c_2(3+\lambda_\theta) + c_3(1-\lambda_\varphi)} \tag{3.26}$$

where c_1, c_2 and c_3 are real numbers. Considering a specific set of parameters (c_1, c_2, c_3), Eq. 3.26 can be rewritten as:

$$\tilde{\lambda} \equiv \mathcal{F}_{-3,0,1} = \frac{\lambda_\theta + 3\lambda_\varphi}{1-\lambda_\varphi}. \tag{3.27}$$

$\tilde{\lambda}$ is the frame invariant parameter and it has been largely used in many quarkonium polarization analyses. If polarization parameters are determined in more than one frame, this observable becomes particularly important to check the consistency of the measurements.

3.2 Quarkonium polarization: experimental results

Quarkonium polarization have been widely studied by different experiments and in different collision systems. Polarization measurements appeared to be the ideal test ground for many of the theoretical models on the market, since some of them were predicting completely different degrees of polarization according to the state in which the quarkonium is produced. For instance, NRQCD LO calculations predicted a strong transverse polarization for high-p_{T} J/ψ, where gluon fragmentation is expected to be the dominant process. Since the fragmenting gluon is "almost" on-shell, it has to be transversely polarized and consequently also the $c\bar{c}$ pair has to be transversely polarized. Despite the success of NRQCD in the description of quarkonium cross sections, the measurements at the LHC did not confirm the theoretical expectations and it was clear that more efforts in the NLO calculations were necessary to possibly solve this puzzle. In the following the most significant results from Tevatron, RHIC and LHC experiments will be reported and discussed.

3.2.1 Tevatron

Quarkonium polarization was studied at Tevatron using data collected in p$\bar{\mathrm{p}}$ collisions during Run I and II.

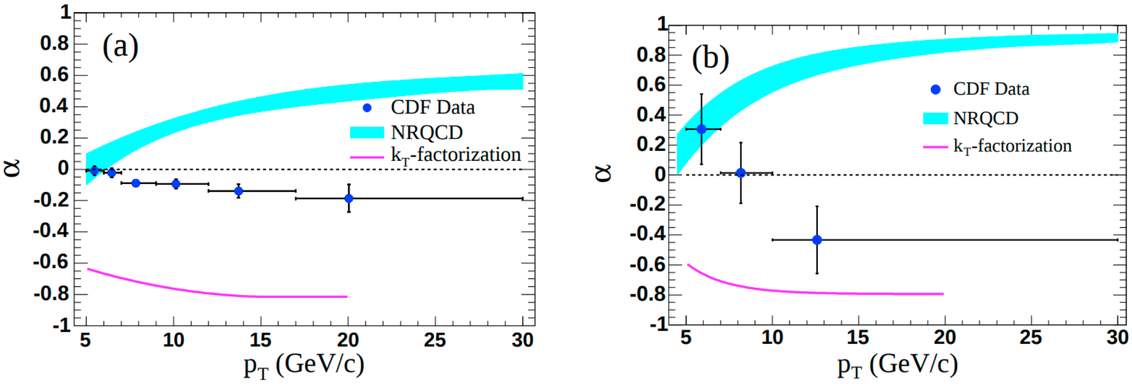

Figure 3.4: J/ψ (a) and ψ(2S) (b) λ_θ parameter (α) as a function of p_{T} measured by the CDF collaboration at $\sqrt{s} = 1.96$ TeV at mid-rapidity ($|y| < 0.6$) [144]. Results are compared with NRQCD [145] and CSM k_{T} factorization [146] predictions.

The CDF collaboration measured J/ψ and ψ(2S) polarization at mid-rapidity ($|y| < 0.6$) as a function of transverse momentum [144]. As shown in Fig. 3.4, the disagreement among data and theoretical predictions is evident, especially for NRQCD, which is not able to describe the data trend. A similar situation is observed for $\psi(2S)$, even if the size of the uncertainties prevents from drawing a firm conclusion. Moreover, these results were found to be in disagreement with the Run I measurements performed at $\sqrt{s}$ = 1.8 TeV [147], where for J/ψ an opposite trend as a function of p_T was observed.

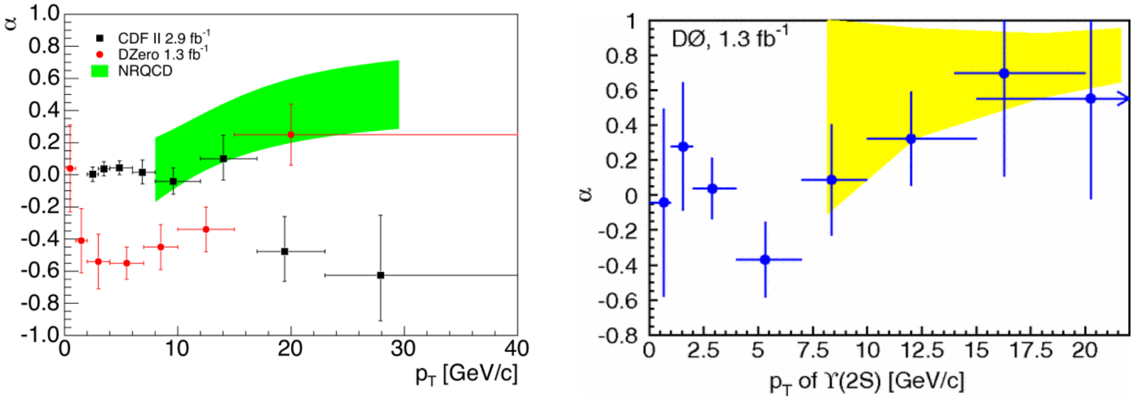

Figure 3.5: Left panel: $\Upsilon(1S)$ λ_θ parameter (α) as a function of p_T measured by the D0 [148] and CDF [149] collaborations at $\sqrt{s}$ = 1.96 TeV. Right panel: $\psi(2S)$ λ_θ parameter (α) as a function of p_T measured by the D0 collaboration at $\sqrt{s}$ = 1.96 TeV [148]. Both results are compared with LO NRQCD [150] predictions (green/yellow band)

Exploiting the large data sample collected during Run II, the D0 collaboration managed to measure bottomonium polarization for the $\Upsilon(1S)$ and $\Upsilon(2S)$ states [148]. Differently from charmonia, in this case the NRQCD factorization approach seemed to describe the trend of experimental points in the high p_T region, while at low p_T no model is able to match the data points. This measurement is in contradiction with the CDF one [149], which is shown in Fig. 3.5 and does not exhibit such a strong longitudinal polarization for $\Upsilon(1S)$. These sets of results pointed to an unclear situation which raised even more interest in the future measurements at RHIC and LHC.

3.2.2 RHIC

The J/ψ polarization has been widely investigated at RHIC in proton-proton collisions. In particular the PHENIX [151] and STAR [152] collaborations published a first set of results at $\sqrt{s}$ = 200 and 510 GeV. Both the measurements are in agreement with the scenario of unpolarized J/ψ.

Recently the STAR collaboration extracted the λ_θ, λ_φ and $\lambda_{\theta\varphi}$ parameters in the helicity and Collins-Soper reference frames as a function of p_{T} considering both the dielectron ($|y| < 1$) and dimuon ($|y| < 0.5$) decay channels at $\sqrt{s} = 200$ GeV [153]. All the polarization parameters are compatible with zero and do not exhibit a strong p_{T}-dependence, showing a fair agreement among the two decay channels, even if a slightly different kinematic range is covered. As shown in Fig. 3.6, among the various theoretical models, the one implementing NRQCD calculations performed in the Color Glass Condensate effective field theory (CGC + NRQCD) [139] agrees the best overall. This approach includes contributions from both the color-singlet and color-octet intermediate states and seems to solve some of the issues of the collinear factorization formalism in the calculation of the $c\bar{c}$ cross section at low-p_{T}.

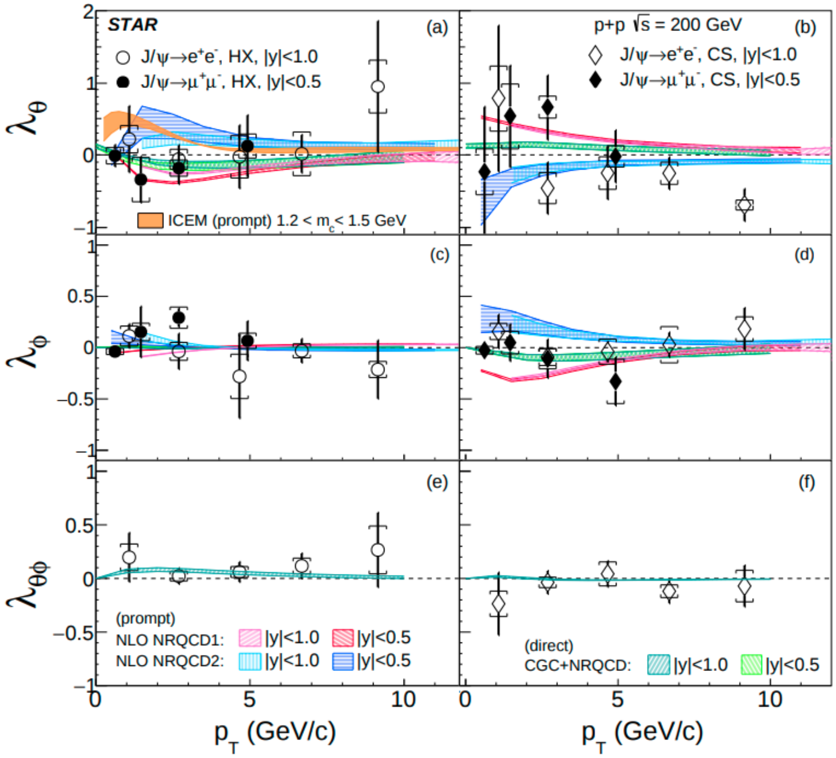

Figure 3.6: J/ψ polarization parameters as a function of p_{T} in the helicity (HX) and Collins-Soper (CS) reference frames for the dielectron (open point) and dimuon (filled point) [153] measured by the STAR collaboration. Data are compared with models predictions [154, 155, 139, 156]. ICEM and the two NLO NRQCD calculations are for prompt J/ψ, while the CGC+NRQCD is for direct J/ψ.

3.2.3 LHC

The beginning of the LHC era significantly expanded the possibility to investigate polarization, with the large center-of-mass energy reached by the accelerator allowing to collect huge data samples. The first measurement of J/ψ polarization was performed by the ALICE experiment at $\sqrt{s} = 7$ TeV in the rapidity range $2.5 < y < 4$ and for $2 < p_{\mathrm{T}} < 8$ GeV/c [157]. As shown in Fig. 3.7, this first result exhibited a λ_θ value compatible with zero and represented a serious issues for the theoretical models. In fact NRQCD at leading order (LO) predicted a strong transverse polarization, while the NLO Color-Singlet model pointed to a large longitudinal polarization in the helicity frame ($\lambda_\theta \sim -0.6$) at $p_{\mathrm{T}} \sim 5$ GeV/c [158].

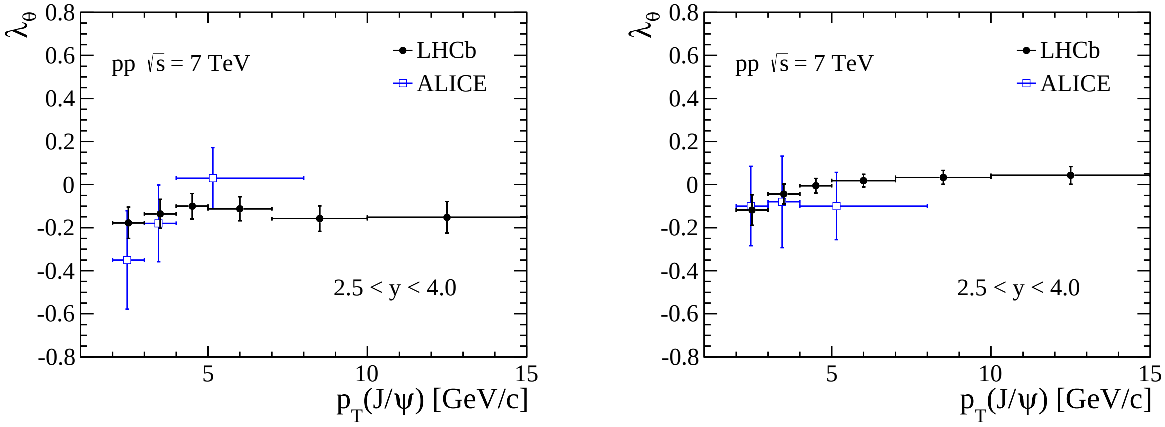

Figure 3.7: J/ψ λ_θ parameter measured by the ALICE [157] and LHCb [159] experiments in pp collisions at $\sqrt{s} = 7$ TeV in the forward rapidity region ($2.5 < y < 4$). The results corresponding to the helicity and Collins-Soper reference frames are shown in the left and in the right panel respectively.

The ALICE results was confirmed by the following LHCb measurement at the same center-of-mass energy, but in a slightly larger rapidity range ($2 < y < 4.5$) and extending the p_{T}-region up to 15 GeV/c [159]. In both helicity and Collins-Soper reference frames, λ_φ and $\lambda_{\theta\varphi}$ parameters are consistent with zero, while λ_θ shows a small but significant longitudinal polarization in the helicity reference frame. In particular, the weighted average of the LHCb results calculated over all the p_{T} and y bins is

$$\lambda_\theta^{\mathrm{HE}} = -0.145 \pm 0.027, \tag{3.28}$$

and represents up to now one of the most precise measurements for a hadron collider. In addition, the study of the rapidity dependence for λ_θ was performed, showing a weak dependence on this variable. The ALICE collaboration measured the J/ψ polarization at $\sqrt{s}$ = 8 TeV and it showed a fair agreement with both the results discussed previously. The polarization parameters are shown in Fig. 3.8 and compared with NLO CSM [158] and NRQCD [158, 160] predictions.

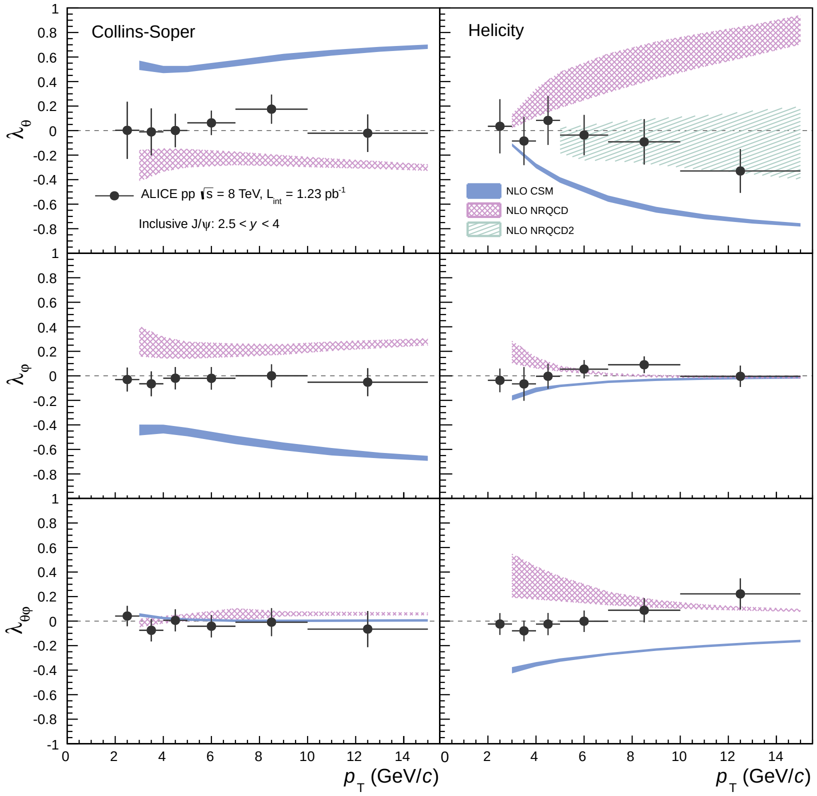

Figure 3.8: Inclusive J/ψ polarization parameters in pp collisions at $\sqrt{s}$ = 8 TeV compared with model predictions of NLO CSM [158] NRQCD [158] and NRQCD2 [160].

The CMS collaboration measured J/ψ and ψ(2S) polarization parameters as a function of p_T at $\sqrt{s}$ = 7 TeV in three different rapidity ranges $|y| < 0.6$, $0.6 < |y| < 1.2$ and $1.2 < |y| < 1.5$ [161]. The J/ψ result covers $14 < p_T < 70$ GeV/c, while the ψ(2S) one $14 < p_T < 50$ GeV/c. The importance of this measurement is related to the wide transverse momentum range investigated, which is particularly interesting since LO NRQCD predicted a large transverse polarization at high-p_T. Nevertheless all the polarization parameters are compatible with zero within the uncertainties, in a complementary transverse momentum range with respect to ALICE and LHCb.

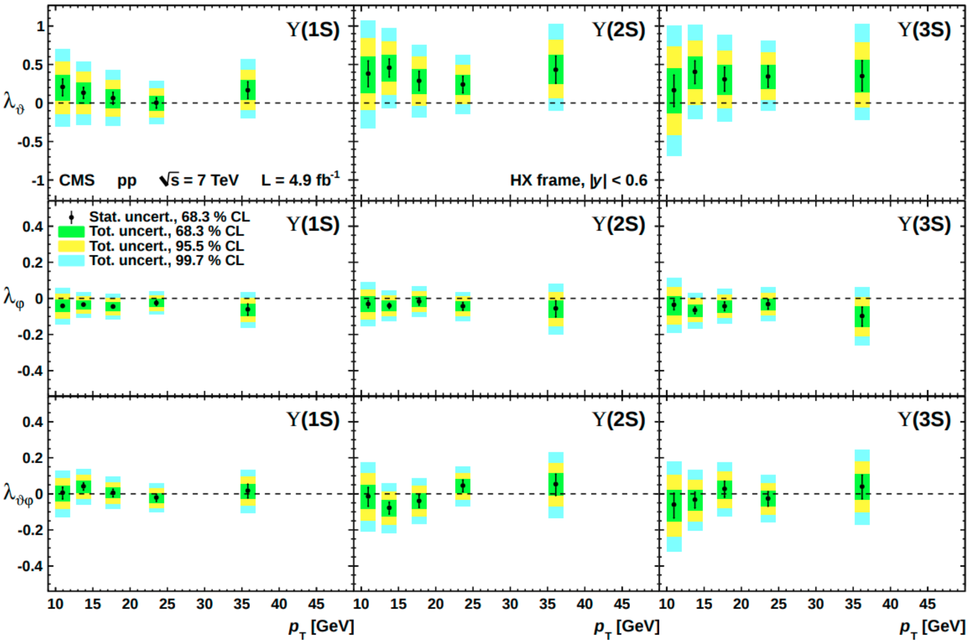

Figure 3.9: Υ(1S), Υ(2S) and Υ(3S) polarization parameters as a function of p_{T} in $|y| < 0.6$ in the helicity (HX) reference frame [162].

CMS measured also the polarization parameters for Υ(1S), Υ(2S) and Υ(3S) in the range $10 < p_{\mathrm{T}} < 50$ GeV/c for $|y| < 0.6$ and $0.6 < |y| < 1.2$, as shown in Fig. 3.9. No evidence for large transverse or longitudinal polarization is observed in the explored kinematic region. The same measurement was performed by LHCb in the forward rapidity region for $p_{\mathrm{T}} < 20$ GeV/c at $\sqrt{s} = 7$ and 8 TeV [163]. All the polarization parameters are small and do not exhibit a strong transverse or longitudinal polarization, in agreement with the CMS measurement.

3.3 Quarkonium polarization in heavy-ion collisions

Quarkonium polarization in heavy-ion collisions is a relatively unexplored field, mainly because of the complexity of the system, characterized by a series of effects which may or may not have a significant impact on the measured polarization. This reason, combined

with the lack of experimental measurements, resulted in a limited theory effort to provide predictions for this observable. The first study of quarkonium polarization in heavy-ion collisions, described in Ref. [164], showed that this observable can be used as a signature for the QGP formation. As discussed in the previous sections, the measurements in pp collisions showed that charmonia and bottomonia appeared to be unpolarized. The discrepancy with the LO QCD predictions available at that time was ascribed to the influence of non-perturbative effects. Indeed, the heavy quark pair production occurs at a short time scale $\tau_{\text{prod}} \sim 1/2m_{\text{Q}}$, while the formation of the bound state is a soft process, characterized by $\tau_{\text{bind}} = 1/\varepsilon$, where ε is the binding energy. For a Coulomb-like interaction $\varepsilon \sim \alpha_{\text{S}} m_{\text{Q}}^2 \ll m_{\text{Q}}$, therefore the binding process is certainly affected by non-perturbative processes, and this may significantly impact both the cross section and the polarization measurements. However, if the heavy quarkonium formation occurs inside the QGP, approximated as a weakly coupling system, the non-perturbative component might be neglected. For this reason dense parton matter could screen away a large part of the quarkonia, in particular the less bound states $\psi(2\text{S})$ and χ_{c}, but those that survive would carry their original polarization, as arising from the production process.
Assuming the validity of this approach and taking into account the modification of the J/ψ feed-down fractions due to the larger suppression in the plasma for excited quarkonium states, in Ref. [164] J/ψ was expected to be found at $p_{\text{T}} \sim 0$ with:

$$\lambda_\theta \simeq 0.35 \div 0.4, \tag{3.29}$$

which corresponds to a remarkable increase of the polarization going from hadron to heavy-ion collisions.

From an experimental point of view, J/ψ polarization was measured in proton-nucleus collisions by the HERA-B [165] and NA60 [166] collaborations. HERA-B extracted the polarization parameters in p–C and p–W collisions, with a 920 GeV proton beam, while NA60 performed the measurements in p–A collisions with two different beam energies, 158 and 400 GeV. As shown in the left panel of Fig. 3.10, the HERA-B results exhibits a clear trend from negative to null values for the λ $(= \lambda_\theta)$ parameter, while for ν $(= \lambda_\phi)$ no significant evolution is observed as a function of p_{T}. These measurements are in agreement with the NA60 ones, which in addition do not show any clear dependence on the center-of-mass-energy.
The only existing measurement of the J/ψ polarization in nucleus-nucleus collisions was performed by the NA60 collaboration [166] in In-In collisions at 158 GeV incident energy. These results, obtained in the helicity reference and shown in the right panel of Fig. 3.10,

are compatible with zero within the uncertainties. It is also important to notice that λ $(=\lambda_\theta)$ and ν $(=\lambda_\phi)$ do not exhibit a clear dependence with respect to both the transverse momentum and the collision centrality, even if the statistical and systematic uncertainties prevents a firm conclusion on a possible smooth trend for the polarization parameters as a function of these variables.

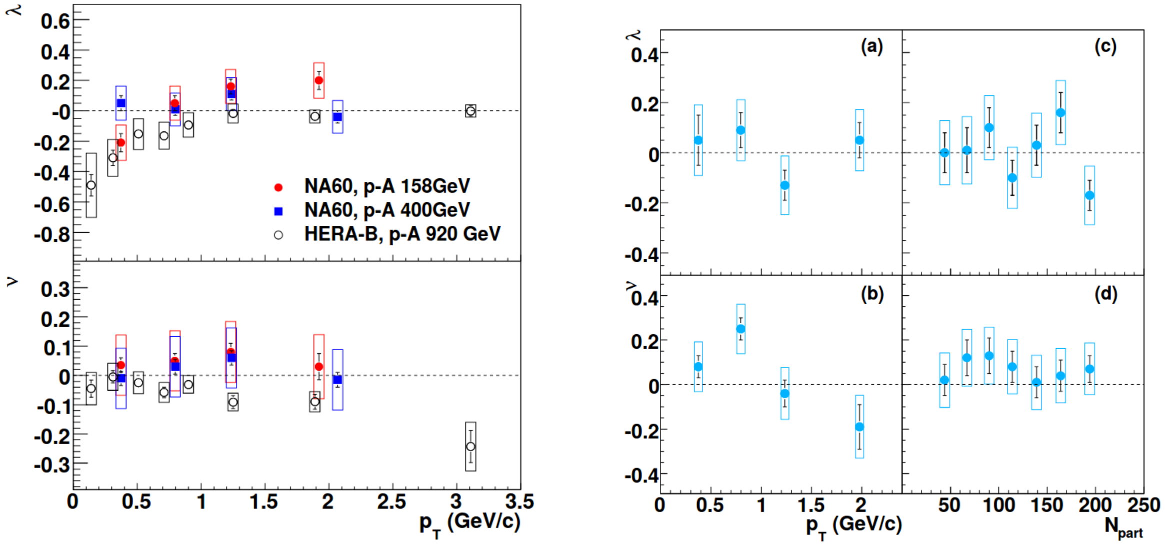

Figure 3.10: Left panel: J/ψ polarization parameters λ $(=\lambda_\theta)$ and ν $(=\lambda_\phi)$ as a function of p_{T} in proton-nucleus collisions measured by the HERA-B [165]and NA60 [166] collaborations. HERA-B result is obtained with a 920 GeV proton beam, while NA60 one is obtained for 158 and 400 GeV. Right panel: J/ψ polarization parameters λ $(=\lambda_\theta)$ and ν $(=\lambda_\phi)$ as a function of p_{T} and of the mean number of collision participants [166]. The results are obtained in the helicity reference frame in In–In collisions at 158 GeV.

3.3.1 Polarization: angular momentum and magnetic field

The study of polarization of particle production in heavy-ion collisions gives the possibility to investigate some specific effects relative to these interactions. In particular, an extremely intense electromagnetic field, induced by the moving charges, is expected to be created. The magnetic field is estimated to decrease rapidly as a function of the time (see Fig. 3.11), but reaching a value of $10^{14}-10^{15}$ T for $\tau < 0.5$ fm/c [167], and for this reason it is supposed to induce various kind of phenomena. For instance, it was suggested that in

the vicinity of the phase transition the spin alignment along the magnetic field direction could determine an imbalance of left and right-handed quarks, generating an electromagnetic current. This mechanism, known as *chiral magnetic effect* (CME) [168], is under study at RHIC and at the LHC, and charge-dependent correlations measurements show effects that could be consistent with the CME predictions [169, 170, 171].
Another measurement which seems to confirm the formation of sizable magnetic field in heavy-ion collisions is the charge dependence of the directed flow (v_1). In fact, when measured with respect to the spectator plane[1], the v_1 should be sensitive to the presence of a magnetic field. The latter is on average perpendicular to the spectator plane and can modify the directed flow charge dependence through two different mechanisms: 1.) the Lorentz force experienced by charged particles propagating inside $\vec{B}$, 2.) the electric field generated by the decrease of the magnetic field as a function of time.

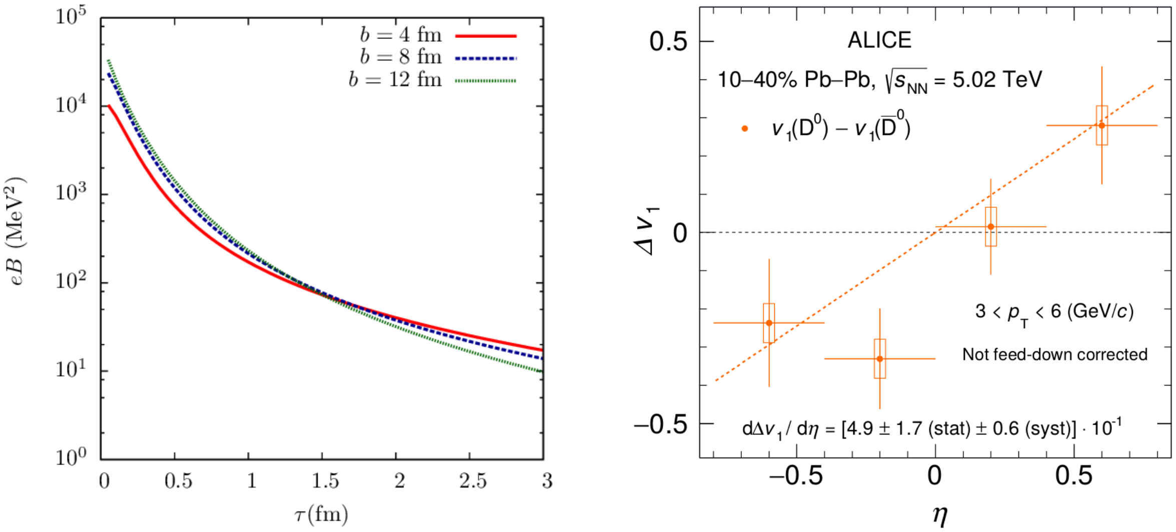

Figure 3.11: Left panel: magnetic field (multiplied by e) at the origin $r = 0$ in Au-Au collisions at $\sqrt{s_{\mathrm{NN}}} = 200$ GeV [167]. Right panel: Δv_1 for $D^0/\bar{D}^0$ mesons as a function of pseudorapidity in Pb-Pb collisions as $\sqrt{s_{\mathrm{NN}}} = 5.02$ TeV [172].

The ALICE collaboration measured the difference between the directed flow (Δv_1) of D^0 and $\bar{D}^0$ in Pb-Pb collisions at $\sqrt{s_{\mathrm{NN}}} = 5.02$ TeV [172]. D-mesons are chosen because the charm (anti-charm) quarks are produced in the early stages of the collision, when the magnetic field is more intense, therefore they should be more affected by the large $\vec{B}$-field

---

[1] defined by the deflection direction of the collision spectators

with respect to light quarks. As shown in Fig. 3.11, Δv_1 as a function of pseudorapidity exhibits a positive slope ($\mathrm{d}\Delta v_1/\mathrm{d}\eta = [4.9 \pm 1.8] \times 10^{-1}$) in semi-central ($10-40\%$) Pb–Pb collisions. If compared to the Δv_1 for charged hadrons [172], the D-mesons one is found to be around three order of magnitude larger.

Another important property of the medium created in the collision is the potential presence of a large angular momentum ($\vec{L}$). Differently from the magnetic field which is short lived, the angular momentum is conserved and it could have an impact on some experimental observables. Among them spin-orbit interactions are of particular interest, as they could determine the polarization of quarks and a consequent polarization of the vector mesons along $\vec{L}$ [173]. The spin alignment is quantified by the 3×3 Hermitian spin-density matrix [174]. The matrix element ρ_{00} can be experimentally evaluated and it is obtained from the angular distribution of the decay products of the vector meson with respect to a quantization axis. In these studies the latter is normally chosen as the vector perpendicular to the *reaction plane*, defined by the beam axis and the impact parameter, or the normal to the *production plane*, defined by the flight direction of the vector meson and the beam axis.

From an experimental point of view ρ_{00} can be extracted by fitting the vector meson angular distribution with:

$$\frac{\mathrm{d}N}{\mathrm{d}\cos\theta^*} \propto 1 - \rho_{00} + \cos^2\theta^*(3\rho_{00} - 1) \tag{3.30}$$

where θ^* is the angle formed by the polarization axis and the vector meson decay daughter. If there is no spin then alignment $\rho_{00} = 1/3$ and the distribution in Eq. 3.30 is uniform. Otherwise, any deviation from $\rho_{00} = 1/3$ leads to an anisotropy in the angular distribution, pointing to a preferred spin state for the vector meson.

A first evidence of spin alignment in heavy-ion collisions has been recently obtained by the ALICE collaboration, which measured the ρ_{00} parameter for K^{*0} and ϕ mesons [175]. As shown in Fig. 3.12, for the K^{*0} meson ρ_{00} is significantly lower than 1/3 for $p_{\mathrm{T}} < 2$ GeV/c with respect to the event and production planes in semi-central ($10-50\%$) Pb–Pb collisions. The result is compared with the same measurement for the spin zero hadron K^0_{S}, which, as expected, is compatible with 1/3 within the uncertainties. A consistency check is performed, repeating the measurement for $K^{*0}(892)$ and $\phi(1020)$ mesons in pp collisions. Here the result is compatible with 1/3, reinforcing the interpretation that the effect observed in Pb–Pb is due to the spin-orbit coupling in the "rotating" QGP. Finally ρ_{00} is extracted for a randomly defined event plane and also in this case the result is found to be consistent with 1/3.

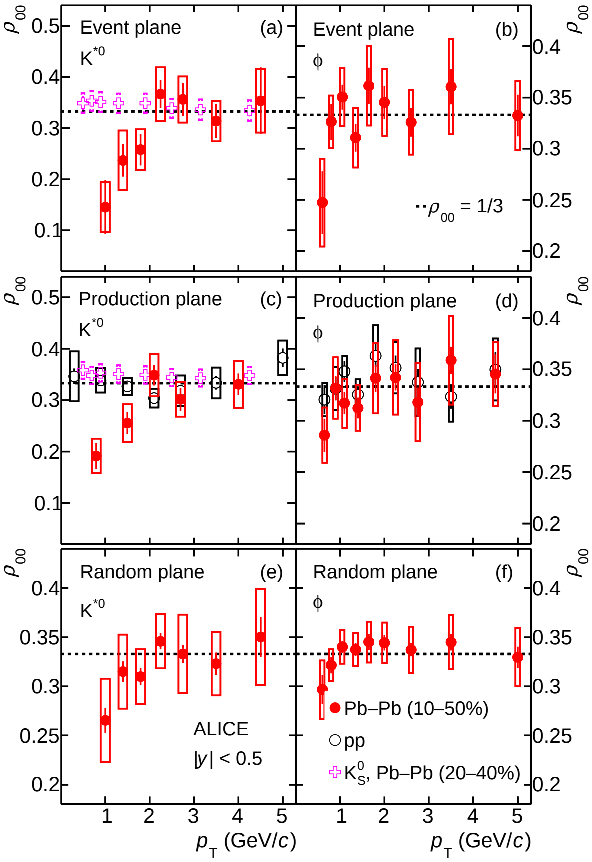

Figure 3.12: ρ_{00} p_{T} dependence for K^{*0}, ϕ and K^0_{S} mesons in Pb-Pb collisions at $\sqrt{s_{\mathrm{NN}}} = 5.02$ TeV and in pp collisions at $\sqrt{s} = 13$ TeV [175]. Results are obtained with respect to the event plane (a,b), production plane (c,d) and with respect to a random plane (e,f).

In summary, in collisions among heavy nuclei various mechanisms related to the formation of large electromagnetic fields and angular momenta could be present and the recent experimental observations seem to confirm these expectations. It then becomes naturally interesting to understand if these effects could have an impact on quarkonium polarization and how sizable they are. In particular the large $\vec{B}$-field could be investigated via quarkonium polarization measurements. Analogously to the K^{*0} meson, a reference frame in which the quantization axis is oriented perpendicularly to the event plane has to be defined, but the different time scale associated to the production of the light and heavy quarks, could make quarkonia more sensitive to the short living magnetic field.

Chapter 4

The ALICE experiment

4.1 The Large Hadron Collider

The Large Hadron Collider (LHC) is the most powerful and world's largest particle accelerator. It is the last element of the CERN accelerating chain which includes the PS (Proton Synchrotron) and the SPS (Super Proton Synchrotron), now used as injectors of the accelerating chain. All the structure is placed between 45 and 170 m underground into the 27 km tunnel previously used for the Large Electron-Positron collider (LEP). The whole apparatus is designed to accelerate protons at a maximum center-of-mass energy of 14 TeV with a peak luminosity of $\mathcal{L} = 10^{34}$ cm^{-2}s^{-1} and Pb ions at a center-of-mass energy per nucleon pair of $\sqrt{s_{\mathrm{NN}}} = 5.5$ TeV with a peak luminosity of $\mathcal{L} = 10^{27}$ cm^{-2}s^{-1}. The two colliding beams rotate in opposite directions into separate pipes, which are embedded inside superconducting dipole magnets. The latter are 14.3 m long and are cooled down to 1.9 K by means of liquid helium.

From the start of the LHC operations until now, the data taking was organized into two campaigns, Run 1, from 2009 to 2013 and Run 2, from 2015 to 2018, separated by the Long Shutdown 1, where the machine was upgraded to increase the beam energy. During these periods LHC delivered pp collisions at $\sqrt{s} = 0.9$, 2.76, 5.02, 7, 8 and 13 TeV, p–Pb collisions at $\sqrt{s_{\mathrm{NN}}} = 5.02$ and 8.16 TeV and Pb–Pb collisions at $\sqrt{s_{\mathrm{NN}}} = 2.76$ and 5.02 TeV. In addition, a short data taking period was dedicated to test another nuclear species, colliding Xe–Xe nuclei at $\sqrt{s_{\mathrm{NN}}} = 5.44$ TeV.

Along the LHC ring there are four main experiments: CMS (Compact Muon Solenoid) and ATLAS (A Toroidal LHC ApparatuS) are general purpose detectors, while LHCb (Large Hadron Collider beauty) and ALICE (A Large Ion Collider Experiment) are mainly dedicated to beauty physics and to study the Quark-Gluon Plasma, respectively. In the following the ALICE experiment is discussed with more details.

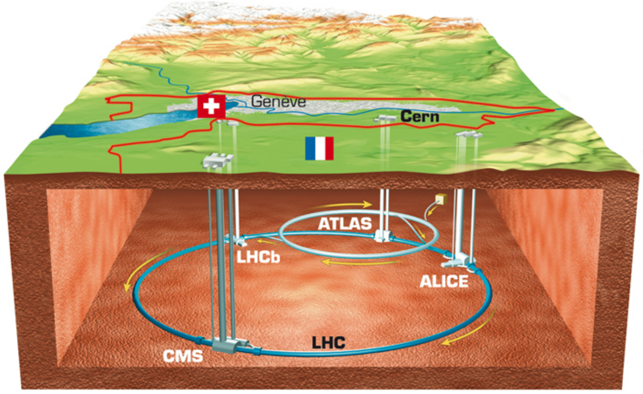

Figure 4.1: The Large Hadron Collider (LHC) and its main experiments.

4.2 ALICE detectors

The main purpose of the ALICE experiment is the study of the physics of strongly interacting matter in ultra-relativistic heavy-ion collisions. It is also designed for proton-proton and proton-nucleus collisions, which represent an important part of its physics program. The experiment itself can be divided into three main groups of detectors:

1. *central barrel detectors* (ITS, TPC, TRD, TOF, HMPID, PHOS, CPV, DCal and EMCal) are embedded into a solenoid with a magnetic field of $B = 0.5$ T and are used for tracking and identification of charged particles and photons.
2. *muon spectrometer* covers the forward region with respect to the interaction point and is designed for muon tracking and triggering.
3. *forward detectors* (FMD, PMD, V0, T0, AD and ZDC) are used mainly for triggering, event characterization and beam luminosity measurements.

The detector is completed by an array of scintillators to trigger on cosmic rays (ACORDE). In Fig. 4.2 a schematic of the ALICE experiment with all its main detectors is reported.

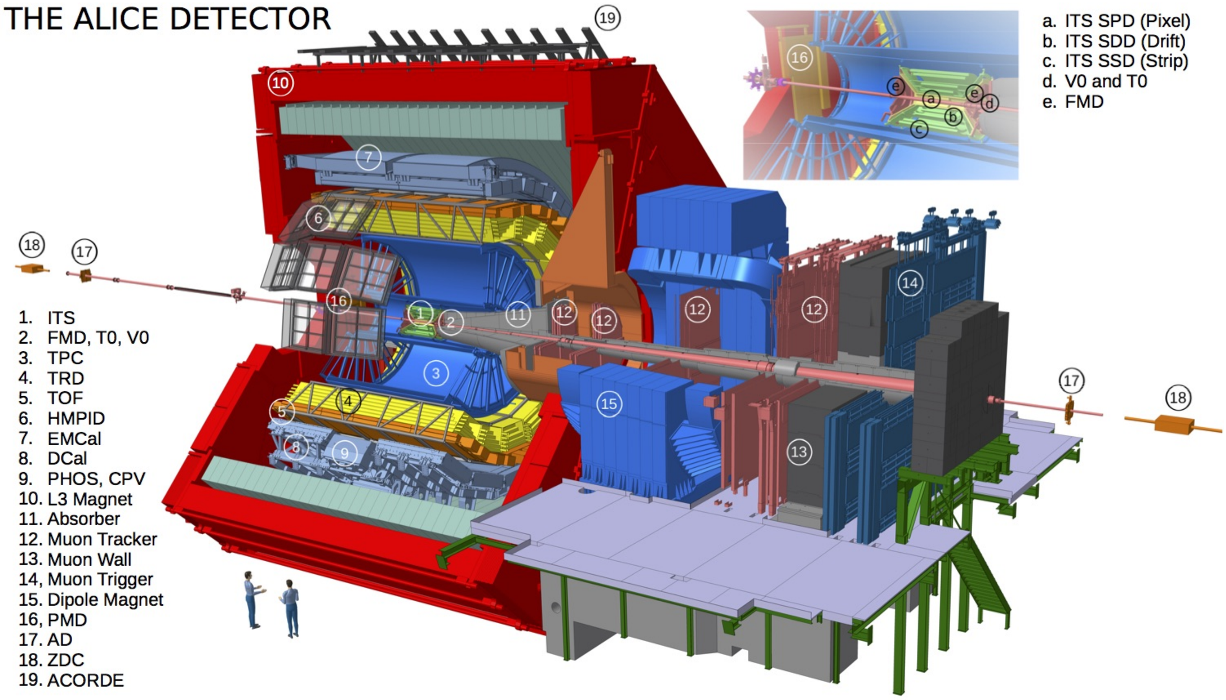

Figure 4.2: Schematic of the ALICE experiment. Figure from ALICE figure repository ©.

4.3 Central barrel

The section of the ALICE experimental apparatus positioned at central rapidity is named *central barrel* and it is composed by several detectors, each of them with different purposes. All the structure surrounds the interaction point, covering the pseudorapidity range $|\eta| < 0.9$, and it is placed inside the magnetic field of up to 0.5 T generated by a warm solenoid magnet for the measurement of particle momenta.

4.3.1 Inner Tracking System (ITS)

The Inner Tracking System is the detector closest to the beam pipe and its main tasks are to determine the primary vertex position with a space resolution better than 100 μm, to reconstruct the secondary vertices from the decays of D mesons, B mesons and hyperons, to track and identify particles with momentum below 200 MeV/c and to improve the momentum resolution of tracks reconstructed in the TPC and TOF.

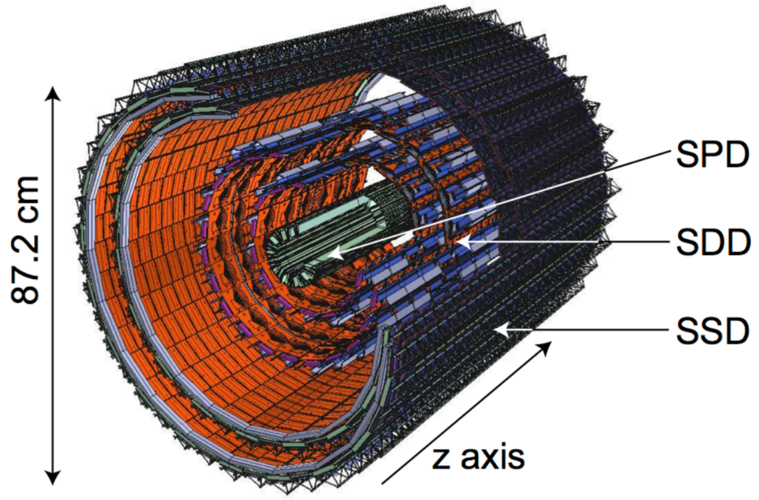

Figure 4.3: Schematic of the ITS. Starting from the inner part it is possible to recognise the SPD, the SDD and the SSD. Figure taken from [176].

The ITS surrounds the beam pipe, made of a 800 μm-thick beryllium cylinder of 6 cm outer radius, which is coaxial with the ITS six detector layers. The innermost radius of the ITS is the minimum allowed by the beam pipe, while the outer one is determined by the necessity to match tracks with those in the TPC. The overall pseudorapidity coverage corresponds to $|\eta| < 0.9$ for primary vertices located within $z = 60$ mm with respect to the nominal interaction point. To cope with the high particle density expected in heavy-ion collisions (~100 particles/cm^2 in Pb-Pb collisions at $\sqrt{s_{\rm NN}} = 5.5$ TeV) Silicon Pixel Detectors (SPD) are chosen for the first two layers, given the high spatial resolution and the fast response of this technology. The middle layers are made of Silicon Drift Detectors (SDD), which provide a bi-dimensional spatial information with a lower resolution with respect to the SPD. Finally the outer layers use Silicon Strip Detectors (SSD) which provide a complementary information on track positions. The SDD and SSD can be also used for particle identification via dE/dx measurement for low momentum tracks, making the ITS stand-alone a low-$p_{\rm T}$ spectrometer. All detector elements are optimized to provide minimum material budget, which ranges from 0.8 to 1.2% X_0 for all the six layers. In addition, the ITS components are tested considering a total dose during the lifetime of the experiment which varies from few tens of Gy to 2.7 kGy, for the outer and the inner part respectively.

Silicon Pixel Detector (SPD)

The two innermost layers of the ITS consist of Silicon Pixel Detectors (SPD). The chosen technology is based on hybrid silicon pixels, consisting of a two-dimensional matrix of reverse-biased silicon detector diodes. Each diode is connected through a conductive solder bump to a contact on the readout chip, which corresponds to the input of the readout cell. The sensor matrix is composed by 256 × 160 cells with the size of 50 μm ($r\phi$) times 425 μm (z), for a total thickness of 200 μm.
Located at radial distance of 3.9 and 7.6 cm, the two layers of the SPD are the closest detector elements to the interaction point and for this reason they are tested to operate considering an integrated dose of 2.7 kGy for 10 years of data taking (track density $\sim$50 tracks/cm^2). In addition, the front-end electronics dissipates a power of $\approx$1.35 kW, hence the detector is equipped with a cooling system based on C_4H_{10} evaporation.

Silicon Drift Detector (SDD)

The two intermediate layers of the ITS are based on Silicon Drift Detectors (SDD). Positioned at 15.0 and 23.9 cm from the interaction point, at this distance the particle density is expected to reach up to 7 cm^{-2}. The detector modules are produced from homogeneous high-resistivity Neutron Transmutation Doped silicon [177], characterized by a sensitive area of $70.10(r\phi)\times75.26(z)$ mm^2. A central cathode strip, to which a HV bias of -2.4 kV is applied, splits the sensitive area into two drift regions. The detector volume is fully depleted by 291 p-type (p^+) cathode strips with 120 μm pitch, which generate the drift field parallel to wafer surface.
When a charged particle crosses the detector volume, the electrons produced in the ionization process drift from the generation point to the collecting anodes, which are 256 for each half. The SDD provides one of the two coordinates of the hit position through the determination of the drift time. The other one is obtained by the centroid position of the charge distribution collected by the anodes. As previously mentioned, this detector can be also used for particle identification purposes. This is possible considering that the total charge collected by the anodes is proportional to the energy deposited in the detector, hence this allows to evaluate the dE/dx in the non-relativistic region.

Silicon Strip Detector (SSD)

The two outer layers of the ITS use double sided Silicon Strip Detectors (SSD) [178] and are positioned at 38 and 43 cm from the interaction point. They are fundamental to match tracks coming from ITS and going towards the TPC, and, as the SDD, they provide in addition particle identification for low momentum particles. The 300 μm thick sensors are made of 768 strips on each side, with a pitch of 95 μm. The connection among the sensor and the electronics is obtained using kapton/aluminium cables [179], while the support of the detection modules is made of Carbon Fiber Composite material. As for the other ITS components, these choices allow to minimize the material budget. The SSD modules are mounted with strips in parallel to the magnetic field, which optimizes the resolution in the bending direction. The 2D hit position is obtained applying an additional set of strips on the backside, rotated by 35 mrad with respect to those in the inner side.

4.3.2 Time Projection Chamber (TPC)

The Time Projection Chamber (TPC) [180] is the main tracking detector of the central barrel and it is designed to provide charged-particle momentum measurements and vertex determination [181]. It is also the main PID detector, providing this information via the specific energy loss ($\mathrm{d}E/\mathrm{d}x$) of particles crossing its volume. The TPC is a cylindrical detector, with a radius of 250 cm and an overall length of 500 cm, covering the pseudo-rapidity interval $|\eta| < 0.9$ for tracks with full radial length (matches in the ITS, TRD and TOF detectors) and the full azimuth. A wide p_{T} range is covered, from 0.1 GeV/c and up to 100 GeV/c, with a resolution of 5% for $p_{\mathrm{T}} < 20$ GeV/c and 35% for $p_{\mathrm{T}} \sim 100$ GeV/c in standalone mode.

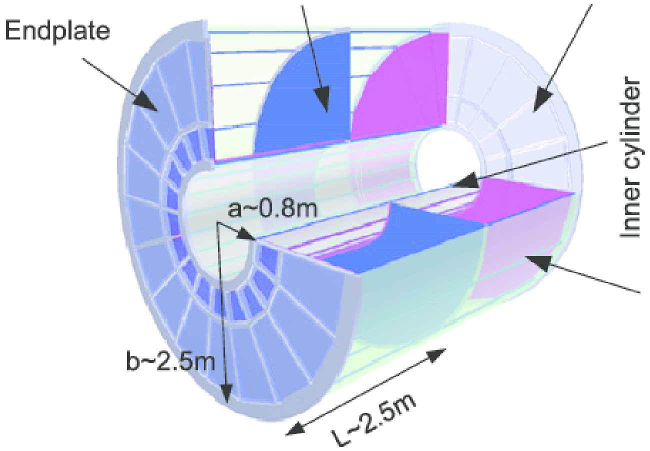

Figure 4.4: The TPC layout.

The detector is filled with a 90 m^3 mixture of $Ne/CO_2/N_2$ (90/10/5) and it is divided into two halves by a central cathode which generates a 400 V/cm drift field. When a particle crosses the gas volume, the electrons produced in the ionization process are transported by the electric field on either sides of the central electrode to the end plates. Because of the gas mixture and the high voltage, the maximum drift velocity is 2.7 cm/μs, corresponding to a drift time of $\sim$90 μs. The signal is then collected on the end plates by multi-wire proportional chambers, with a cathode pad readout, which are mounted in 18 trapezoidal sectors. The drift gas $Ne/CO_2/N_2$ is chosen for its properties of drift speed, low diffusion, low radiation length, aging and stability properties, nevertheless Ne/CO_2 is a "cold gas". This means that a thermal stability of $\Delta T \leq 0.1$ K has to be kept, and for this purpose heat screens (shielding from the neighbour detectors) and cooling circuits are necessary.
The front-end electronics has to read out the signal from 560000 pads located in the readout chambers in the end caps. Every readout channel is composed by three basic functional units: amplification, compression and noise reduction. After all these steps the event size is 90 MB for Pb-Pb collisions and 1-4 MB for pp collisions, which allows the acquisition of 300 and 1000 events/s respectively.

4.3.3 Transition Radiation Detector (TRD)

The Transition Radiation Detector (TRD) [182] provides electron identification for momenta above 1 GeV/c [181]. This detector exploits the transition radiation emitted by electrons crossing a radiator in combination with the specific energy loss inside a gas mixture to obtain the proper pion rejection capability. Together with the information from ITS and TPC, the TRD can be used to study in pp and Pb-Pb collisions the vector-meson production, dilepton continuum and detect open charm and open beauty in semi-leptonic decays.
The TRD consists of 18 sectors, each of them containing 30 modules arranged in five stacks along the z-axis and six layers in the radius. Every detector element is composed by a fiber/foam radiator directly glued on the electrode, a drift section and a multi-wire proportional chamber with pad readout, for an overall thickness of 85 mm.
An ionizing particle produces electrons crossing the drift volume, which is filled with a mixture of Xe and CO_2 (85:15) In addition, in case of particles exceeding the transition radiation threshold ($\gamma \approx 1000$), 1.45 X-ray photons are produced in the energy range of 1 to 30 keV and, due to the high-Z of the counting gas, are converted inside the drift region. At this point, electrons from ionization and conversion move towards the anode wires, in proximity of which the amplification process occurs, and the signal is induced on readout pads. For particles with $p_{\mathrm{T}} = 2$ GeV/c an efficient electron/pion discrimination is achieved

via 1.) the increased specific energy loss of electrons compared to pions 2.) the transition radiation absorption generated by electrons. The TRD standalone momentum resolution ranges around 2.5-3% for $p_{\mathrm{T}} < 2$ GeV/c, while including it in the central barrel tracking allows to obtain a $\delta p_{\mathrm{T}}/p_{\mathrm{T}} \approx 5\%$ up to momenta of ~ 100 GeV/c. The event size ranges around 6 kB for pp and 11 MB for Pb-Pb collisions, while the trigger rate limit is 100 kHz.

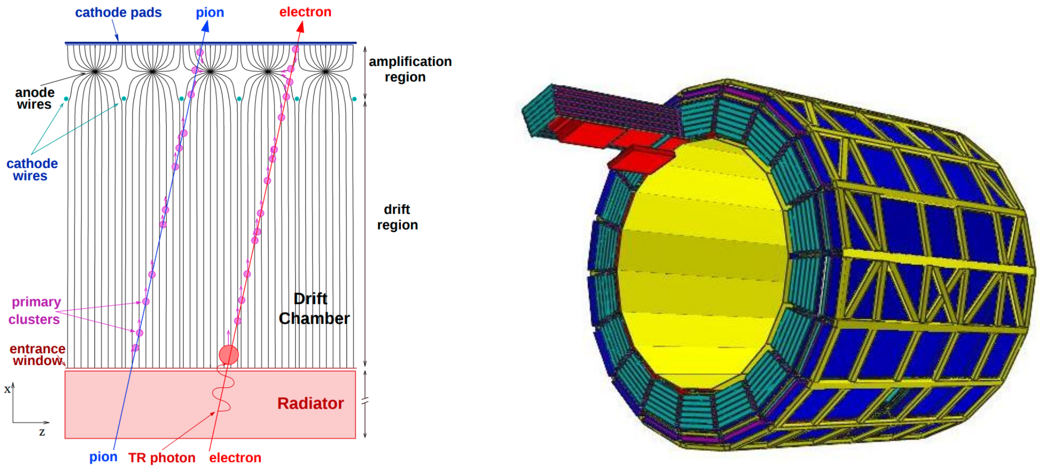

Figure 4.5: Left panel: schematic cross-sectional view of a detector module in the $r - z$ plane. Right panel: the TRD layout. Figures taken from [181].

4.3.4 Time Of Flight (TOF)

The Time-Of-Flight (TOF) [183] detector is a large area array which covers the central pseudorapidity ragion ($|\eta| < 0.9$) and it is used for particle identification in the intermediate p_{T} region [181]. This range corresponds to $p_{\mathrm{T}} < 2.5$ GeV/c for pions and kaons and reaches 4 GeV/c for protons, with a K/p and π/K discrimination better than 3σ.
The TOF covers a cylindrical volume and it is divided into 18 sectors in φ and 5 segments in the z direction, 3.7 m far from the beam pipe. Since a large area needs to be covered, a gaseous detector was chosen, and after an intense R&D work, Multi-Gap Resistive-Plate Chambers (MRPC) [184] were found to be the best solution. Thanks to the high and uniform electric field over all the detector volume, any ionization produced by a traversing charged particle immediately starts the gas avalanche process, which induces the signal on the pick-up electrodes. Remarkably, the overall time resolution is better than 80 ps, while the efficiency is close to 100%.

The MRPC technology has many advantages: 1.) chambers can operate at atmospheric pressure; 2.) since the signal is the analogue sum of the signals from many gaps, the peak is well separated from zero and has no late tails; 3.) the construction technique is rather simple; 4.) it works at high-gain because the resistive plates quench the streamers. The gas mixture is composed by $C_2H_2F_4$ (90%), $i - C_4H_{10}$ (5%) and SF_6 (5%) and it was chosen for its aging properties and rate capabilities.

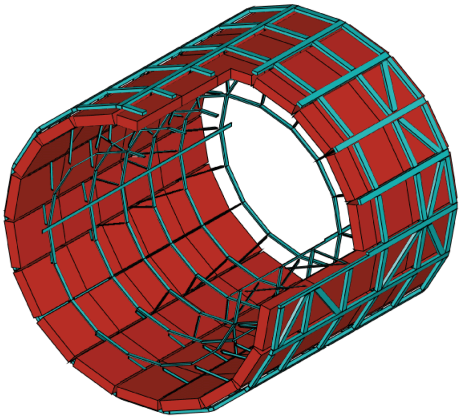

Figure 4.6: The TOF layout.

4.3.5 High Momentum Particle Identification Detector (HMPID)

The main purpose of the High Momentum Particle Identification Detector (HMPID) [185] is to enhance the PID capability beyond the range allowed by ITS, TPC and TOF and it is dedicated to the measurement of identified hadrons for $p_{\mathrm{T}} > 1$ GeV/c. In addition, the detector is optimized to extend the π/K and K/p discrimination up to 3 and 5 GeV/c respectively.

Designed as a single-arm array covering the an acceptance of 5% of the central barrel solid angle, the HMPID is based on proximity Ring Imaging Cherenkov (RICH) counters arranged in seven modules of about 1.5 m^2 each. The momentum range covered by the HMPID is defined by the radiator, which is a 15 mm thick layer of liquid C_6F_4, characterized by a refraction index of $n = 1.2989$ at $\lambda = 175$ nm, which corresponds to $\beta_{min} = 0.77$. As shown in Fig. 4.7, the photons emitted by a charged particle crossing the radiator are collected by the photon counters. The latter are composed by a thin layer of CsI deposited onto the pad cathode of Multi-Wire Pad Chamber (MWPC), and with an overall surface of 11 m^2, the HMPID represents the largest application of this technology.

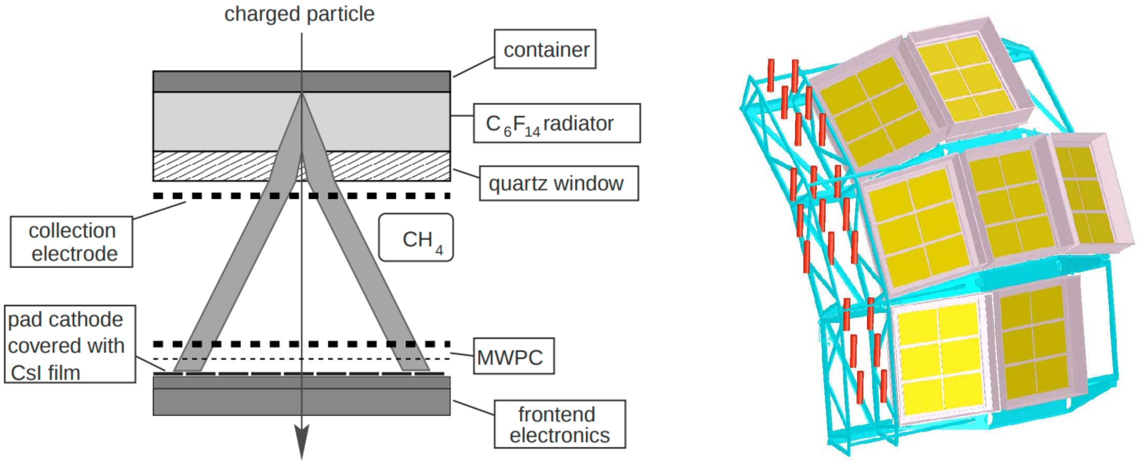

Figure 4.7: Left panel: working principle of the RICH detector. Right panel: the HMPID layout. Figures taken from [181].

4.3.6 PHOton Spectrometer (PHOS)

The Photon Spectrometer (PHOS) [186] is a high resolution electromagnetic spectrometer which covers a limited acceptance domain at central rapidity. Its main purposes are the measurements of the low-p_T direct photons radiated by the plasma and the study of the jet-quenching through the measurement of the γ-jet correlations and the production of high-p_T π^0.

The PHOS consists of a highly segmented calorimeter (PHOS) and a Charged-Particle Veto (CPV) arranged in five modules. It is positioned on the bottom of the ALICE setup, at 460 cm from the interaction point, covering 100° in the azimuthal angle and the pseudorapidity range $|\eta| < 0.12$. Each PHOS module is divided into 3584 detection cells, organized in 56 rows and 64 columns. A detection cell consists of a 22×22×180 mm^3 lead-tungstate ($PbWO_4$) crystal, while the readout electronics is composed by Avalanche Photo-Diodes (APD) and low-noise preamplifiers, directly glued onto the end face of the crystal itself.

4.3.7 ElectroMagnetic Calorimeter (EMCal)

Positioned on the top of the ALICE structure, close to the magnet coils, the Electromagnetic Calorimeter (EMCal) [187] is designed to study jet quenching and it is used for triggering on photons, electrons and jets.
Positioned at ∼4.5 meters from the beam line, approximately at the opposite of the PHOS, the EMCal covers 107° in the azimuthal angle and the pseudorapidity range $|\eta| < 0.7$. The detector, whose technology consists of a layered Pb-scintillator sampling calorimeter, is segmented into 12288 towers in projective geometry with respect to the interaction vertex. The Pb to scintillator ratio is 1:1.22, which determines an average density for the detector of 5.68 g/cm^3.

4.4 Muon spectrometer

The muon spectrometer is designed to measure muon production from the decays of quarkonia (J/ψ, ψ(2S), Υ(1S), Υ(2S) and Υ(3S)), low mass vector mesons (ρ, ω and ϕ), heavy flavor hadrons and weak bosons. The detector covers the polar angle range 171° – 178°, which corresponds to the pseudorapidity region $-4.0 < \eta < -2.5$, and has a total length of 17 m.
The muon spectrometer design is driven by the specific requirements of the research program. First of all the geometrical acceptance is chosen as large as possible to cope with the limited statistics for some of the quarkonium states under study, in particular the Υ family. The forward rapidity coverage allows the measurement of low-p_{T} charmonia down to zero p_{T}, where muons are Lorentz boosted and can be selected by a system of absorbers which reduces the hadron flux and allows muon identification. The absorber had to be optimized using materials that minimize the multiple scattering, in order to achieve a good track resolution. To resolve the Υ(1S), Υ(2S) and Υ(3S) peaks, a mass resolution better than 100 MeV/c^2 for $p_{\mathrm{T}} < 10$ GeV/c is required, hence, determining the strength of the magnetic field and the spatial resolution of the tracking system.
To achieve these goals the ALICE muon spectrometer is composed by a system of absorbers, a dipole magnet, a muon tracker, a passive iron wall and a muon trigger system. A schematic of the muon spectrometer is shown in Fig. 4.8 and each component will be discussed in more detail in the following.

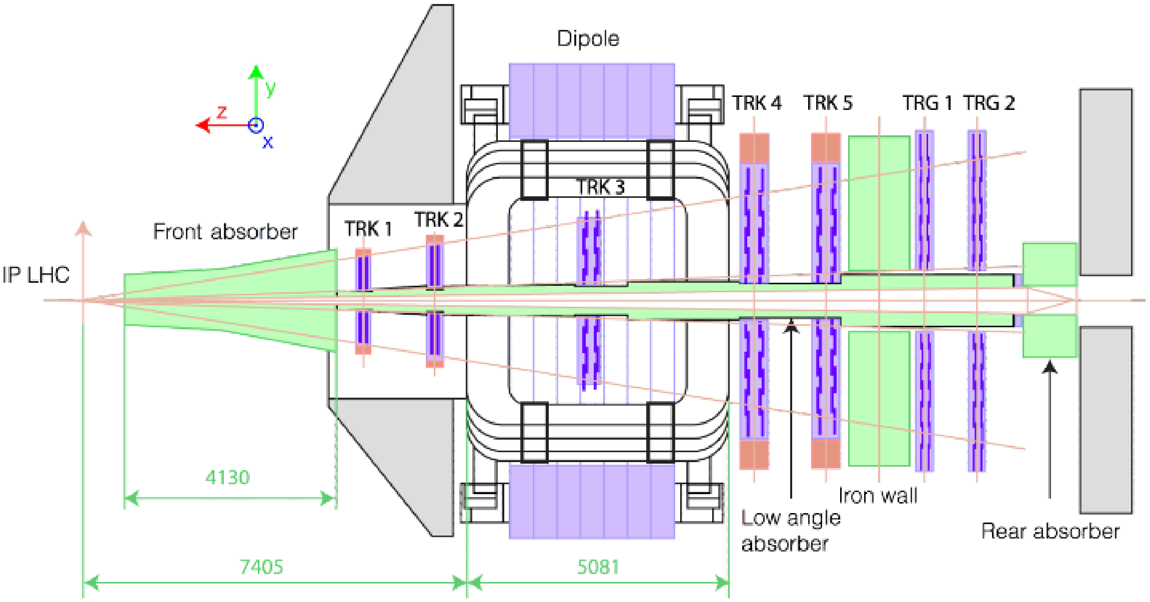

Figure 4.8: Schematic drawing of the muon spectrometer [181]. Lengths are given in cm.

4.4.1 Absorbers

The Muon Spectrometer needs to be shielded from the large hadronic background produced especially in nucleus-nucleus collision, and for this reason one of its main component is a system of absorbers. The first one is the *front absorber*, which is partly located inside the central barrel, starting at 90 cm from the interaction point. Characterized by a total length of 4.13 m, it is designed to filter out hadrons and limit the production of muons from the decays of pions and kaons. At the same time the material is chosen to limit multiple scattering of muons from quarkonium decays. The part close to the interaction point is made of carbon and the low Z of this material indeed allows to reduce multiple scattering effects. The rear part is made of concrete, lead and boronated polyethylene to absorb secondary particles produced into the absorber and low energy protons and neutrons. The external coating is made of lead and boronated polyethylene in order to avoid particles recoil into the TPC. The layout of the front absorber is shown in Fig. 4.9.
In addition, a small-angle *beam shield* made of tungsten, lead and stainless steel, is included to suppress the background produced in the interaction between low angle particles and the residues of gas in the pipe (*beam gas*). An *iron wall*, which works as muon filter, is located between the tracking chambers and the trigger system, 14.5 m away from the interaction

point. Its purpose is to stop hadrons surviving the front absorber and low momentum muons mainly from pion and kaon decays. In order to be detected in the spectrometer, a muon must have at least $p \sim 4$ GeV/c. Finally, a further *rear absorber* provides the shielding from beam gas interactions.

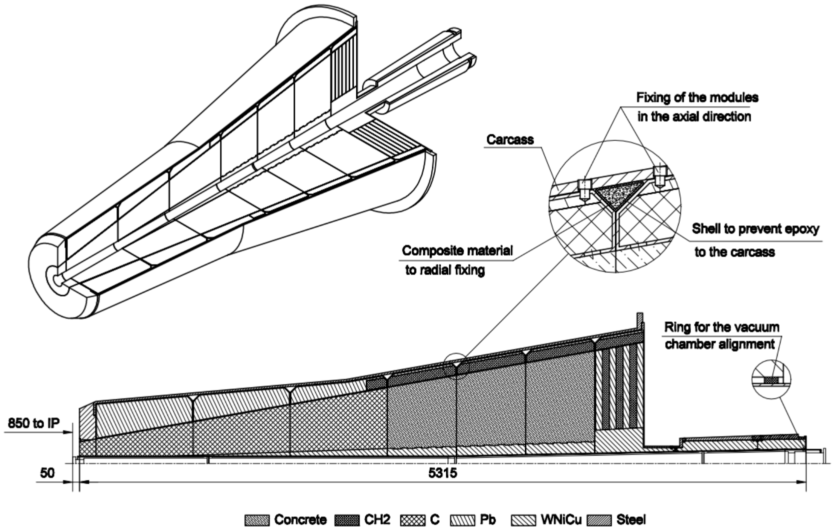

Figure 4.9: Layout and section of the ALICE front absorber [181].

4.4.2 Dipole magnet

Located at 7 m from the interaction point, a warm dipole magnet is used to determine the momentum and the electric charge of particles produced in the interaction point. The integral of the magnetic field provided is 3 T·m and the value was tuned to reach an optimal mass resolution. The magnetic field is perpendicular to the beam pipe, defining the plane $z - y$ as the bending plane, where muons are deviated, and the plane $x - z$ as the non-bending plane. The cooling is provided with demineralized water, which allows to maintain the temperature in the range $15° - 25°$ C.

4.4.3 Muon tracker

In order to achieve the invariant mass resolution of 100 MeV/c^2, necessary to resolve the Υ family peaks, the muon tracking system is characterized by a spatial resolution better than

100 μm. The detector covers a total area of $\sim$ 100 m^2 and can operate at the maximum hit density of $\sim 5 \times 10^{-2}$ cm^{-2}. The detection technology adopted to detect the muon tracks is the Cathode Pad Chamber. Each of them is composed by two readout cathode planes with a plane of anode wires in between. The space between cathodes is filled with a mixture of Ar and CO_2, which is ionized when traversed by a charged particle. The produced electrons generate an avalanche after having drifted towards the nearest anode wire, and the resulting ion cloud induces a charge distribution on the cathode planes, allowing to determine the position of the track.
The chambers are arranged in 5 stations, two before, one inside and two after the dipole magnet, and to keep the occupancy around 5%, a fine-granularity segmentation of the readout pads is needed (see Fig. 4.10). For instance, 4.2×6.3 mm^2 pads are used in the first station, close to the beam pipe, given the higher density of particles produced in that region, while larger pads are mounted at larger radius, keeping the total number of channels around 10^6. In order to reduce the impact of the multiple scattering on the track resolution, composite materials (e.g. carbon fiber) are used and each chamber is 0.03 X_0 thick. Given the different size of the stations, ranging from few square meters for station 1 to more than 30 m^2 for station 5, two different designs were adopted. The first two stations are based on a quadrant structure, while for the other three a slat architecture was chosen. Both quadrants and slats overlap in order to avoid dead zones.

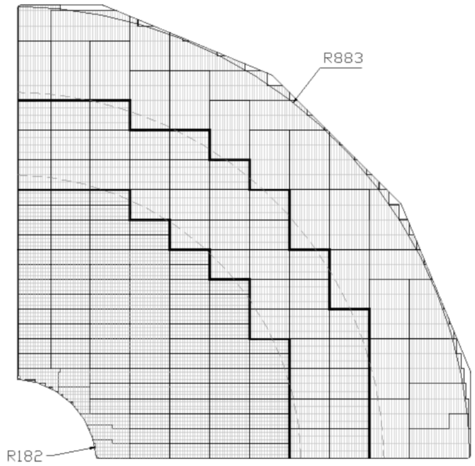

Figure 4.10: Cathode plane layout of Station 1.

The measurement of the spectrometer alignment is particularly relevant to reach the required track resolution. The initial geometry of the system is evaluated via dedicated

runs without magnetic field carried out at the beginning of each data taking period. The detector position can be slightly modified when switching on the magnetic field during the data taking and the possible displacements are recorded by the Geometry Monitoring System (GMS). The latter consists of an array of 460 optical sensors which are installed on platforms placed at the corners of the tracking chambers and can achieve a resolution on the position better than 40 μm.
The choice of the front-end electronics depends on the necessity to read about one million channels up to kHz rate. This requirement is satisfied using a 64 channel board called MANU (MAnas NUmérique). The digitization is done on board, where the signal of four 16-channels charge amplifier chips (Multiplexed ANAlogic Signal processor, MANAS) are sent to 12-bits ADCs and to Muon Arm Readout Chip (MARC). The connection among the MANUs and readout system, named CROCUS (Cluster Read Out Concentrator Unit System) is provided by the PATCH (Protocol for ALICE Tracking Chambers) buses. Finally, the trigger signals are sent by CROCUS to the DAQ.

4.4.4 Muon trigger

The trigger system is mainly designed to select high p_{T} muons produced in heavy quarkonia and open charm decays, while events with low p_{T} muons, which mainly come from pion and kaon decays, are rejected. This rejection is performed applying a cut in p_{T} at trigger level to the muons, which can be programmed with two different thresholds in parallel. Their values can range from ~ 0.5 to ~ 4 GeV/c.
The muon trigger system is located after the iron wall and consists of 4 Resistive Plate Chamber (RPC) planes, arranged in two stations (MT1 and MT2) and corresponding to a total area of 140 m^2. Each RPC is made of two resistive Bakelite electrodes ($\rho \sim 3 \times 10^9$ Ωcm), separated by 2 mm wide gas gap. The electrodes are coated on the gap side with linseed oil, to improve its smoothness, while the two external surfaces are painted with graphite, one connected to the high voltage, the other to the ground. The RPCs operate in maxi-avalanche mode, with a gas mixture composed by $\mathrm{C_2H_2F_4}$ (89.7%), $\mathrm{i-C_2H_{10}}$ (10%) and $\mathrm{SF_6}$ (0.3%).
When a charged particle crosses the gas volume, the electron produced in the ionization process drifts towards the anode planes, inducing a signal on the electrodes. Since the latter are segmented in parallel strips, placed on both the sides of the RPC and rotated by 90° one respect to the other, they provide the hit x and y position.
The transverse momentum of muons is evaluated measuring the deviation in their trajectory by the dipole magnet, and the same principle is used for the application of the low and high-p_{T} trigger threshold. The RPC are equipped with dual-threshold front-end

discriminators which are adapted to achieve the required time resolution of 1-2 ns for the identification of the bunch crossing.

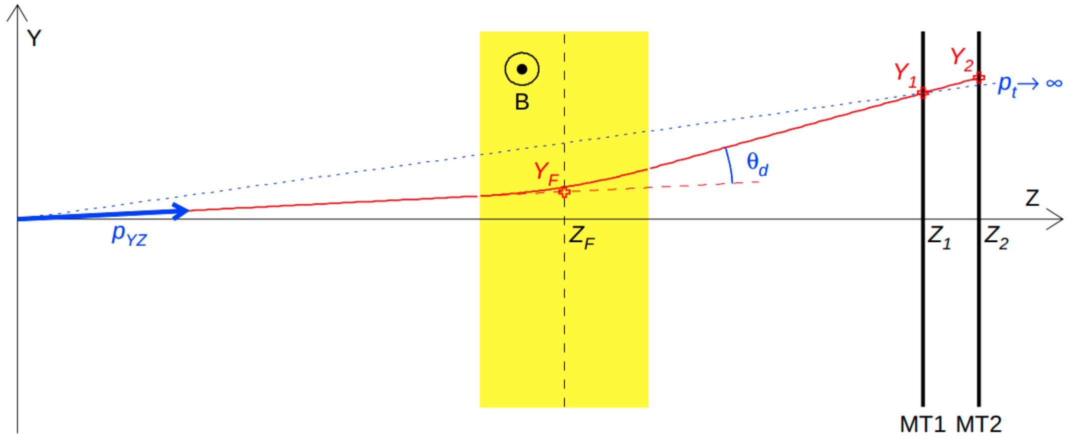

Figure 4.11: The muon arm trigger principle, based on the estimation of the track's transverse momentum.

The trigger electronics is divided in three levels: local, regional and global. The local trigger algorithm searches for a track pointing to the primary vertex using the information of all 4 RPC planes. A track is defined when there is a hit on at least 3 planes out of 4, in both the bending and non-bending planes. As shown in Fig. 4.11, the low and high-p_{T} trigger condition is evaluated measuring the deviation $\delta Y = Y_2 - Y_\infty$. Y_∞ corresponds to the y coordinate on MT2, extrapolated connecting the interaction point and the hit on MT1, which is equivalent to a muon track with infinite momentum ($p_{\mathrm{T}} \rightarrow \infty$). The different p_{T} cuts are pre-loaded in look-up tables located in the trigger electronics and corresponding to different values of the deviation δY. Finally the regional and the global levels gather the signal from all local boards, delivering the single muon, like-sign and unlike-sign dimuon triggers of the whole detector. These trigger signals, together with those coming from fast detectors (SPD, V0, T0), represent the Level-0 (L0) trigger and have to be provided at the Central Trigger Processor in about 1 μs.

The ALICE Central Trigger Processor can deliver six different trigger signals, which are identified by the following code names:

- **MSL**: single muon track above the low-p_{T} threshold

- **MSH**: single muon track above the high-p_{T} threshold
- **MUL**: pair of unlike-sign muon tracks above the low-p_{T} threshold
- **MUH**: pair of unlike-sign muon tracks above the high-p_{T} threshold
- **MLL**: pair of like-sign muon tracks above the low-p_{T} threshold
- **MLH**: pair of like-sign muon tracks above the high-p_{T} threshold

In the majority of standard quarkonium analyses performed at forward rapidity, the MUL trigger condition is required, together with MLL, which is mainly used for the background subtraction [188].

4.5 Forward detectors

As mentioned before, the main purposes of global detectors are triggering and event characterization and the most important of them are:

4.5.1 Zero Degree Calorimeter (ZDC)

The Zero Degree Calorimeter (ZDC) provides the centrality estimate by measuring the energy deposited in the detector by the non-interacting (spectator) nucleons. This detector also provides a Level 1 (L1) trigger (for more details see Section 4.6) and, given the position sensitivity of the detector, also an estimate of the reaction plane in nuclear collisions.
Two sets of ZDCs are located on the two sides of the interaction point along the beam line, at a distance of 116 m. Each one consists of a pair of hadronic calorimeters, one for protons (ZP) and one for neutrons (ZN). The system is completed by two small electromagnetic calorimeters (ZEMs), positioned at 7 m from the interaction point and on the opposite side of the muon arm, which measure the energy carried mainly by photons from π^0 decays. The hadronic ZDCs are quartz fibers sampling calorimeters. When a hadron crosses the dense absorber, it generates a shower which produces Cherenkov radiation in the quartz fibers interspersed in the absorber. One out of every two fibers is sent to a Photo Multiplier Tube (PMT), while the remaining are sent to other four PMTs, one for each tower in which the ZDC is divided. The choice of quartz fibers lies in the intrinsic radiation hardness of this material, since the detector is exposed to a harsh radiation environment (up to 10^4 Gy/day).

Differently from ZP and ZN, the ZEM fibers and plates are oriented at 45° with respect to the beam axis. This choice is due to the Cherenkov light, which has a production peak around 45°, therefore with this configuration the detector response is maximized.

4.5.2 V0

The V0 is a small angle detector consisting of two arrays of scintillators installed on both the sides of the interaction point, named V0A and V0C [189]. The detector provides minimum bias trigger for pp and A–A collisions, and is used as a centrality estimator. This is achieved considering that the signal in the V0 arrays is proportional to the number of primary particles produced in the collision. Applying cuts on the V0 signal allows one to obtain three different centrality triggers, the peripheral, semi-central and central triggers. The V0A and V0C detectors are located at 340 cm and 90 cm from the interaction point respectively, covering the pseudorapidity ranges $2.8 < \eta < 5.1$ (V0A) and $-3.7 < \eta < -1.7$ (V0C). Both detectors are segmented into 32 individual counters, distributed in 4 rings, and are made of a scintillating material with 1 mm diameter Wave-Length Shifting fibers. The signal is then delivered to the front-end electronics after having been amplified by a photomultiplier tube.

4.5.3 T0

The T0 detector [189] provides the start time (T0) for the TOF, the measure of the vertex position with a precision of ±1.5 cm and a L0 trigger. The T0 consists of two arrays of Cherenkov counters, positioned at 375 cm and 72.7 cm from the interaction point respectively and covering the pseudorapidity ranges $4.61 < \eta < 4.92$ (T0A) and $-3.28 < \eta < -2.97$ (T0C). Each counter has a quartz radiator 20 mm thick and 20 mm in diameter, which is coupled to the PMT. The detector provides the timing signal corresponding to the real time of the collision with a precision of about 50 ps.

4.5.4 Photon Multipicity Detector (PMD)

The Photon Multiplicity Detector (PMD) measures the multiplicity and spatial distribution of photons in the forward pseudorapidity region $2.3 \leq \eta \leq 3.7$. This detector exploits the pre-shower method, where a three radiation length converter is sandwiched among 2 layers of gas proportional counters, arranged into a honeycomb cellular structure. The detector's granularity is optimized according to the requirements of low occupancy and high purity of photon detection.

4.5.5 Forward Multipicity Detector (FMD)

The Forward Multiplicity Detector (FMD) provides the charged particle multiplicity information in the forward pseudorapidity regions $-3.4 < \eta < -1.7$ and $1.7 < \eta < 5.0$. Located on either side of the ITS, FMD2 and FMD3 cover approximately the same acceptance, while the FMD1 si positioned more downstream from the interaction point, on the opposite side with respect to the muon arm. Each detector consists of an inner and an outer ring of 10 and 20 silicon sensors respectively, and is designed to measure up to 20 ionizing particles per single strip before saturating.

4.6 ALICE trigger and data acquisition

In the ALICE experiment the trigger decision is generated by the Central Trigger Processor (CTP) which collects the information from all the detector signals. Events with different features are selected by the CTP at rates which can be scaled down according to the restrictions imposed by the bandwidth of the Data Acquisition system (DAQ) and to suit the physics requirements. The CTP has to evaluate the trigger inputs at every machine cycle ($\sim$ 25 ns), and given the different processing time for the various detectors, the trigger system is organized in three levels, level 0 (L0), level 1 (L1) and level 2 (L2) [190]:

- Level 0: trigger inputs from the fastest detectors, in particular T0, V0, SPD, TOF, PHOS, EMCal (photon trigger) and muon trigger. The CTP combines them with AND and OR logic to fulfill the conditions of a certain trigger class. The trigger signals are available 1.2 μs after the collision.
- Level 1: trigger inputs from slower detectors, as EMCal (neutral-jet trigger), TRD and ZDC. The trigger decision is made 6.5 μs after L0, due to the online calculation of some the event features.
- Level 2: the trigger decision is taken after $\sim$ 100 μs, which corresponds to the drift time of the TPC. It is devoted to trigger the sending of the event data to Data Acquisition (DAQ) and in parallel to the High Level Trigger (HLT).

The ALICE trigger system has a past-future projection circuit which controls if there are events of the requested type in the time window (i.e. TPC drift time) before and after the collision, to reject pile-up events.
The Data Acquisition (DAQ) system carries out the dataflow from the detectors to the data storage. After the CTP decision to acquire a certain event, the trigger signal is sent to the detector front-end electronics. The data are then transferred to a farm of computers, named Local Data Concentrators (LDC), where the data fragments which correspond to a specific event are processed and assembled into sub-events. The combined information from different LDCs is elaborated by the Global Data Collector (GDC) to build the event, which is then sent to the CERN storage facilities. In the reconstruction, raw data are then processed to produce the Event Summary Data (ESD), which are in turn filtered to produce the Analysis Object Data (AOD). In parallel with the raw data processing, the detectors alignment and calibration information are collected and stored inside the Offline Condition Data Base (OCDB).

Chapter 5

J/ψ polarization in Pb–Pb collisions

In this chapter the first inclusive J/ψ polarization measurement in Pb–Pb collisions carried by the ALICE experiment is presented. The result, which is the main outcome of this thesis, is obtained in the dimuon decay channel at forward rapidity, exploiting the full Run 2 dataset, collected in 2015 and 2018 at the center-of-mass energy of $\sqrt{s_{\mathrm{NN}}} = 5.02$ TeV. The analysis is performed as a function of the J/ψ transverse momentum, in the range $2 < p_{\mathrm{T}} < 10$ GeV/c, and in four different centrality classes. In addition, a feasibility study on J/ψ polarization with respect to the event plane will be also presented.

The results on J/ψ polarization as a function of the transverse momentum are reported in the paper "*First measurement of quarkonium polarization in nuclear collisions at the LHC*" [1], submitted for publication to Physics Letters B, while the J/ψ polarization result as a function of centrality has been approved as preliminary by the ALICE collaboration.

5.1 Analysis strategy description

Polarization measures the degree to which the spin of a particle is aligned with respect to a chosen direction and it can be evaluated studying the anisotropies in the angular distribution of the decay products. Considering the J/ψ ($J^{\mathrm{PC}} = 1^{--}$) dimuon decay channel, the angular distribution follows the functional shape discussed in Chapter 3 and valid for a two-body decay:

$$W(\cos\theta,\varphi) \propto \frac{\mathcal{N}}{3+\lambda_\theta} \cdot (1 + \lambda_\theta \cos^2\theta + \lambda_\varphi \sin^2\theta \cos 2\varphi + \lambda_{\theta\varphi} \sin 2\theta \cos\varphi). \tag{5.1}$$

This expression depends on the three polarization parameters (λ_θ, λ_ϕ, $\lambda_{\theta\phi}$) and is a function of θ and ϕ, the polar and azimuthal angles respectively, conventionally defined as the angles between the momentum of the positive lepton and the quantization axis. In analogy with the previous polarization analyses, the adopted reference frames are helicity (HE) and Collins-Soper (CS). This choice has two main advantages, first of all it eases the comparison with the existing measurements, secondly it allows to validate the consistency of the results computing the frame invariant parameter ($\tilde{\lambda}$) in the two reference systems and comparing them.

The extraction of the J/ψ polarization parameters is performed according to the following steps:

1. *binning definition*: the available data sample is split into several p_{T} and centrality bins and, in turn, each of them is divided into a certain number of $\cos\theta$ and ϕ bins.
2. *signal extraction*: the invariant mass spectrum corresponding to each $\cos\theta$ and ϕ range is fitted with a combination of signal and background functions, in order to extract the J/ψ raw yield.
3. *$A \times \varepsilon$ correction*: the J/ψ raw yield has to be corrected by the product of acceptance times efficiency ($A \times \varepsilon$) evaluated with a Monte Carlo simulation, in order to take into account the detector coverage and its inefficiencies.
4. *Extraction of the polarization parameters*: polarization parameters are evaluated fitting the corrected J/ψ yield with the angular distribution shown in Eq. 5.1

In principle this procedure can be performed following the so-called *2D-approach*, where the J/ψ raw yield and $A \times \varepsilon$ are evaluated on a two-dimensional map as a function of $\cos\theta$ and ϕ. Nevertheless, this is not always possible, since it is necessary to collect a large data sample to have a sufficiently large number of candidates in the 2D map. For this reason the *1D approach* can be performed, studying separately the $\cos\theta$ and ϕ distributions. This is possible because the $\cos\theta$ and ϕ dependence in Eq. 5.1 can be factorized integrating over ϕ and $\cos\theta$ respectively, and obtaining:

$$W(\cos\theta) \propto \frac{1}{3+\lambda_\theta}(1+\lambda_\theta \cos^2\theta) \tag{5.2}$$

$$W(\phi) \propto 1 + \frac{2\lambda_\phi}{3+\lambda_\theta}\cos(2\phi) \tag{5.3}$$

Since $\lambda_{\theta\phi}$ vanishes in both the integrations, an *ad hoc* variable ($\tilde{\phi}$) is defined to allow the extraction of this polarization parameter:

$$\begin{cases} \tilde{\phi} \ = \ \phi \ - \ \frac{3}{4}\pi \quad \text{for } \cos\theta < 0 \\ \tilde{\phi} \ = \ \phi \ - \ \frac{1}{4}\pi \quad \text{for } \cos\theta > 0 \end{cases} \tag{5.4}$$

and $\lambda_{\theta\phi}$ can be extracted from:

$$W(\tilde{\phi}) \propto 1 + \frac{\sqrt{2}\lambda_{\theta\phi}}{3+\lambda_\theta}\cos(\tilde{\phi}) \tag{5.5}$$

The 2D-method has the advantage to preserve the natural multidimensionality of the analysis, given the existing correlation between angular variables; on the other hand the signal extraction procedure is in general more difficult, especially for narrow $\cos\theta$ and ϕ cells. On the contrary, in the 1D-approach the signal extraction procedure is simpler, but the final result could be more sensitive to possible detector effects, in particular due to the choice of the Monte Carlo input parametrization for the $A \times \varepsilon$ calculation. In most of the previous polarization analyses in pp collisions, the one-dimensional approach was performed, nevertheless the sizable data sample collected by the ALICE experiment during Run 2 provides the conditions to apply the 2D method (this is the case for the J/ψ polarization study as a function of p_{T}, which will be discussed in more details in the following).
As discussed in Section 3.1, the J/ψ angular momentum can be expressed as the a linear combination of its third component J_{z} eigenvectors:

$$|J, J_{\mathrm{z}}\rangle_{\mathrm{J}/\psi} \ = \ b_{-1}|1,-1\rangle + \ b_0|1,0\rangle + \ b_{+1}|1,+1\rangle \tag{5.6}$$

where the coefficients b_{-1}, b_0 and b_{+1} assume different values according to the particle polarization state, and in particular:

- $b_0 \ = \ 1$, $b_{\pm1} \ = \ 0$ in case of longitudinal polarization
- $b_0 \ = \ 0$, $|b_{-1}|^2 + |b_{+1}|^2 = 1$ in case of transverse polarization

The polarization parameters are directly connected to these coefficients, so that it is possible to identify the values of $(\lambda_\theta, \lambda_\phi, \lambda_{\theta\phi})$ corresponding to the three most significant polarization configurations:

- for $(\lambda_\theta, \lambda_\phi, \lambda_{\theta\phi}) \ = \ (0,0,0)$ J/ψ is not polarized

- for $(\lambda_\theta, \lambda_\phi, \lambda_{\theta\phi}) = (-1, 0, 0)$ J/ψ is longitudinally polarized
- for $(\lambda_\theta, \lambda_\phi, \lambda_{\theta\phi}) = (+1, 0, 0)$ J/ψ is transversally polarized

Considering the functional shape in Eq. 5.1, it is easy to see that in case of no polarization the angular distribution is expected to be uniform as a function of $\cos\theta$ and ϕ, otherwise in case of transverse or longitudinal polarization the distribution assumes the shapes shown in Fig. 5.1.

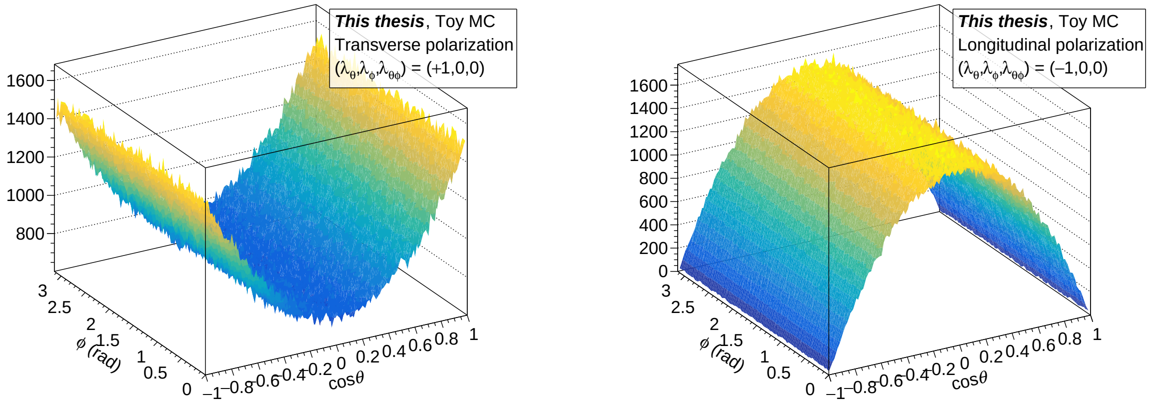

Figure 5.1: $(\cos\theta$,$\phi)$ distributions for transverse (left panel) and longitudinal (right panel) polarization generated in a toy Monte Carlo simulation.

5.2 Data sample and analysis cuts

In the Muon Spectrometer [190], the triggered events are reconstructed using the raw information from the detector, represented by the particle hits crossing the tracking chambers. A Maximum Likelihood Expectation Maximization algorithm [191] is used for cluster finding while the hit spatial location is determined by means of a fit with a 2D Mathieson function [192]. To reconstruct the trajectory of the particles across the five tracking stations an algorithm based on the Kalman filter is used. The tracks are then extrapolated to the vertex position which is measured by the ITS, applying a further correction to the track kinematic parameters to take into account the multiple scattering and the energy loss in the front absorber.

The analysis discussed in this chapter is performed using the data sample collected by the ALICE experiment in Pb–Pb collisions at the center-of-mass energy of $\sqrt{s_{\mathrm{NN}}} = 5.02$ TeV in 2015 and 2018. Both samples were collected from the beginning of November to the beginning of December, for a total integrated luminosity which amounts to $\mathcal{L}_{\mathrm{int}} \sim 750\ \mu\mathrm{b}^{-1}$. The ALICE data taking is organized in "periods", which include data collected under relatively uniform conditions. In particular, the 2015 data sample is characterized by one single period (LHC15o) with 137 runs, while the 2018 one is divided into two periods (LHC18q and LHC18r) with 130 and 99 runs respectively. The list of runs that can be used for data analysis is obtained according to a series of selection steps:

1. during the data taking the run has to be labelled as "good run" by the data acquisition (DAQ) expert.

2. for analyses which involve muon detection, the read out detectors can include the muon system (muon tracker and muon trigger), the electromagnetic calorimeter, photon spectrometer (PHOS), T0, V0, the diffractive detector (AD), Zero degree Calorimeter (ZDC) and the Silicon Pixel Detector (SPD).

3. the run has to satisfy specific quality requirements (quality assurance or QA), which depend on the group of detectors involved. For instance, in the muon spectrometer those requirements are related to the efficiency stability for the muon trigger chambers, the number of tracks per muon trigger,...

For J/ψ, and in general for all quarkonium analysis, events corresponding to a dimuon trigger named CMUL7-B-NOPF-MUFAST are selected. In Table 5.1 a summary of the main features corresponding to the three data taking periods is reported.

Year	System	$\sqrt{s_{\mathrm{NN}}}$ (TeV)	Period	Runs	CMUL7 triggers
2015	Pb–Pb	5.02	LHC15o	137	1.2×10^8
2018	Pb–Pb	5.02	LHC18q	130	1.1×10^8
			LHC18r	99	1.6×10^8

Table 5.1: Run statistics corresponding to the 2015 and 2018 data taking periods.

The CMUL7 trigger is defined as the coincidence of signals in the V0A and V0C detectors with the presence of a pair of unlike sign track segments exceeding the low-p_{T} threshold in the Muon Trigger system. As explained in Section 4.4.4, this threshold is programmable and in Pb–Pb collisions it is usually set to $p_{\mathrm{T}}^{\mu} = 1$ GeV/c, which corresponds to the value at which the single muon efficiency reaches 50% [193], as shown in the left panel of Fig. 5.2. For $p_{\mathrm{T}}^{\mu} = 2.5$ GeV/c the efficiency reaches a plateau value of ~ 98%. Moreover, the efficiency of the RPCs for the muon trigger stations remains stable all along the data taking periods with small fluctuations around the central value corresponding to ~ 98%, as shown in the right panel of Fig. 5.2.

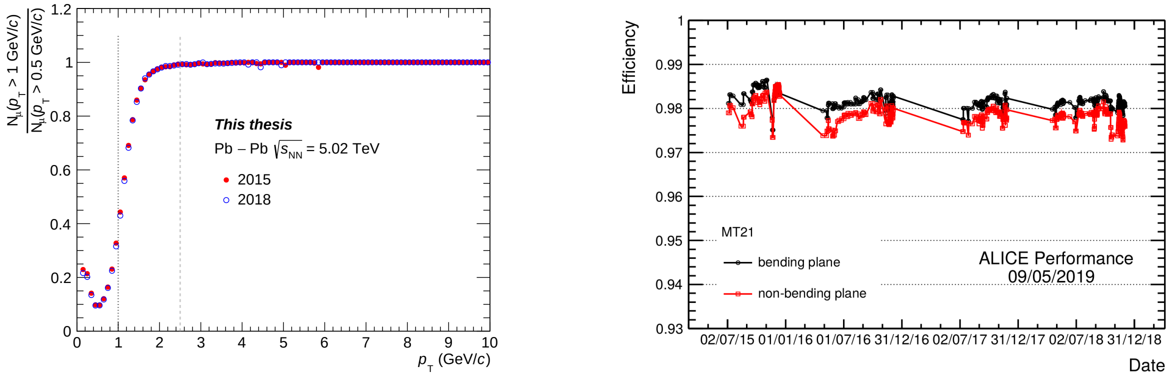

Figure 5.2: Left panel: single muon trigger efficiency as a function of the transverse momentum for 1 GeV/c threshold. Right panel: efficiency of the RPCs for the muon trigger station MT21 as a function of time in the years 2015 to 2018.

Events corresponding to the most central 90% of the inelastic Pb–Pb cross section are selected, since for the most peripheral events the coincidence between V0A and V0C cannot anymore detect efficiently the presence of an inelastic Pb–Pb interaction.

The sample of dimuons is obtained combining the muon pairs reconstructed in the Muon Spectrometer acceptance, applying a series of cuts at the single track level:

- single muon pseudorapidity in the range $-4 < \eta_{\mu} < -2.5$, to reject tracks at the edges of the muon spectrometer.
- radial transverse position of the muon tracks at the end of the absorber (R_{abs}) in the range $17.6 < R_{abs} < 89.5$ cm, to remove tracks undergoing multiple Coulomb scatterings in the low-angle absorber part characterized by high Z material.
- muon tracks reconstructed in the tracking chambers are required to match a track segment reconstructed in the trigger system. This cut removes tracks produced in the beam shield and hadrons misidentified as muons, since most of them are stopped by the iron wall, which is positioned upstream of the muon trigger system.

- application of the $p \times$ DCA cut. As the name suggests this cut is based on the product between the particle momentum (p) and the distance of closest approach of the muon track to the primary interaction vertex (DCA). By means of an appropriate cut on this variable it is possible to remove efficiently muons not originated at the interaction vertex, such as those coming from beam-gas interactions. The cut is performed on the product of these two quantities because in this way its distribution is approximately independent on the muon track momentum.

In addition further cuts are applied to each dimuon candidate:

- dimuons are selected in the mass window $2 < m_{\mu\mu} < 5$ GeV/c^2. This mass window is chosen to have a sufficiently large range to define the background shape, which is crucial in the signal extraction procedure.
- dimuons rapidity is required to be in the range $2.5 < y_{\mu\mu} < 4$, to cope with the spectrometer acceptance.
- dimuons are required to have a total charge equal to zero, which corresponds to have two opposite sign muons.

5.3 Signal Extraction

The procedure chosen for this analysis consists in performing a fit to the opposite sign dimuon invariant mass distribution using different combinations of functions describing the signal and the background. The use of various shapes in the signal extraction is normally done to have under control the stability of the result and to evaluate the presence of potential systematic effects related to the choice of the fitting functions.
In this analysis the signal shape is described by *pseudo-Gaussian* functions [194], with the non-Gaussian tails due to the fluctuations in the energy loss, radiative decays and multiple scattering for the muons. The J/ψ and ψ(2S) signals are described by the *extended Crystal Ball* and by the NA60 functions, whose implementations are reported in the following.

- The *extended Crystal Ball* (CB2) consists of a Gaussian core and two power-law tails. The latter are attributed to fluctuations in energy-loss effects, to the multiple Coulomb scattering in the front absorber and to the radiative decays.

$$f(x; N, \bar{x}, \sigma, t_1, t_2, p_1, p_2) = N \cdot \begin{cases} A \cdot (B - t)^{-p_1} & , t \leq t_1 \\ e^{-\frac{1}{2} \cdot t^2} & , t_1 < t < t_2 \\ C \cdot (D + t)^{-p_2} & , t \geq t_2 \end{cases} \tag{5.7}$$

where

$$\begin{aligned} t &= \frac{x - \bar{x}}{\sigma} \\ A &= \left(\frac{p_1}{|t_1|} \right)^{p_1} \cdot e^{-\frac{|t_1|^2}{2}} \\ B &= \frac{p_1}{|t_1|} - |t_1| \\ C &= \left(\frac{p_2}{|t_2|} \right)^{p_2} \cdot e^{-\frac{|t_2|^2}{2}} \\ D &= \frac{p_2}{|t_2|} - |t_2| \end{aligned}$$

The parameters A, B, C and D are defined so that the function is continuous in its first derivative.

- The *NA60* function, introduced for the charmonium signal extraction by the homonymous collaboration [195], is a Gaussian around the resonance pole and has a mass-dependent width on the left and the right side:

$$f(x; N, \bar{x}, \sigma, t_1, t_2, p_1, ..., p_6) = N \cdot e^{-\frac{1}{2}(\frac{t}{t_0})^2} \quad \text{with} \quad t = \frac{x - \bar{x}}{\sigma} \tag{5.8}$$

where

$$t_0 = \begin{cases} 1 + (p_1(t_1 - t))^{p_2 - p_3\sqrt{t_1 - t}} & , t \leq t_1 \\ 1 & , t_1 < t < t_2 \\ 1 + (p_4(t - t_2))^{p_5 - p_6\sqrt{t - t_2}} & , t \geq t_2 \end{cases}$$

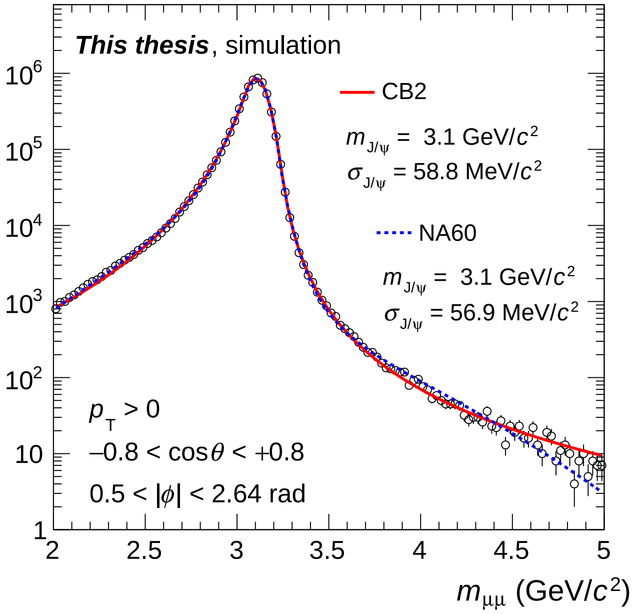

Figure 5.3: Example of Monte Carlo invariant mass spectrum for J/ψ with $p_{\mathrm{T}} > 0$. The distribution is fitted with an extended Crystal Ball function (red solid line) and with the NA60 function (blue dotted line).

In Fig. 5.3 an example of fit to a Monte Carlo invariant mass spectrum is shown.

In Pb–Pb collisions the signal tail parameters are normally fixed to values obtained from the Monte Carlo or from high-statistics proton-proton data samples. The large background, typical of heavy-ion collisions, prevents the possibility of fixing the tail parameters directly on the Pb–Pb invariant mass fits. In most quarkonium analyses, the variation of the tail parameters may provide a significant contribution to the signal extraction systematic. However, it was observed that in this analysis this effect, when present, tends to be constant as a function of the angular variables of the J/ψ, and has a very small impact on the final result, which depends on the degree of asymmetry of the $\cos\theta$ and ϕ distributions but not on their normalization.

Differently from tail parameters, the choice of the width of the signal (σ) in the fit procedure plays a role in the evaluation of the polarization parameters. While in principle it could be better to leave the signal width as a free parameter of the fits, this is not always possible, also due to the fact that in the region close to $|\cos\theta| \sim 1$ the available number of candidates strongly decreases. Therefore in this analysis the signal is extracted both fixing and keeping free the J/ψ width and differences in the two results will be used in the evaluation of a systematic uncertainty.

In the selected mass range ($2 < m_{\mu\mu} < 5$ GeV/c^2) a contribution from the ψ(2S) is also present. Despite the low statistics expected for this excited state in Pb–Pb collisions, in kinematic ranges where the combinatorial background is less dominant, as at high-p_{T}, the ψ(2S) can be observed. Hence, for completeness it has been decided to include it in the fit to the invariant mass spectrum. As already done in other quarkonium analyses, the ψ(2S) mass and width are bound to the J/ψ one according to the following equations:

$$m_{\psi(2\mathrm{S})} = m_{\mathrm{J}/\psi}^{\mathrm{FIT}} + \Delta m^{\mathrm{PDG}} \tag{5.9}$$

$$\sigma_{\psi(2\mathrm{S})} = \sigma_{\mathrm{J}/\psi}^{\mathrm{FIT}} \cdot \frac{\sigma_{\psi(2\mathrm{S})}^{\mathrm{MC}}}{\sigma_{\mathrm{J}/\psi}^{\mathrm{MC}}} \tag{5.10}$$

where $m_{\mathrm{J}/\psi}^{\mathrm{FIT}}$ and $\sigma_{\mathrm{J}/\psi}^{\mathrm{FIT}}$ are the J/ψ mass and width obtained in the fit to the dimuon invariant mass spectrum, Δm^{PDG} corresponds to the difference in mass between J/ψ and ψ(2S) as reported by the Particle Data Group (PDG) [5] ($\Delta m^{\mathrm{PDG}} = 3.686 - 3.096 = 0.59$ GeV/c^2) and $\sigma_{\psi(2\mathrm{S})}^{\mathrm{MC}}/\sigma_{\mathrm{J}/\psi}^{\mathrm{MC}}$ is the ratio of the ψ(2S) to J/ψ widths as extracted from the Monte Carlo simulations.

The background in the mass region under study is predominantly composed by uncorrelated $\mu^+\mu^-$ pairs and by semi-leptonic decays of charmed hadrons, and in general it can be described adopting phenomenological functions. The two shapes used for the background fit are a *Variable Width Gaussian* (VWG) and the product of a fourth degree polynomial function times an exponential function.

- The *Variable Width Gaussian* (VWG), a Gaussian with a mass-dependent width, is defined as follows :

  $$f(x; N, \bar{x}, A, B) = N \cdot e^{\frac{(x-\bar{x})^2}{2\sigma^2}} \tag{5.11}$$

  where

  $$\sigma = A + B \cdot \frac{(x - \bar{x})}{\bar{x}}$$

- The product of a polynomial times an exponential is also used for the description of the background because it is rather effective in the fit of data points and very easy in the implementation :

$$f(x; N, p_0, p_1, p_2, p_3) = N \cdot e^{p_0 x} \cdot (p_1 + p_2 x + p_3 x^2 + p_4 x^3 + p_5 x^4) \tag{5.12}$$

In Fig. 5.4 an example of the fit to the invariant mass distribution is shown. The J/ψ signal has been removed and the background is parametrized with the previously discussed functions, which both provide a good description of the data points.

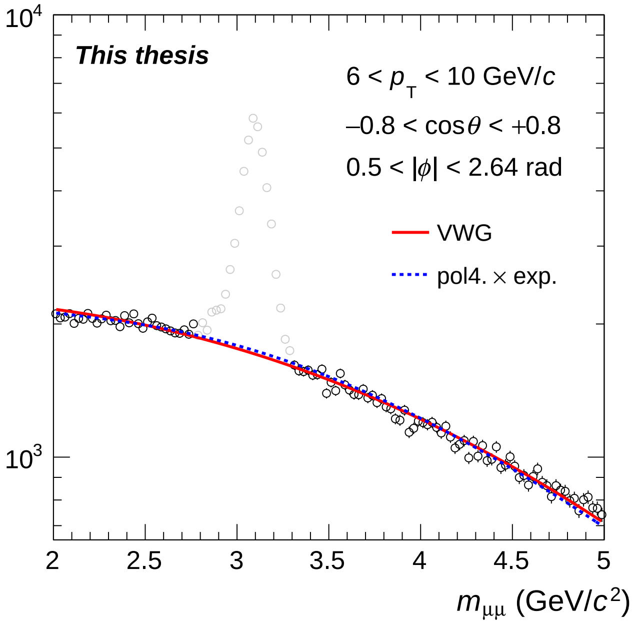

Figure 5.4: Example of fit to the background with a variable width Gaussian (red solid line) and a polynomial times an exponential function (blue dotted line), after having removed the signal peak.

5.3.1 Yield extraction: p_T dependence

The signal extraction procedure as a function the transverse momentum is performed choosing a p_T-binning which allows to have a large number of J/ψ candidates and to cope with the rapidly decreasing signal with the increasing p_{T}. It was found, after a series of preliminary tests, that three p_{T} bins covering the ranges 2−4, 4−6 and 6−10 GeV/c provide a good significance of the J/ψ signal, reducing the impact of the statistical fluctuations. In this work, the J/ψ raw yield is extracted for $p_{\mathrm{T}} > 2$ GeV/c, as already done in he other polarization analyses in proton-proton collisions [157, 196]. This choice is related to the detector acceptance and can be explained taking into account J/ψ decay kinematics. For large $\cos\theta$ values the two muons are "almost" aligned with respect to the quantization axis, the μ^{+} is parallel while the μ^{-} is anti-parallel. Boosting the two muons in the laboratory frame, the μ^{+} receives a large momentum, differently the μ^{-} will have low momentum, given its opposite direction with respect to the boost. Therefore, for low-p_{T} J/ψ, one of the two leptons will have very low momentum and won't pass the absorber. This results in the loss of $A \times \varepsilon$, which rapidly drops to zero for large $\cos\theta$ values.

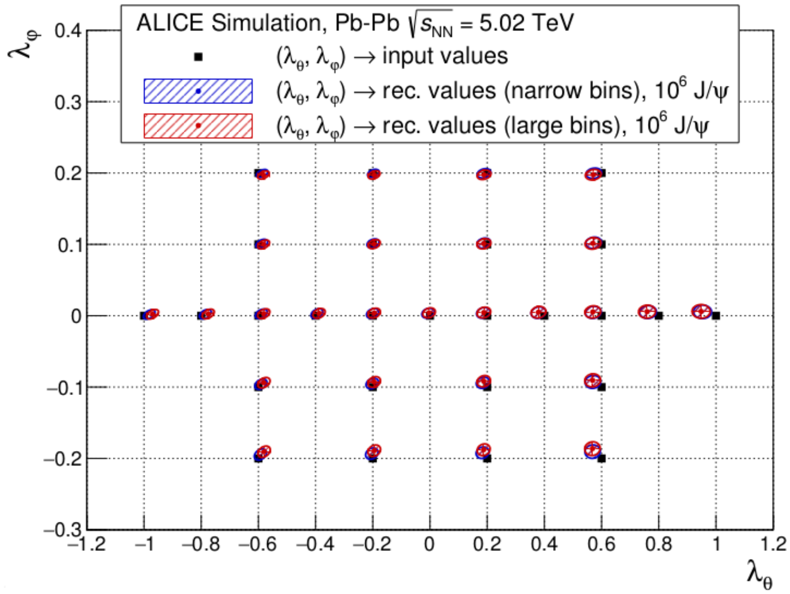

Figure 5.5: Closure test performed to check the feasibility of the 2D approach. Different bin choices (narrow with blue points, large with red points) are compared with the generated ones (black squares). The colored area around the points represent the 1σ contour.

For this analysis the signal extraction is performed through the previously mentioned *2D approach*, where the J/ψ raw yield is evaluated on a two-dimensional map as a function of $\cos\theta$ and ϕ. Before extracting the signal, a preliminary test has been performed on a Monte Carlo simulation, to evaluate the validity of the method. In particular different J/ψ

samples are generated with a certain degree of polarization, with a statistical precision significance consistent with the one observed in data ($\sim 10^6$ J/ψ). The obtained $(\cos\theta, \phi)$ distributions are then fitted with Eq. 5.1 to extract the λ_θ and λ_ϕ parameters and the one standard deviation contour. The test is repeated considering two alternative choices for the $\cos\theta$ and ϕ binning, one larger and one narrower. As shown in Fig. 5.5 the results are all compatible with the generated polarization within 1σ, without a significant difference among the two bin choices.
After this preliminary check the $\cos\theta$ and ϕ binning for the two-dimensions grid is chosen and for each $(\cos\theta, \phi)$ cell the raw yield is extracted. The grid size is optimized in order to have a sufficient dimuon population for each cell, a reasonable signal-to-background ratio and to be as narrow as possible. This last requirement is related to the $A \times \varepsilon$ correction, which will be discussed with more details in Section 5.4.

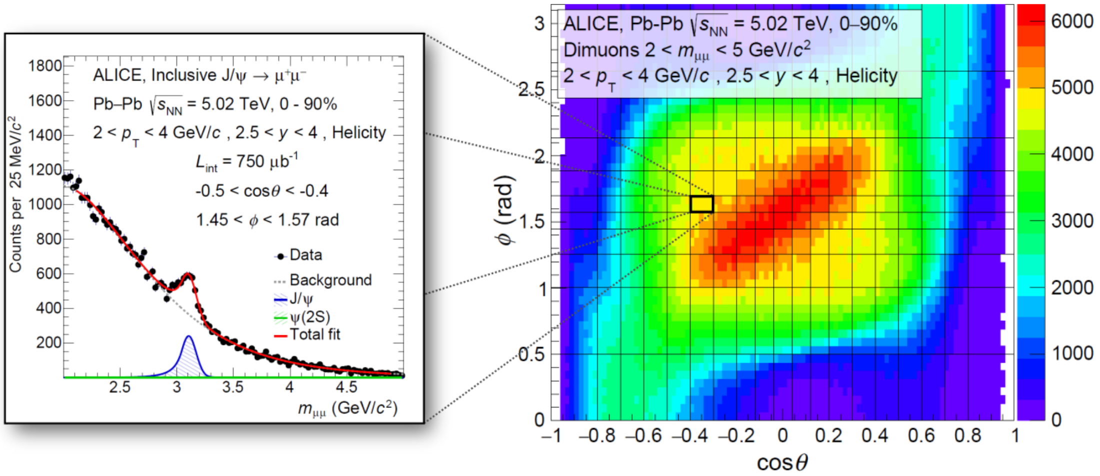

Figure 5.6: Example of signal extraction and corresponding $(\cos\theta, \phi)$ cell on the two-dimensions map populated with dimuons in the mass range $2 < m_{\mu\mu} < 5$ GeV/c^2 and for $2 < p_{\rm T} < 4$ GeV/c.

In Fig. 5.6 the two-dimension grid is shown superimposed to the $(\cos\theta, \phi)$ dimuon distribution. It counts 19 bins in $\cos\theta$ and 10 bins in ϕ. The bin width changes according to the statistics available and it can be seen that the grid is finer for $\cos\theta \sim 0$ and $\phi \sim \pi/2$, where the dimuon population is larger. As previously mentioned, the $A \times \varepsilon$ rapidly drops to zero for $|\cos\theta| \sim 1$, and therefore there is a relatively small J/ψ population in that range. This could be problematic in the extraction of the polarization parameters, because for large $\cos\theta$ the corrected yield will be dominated by statistical fluctuations. For this reason it was decided to exclude the ranges $|cos\theta| > 0.8$, $\phi < 0.5$ and $\phi > 2.64$ rad, creating

a *fiducial area* within which the λ_θ, λ_ϕ and $\lambda_{\theta\phi}$ parameters are extracted.
For each dimuon invariant mass spectrum the J/ψ raw yield is extracted by means of a *maximum likelihood fit* in the mass range $2.1 < m_{\mu\mu} < 4.9$ GeV/c^2. The J/ψ mass is kept free in the fit, while the width is fixed to the one extracted from the Monte Carlo for each $(\cos\theta, \phi)$ cell according to the following choice:

$$\sigma_{\mathrm{J}/\psi}(\cos\theta,\phi) = \sigma^{\mathrm{MC}}_{\mathrm{J}/\psi}(\cos\theta,\phi)\cdot(\sigma_{\mathrm{J}/\psi}/\sigma^{\mathrm{MC}}_{\mathrm{J}/\psi})\big|_{\mathrm{Integrated}} \tag{5.13}$$

The term $\sigma_{\mathrm{J}/\psi}/\sigma^{\mathrm{MC}}_{\mathrm{J}/\psi}$ is a scaling factor obtained comparing the J/ψ width in data and Monte Carlo for the $(\cos\theta, \phi)$ integrated spectrum and is applied to account for a small discrepancy found between simulation and real data.

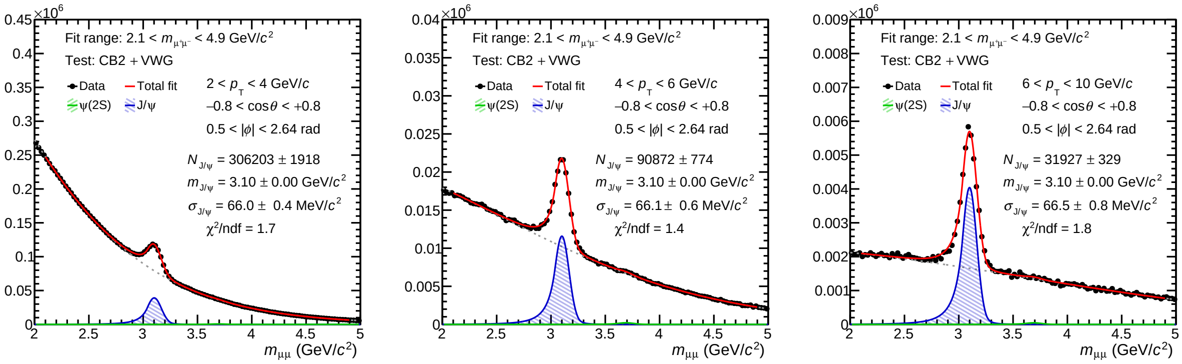

Figure 5.7: Fit to the $\mu^+\mu^-$ invariant mass spectrum for dimuons inside the $(\cos\theta, \phi)$ fiducial region and for different p_T ranges: $2 < p_\mathrm{T} < 4$ GeV/c left panel, $4 < p_\mathrm{T} < 6$ GeV/c central panel, $6 < p_\mathrm{T} < 1$ GeV/c right panel.

In Fig. 5.7 the fit to the dimuon invariant mass distributions corresponding to the selected p_T ranges and integrated over the fiducial $(\cos\theta, \phi)$ region are shown. It can be seen that the number of J/ψ decreases rapidly from $2 < p_\mathrm{T} < 4$ GeV/c ($N_{\mathrm{J}/\psi} \sim 3.06 \times 10^5$) to $6 < p_\mathrm{T} < 10$ GeV/c ($N_{\mathrm{J}/\psi} \sim 3.19 \times 10^4$).

In Fig. 5.8 the J/ψ raw yield is shown on two-dimensions maps for the helicity and Collins-Soper reference frames in the three p_T bins under study. The empty cells corresponds to not converging fits or with large χ^2 ($\chi^2/ndf > 2$) which are not included in the extraction of the polarization parameters. In Table 5.2 a summary of the binning and the corresponding J/ψ data sample are reported.

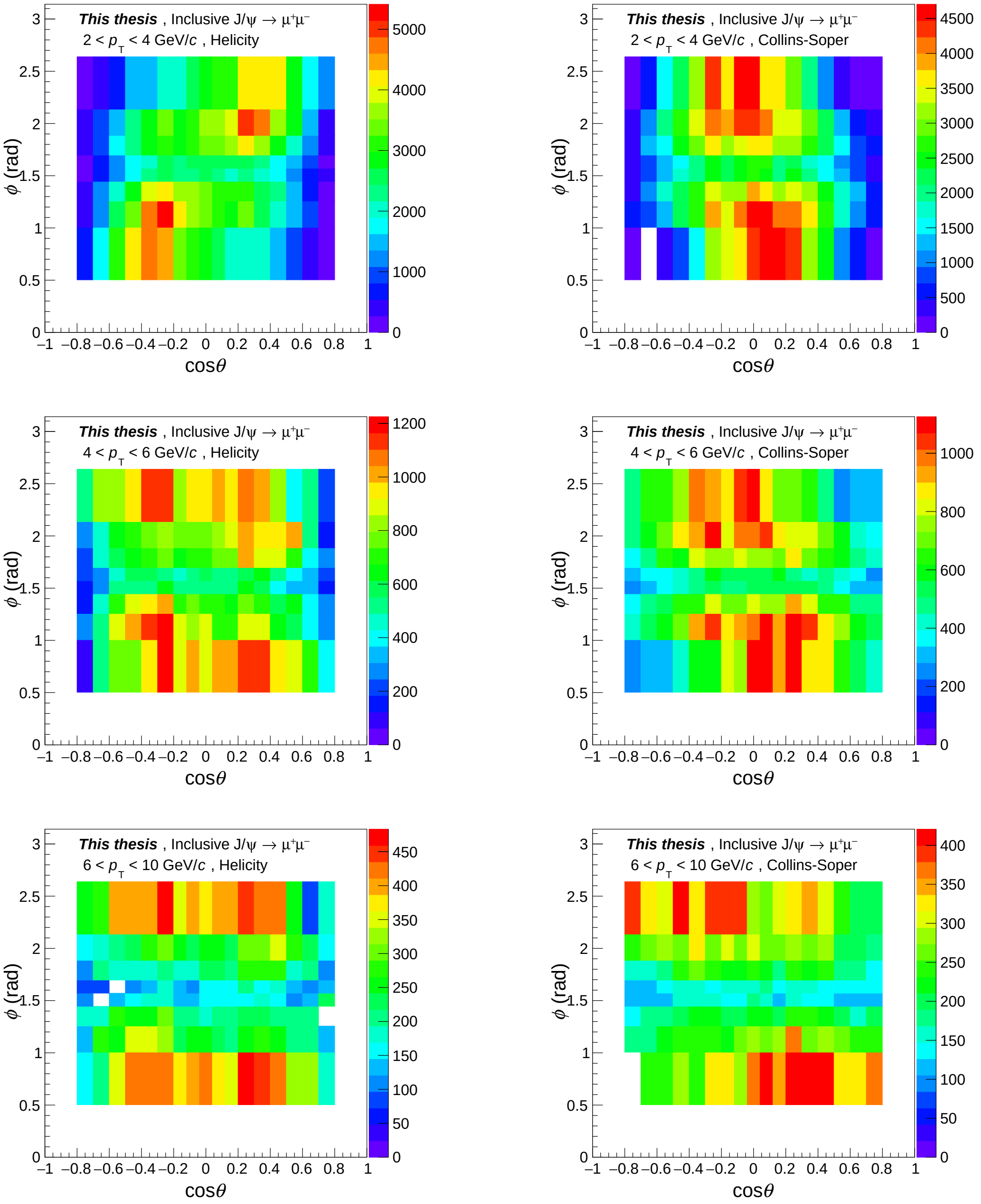

Figure 5.8: J/ψ raw yield as a function of the angular variables cosθ and ϕ in the helicity (left plots) and Collins-Soper (right plots) reference frames. The signal function used for the fit is the CB2 while the background is a Variable-Width Gausian. From top to bottom the p_{T} ranges under study: $2 < p_{\mathrm{T}} < 4$ GeV/c, $4 < p_{\mathrm{T}} < 6$ GeV/c and $6 < p_{\mathrm{T}} < 10$ GeV/c.

centrality (%)	[0 – 90]		
$\cos\theta$	[−0.8 – 0.8] (17 bins)		
ϕ (rad)	[0.5 – 2.64] (8 bins)		
p_{T} (GeV/c)	[2 – 4]	[4 – 6]	[6 – 10]
$N_{\mathrm{J}/\psi}$	306203 ± 1918	90872 ± 774	31927 ± 329

Table 5.2: Summary of $\cos\theta$, ϕ and p_{T} binning adopted with the corresponding J/ψ sample.

5.3.2 Yield extraction: centrality dependence

The J/ψ raw yield extraction as a function of centrality is performed in the p_{T} range $2 < p_{\mathrm{T}} < 6$ GeV/c. The choice of this transverse momentum region is related to the large data sample necessary to study polarization in multiple centrality classes. In this analysis the centrality determination is performed via the measurement of a signal proportional to forward hadron multiplicity. This signal is obtained by means of the V0 detector, and more precisely using the sum of the signals from the V0A and V0C scintillators, located at both sides of the interaction point. In fact this estimator has an optimal resolution, which ranges from 0.5% to 2% moving from central to peripheral collisions [197]. As shown in Fig. 5.9, the centrality distribution for CMUL7 triggered dimuons exponentially decreases from central to peripheral collisions and a similar behavior is expected for the J/ψ raw yield. Four centrality classes are chosen: 0–20%, 20–40%, 40–60% and 60–90%.

Differently from the analysis as function of p_{T}, the method used for the J/ψ raw yield extraction is the *1D-approach*. In fact, since the number of J/ψ varies from $\sim 2.5 \times 10^5$ to $\sim 9.7 \times 10^3$ moving from 0–20% to 60-90%, the 2D-method is not feasible for peripheral collisions because the $(\cos\theta, \phi)$ map cannot be filled properly. The chosen binning in $\cos\theta$ and ϕ is the same as the one used for the p_{T} analysis, while for the additional variable $\tilde{\phi}$, 10 bins of equal width are defined in the range $0 < \tilde{\phi} < 2\pi$. In Table 5.3 a summary of the binning adopted for the different variables and the corresponding J/ψ sample is reported.

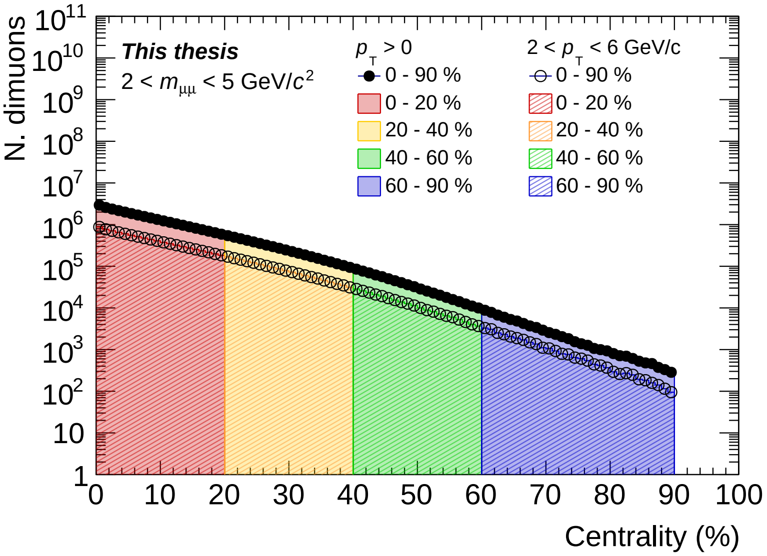

Figure 5.9: Centrality distribution for CMUL7 triggered dimuons in the mass range $2 < m_{\mu\mu} < 5$ GeV/c^2 corresponding to the full Run 2 Pb–Pb data sample. The distribution is obtained for two different $p_{\rm T}$ ranges, the first for $p_{\rm T} > 0$, the second for $2 < p_{\rm T} < 6$ GeV/c.

$p_{\rm T}$ (GeV/c)	[2 – 6]			
$\cos\theta$	[−0.8 – 0.8] (17 bins)			
ϕ (rad)	[0.5 – 2.64] (8 bins)			
$\tilde{\phi}$ (rad)	[0 – 6.28] (10 bins)			
centrality (%)	[0 – 20]	[20 – 40]	[40 – 60]	[60 – 90]
$N_{{\rm J}/\psi}$	250562 ± 1835	102420 ± 817	34295 ± 359	9744 ± 140

Table 5.3: Summary of the $\cos\theta$, ϕ, $\tilde{\phi}$ and centrality binning adopted with the corresponding J/ψ sample.

The J/ψ raw yield is extracted using the maximum likelihood method and the width is fixed to the Monte Carlo according to Eq. 5.13. The overall quality of the fits is good and the χ^2/ndf is always lower than 2.

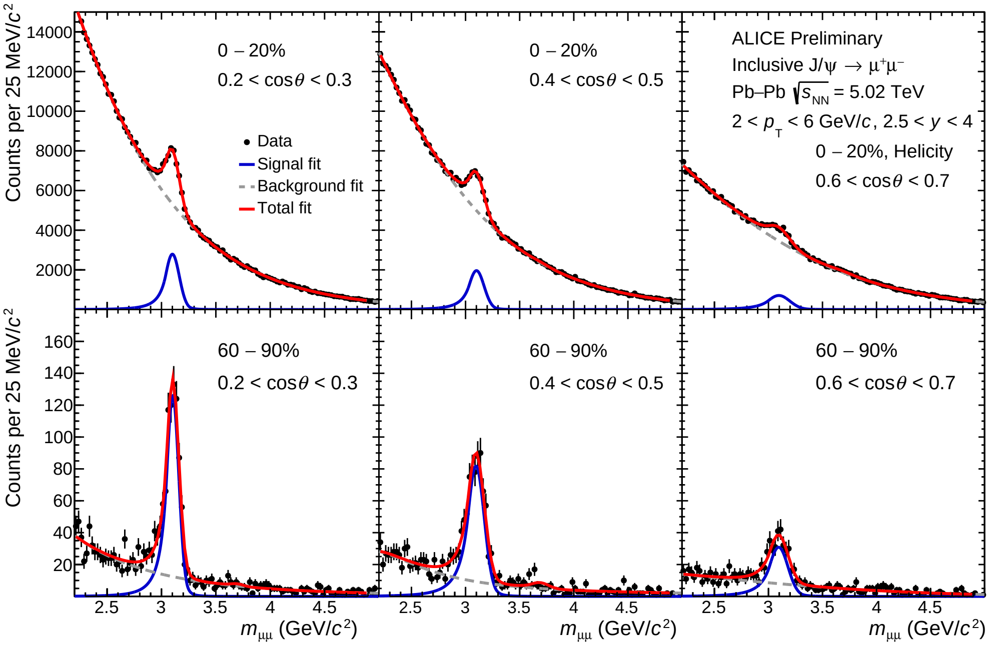

Figure 5.10: Fit to the dimuon invariant mass spectra for three cos θ ranges (0.2–0.3, 0.4–0.5, 0.6–0.7) and in two centrality classes, 0–20% (top panels) and 60–90%.

In Fig. 5.10 the fits to the dimuon invariant mass spectra are shown for different cos θ and centrality ranges. It can be noticed that the signal-to-background ratio is larger for $60 - 90\%$ than $0 - 20\%$, a crucial feature which makes possible the extraction of the J/ψ yield also in peripheral collisions, despite the difference of more than two orders of magnitude in terms of number of candidates with respect to central events.

The results of the signal extraction as a function of cos θ, ϕ and $\tilde{\phi}$ is shown in Fig. 5.11 for different centrality classes and for a specific combination of signal and background functions (CB2+VWG). The raw yield is normalized to the bin width.

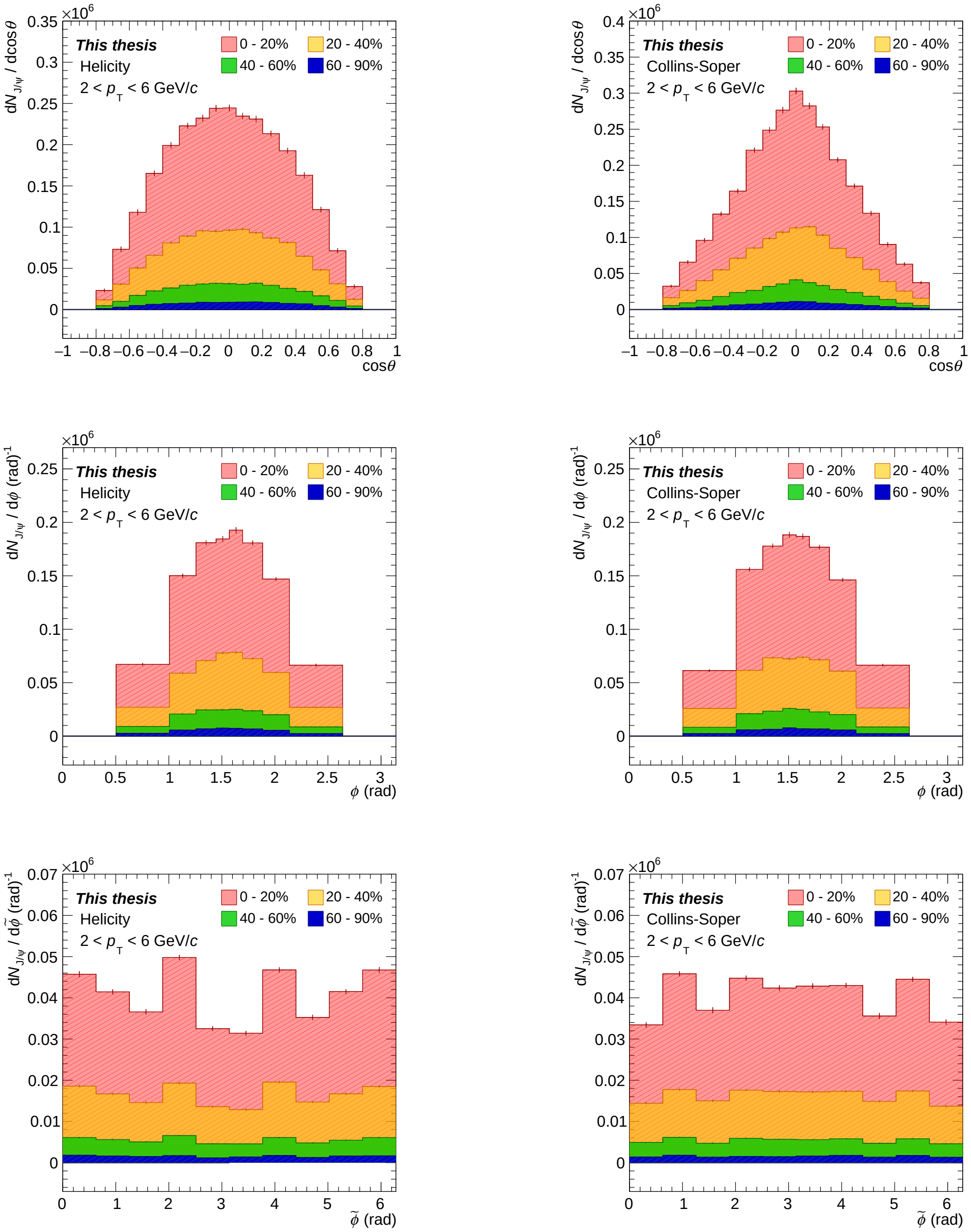

Figure 5.11: J/ψ raw yield normalized to the bin width as a function of $\cos\theta$, ϕ and $\tilde{\phi}$ (from top to bottom) in the helcity (left side) and Collins-Soper (right side) reference frames for the centrality classes 0–20%, 20–40%, 40–60% and 60–90%.

5.4 $A \times \varepsilon$ correction

The term acceptance-times-efficiency ($A \times \varepsilon$) is used to indicate the product of two quantities:

- the *acceptance*, which is related to the geometrical coverage of the experimental apparatus and to the particle decay kinematics;
- the *efficiency*, which is related to the detector performances and to the reconstruction algorithm. In the specific case of the ALICE muon spectrometer it includes the contributions of trigger, tracking and matching efficiencies;

The $A \times \varepsilon$ provides the fraction of J/ψ which can be reconstructed in the considered kinematic domain and is used to correct the raw yield:

$$N^{\mathrm{Corr}}_{\mathrm{J}/\psi} = \frac{N^{\mathrm{Raw}}_{\mathrm{J}/\psi}}{(A \times \varepsilon)_{\mathrm{J}/\psi}} \tag{5.14}$$

The acceptance-times-efficiency is evaluated with a Monte Carlo simulation, performed through the *Aliroot* framework which includes a complete modelization of the ALICE set-up and is based on the ROOT package [198]. The experimental geometry included in Aliroot is based on detectors drawings. However there may be deviations from the nominal geometry, due to mechanical and thermal stresses, that may induce small displacements in the detector elements and need to be corrected in order to minimize the loss of accuracy in the simulation. This is performed through a set of procedures, named *offline alignment*, and based on the detection of straight tracks in the muon spectrometer. This kind of information is stored in the *Offline Conditions Data Base* (OCDB) in addition to the efficiency maps, which have an updated description of the dead and noisy elements of the detectors in the experimental apparatus.

The simulation process in normally divided into three main steps:

1. the J/ψ is generated with a certain p_{T} and y, according to the distributions provided in input to the simulation (*input shapes*) and which are directly tuned on real data. In addition, the degree of polarization can be also tuned, but in centralized Monte Carlo productions, which are used in several analyses, it is normally set to zero.

2. the generated J/ψ is decayed into a muon pair.
3. the muon pair is propagated inside the experimental apparatus and the corresponding digital responses of the detectors are stored. Subsequently, starting from this information, the muon tracks are reconstructed using the same algorithm of real data.

The output of the Monte Carlo simulation includes both generated and reconstructed events, so that the $A \times \varepsilon$ can be computed as:

$$A \times \varepsilon(p_{\mathrm{T}}, y, \cos\theta, \phi) = \frac{N_{\mathrm{Rec}}(p_{\mathrm{T}}, y, \cos\theta, \phi)}{N_{\mathrm{Gen}}(p_{\mathrm{T}}, y, \cos\theta, \phi)} \tag{5.15}$$

where N_{Rec} and N_{Gen} are the number of reconstructed and generated events respectively, for a certain $(p_{\mathrm{T}}, y, \cos\theta, \phi)$ range. In order to mimic as much as possible the conditions of the real experiment, the Monte Carlo simulation is performed separately for each data taking run and the number of simulated J/ψ is proportional to the number of collected dimuon triggers (CMUL7).

The p_{T} and y shapes provided as input to the Monte Carlo simulation should be tuned on Pb–Pb data at $\sqrt{s_{\mathrm{NN}}} = 5.02$ TeV. Since the J/ψ transverse momentum and rapidity distributions are not known a priori, an *iterative procedure* is performed, which consists of the following steps:

- **step 0**: the J/ψ raw yield is extracted from data as a function of p_{T} and y. The acceptance-times-efficiency used for the correction is evaluated via a Monte Carlo simulation whose input shapes approximatively reproduce the expected distributions. The aim of this first step is to provide a realistic spectral shape, while the subsequent iterations will improve it, making it closer and closer to real data. The data are corrected for the $A \times \varepsilon$ obtained and the resulting distribution is then fitted with phenomenological functions which are found to describe properly the transverse momentum and rapidity spectra:

$$f(p_{\mathrm{T}}) = p_0 \cdot \frac{p_{\mathrm{T}}}{\left[1 + \left(\frac{p_{\mathrm{T}}}{p_1}\right)^{p_2}\right]^{p_3}} \tag{5.16}$$

$$f(y) = p_0 \cdot \exp\left[-\frac{1}{2} \cdot \left(\frac{y - p_1}{p_2}\right)^2\right] \tag{5.17}$$

- **step 1**: the shapes obtained from the fit to the corrected p_{T} and y distributions are used as input for another Monte Carlo simulation. The new $A \times \varepsilon$ is used to correct the J/ψ raw yield, which is than fitted to extract a new set of input shapes.

- **step 2**: the same procedure is repeated several times, obtaining a new parametrization for each iteration. The process is repeated until the input shapes do not vary significantly from one step to the following one.

The parametrization obtained at the last step of the iterative procedure is used for the final Monte Carlo production. As previously mentioned, the J/ψ are generated unpolarized in the simulation, which corresponds to a "flat" angular distribution. This could be a valid initial assumption because all the experimental measurements at the LHC in proton-proton collisions exhibit small or no polarization. However the situation may be different for Pb–Pb and the potential effect due to any measured deviation with respect to a null value of λ_θ, λ_ϕ and $\lambda_{\theta\phi}$ will have to be taken into account, as detailed in Section 5.6.3.
It was previously mentioned that this analysis is performed for $p_{\mathrm{T}}^{\mathrm{J}/\psi} > 2$ GeV/c, since configurations in which the muons are emitted in parallel to the polarization axis in the J/ψ rest frame are disfavored for low-p_{T}. This is properly reproduced in the Monte Carlo, where, as shown in Fig. 5.12, it is clearly visible that for $|\cos\theta| \sim 1$ the acceptance-times-efficiency drops to zero for $p_{\mathrm{T}}^{\mathrm{J}/\psi} < 2$ GeV/c. In the figure the fiducial $(\cos\theta, p_{\mathrm{T}})$ region is also represented as a black rectangle.

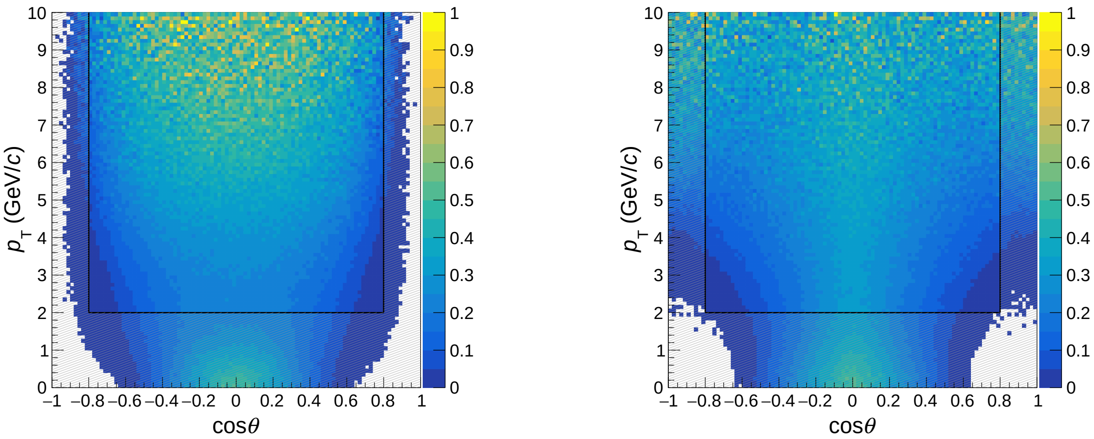

Figure 5.12: $A \times \epsilon$ as a function of $\cos\theta$ and p_{T} in the helicity (left panel) and Collins-Soper (right panel) reference frames. The fiducial region is indicated with a black rectangle.

5.4.1 $A \times \varepsilon(\cos\theta, \phi)$: p_{T} dependence

Consistently to the signal extraction, in the polarization analysis as a function of p_{T} the $A \times \varepsilon$ is evaluated on a two-dimensions $(\cos\theta, \phi)$ map. In the Monte Carlo production, the J/ψ transverse momentum and rapidity shapes are tuned on Pb–Pb data at $\sqrt{s_{\mathrm{NN}}} = 5.02$ TeV, integrated over centrality in 0–90%.

Two different simulations are performed, corresponding to the 2015 (LHC18c11_nofastb) and 2018 (LHC19i1) Pb–Pb data taking periods, and the run-by-run statistics is proportional to number of dimuon triggers (CMUL7). The simulation is named "*pure signal*" since only J/ψ and no background are generated. The production is centrally managed by the ALICE Data Preparation Group (DPG), given the large amount of statistics and computing resources required. In Table 5.4 information on the used Monte Carlo productions is shown.

In both the simulations J/ψ are generated unpolarized. The potential presence of a deviation from zero for any polarization parameter should be taken into account by performing an iterative tuning of the input $\cos\theta$ and ϕ shapes, similarly to the one mentioned for y and p_{T}. However, in a 2D approach, if the grid adopted for the signal extraction and the $A \times \varepsilon$ evaluation is sufficiently narrow, the choice of the input distribution for the angular variables is not crucial. In fact for a very "granular" binning in $\cos\theta$ and ϕ the distribution of the generated J/ψ can be approximately considered as flat in each cell. On the other hand, larger bins must be used in the region close to $|\cos\theta| = 1$, which might lead to a potential source of systematic effect, that will be discussed as detailed in Section 5.6.3.

Year	System	$\sqrt{s_{\mathrm{NN}}}$ (TeV)	Production name
2015	Pb–Pb	5.02	LHC18c11_nofastb
2018	Pb–Pb	5.02	LHC19i1

Table 5.4: Summary of the Monte Carlo productions used for the J/ψ polarization analysis as a function of p_{T}.

In Fig. 5.13 the two-dimensional $A \times \varepsilon$ map is shown for the helicity and Collins-Soper reference frames, in $2 < p_{\mathrm{T}} < 4$ GeV/c. In both the figures the ranges $|\cos\theta| > 0.8$, $\phi < 0.5$ rad $\phi > 2.64$ rad are not shown since they are outside the fiducial region and therefore not considered in the signal extraction and for the polarization parameters estimation.

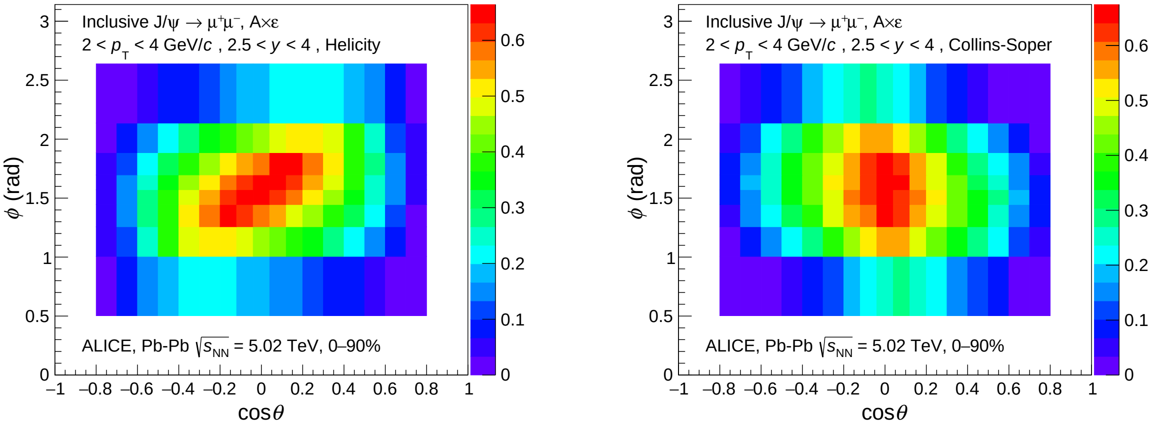

Figure 5.13: Acceptance-times-efficiency as a function of $\cos\theta$ and ϕ for $2 < p_{\mathrm{T}} < 4$ GeV/c in the helicity (left panel) and Collins-Soper (right panel), reference frames.

5.4.2 $A \times \varepsilon(\cos\theta, \phi, \tilde{\phi})$: centrality dependence

In the polarization analysis as a function of centrality a different Monte Carlo production is used, known as "*embedding*". The name derives from the fact that in this simulation the generated J/ψ is "embedded" into a real minimum bias triggered event. This feature allows to reproduce properly the dependence of the reconstruction efficiency on the collisions centrality, necessary for a centrality dependent analysis.

Year	System	$\sqrt{s_{\mathrm{NN}}}$ (TeV)	Production name
2015	Pb–Pb	5.02	LHC16e2 LHC16e2_plus
2018	Pb–Pb	5.02	LHC19a2

Table 5.5: Summary of the Monte Carlo productions used for the J/ψ polarization analysis as a function of collisions centrality.

The p_{T} and y input shapes are parametrized according to the Pb–Pb data collected at $\sqrt{s_{\mathrm{NN}}} =$ 5.02 TeV and the J/ψ is generated unpolarized. Differently from the polarization analysis as a function of p_{T}, a set of corrections has to be applied to the Monte Carlo, in order to take into a account various effects:

- *minimum bias to dimuon trigger correction*: for the embedding simulations the generated run-by-run statistics is propotional to the number of minimum bias triggers (i.e. CINT7-B-NOPF-MUFAST[1]), while in the data events are selected according to the dimuon trigger (i.e. CMUL7-B-NOPF-MUFAST). For this reason all Monte Carlo events for a certain run have to be weighted according to the the real run statistical weight in terms of CMUL7 triggers.

- *mean number of collisions correction*: in the embedding Monte Carlo the distribution of events as a function of centrality is flat, as expected for minimum bias triggers. However the dimuon trigger number rapidly decreases from central to peripheral collisions, as shown in Fig. 5.9. In order to account for this difference every Monte Carlo event is weighted according to the mean number of collisions ($\langle N_{\mathrm{coll}} \rangle$) corresponding to its centrality class. Since the production probability for a J/ψ is also proportional to N_{coll}, this correction allows to fairly reproduce the centrality distribution of the CMUL7.

- *p_{T} and y shape correction*: the transverse momentum and rapidity shapes provided as input to the Monte Carlo simulation are tuned on the corresponding distributions in data integrated over the centrality interval 0–90%. Indeed it is known from previous studies [199] that the J/ψ p_{T} and y distributions evolve as a function of centrality, with the transverse momentum spectrum becoming "harder" from peripheral to central collisions. Given the existing correlation among the angular variables, p_{T} and rapidity, this effect has to be taken into account applying to each Monte Carlo J/ψ the weight:

  $$w = \frac{f(p_{\mathrm{T}}, y)^{i-j\%}}{f(p_{\mathrm{T}}, y)^{0-90\%}} \tag{5.18}$$

  where $f(p_{\mathrm{T}}, y))^{i-j\%}$ is the p_{T} and y input shape for the (i, j) centrality class.

The p_{T} and y re-weighting can have a significant impact not only on the acceptance-times-efficiency normalization, but also on its shape as a function of the angular variables.
The extraction of the p_{T} and y shapes for different centrality classes is performed exploiting the full Run 2 statistics, the largest Pb–Pb data sample available for the ALICE experiment. The input shapes were obtained in a separate preliminary analysis, with the corrected yields as a function of rapidity fitted with Eq. 5.17, while for transverse

---

[1] trigger obtained as the coincidence of the signals in the V0A and V0C detectors

momentum, the following parametrization is used:

$$f(p_{\mathrm{T}}) = p_0 \cdot \frac{p_{\mathrm{T}}}{\left[1+\left(\frac{p_{\mathrm{T}}}{p_1}\right)^{p_2}\right]^{p_3}} + p_4 \cdot e^{-p_5 \cdot p_{\mathrm{T}}}, \tag{5.19}$$

where the exponential term added to Eq. 5.16 was found to give a better fit at high p_{T}. In Fig. 5.14 the evolution of the p_{T} and y input shapes for different centrality classes is shown.

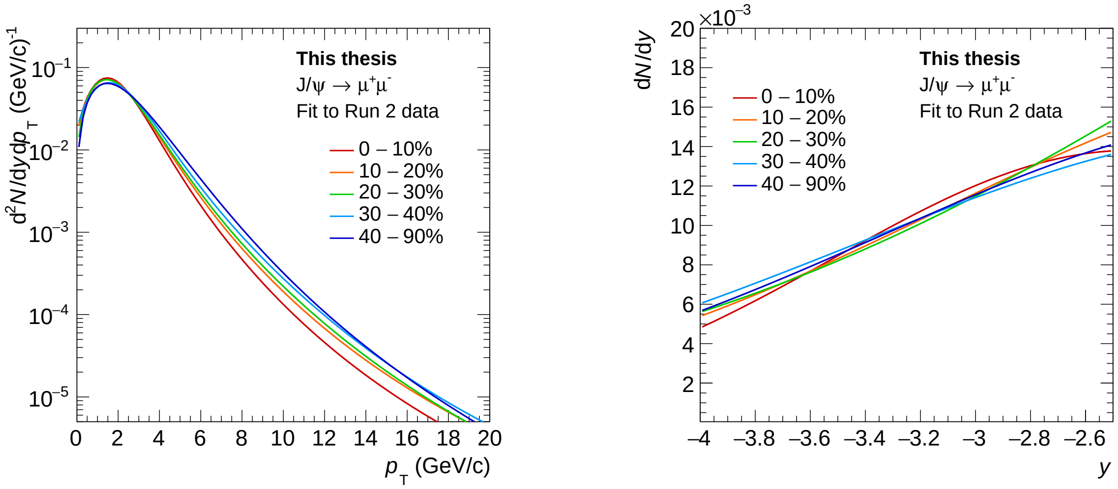

Figure 5.14: Normalized J/ψ transverse momentum (left panel) and rapidity (right panel) distributions for different centrality classes evaluated by fitting the full Run 2 data sample collected by the ALICE experiment.

The $A \times \varepsilon$ is evaluated separately for the three angular variables, following the 1D approach as in the signal extraction. In Fig. 5.15 the acceptance-times-efficiency as a function of centrality is shown after having applied the corrections previously described to the Monte Carlo. The ratio between the various centrality classes (0–20%, 20–40%, 40–60%, 60–90%) and the integrated one (0–90%) shows that the $A \times \varepsilon$ shape can vary from 10 to 20% for large $\cos\theta$ values. This is clearly a significant effect and has an impact on the final polarization parameters.

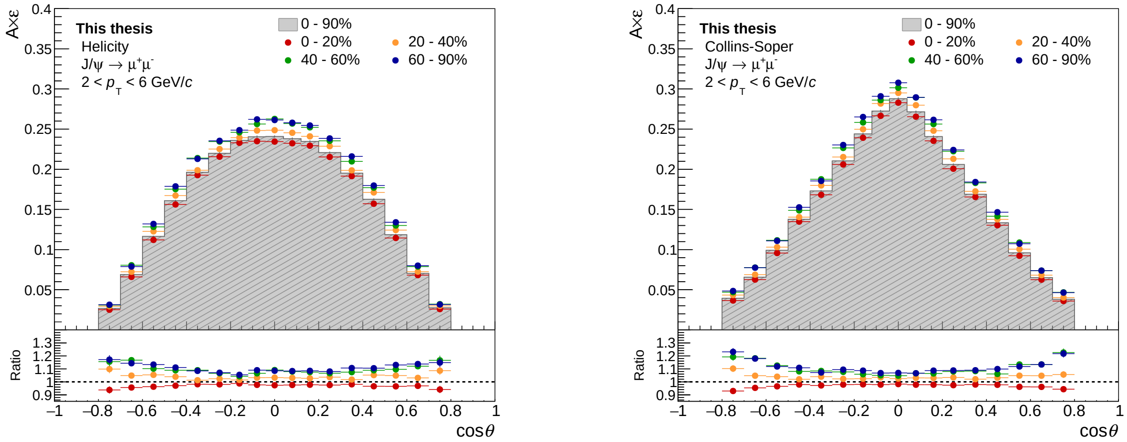

Figure 5.15: Acceptance-times-efficiency as a function of $\cos\theta$ in helicity and Collins-Soper reference frames. The results are shown for five different centrality classes: 0–20%, 20–40%, 40–60%, 60–90% and 0–90%. In the bottom panel the ratio between the different centrality classes and the integrated one (0–90%) is shown.

5.5 Polarization parameters extraction

The extraction of the λ_θ, λ_ϕ and $\lambda_{\theta\phi}$ parameters is performed by fitting the acceptance corrected angular distribution of the J/ψ. Since the study of polarization as a function of the transverse momentum and collisions centrality follows two slightly different strategies, also the fitting procedures are not exactly the same.

5.5.1 Polarization fit: p_T dependence

In the J/ψ polarization analysis as a function of p_T the 2D approach is followed. The corrected J/ψ yield, evaluated on the $(\cos\theta, \phi)$ map, is directly fitted with the distribution of Eq. 5.1 with the χ^2 minimization method. In this way all the polarization parameters are extracted in one single fit, preserving the multidimensionality of the analysis. When considering the J/ψ yields extracted with different combinations of signals and background functions, the overall result is rather stable, and the χ^2 normalized to the number of degrees of freedom (ndf) ranges between 1 and 1.5.

In Fig. 5.16 an example of the two-dimensional fit is shown. As already mentioned, the fit is restricted to the fiducial region $-0.8 < \cos\theta < 0.8$ and $0.5 < \phi < 2.64$ rad, to exclude ranges with limited J/ψ statistics and very small acceptance-times-efficiency. The projection of the corrected distribution and the fitting function along $\cos\theta$ and ϕ are also shown, in order to check the quality of the fit, given that the 2D plot makes a more difficult visualization.

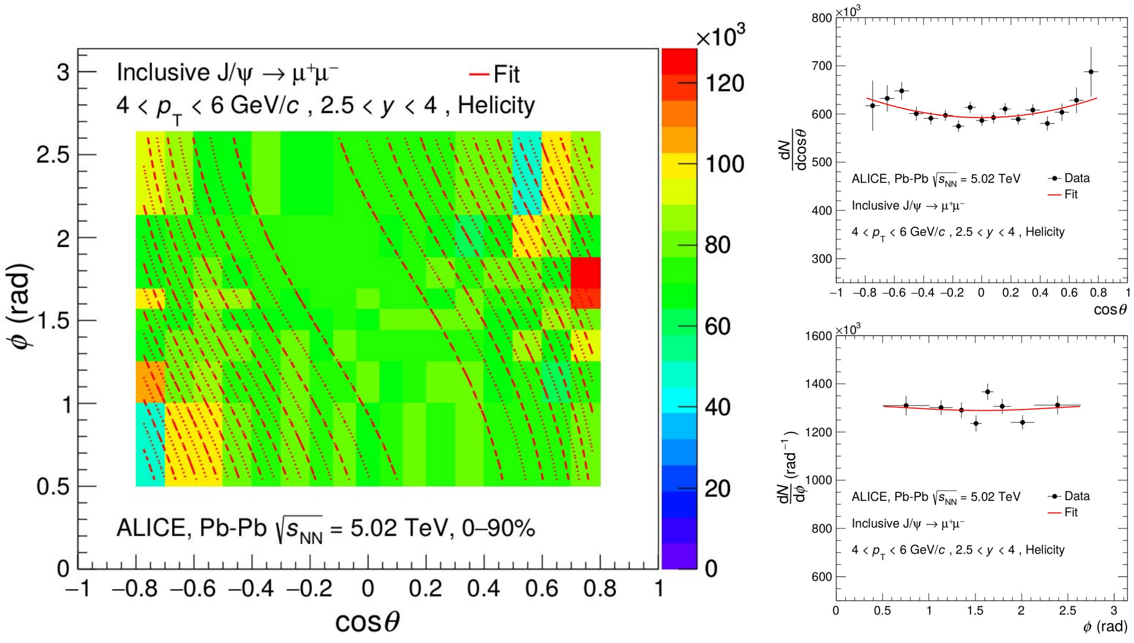

Figure 5.16: Left panel: fit to the J/ψ corrected distribution as a function of $\cos\theta$ and ϕ for $4 < p_{\mathrm{T}} < 6$ GeV/c in the helicity reference frame. Right panel: projection of the two-dimensions distribution and fitting function along $\cos\theta$ and ϕ for $4 < p_{\mathrm{T}} < 6$ GeV/c in the helicity reference frame.

5.5.2 Polarization fit: centrality dependence

The polarization parameters as a function of centrality are extracted using the one-dimension approach, where the $\cos\theta$, ϕ and $\tilde{\phi}$ distributions are studied separately. Since all the fitting functions share the λ_θ parameter, as reported in Eqs. 5.2, 5.3 and 5.5, the ideal approach consists in the simultaneous fit of the three distributions via the χ^2 minimization method. The fit range is restricted to $-0.8 < \cos\theta < 0.8$ and $0.5 < \phi < 2.64$ for the same reasons discussed in the 2D approach, while for $\tilde{\phi}$ the full domain ($0 < \tilde{\phi} < 2\pi$) is adopted, given the uniformity of the acceptance-times-efficiency for this variable. In Fig.5.17 an example of the fit to the $\cos\theta$ distribution is shown for two centrality classes.

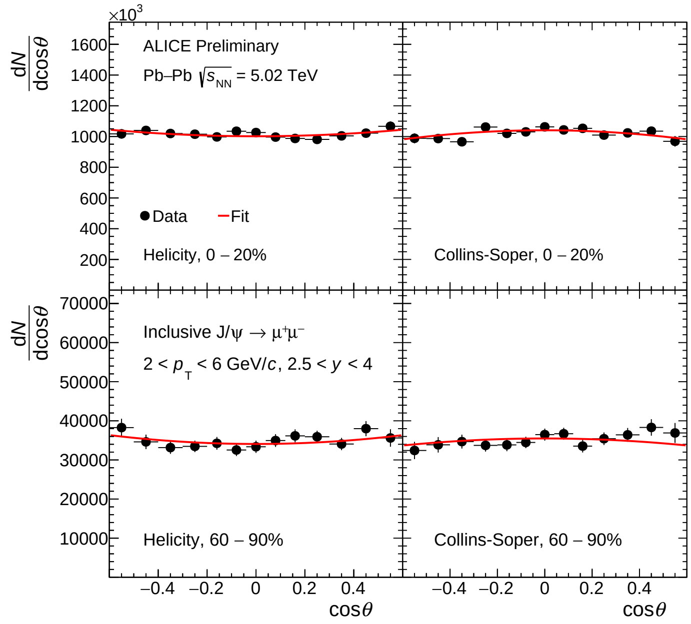

Figure 5.17: Fit to the J/ψ corrected distribution as a function of $\cos\theta$ for two different centrality classes, 0–20% and 60–90%, in the helicity (left panels) and Collins-Soper (right panel) reference frames.

5.6 Systematic uncertainties

In this section the main sources of systematic uncertainties will be discussed. The general strategy followed in their evaluation consists in varying some features of the elements previously discussed (e.g. signal and background functions, input Monte Carlo shapes,...) and evaluating the impact on the polarization parameters estimation. Four main uncertainty sources have been identified:

- **signal extraction**: the systematic associated to the choice of the signal and background functions used in the J/ψ raw yield extraction. The possibility of fixing or keeping free the J/ψ width in the fits is also investigated.

- **trigger efficiency**: the systematic uncertainty associated to the single muon trigger efficiency
- **input Monte Carlo shapes**: the systematic uncertainty associated to the p_{T} and y shapes used as input for the Monte Carlo simulation
- **difference 1D–2D**: the systematic uncertainty related to the choice between 1D and 2D method

The systematic uncertainty related to the tracking efficiency is not included in this analysis because it was checked that it does not modify the shape of the J/ψ angular distribution, but only the normalization. Therefore it should not affect the extraction of the polarization parameters.

5.6.1 Systematic uncertainty due to the signal extraction

The J/ψ raw yield extraction is performed by fitting the dimuon invariant spectrum with a combination of signal and background functions. Since the polarization parameters may exhibit a dependence on the function used to fit the invariant mass distribution, λ_θ, λ_ϕ and $\lambda_{\theta\phi}$ are evaluated for each choice.
As detailed in Section 5.3, the selected functions are:

- signal: *extended crystal ball* (CB2) and NA60 functions
- background: *Variable Width Gaussian* (VWG) and a four degree polynomial function multiplied by an exponential (Pol4.×exp.)

therefore a total of four tests is performed. The mass parameter is kept free in the fit, while the signal tails are fixed to those extracted from the Monte Carlo. In fact it was checked that, despite the fact that the raw yield normalization depends on the chosen set of tail parameters, the shape of the spectrum as a function of the angular variables does not change, hence this contribution can be neglected. Finally the J/ψ width is fixed to the Monte Carlo one according to Eq. 5.13.
In Fig. 5.18 the comparison between the polarization parameters obtained for the different signal and background shapes is shown as function of p_{T}. The average of the central values and of the statistical uncertainties for all the tests is represented in black, while the systematic uncertainty, the empty box, is calculated as the root mean square (RMS) of the

results. It is found to vary between ∼0.002 and ∼0.03 and in general it is larger at low-p_{T}. This can be explained considering that the combinatorial background is dominant in that range and it may affect more significantly the raw yield extraction.

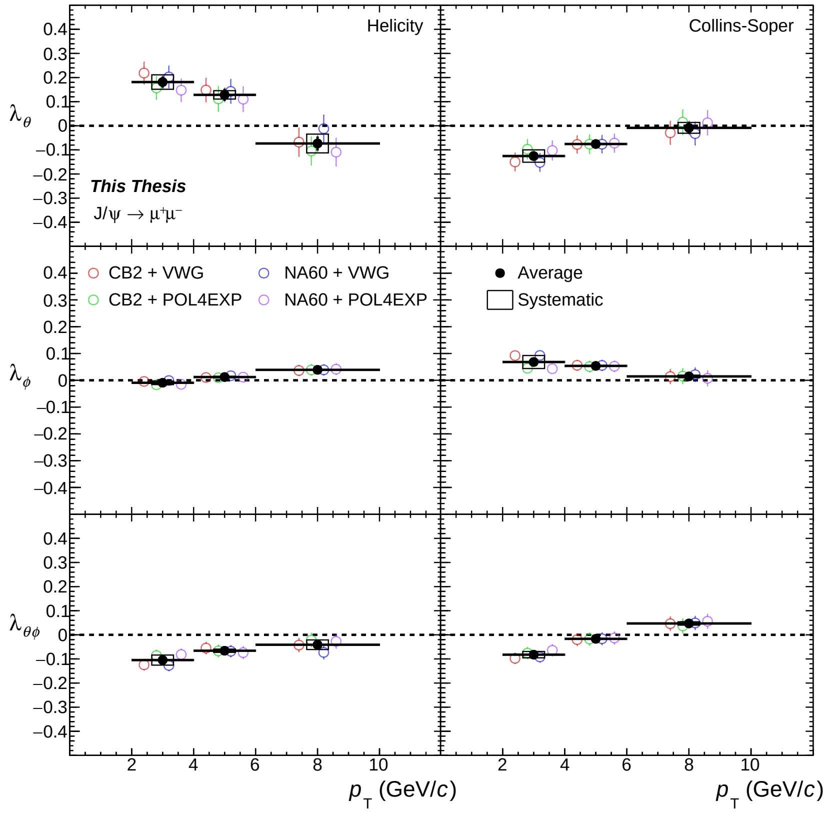

Figure 5.18: Comparison between the polarization parameters as a function of p_{T} for different choices of the signal and background shapes.

The J/ψ width has been kept fixed in this evaluation because this was found to help the fit to converge in the less-populated $(\cos\theta, \phi)$ cells. Nevertheless this choice has an impact on the polarization parameters extraction, since in the simulation the J/ψ width exhibits a slight dependence on the angular variables. For this reason a further systematic source is evaluated, comparing the average of the results obtained with the J/ψ width fixed or kept free in the fit to the invariant mass spectrum.

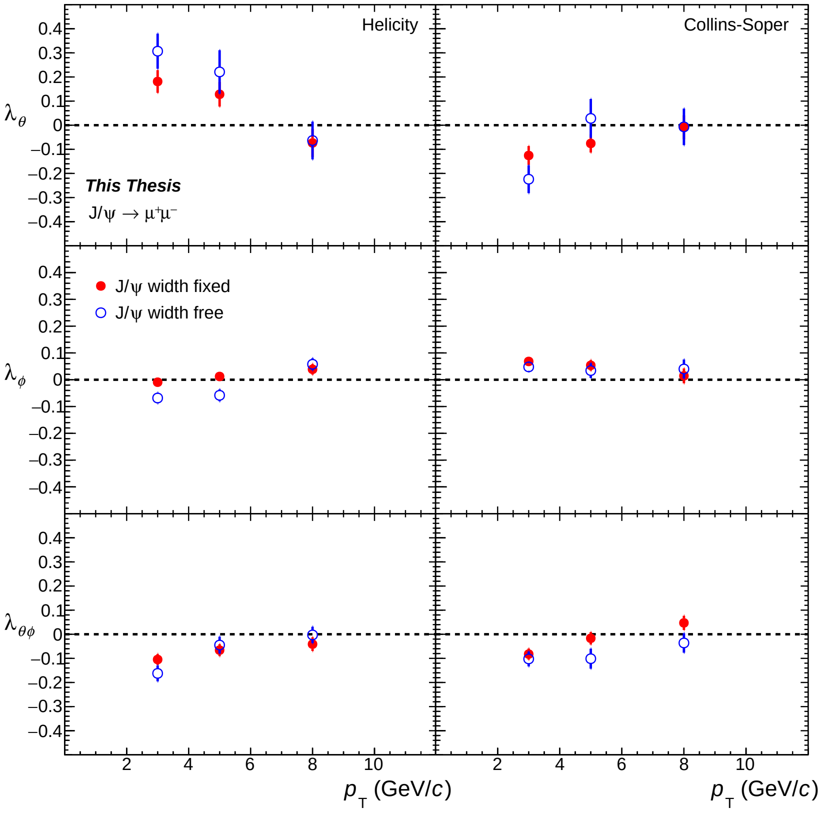

Figure 5.19: Comparison between λ_θ, λ_ϕ and $\lambda_{\theta\phi}$ as a function of p_T obtained keeping free or fixing the J/ψ width in the signal extraction.

In Fig. 5.19 the comparison between the two sets of results is shown and it can be noticed that similarly to the signal-background variation, also in this case the difference is larger at low-p_T. The systematic is evaluated as the *half difference* of the λ_θ, λ_ϕ and $\lambda_{\theta\phi}$ values for the two choices and it is found to range between ∼0.001 and ∼0.06.

In the polarization analysis as a function of centrality the systematic related to the signal extraction procedure is evaluated following the same strategy. Also in this case the signal-background shape variation, together with binding or not the J/ψ width to the Monte

Carlo, provide non-negligible contributions to the λ_θ, λ_ϕ and $\lambda_{\theta\phi}$.

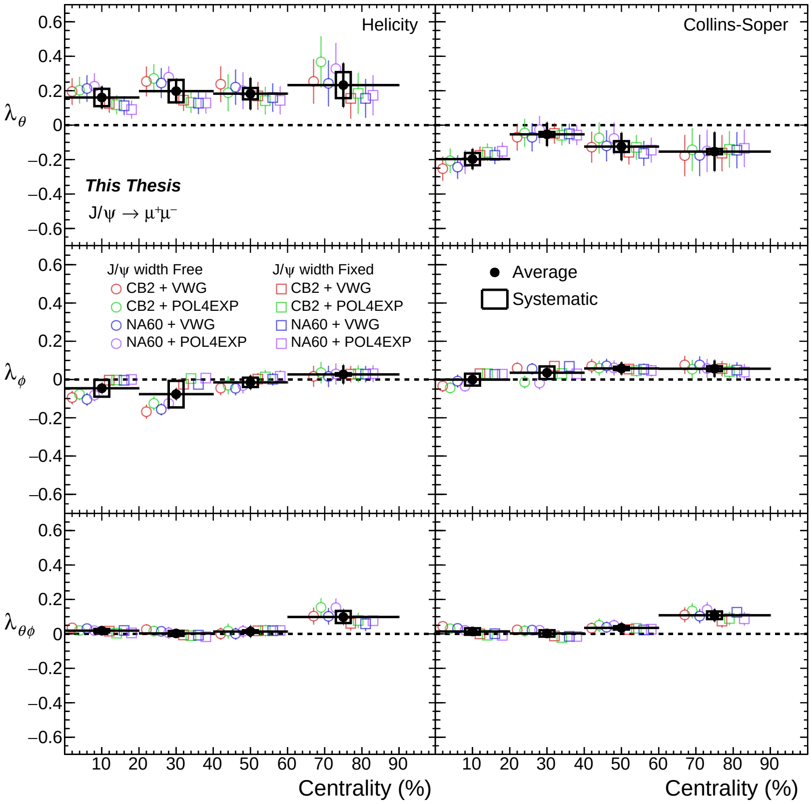

Figure 5.20: Polarization parameters obtained using different signal and background shapes in the raw yield extraction and keeping free/fixed to the Monte Carlo the J/ψ width.

In Fig. 5.20 λ_θ, λ_ϕ and $\lambda_{\theta\phi}$ are shown for different choices of signal and background shapes and, at the same time, keeping free or fixing to the Monte Carlo the J/ψ width. The average of all the results and their statistical uncertainties are shown in black, while the overall systematic is represented as an empty black box. The latter ranges between ∼0.01 and ∼0.08, and is considered as uncorrelated as a function of centrality.

5.6.2 Systematic uncertainty due to the trigger efficiency

A source of systematic uncertainty is related to the evaluation of the trigger efficiency and can be estimated via the calculation of the *trigger response function*. The latter is computed as the ratio between the number of muons passing the low-p_{T} threshold ($p_{\mathrm{T}} > 1$ GeV/c) divided by the number of muons of passing the all-p_{T} threshold ($p_{\mathrm{T}} > 0.5$ GeV/c). The result, evaluated as a function of the single muon transverse momentum, exhibits a rapid increase for $p_{\mathrm{T}} < 2$ GeV/c and a plateau corresponding to a ∼98% efficiency. This shape is parametrized with a *smeared step function*:

$$f(p_{\mathrm{T}}) = \frac{N}{(1 + e^{-b\cdot(p_{\mathrm{T}} - x_0)})} \tag{5.20}$$

where b is related to the curvature of the function, while x_0 to the inflection point. In the comparison among the trigger response functions evaluated in the data and in the Monte Carlo, a small shift is observed for $p_{\mathrm{T}} < 2$ GeV/c and this can have an effect on the polarization parameter estimation. In particular, a non-proper description in the simulation of the detector efficiency at low-p_{T} could determine a modification of $A \times \varepsilon$ at the edges of the $\cos\theta$ domain (see Section 5.3) and modify the shape of the J/ψ corrected distribution.

The systematic associated to the trigger efficiency is evaluated correcting the Monte Carlo for the discrepancy between data and simulation and re-calculating the acceptance-times-efficiency. In particular, every single muon in the Monte Carlo is weighted in the following way:

$$w(p_{\mathrm{T}}) = \frac{\varepsilon_{\mathrm{DATA}}^{\mathrm{Low/All}}}{\varepsilon_{\mathrm{MC}}^{\mathrm{Low/All}}}(p_{\mathrm{T}}) \tag{5.21}$$

where ε indicates the trigger efficiency obtained for a certain muon p_{T} value. In Fig. 5.21, the trigger response function in data and Monte Carlo are shown for the 2015 (LHC15o) and the 2018 (LHC18q + LHC18r) Pb–Pb data taking periods in three different single muon pseudorapidity ranges $2.5 < \eta_\mu < 3$, $3 < \eta_\mu < 3.5$ and $3.5 < \eta_\mu < 4$. It can be noticed that the difference between data and simulation can be as large as 10% for $p_{\mathrm{T}} \sim 2$ GeV/c.

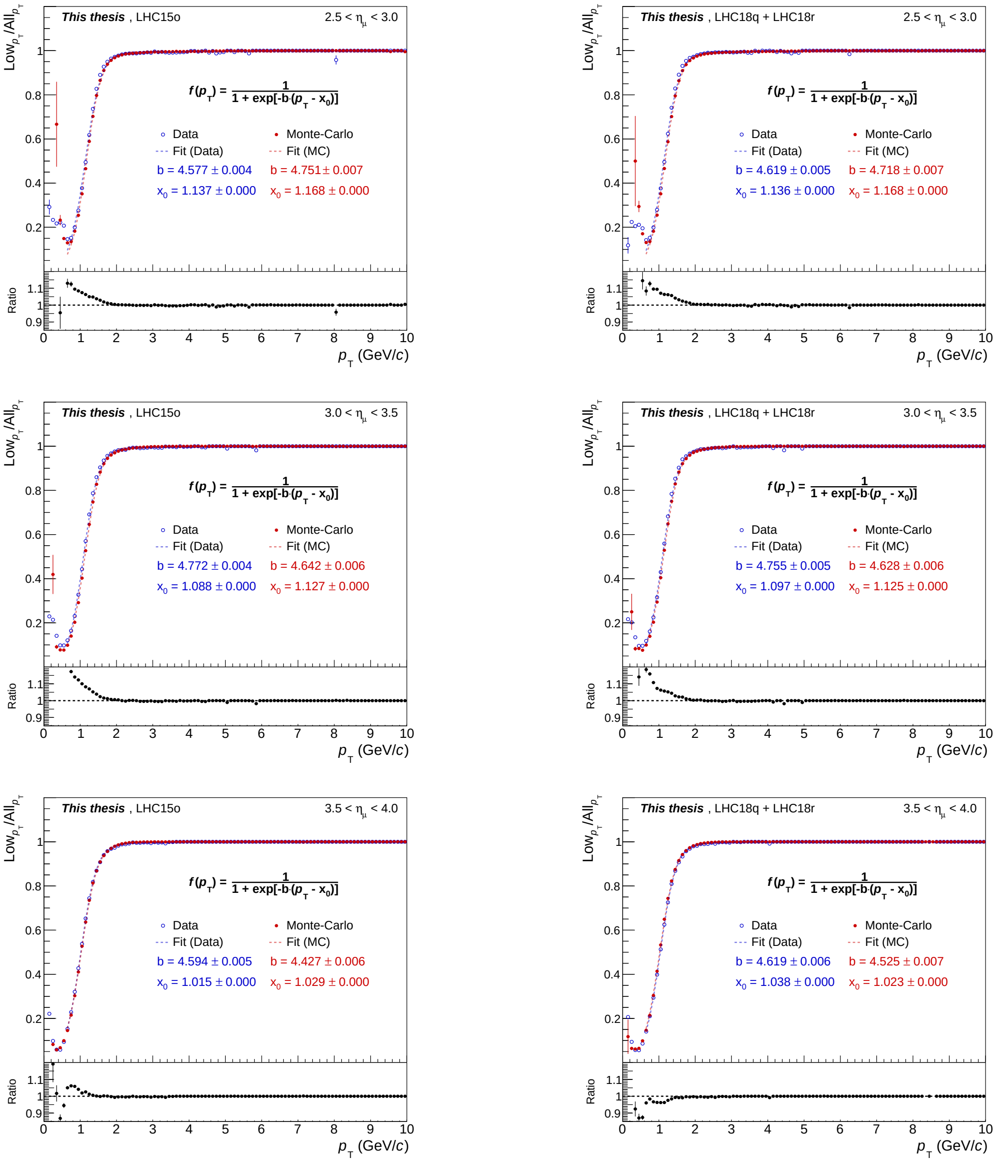

Figure 5.21: Trigger response functions as function of p_T in 3 pseudorapidity bins: $2.5 < \eta < 3.0$, $3.0 < \eta < 3.5$ and $3.5 < \eta < 4.0$. On the left side plots refers to the LHC15o period, while on the right to LCH18q + LHC18r. In the top part of each plot the trigger response function from data (blue) and Monte Carlo (red) are shown, while in the bottom part the ratio is reported.

In Fig. 5.22 the polarization parameters are shown before and after the Monte Carlo re-weighting. As expected the effect is larger in the low-p_{T} range, since for muons corresponding to that region the difference between data and simulation is larger. The systematic is evaluated as the half-difference of the two results and it is found to range between ∼0.001 and ∼0.043.

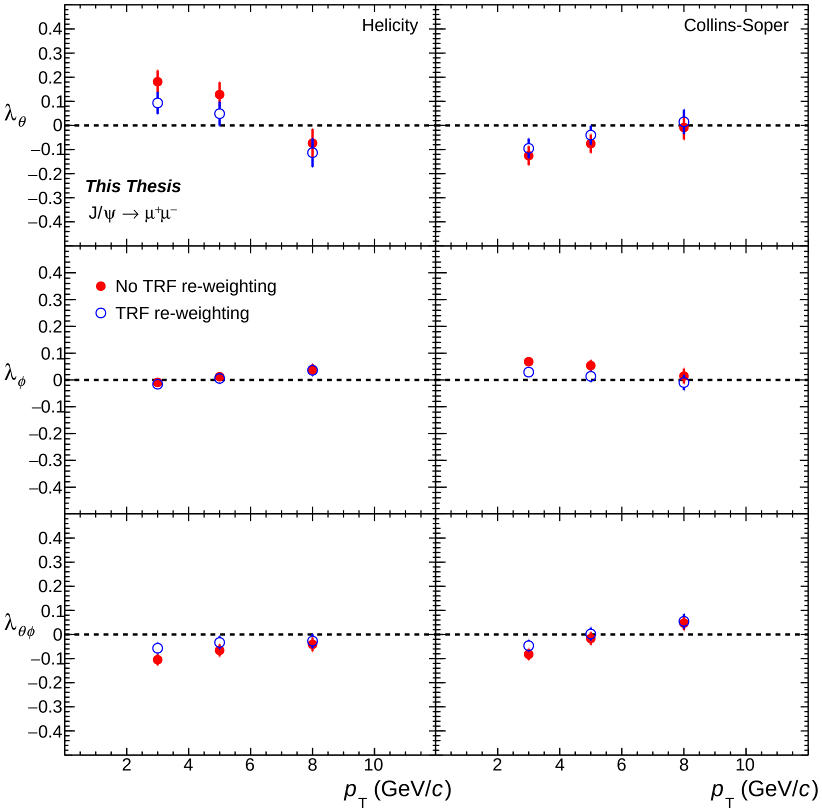

Figure 5.22: Comparison between λ_θ, λ_ϕ and $\lambda_{\theta\phi}$ with and without the $A \times \epsilon$ re-weighting (respectively orange/light blue and red/blue points).

5.6.3 Systematic uncertainty due to input Monte Carlo shapes

In the Monte Carlo simulation J/ψ are generated unpolarized, even if polarization parameters different from zero can be measured. This choice can lead to systematic effects especially when the binning adopted is wide. In order to evaluate this effect an iterative procedure is performed. In the first step the original Monte Carlo production (J/ψ unpolarized) is used to obtain a first estimation of the polarization parameters ("*1st iteration*"). The values of λ_θ, λ_ϕ and $\lambda_{\theta\phi}$ obtained in this first step are then used in a new Monte Carlo production where J/ψ are generated with the polarization extracted from the first step. The resulting $A \times \varepsilon$ is used to correct again the J/ψ raw yield and to estimate a new set of polarization parameters ("*2nd iteration*"). The procedure is repeated until the result of an iteration does not differ significantly from the previous one.

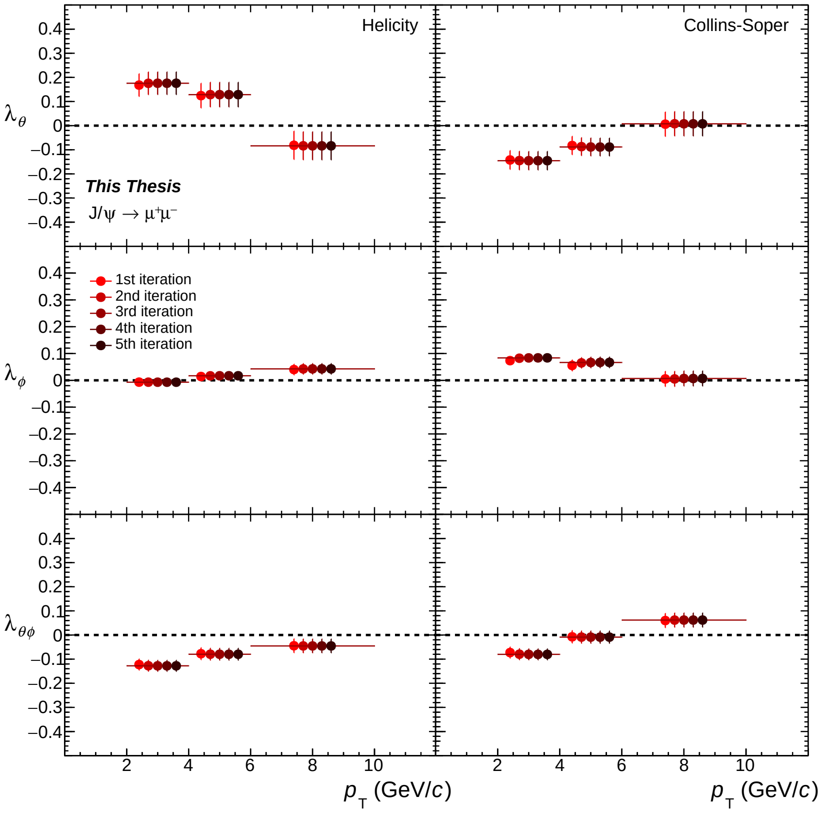

Figure 5.23: Comparison of polarization parameters as a function of p_{T} for different iteration steps.

In the analysis of J/ψ polarization as a function of p_{T} five iterations are performed, as shown in Fig. 5.23, and the effect is found to be negligible, also because the extracted polarization parameters are small. The same procedure is performed in the analysis as a function of centrality and also in this case there is a little difference between the various iterations.

Another effect which is taken into account is related to the p_{T} and y input shapes used in the Monte Carlo. As already mentioned the J/ψ are generated according to Eq. 5.16 and 5.17, which are tuned on the corresponding spectra measured in Pb–Pb collisions. The presence of a systematic effect is evaluated varying of the shape according to the statistical uncertainty observed in the data ($\pm\Delta(p_{\mathrm{T}})$ and $\pm\Delta(y)$). In Fig. 5.24 the p_{T} and y input distributions are shown, comparing the default one with two alternative shapes. The acceptance-times-efficiencies obtained in this way are used to correct the Monte Carlo distribution of reconstructed events, which is then fitted with $W(\cos\theta, \varphi)$. In fact, since in the pure simulation J/ψ are generated flat as a function of the angular variables, the presence of a systematic effect related to the different input shapes should determine a deviation from the default polarization ($\lambda_\theta, \lambda_\phi, \lambda_{\theta\phi} = 0$). Moreover, the use of the Monte Carlo instead of the data should limit the impact the statistical uncertainties in the fit to extract the polarization parameters.

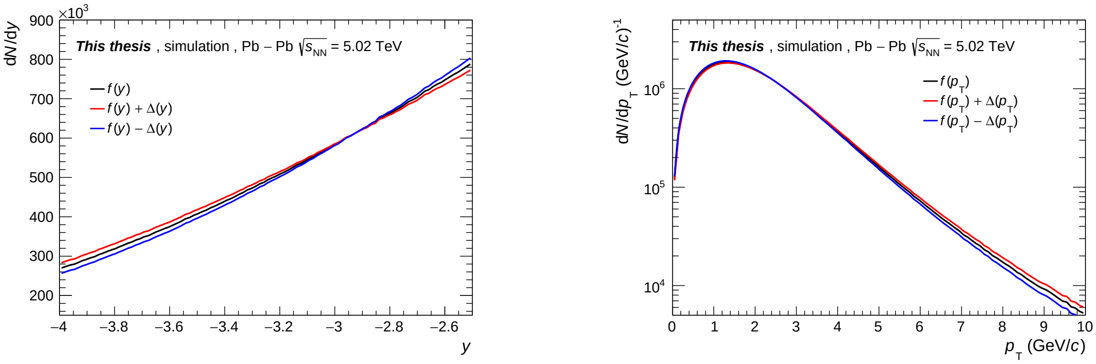

Figure 5.24: Comparison between the J/ψ y and p_{T} Monte Carlo distributions obtained varying the original shape (black points) inside the experimental uncertainties.

In Fig. 5.25 the comparison between the polarization parameters obtained with the different sets of p_{T} and y distributions is shown. It can be noticed that with the default shapes the polarization parameters are all compatible with zero, while with the alternative ones small deviation are observed especially for λ_θ. The maximum difference is adopted as systematic uncertainty and it is found to range among ∼0.001 and ∼0.03.

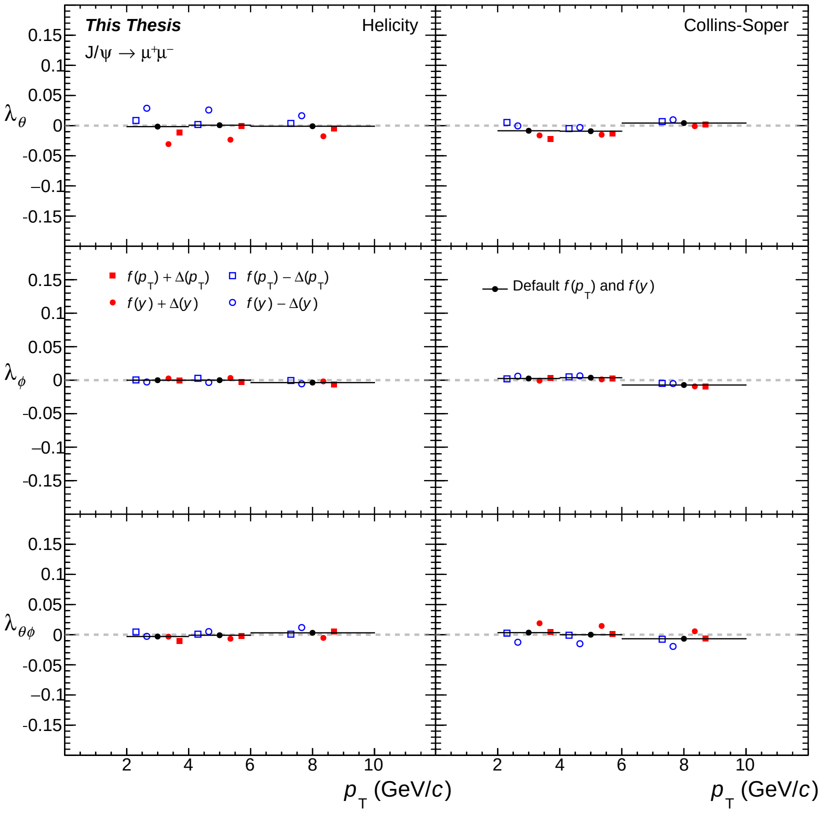

Figure 5.25: Comparison between the three polarization parameters obtained using the alternative and the default p_{T} and y distributions in the Monte Carlo generation.

5.6.4 Systematic uncertainty due to the choice of the 1D–2D method

A further source of systematic uncertainty could be represented by the choice of the method adopted in the extraction of the polarization parameters. As detailed previously, in the centrality-dependent analysis λ_θ, λ_ϕ and $\lambda_{\theta\phi}$ are extracted following the one-dimension approach, while as a function of p_{T} the two-dimension one is chosen. The latter is in principle less subject to biases, because it allows to extract the polarization parameters in one shot. In addition the 1D procedure is more sensitive to the input shapes provided in the Monte Carlo. For the centrality analysis, where the 2D approach is not feasible, it was decided to include a further systematic uncertainty, calculated as the half-difference between the result integrated over centrality (0–90%) obtained with the 1D approach and the weighted average[2] of the results as a function of p_{T}, evaluated with the 2D procedure in the range $2 < p_{\mathrm{T}} < 6$ GeV/c. In Fig. 5.26 the comparison between the results in $2 < p_{\mathrm{T}} < 6$ GeV/c is shown. The systematic is found to vary between ∼0.01 and ∼0.05.

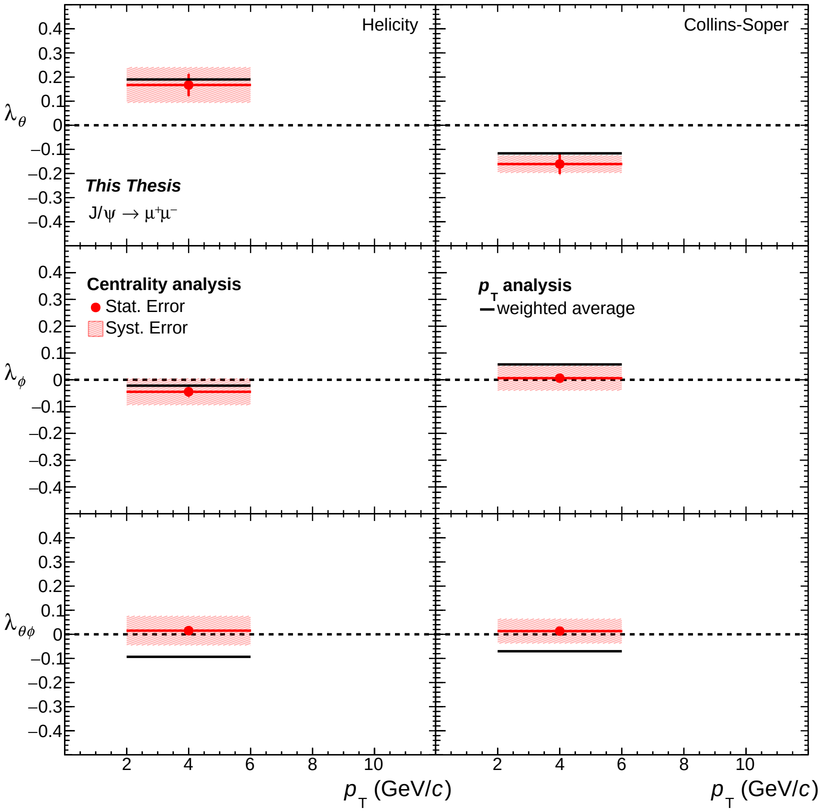

Figure 5.26: Comparison between the polarization parameters integrated over centrality (0-90%, red box) and the weighted average of the results in $2 < p_{\mathrm{T}} < 6$ GeV/c (black line). The red box include the systematic uncertainty on the difference among 1D and 2D methods.

---

[2] the weight is represented by the sum in quadrature of statistical and systematic uncertainties

5.6.5 Summary of the systematics

The summary of the main systematic uncertainties is reported in Tables 5.6 and 5.7 .

		Helicity			Collins-Soper		
Source	p_{T}(GeV/c)	[2–4]	[4–6]	[6–10]	[2–4]	[4–6]	[6–10]
Signal	λ_θ	0.070	0.049	0.039	0.055	0.052	0.022
	λ_ϕ	0.031	0.035	0.009	0.026	0.010	0.014
	$\lambda_{\theta\phi}$	0.036	0.013	0.028	0.016	0.042	0.043
Trigger	λ_θ	0.043	0.040	0.018	0.015	0.018	0.011
	λ_ϕ	0.004	0.003	0.001	0.020	0.020	0.011
	$\lambda_{\theta\phi}$	0.024	0.017	0.007	0.017	0.010	0.003
Input MC	λ_θ	0.030	0.024	0.017	0.009	0.007	0.006
	λ_ϕ	0.002	0.003	0.002	0.003	0.003	0.002
	$\lambda_{\theta\phi}$	0.001	0.006	0.008	0.015	0.015	0.013

Table 5.6: Systematic uncertainties on λ_θ, λ_ϕ and $\lambda_{\theta\phi}$ as a function of p_{T}.

		Helicity				Collins-Soper			
Source	(%)	[0–20]	[20–40]	[40–60]	[60–90]	[0–20]	[20–40]	[40–60]	[60–90]
Signal	λ_θ	0.050	0.065	0.033	0.076	0.036	0.014	0.031	0.015
	λ_ϕ	0.044	0.069	0.024	0.006	0.031	0.033	0.009	0.013
	$\lambda_{\theta\phi}$	0.010	0.014	0.007	0.035	0.019	0.019	0.010	0.022
Trigger	λ_θ	0.043	0.043	0.043	0.043	0.015	0.015	0.015	0.015
	λ_ϕ	0.004	0.004	0.004	0.004	0.020	0.020	0.020	0.020
	$\lambda_{\theta\phi}$	0.024	0.024	0.024	0.024	0.017	0.017	0.017	0.017
Input MC	λ_θ	0.030	0.030	0.030	0.030	0.009	0.009	0.009	0.009
	λ_ϕ	0.002	0.002	0.002	0.002	0.003	0.003	0.003	0.003
	$\lambda_{\theta\phi}$	0.001	0.001	0.001	0.001	0.015	0.015	0.015	0.015
2D–1D	λ_θ	0.011	0.011	0.011	0.011	0.022	0.022	0.022	0.022
	λ_ϕ	0.011	0.011	0.011	0.011	0.026	0.026	0.026	0.026
	$\lambda_{\theta\phi}$	0.054	0.054	0.054	0.054	0.042	0.042	0.042	0.042

Table 5.7: Systematic uncertainties on λ_θ, λ_ϕ and $\lambda_{\theta\phi}$ as a function of centrality.

5.7 Results

In this section the J/ψ polarization parameters as function of transverse momentum and collision centrality will be discussed.

5.7.1 Polarization parameters as a function of p_{T}

The J/ψ polarization parameters have been obtained in three transverse momentum bins, from 2 to 10 GeV/c, adopting the 2D approach. The results are shown in Fig. 5.27, while the corresponding numerical values are reported in Table 5.8. The central values and the statistical uncertainties are computed averaging the polarization parameters estimated with different choices of signal and background functions in the raw yield extraction, fixing or keeping free the J/ψ width. The systematic uncertainty is the sum in quadrature of the contributions from the signal extraction, trigger efficiency and Monte Carlo input distributions. For all the p_{T} intervals and in both reference frames the values of the polarization parameters exhibit at most slight deviations from zero. In particular, $\lambda_\theta^{\mathrm{HE}}$ indicates a slight transverse polarization at low p_{T} ($\sim 2.1\sigma$ effect, calculated using the Gaussian approximation), while $\lambda_\theta^{\mathrm{CS}}$ shows a weak longitudinal polarization ($\sim 2.1\sigma$). When increasing p_{T}, the central values of λ_θ become closer to zero. All values of λ_ϕ and $\lambda_{\theta\phi}$ are, in absolute value, smaller than 0.1, except for $\lambda_{\theta\phi}^{\mathrm{HE}}$, which is -0.124 at low p_{T} and deviates from zero by $\sim 2.4\sigma$.

	p_{T} (GeV/c)	Helicity	Collins-Soper
λ_θ	$2 < p_{\mathrm{T}} < 4$	0.218 ± 0.060 ± 0.087	-0.157 ± 0.049 ± 0.058
	$4 < p_{\mathrm{T}} < 6$	0.151 ± 0.071 ± 0.068	-0.057 ± 0.059 ± 0.055
	$6 < p_{\mathrm{T}} < 10$	-0.070 ± 0.068 ± 0.047	-0.008 ± 0.063 ± 0.026
λ_ϕ	$2 < p_{\mathrm{T}} < 4$	-0.029 ± 0.017 ± 0.031	0.061 ± 0.015 ± 0.033
	$4 < p_{\mathrm{T}} < 6$	-0.013 ± 0.019 ± 0.036	0.047 ± 0.024 ± 0.023
	$6 < p_{\mathrm{T}} < 10$	0.047 ± 0.021 ± 0.010	0.024 ± 0.032 ± 0.018
$\lambda_{\theta\phi}$	$2 < p_{\mathrm{T}} < 4$	-0.124 ± 0.028 ± 0.043	-0.090 ± 0.027 ± 0.029
	$4 < p_{\mathrm{T}} < 6$	-0.059 ± 0.030 ± 0.021	-0.040 ± 0.034 ± 0.046
	$6 < p_{\mathrm{T}} < 10$	-0.025 ± 0.031 ± 0.030	0.018 ± 0.035 ± 0.044

Table 5.8: J/ψ polarization parameters, measured as a function of p_{T} for Pb–Pb collisions at $\sqrt{s_{\mathrm{NN}}} = 5.02$ TeV. The first uncertainty is statistical and the second systematic.

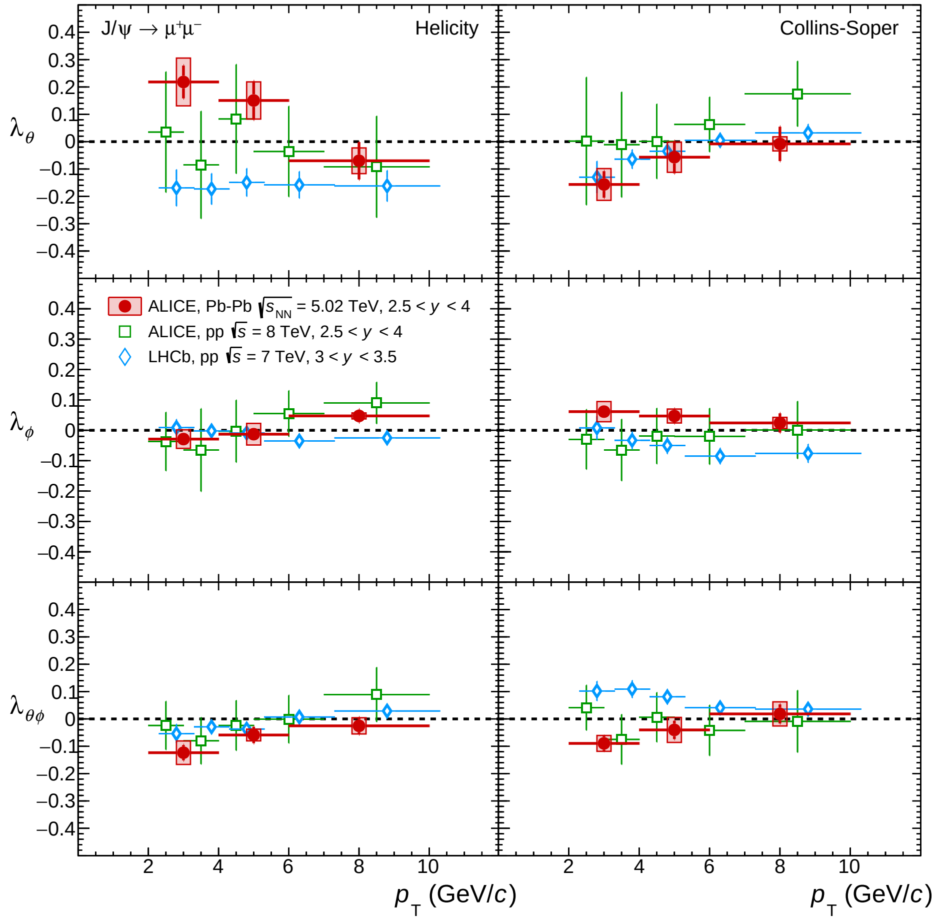

Figure 5.27: Inclusive J/ψ polarization parameters as a function of transverse momentum for Pb–Pb collisions at $\sqrt{s_{\rm NN}} = 5.02$ TeV [1], compared with results obtained in pp collisions by ALICE at $\sqrt{s} = 8$ TeV [196] and by LHCb for prompt J/ψ at $\sqrt{s} = 7$ TeV [159] (the LHCb markers were shifted horizontally by $+0.3$ GeV/c for better visibility) in the rapidity interval $3 < y < 3.5$. The error bars represent the total uncertainties for the pp results, while for Pb–Pb statistical and systematic uncertainties are plotted separately as a vertical bar and a shaded box, respectively. In the left part of the plot the polarization parameters in the helicity reference frame are reported, in the right those for the Collins-Soper frame.

In Fig. 5.27 the results are compared with those obtained in pp collisions by the ALICE and the LHCb collaborations. No significant difference is found with respect to ALICE results at $\sqrt{s} = 8$ TeV, which are compatible with zero, while significant difference is found with respect to the higher-precision LHCb results at $\sqrt{s} = 7$ TeV. For the latter a deviation of 3.3σ is observed for $2 < p_{\mathrm{T}} < 4$ GeV/c in the helicity reference frame, where pp data [159] indicate a small but significant degree of longitudinal polarization, while the Pb–Pb results favor a slightly transverse polarization. It should be noted that ALICE results refer to the inclusive production, while LHCb measured prompt J/ψ. In principle the polarization parameters could be modified if the J/ψ from B-hadron decays are included in the analyzed sample. Nevertheless, the CDF collaboration measured a small polarization value for non-prompt J/ψ in $p\bar{p}$ collisions ($\lambda_{\theta}^{\mathrm{HE}} \sim -0.1$ [144]), in agreement with expectations of a highly diluted polarization when the quantization axis is the J/ψ and not the B-hadron momentum. In addition, it should be considered that the fraction of non-prompt J/ψ in the studied p_{T} region is not dominant (∼15%, measured by the LHCb collaboration [95]), therefore the final contribution to the inclusive polarization is expected to be relatively small, as detailed in Ref. [157].

The difference among Pb–Pb and pp results might originate from the different production and suppression mechanisms in the two systems. First of all, at the LHC it was observed that a large fraction of the detected J/ψ is produced in the recombination of uncorrelated $c\bar{c}$ in the QGP. On the other hand the larger suppression of less-bound quarkonium states (ψ(2S), χ_{c}) could modify the feed down fractions, resulting in a modification of the measured polarization.

In order to check the consistency of the results in the helicity and Collins-Soper reference frames, the frame invariant parameter:

$$\tilde{\lambda} = \frac{\lambda_{\theta} + 3\lambda_{\phi}}{1 - \lambda_{\phi}}, \tag{5.22}$$

is calculated. As shown in Fig. 5.28, the two sets of results are compatible within the uncertainties, which include both the statistical and the systematic contributions. The observed good agreement indicates that no strong bias is present in the analysis, also taking into account that some uncertainties may be correlated between helicity and Collins-Soper.

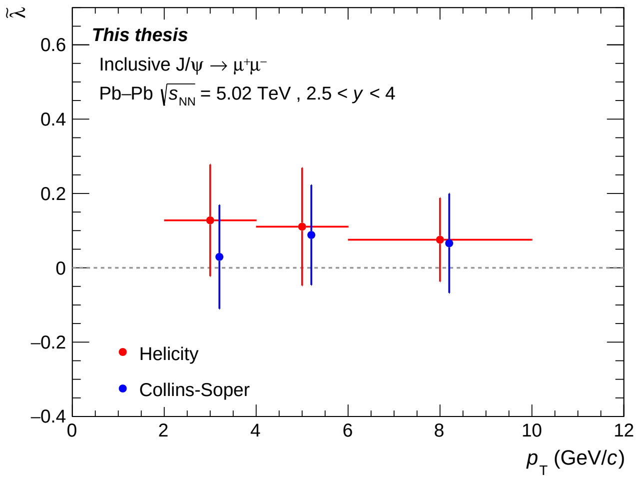

Figure 5.28: The frame invariant parameter $\tilde{\lambda}$ as a function of $p_{\rm T}$ in the helicity and in the Collins-Soper reference frames. The error bar include the contributions of the systematic and statistical uncertainties.

5.7.2 Polarization parameters as a function of centrality

The J/ψ polarization parameters have been evaluated in four centrality classes, covering the interval 0–90%. The results are shown in Fig. 5.29, while the numerical values are reported in Table 5.9.

Analogously to the analysis as a function of the transverse momentum, the central value is the average of the results obtained fixing or keeping free the J/ψ width, changing the signal and background functions. The systematic uncertainty is plotted separating the uncorrelated (signal extraction) from the centrality correlated uncertainties (trigger efficiency, input Monte Carlo shapes, difference between 1D and 2D methods). The λ_θ parameter exhibits a slight transverse and longitudinal polarization in the helicity and Collins-Soper reference frames respectively, with a maximum deviation lower than 2σ. This result is in qualitative agreement with the measurement as a function of $p_{\rm T}$, where the same behavior has been observed in the two reference systems. In particular this was verified comparing the results as a function of centrality and the average, weighted with the statistical and systematic uncertainties, of the results of the transverse momentum analysis in $2 < p_{\rm T} < 6$ GeV/c. The other two parameters, λ_ϕ and $\lambda_{\theta\phi}$, are compatible with zero within the uncertainties, with a maximum 1.7σ deviation for $\lambda_{\theta\phi}$ in the Collins-Soper reference frame. For all the polarization parameters no evident dependence as a function of centrality is observed.

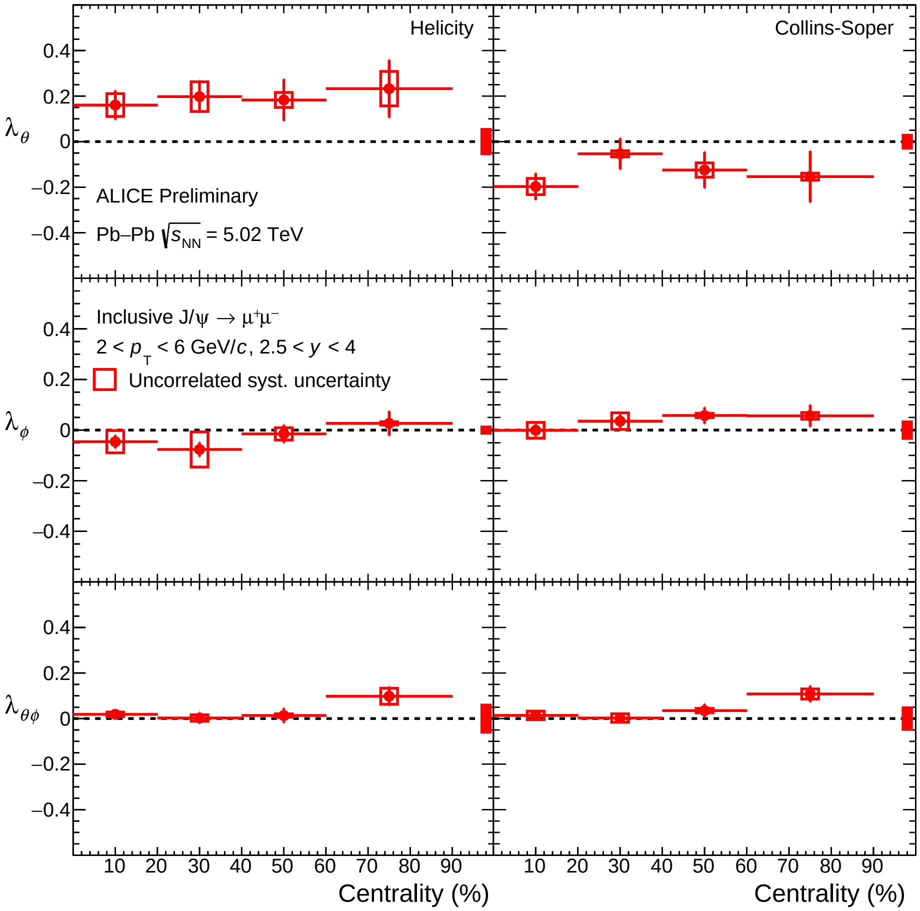

Figure 5.29: Inclusive J/ψ polarization parameters as a function of centrality for Pb–Pb collisions at $\sqrt{s_{\mathrm{NN}}} = 5.02$ TeV. The statistical and uncorrelated systematic uncertainties are plotted separately as a vertical bar and a empty box, while the correlated systematic is plotted as red box around zero.

	centrality (%)	Helicity	Collins-Soper
λ_θ	0–20	0.161 ± 0.064 ± 0.074	-0.197 ± 0.059 ± 0.045
	20–40	0.198 ± 0.069 ± 0.085	-0.053 ± 0.068 ± 0.031
	40–60	0.183 ± 0.092 ± 0.063	-0.125 ± 0.080 ± 0.042
	60–90	0.233 ± 0.127 ± 0.093	-0.154 ± 0.113 ± 0.032
λ_ϕ	0–20	-0.046 ± 0.026 ± 0.046	-0.001 ± 0.024 ± 0.045
	20–40	-0.077 ± 0.028 ± 0.070	0.035 ± 0.026 ± 0.046
	40–60	-0.015 ± 0.036 ± 0.027	0.058 ± 0.032 ± 0.034
	60–90	0.027 ± 0.048 ± 0.014	0.056 ± 0.043 ± 0.035
$\lambda_{\theta\phi}$	0–20	0.019 ± 0.021 ± 0.060	0.014 ± 0.018 ± 0.051
	20–40	0.003 ± 0.025 ± 0.061	0.003 ± 0.023 ± 0.051
	40–60	0.014 ± 0.032 ± 0.060	0.035 ± 0.029 ± 0.049
	60–90	0.098 ± 0.041 ± 0.069	0.108 ± 0.036 ± 0.052

Table 5.9: J/ψ polarization parameters, measured as a function of centrality in Pb–Pb collisions at $\sqrt{s_{\rm NN}} = 5.02$ TeV. The first uncertainty is statistical and the second systematic.

Finally the frame invariant parameter $\tilde{\lambda}$ is calculated and shown in Fig. 5.30. Also in this case the results obtained for the helicity and Collins-Soper reference frames are compatible within the uncertainties, which include the the statistical and systematic contributions.

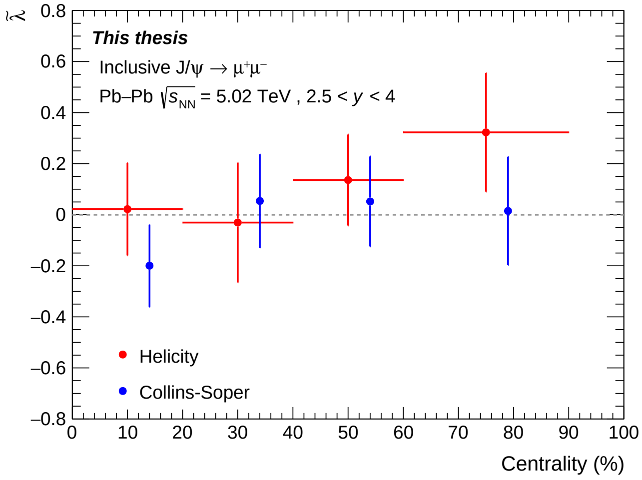

Figure 5.30: $\tilde{\lambda}$ parameter as a function of the centrality in the helicity and in the Collins-Soper reference frames. The error bar includes systematic and statistical uncertainties.

5.8 J/ψ polarization and magnetic field: perspectives

As anticipated in Section 3.3.1, the spin alignment of the J/ψ could be sensitive to the formation of a large magnetic field in the early phase of the heavy-ion collision. It can be induced by spectator protons and even if rapidly decreasing in time, may have an influence on the measured polarization, since the time scale associated to the charm quark production ($\tau_{\mathrm{c-Prod}} \lesssim \hbar/m_{\mathrm{c}} \sim 0.1$ fm/c) is consistent with the maximum value reached by the magnetic field ($\tau_{\vec{B}} \lesssim 0.5$ fm/c) [167]. Albeit it is still matter of discussion if the spin orientation occurs at a partonic level and then is transferred to the bound state, or directly to the J/ψ , this study can be approached with a similar strategy to the one followed by standard polarization analyses.

First of all it is necessary to define an appropriate reference system with respect to which the angular variables are measured. In this case the quantization axis is chosen as the magnetic field direction, which is perpendicular by definition to the reaction plane of the collision, as shown in Fig. 5.31. The reaction plane angle in the laboratory can be estimated by the second harmonic event plane angle Ψ [200], which is evaluated using the azimuthal distribution of reconstructed tracklets in the Silicon Pixel Detector or of signals in the V0 detector.

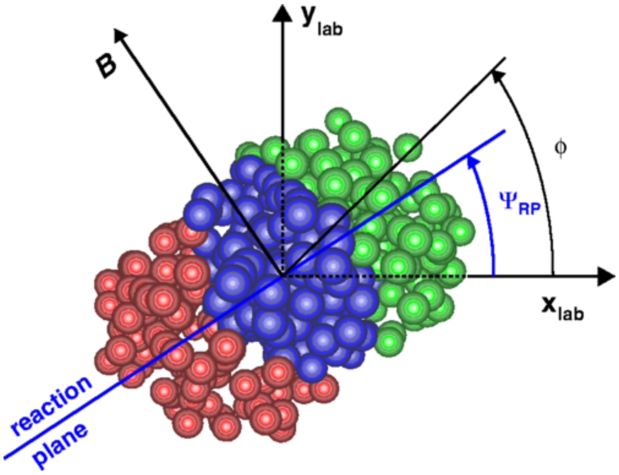

Figure 5.31: Picture representing a schematic of a heavy-ion collision.

To assess the feasibility of such a study and have an idea of the corresponding uncertainties and of possible biases, the event plane of the collision is randomly extracted in the range $-\pi/2 < \Psi < \pi/2$ (*Random Plane*). Since the event plane is completely randomized, no-spin alignment with respect to magnetic field direction should be observed. This preliminary analysis was carried out with a different approach with respect to those used in the thesis work, by directly correcting the invariant mass distribution with a multidimensional $A \times \varepsilon$ map. This method has the advantage to be relatively insensitive to the input shapes used in the Monte Carlo simulation, once its acceptance-times-efficiency binning is sufficiently narrow. In the left panel of Fig. 5.32 an example of the correction map is shown as a function of $\cos\theta$ and p_{T}. The acceptance-times-efficiency is evaluated for each cell and then applied as a weight (w) to each dimuon:

$$w(\cos\theta, p_{\mathrm{T}}) = (A \times \varepsilon(\cos\theta, p_{\mathrm{T}}))^{-1} \tag{5.23}$$

Subsequently a closure test was performed on a Monte Carlo sample. In particular the generated J/ψ distribution as a function of $\cos\theta$ is compared with the reconstructed one after the application of the dimuon-per-dimuon re-weighting. As shown in the right panel of Fig. 5.32, the fair agreement among the two results confirms the goodness of the method and also that, in first approximation, taking into account only the $\cos\theta$ and p_{T} dependence of $A \times \varepsilon$ should be sufficient to perform a satisfactory correction.

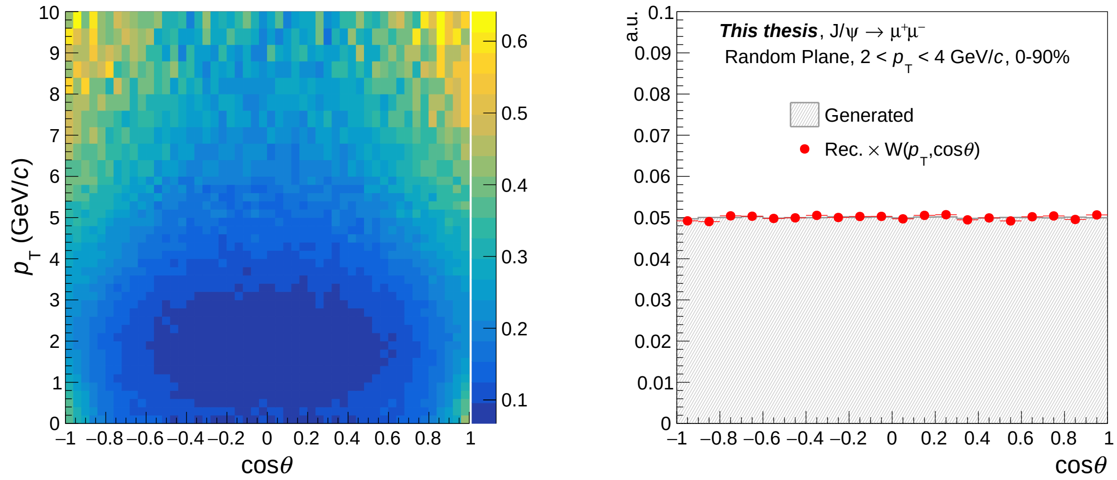

Figure 5.32: Left panel: $A \times \varepsilon$ map as a function of $\cos\theta$ and p_{T} in the RP reference frame. Right panel: normalized $\cos\theta$ distributions for generated J/ψ compared with the distribution of reconstructed J/ψ after the application of the two-dimensions re-weighting.

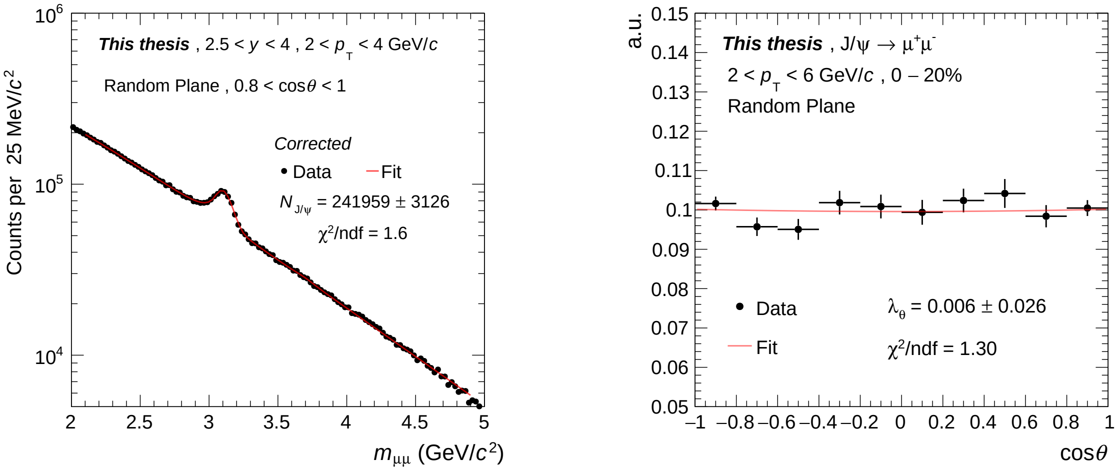

Figure 5.33: Left panel: fits to the raw and $A \times \varepsilon$-corrected invariant mass spectra. The distribution corresponds to $2 < p_{\mathrm{T}} < 4$ GeV/c and $0.8 < \cos\theta < 1$. Right panel: fits to the J/ψ corrected distribution for $2 < p_{\mathrm{T}} < 4$ GeV/c and 0–20%.

After this preliminary check, the re-weighting procedure is performed on real data. In particular the weight $w(\cos\theta, p_{\mathrm{T}})$ is applied to each dimuon satisfying the selection cuts described in Section 5.2 and then used to build the invariant mass distribution from which the J/ψ corrected yield can be directly extracted. In the left panel of Fig. 5.33 the corrected invariant mass distribution is shown.

In the right panel of Fig. 5.33 an example of the fit to the corrected $\cos\theta$ distributions is shown for $2 < p_{\mathrm{T}} < 6$ GeV/c in the centrality class 0–20%. The fit is performed with $W(\cos\theta)$ and it can be observed that the λ_θ parameters are compatible with zero, as expected due to the choice of the random plane. The λ_θ parameter is also extracted in four different centrality classes, 0–20, 20–40, 40–60 and 60–90%, and shown in Fig. 5.34. The central values, the statistical and systematic uncertainties are evaluated considering various tests for the signal extraction procedure, as detailed in Section 5.7. All λ_θ values are again compatible with zero. This observation is in agreement with expectations for J/ψ polarization measured with respect to a random plane and shows the absence of significant bias in the procedure.

In conclusion, the study presented here shows the feasibility of the J/ψ polarization analysis with respect to a random plane. The procedure will be applied to the experimentally determined event plane. As anticipated, such a study will allow to investigate the J/ψ spin alignment with respect to the intense magnetic field generated in heavy-ion collisions. This study, together with the recently published results on the spin alignment of K^{*0} and ϕ mesons [175], the D-mesons Δv_1 [172] and the measurements of global Λ polarization [201], could provide a further contribution to this field of research, expanding our knowledge of the complex mechanisms present in heavy-ion collisions.

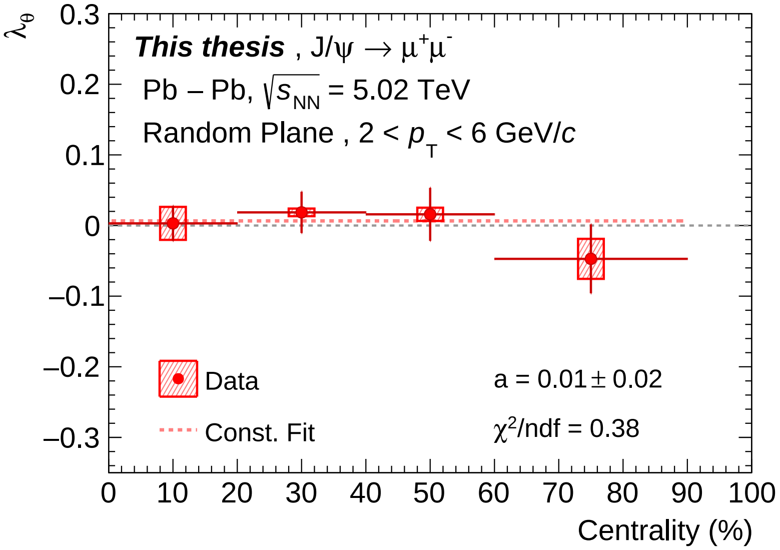

Figure 5.34: λ_θ parameter obtained with dimuon-per-dimuon correction method as a function of centrality in $2 < p_\mathrm{T} < 6$ GeV/c. The the statistical and systematic uncertainties on signal extraction are shown as a error bar and colored box respectively. The result is then fitted with a constant function.

Chapter 6

Υ(1S) polarization in Pb-Pb collisions

The investigation of bottomonium polarization in hadronic collisions was carried out by many experiments, given the theoretical interest in finding a comprehensive description of quarkonium production. The unclear situation after the inconsistent results from CDF [202] and D0 [203] at Tevatron in $p\bar{p}$ collisions, pushed the interest on the new measurements at the LHC. The CMS and LHCb collaborations studied Υ(1S), Υ(2S) and Υ(3S) polarization in pp collisions for $10 < p_{\mathrm{T}} < 50$ GeV/c [162] and $p_{\mathrm{T}} < 30$ GeV/c [163] respectively and they did not observe any significant deviation with respect to zero. These results are in agreement with the NLO NRQCD calculations [204], with the exception of the Υ(3S), for which a large transverse polarization was expected at high-p_{T}.
Analogously to J/ψ, no measurement of Υ(1S) polarization in heavy-ion collisions has been attempted until now at the LHC. The full Run 2 data sample has provided for the first time the possibility to perform this measurement, although with a limited statistical precision.

In this chapter the inclusive Υ(1S) polarization measurement in Pb–Pb collisions carried out with ALICE data is presented. The analysis is performed using the Pb–Pb data sample collected in 2015 and 2018 at the center-of-mass energy $\sqrt{s_{\mathrm{NN}}} = 5.02$ TeV in the rapidity region covered by the muon spectrometer ($2.5 < y < 4$). The results, provided for $p_{\mathrm{T}} < 15$ GeV/c, are reported in the paper "*First measurement of quarkonium polarization in nuclear collisions at the LHC*" [1].

6.1 Data sample and event selection

The analysis strategy used for the extraction of Υ(1S) polarization parameters follows the steps described in Section 5.1. The data sample, collected in 2015 and 2018, is the one used for the J/ψ polarization analysis and is characterized by a total integrated luminosity of $\sim 750\mu\text{b}^{-1}$.
The dimuon sample for the Υ(1S) analysis is obtained applying a series of cuts at the single track level (for more details see Section 5.2):

- single muon pseudorapidity in the range $-4 < \eta_{\mu} < -2.5$
- radial transverse position of the muon tracks at the end of the absorber in the range $17.6 < R_{abs} < 89.5$ cm
- both muon tracks reconstructed in the tracking chambers should match a trigger track reconstructed in the trigger system, above the low p_{T} trigger threshold ($p_{\mathrm{T}} \geqslant 1$ GeV/c)
- pDCA cut applied to remove tracks not pointing to the interaction vertex
- single muon $p_{\mathrm{T}} > 2$ GeV/c. This cut, already applied in other Υ(1S) analyses [205], is found to remove part of the background without reducing significantly the number of resonances. In addition, this cut is also relevant for the evaluation of the systematic uncertainty related to the trigger efficiency, since the exclusion of muons with $p_{\mathrm{T}} < 2$ GeV/c removes the region where the muon trigger is not fully efficient and where there is a discrepancy between the trigger response functions in data and Monte Carlo (see Section 5.6.2).

A further cut on each dimuon candidate is applied:

- dimuon in the mass window $6.5 < m_{\mu\mu} < 13$ GeV/c^2
- dimuon rapidity in the range $2.5 < y_{\mu\mu} < 4$
- total dimuon charge equal to zero

As in the J/ψ analysis the events are selected in the centrality range 0–90%.

6.2 Signal extraction

The extraction of the Υ(1S) raw yield is performed via a fit to the opposite sign dimuon invariant mass spectrum. In particular two sets of functions are used to parametrized the signal and the background:

- signal: extended Crystal Ball (CB2) and NA60 function
- background: variable Width Gaussian (VWG) and a combination of a second-degree polynomial and an exponential function (Pol2.$\times$exp.)

Fitting the invariant mass spectrum for $p_{\mathrm{T}} < 15$ GeV/c and $2.5 < y < 4$, the overall number of Υ(1S) is found to be $\sim 3.4 \times 10^3$. The size of the sample suggests that the analysis cannot be performed following the two-dimension approach, therefore the one-dimension method is the only one feasible.

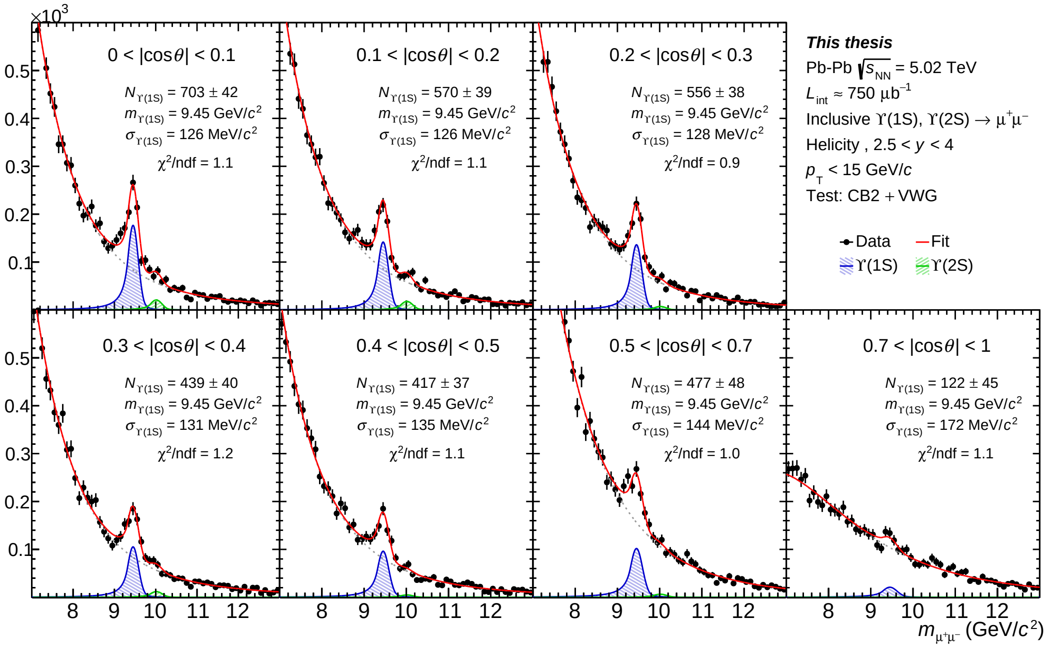

Figure 6.1: Fit to the $\mu^+\mu^-$ invariant mass distribution for dimuon $p_{\mathrm{T}} < 15$ GeV/c.

To maximize the available statistics, the analysis is performed in bins of $|\cos\theta|$, up to $|\cos\theta| = 1$. The sample is then splitted in 7 bins, whose widths become wider moving from $|\cos\theta| = 0$ to $|\cos\theta| = 1$, to cope with the acceptance-times-efficiency decrease. For ϕ and $\tilde{\phi}$, 5 bins of equal widths are defined in the ranges $0 < \phi < \pi$ and $0 < \tilde{\phi} < 2\pi$ respectively.

The Υ(1S) raw yield is extracted with a binned maximum likelihood fit in two different mass ranges, $6.5 < m_{\mu\mu} < 13$ and $7 < m_{\mu\mu} < 12.5$ GeV/c. For the J/ψ analysis, the evaluation of the polarization parameters is found to be insensitive to the choice of the fit range, nevertheless the small size of the Υ(1S) sample suggests to perform also this test for the yield extraction. In the fit to the Υ(1S) peak, the mass parameter is fixed to the one obtained from the integrated spectrum, since the likelihood minimization is observed to benefit form this choice. Analogously also the Υ(1S) width is fixed to the one extracted from Monte Carlo invariant mass distribution, applying a correction factor to take into account the difference on this parameter between data and simulation:

$$\sigma_{\Upsilon(1S)}(\cos\theta,\phi,\tilde{\phi}) = \sigma^{\mathrm{MC}}_{\Upsilon(1S)}(\cos\theta,\phi,\tilde{\phi}) \cdot (\sigma_{\Upsilon(1S)}/\sigma^{\mathrm{MC}}_{\Upsilon(1S)})\big|_{\mathrm{Integrated}} \tag{6.1}$$

The correction factor is calculated as the ratio between the width obtained by fitting invariant mass spectra in data and in the Monte Carlo, both integrated over p_{T} and centrality. The Υ(2S) is included in the fit adopting the same Υ(1S) shapes, while its mass and width parameters are bound to the Υ(1S) according to the equations:

$$m_{\Upsilon(2S)} = m^{\mathrm{FIT}}_{\Upsilon(1S)} + \Delta m^{\mathrm{PDG}} \tag{6.2}$$

$$\sigma_{\Upsilon(2S)} = \sigma^{\mathrm{FIT}}_{\Upsilon(1S)} \cdot \frac{\sigma^{\mathrm{MC}}_{\Upsilon(2S)}}{\sigma^{\mathrm{MC}}_{\Upsilon(1S)}} \tag{6.3}$$

where $m^{\mathrm{FIT}}_{\Upsilon(1S)}$ and $\sigma^{\mathrm{FIT}}_{\Upsilon(1S)}$ are the Υ(1S) mass and width obtained in the fit to the dimuon invariant mass spectrum, Δm^{PDG} corresponds to the difference in mass between Υ(2S) and Υ(1S) as reported by the Particle Data Group [5] ($\Delta m^{\mathrm{PDG}} = 10.023 - 9.460 = 0.563$ GeV/c^2) and $\sigma^{\mathrm{MC}}_{\Upsilon(2S)}/\sigma^{\mathrm{MC}}_{\Upsilon(1S)}$ is the ratio between the Υ(2S) and Υ(1S) widths as extracted from the Monte Carlo. Finally the signal tails are tuned on the Monte Carlo ones.

In Fig. 6.1 an example of the fit to the invariant mass spectrum for different $|\cos\theta|$ ranges is shown and it can be noticed that the number of Υ(1S) decreases rapidly of a factor ~ 7 moving to larger $|\cos\theta|$ values. In Fig. 6.2 the Υ(1S) raw yield normalized to the bin width is shown for all the angular variables in the helicity and Collins-Soper reference frames.

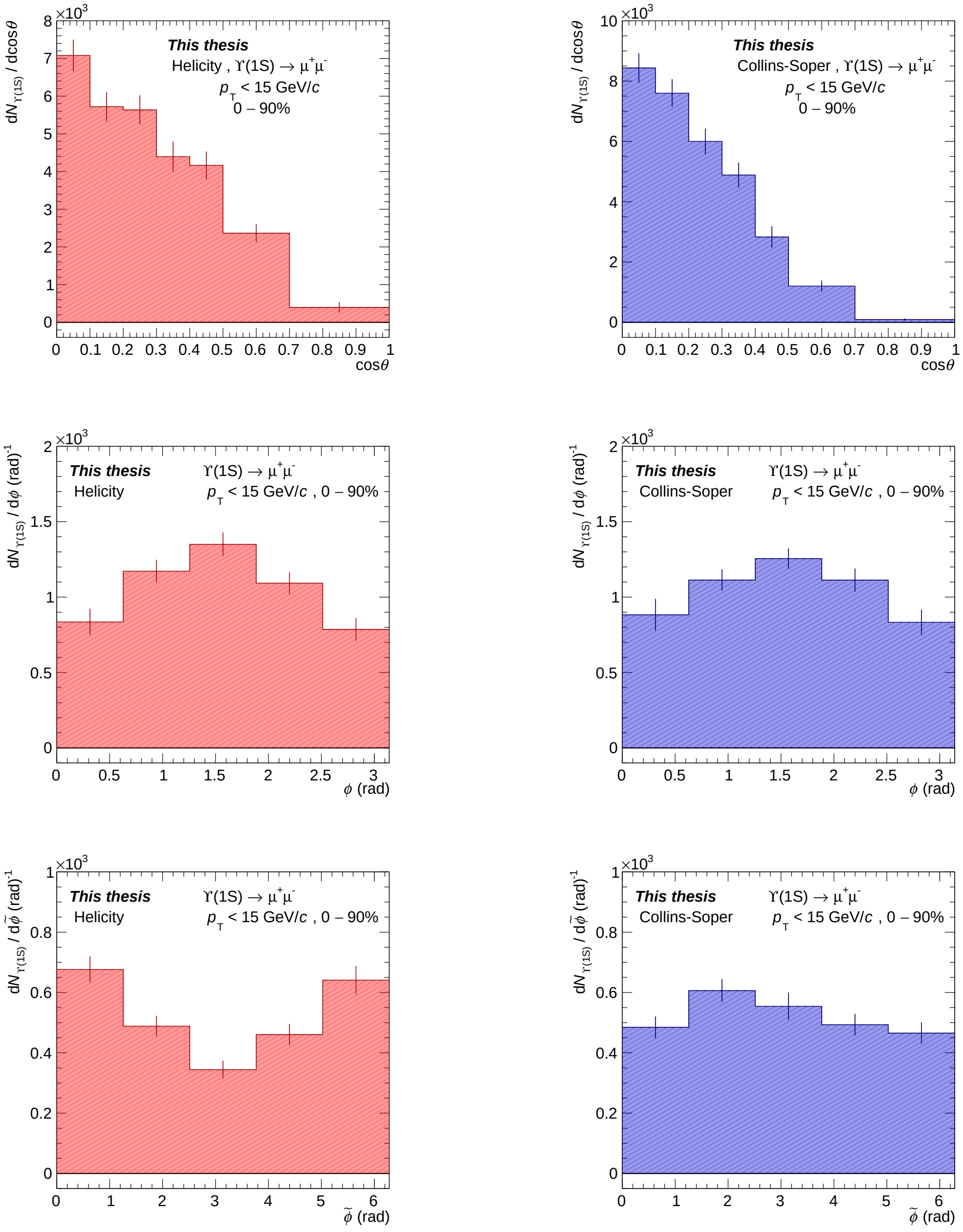

Figure 6.2: Υ(1S) raw yield normalized to the bin width as a function of $\cos\theta$, ϕ and $\tilde{\phi}$ (from top to bottom) in the helcity (left side) and Collins-Soper (right side) reference frames.

6.3 Acceptance-times-efficiency correction

The raw yield extracted from the fit to the invariant mass spectrum needs to be corrected to take into account the geometrical coverage and the performances of the experimental apparatus. This is achieved by means of the same Monte Carlo simulation performed for the J/ψ analysis as a function of the collisions centrality, namely the "embedding" (see Section 5.4.2) which includes a sample of generated ϒ(1S) . The p_{T} and y shapes are tuned on data at $\sqrt{s_{\mathrm{NN}}} = 5.02$ TeV and ϒ(1S) are unpolarized in the simulation.
Since in the Monte Carlo the run-by-run statistics is proportional to the number of minimum bias triggers (CINT7) while for data the dimuon trigger (CMUL7) is adopted, two sets of weights have to be applied:

- *minimum bias to dimuon trigger correction*: Monte Carlo events have to be weighted according to their real statistical weight in terms of CMUL7 triggers.
- *mean number of collisions correction*: Monte Carlo events are weighted according to the mean number of collisions, which allows to fairly reproduce the centrality dependence of the CMUL7 triggers.

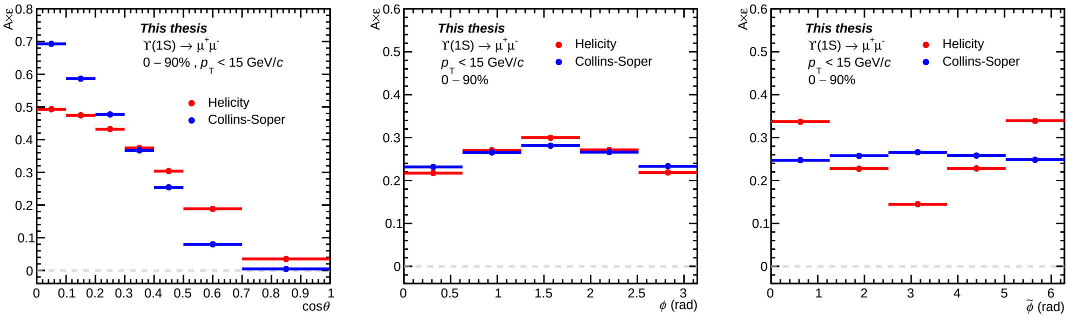

Figure 6.3: $A \times \epsilon$ in the helicity and Collins-Soper reference frame as a function of $\cos\theta$, φ and $\tilde{\varphi}$ for the p_{T} range $0 < p_{\mathrm{T}} < 15$ GeV/c.

Since the results is integrated over centrality (0–90%) no re-weighting is necessary to reproduce properly in the Monte Carlo the evolution of the p_{T} and y shapes as a function of this variable. In Fig. 6.3 the acceptance-times-efficiency is shown for $\cos\theta$, ϕ and $\tilde{\phi}$.

6.4 Polarization parameters extraction

The polarization parameters are extracted by means of the simultaneous fit to the three angular distribution via the χ^2 minimization method. The overall quality of the fits is satisfactory, with χ^2/ndf ranging around 1 for all the angular variables.
In Fig. 6.4 an example of the fit to the Υ(1S) corrected distributions is shown for all the angular variables, in the helicity and Collins-Soper reference frames.

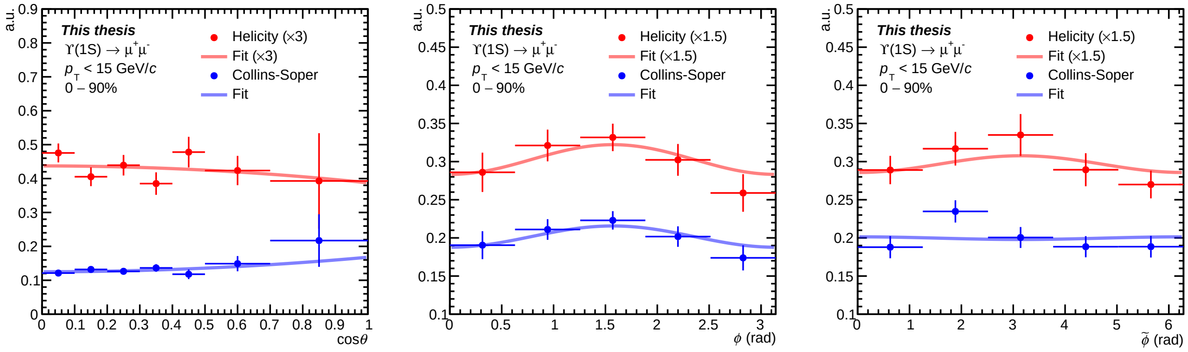

Figure 6.4: Example of fit to the corrected J/ψ distributions normalized to the integral as a function of $\cos\theta$, ϕ and $\tilde{\phi}$ in the helicity (red) and Collins-Soper(blue) reference frames. The helicity points and the correspondig fitting functions are scaled by a factor 3 ($\cos\theta$) and 1.5 (ϕ and $\tilde{\phi}$) for graphic reasons.

6.5 Systematic uncertainties

In the analysis of the Υ(1S) polarization two main sources of systematic uncertainties are taken into account:

- **signal extraction**: the systematic associated to the choice of the signal and background functions used in the Υ(1S) raw yield extraction.
- **input Monte Carlo shapes**: the systematic associated to the $p_{\rm T}$ and y shapes used as input for the Monte Carlo simulation

The main difference with respect to the J/ψ analysis is the absence of the contribution associated to the trigger efficiency, which represented a significant component of the overall systematic uncertainty. The reason of this choice is due to the cut applied on the single muon transverse momentum, which has to be higher than 2 GeV/c and allows to consider only the kinematic region where the muon trigger is fully efficient.

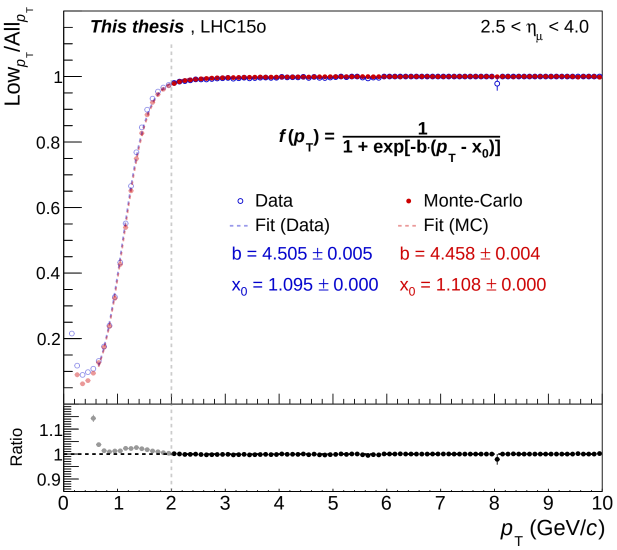

Figure 6.5: Trigger response for data and Monte Carlo of the as a function of the single muon p_{T} and corresponding to Pb–Pb data taking period of 2015 (LHC15o). The gray dashed line represents the p_{T} cut applied on the muon transverse momentum.

6.5.1 Systematic uncertainty due to the signal extraction

The effect of the raw yield extraction on the polarization parameters is evaluated testing different sets of signal and background shapes, in particular the *extended crystal ball* (CB2) and the NA60 functions for the signals, while a *Variable Width Gaussian* (VWG) and a second order polynomial function multiplied by an exponential (Pol2.×exp.) are used for the background.

In addition, the Υ(1S) yield is also obtained for two different fit ranges, $6.5 < m_{\mu\mu} < 13$ GeV/c^2 and $7 < m_{\mu\mu} < 12.5$ GeV/c^2, in order to have more control on the stability of the result. For each test, the corrected number of Υ(1S) is fitted to extract λ_θ, λ_ϕ and $\lambda_{\theta\phi}$, and the root-mean-square of the results provides the systematic associated to the signal extraction, which is found to range among ∼0.01 and ∼0.16.

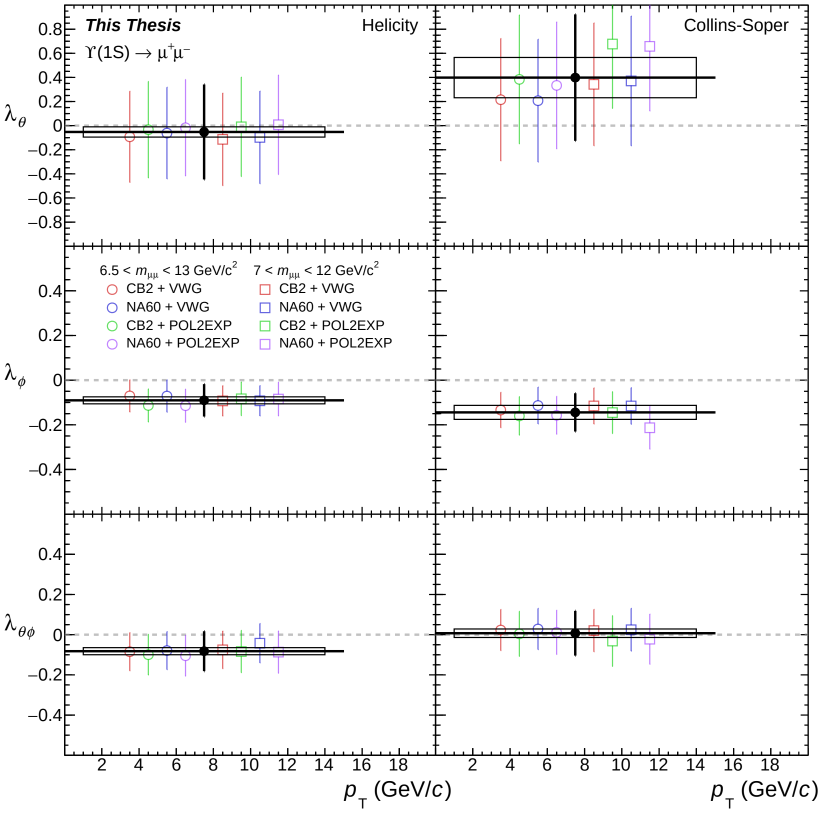

Figure 6.6: Comparison between the polarization parameters as a function of p_{T} for different choices of the signal and background shapes and for different fit ranges.

6.5.2 Systematic uncertainty due to the input Monte Carlo shapes

The systematic uncertainty associated to the p_{T} and y shapes provided as input to the Monte Carlo calculation is analogous to the one described in Section 5.6.3. The polarization parameters obtained with alternative transverse momentum and rapidity distributions ($\pm\Delta(p_{\mathrm{T}})$ and $\pm\Delta(y)$) are compared with the result extracted with the default ones, adopting the maximum difference between the latter and the alternative p_{T} and y shapes as the systematic uncertainty. The latter is found to range between ∼0.001 and ∼0.08.
In Fig. 6.7 the comparison among the values λ_θ, λ_ϕ and $\lambda_{\theta\phi}$ obtained for the different input p_{T} and y shapes is shown.

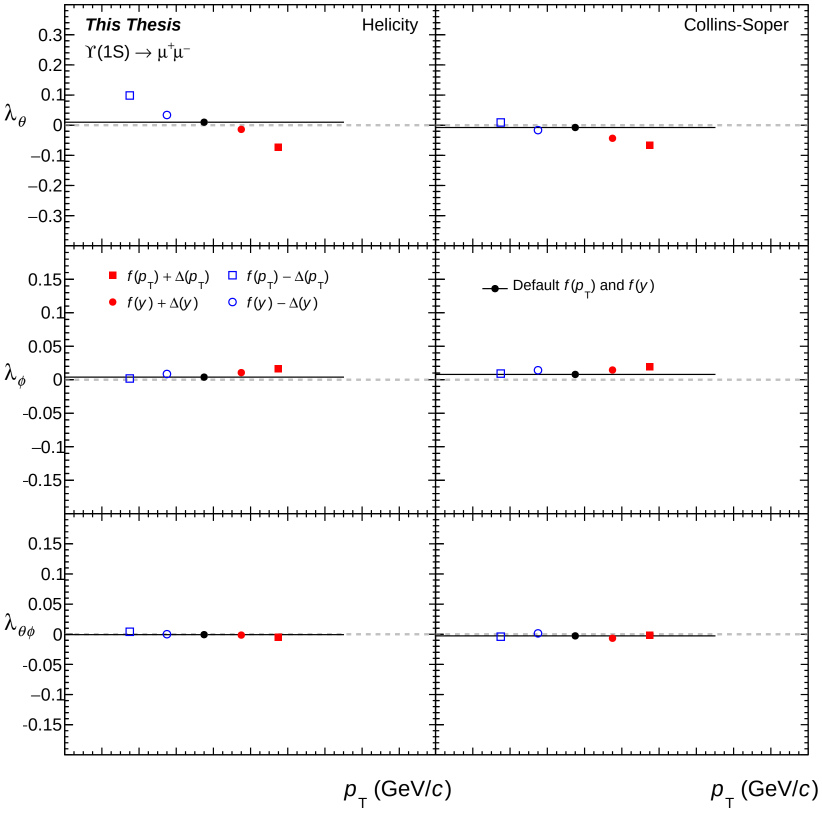

Figure 6.7: Comparison between the three polarization parameters obtained using the alternative and the default p_{T} and y distributions in the Monte Carlo generation.

6.5.3 Summary of the systematics

A summary of the systematic uncertainties evaluated in the Υ(1S) polarization analysis is reported in Table 6.1.

		Helicity		Collins-Soper	
p_{T} (GeV/c)		Signal	Input MC	Signal	Input MC
[0–15]	λ_θ	0.0425	0.0830	0.1670	0.0591
	λ_ϕ	0.0157	0.0128	0.0314	0.0112
	$\lambda_{\theta\phi}$	0.0176	0.0043	0.0212	0.0013

Table 6.1: Summary table of all the systematical uncertainties for the Υ(1S).

6.6 Results

The Υ(1S) polarization parameters have been obtained in a single transverse momentum bin, from 0 to 15 GeV/c, following the 1D method. In Fig. 6.8 λ_θ, λ_ϕ and $\lambda_{\theta\phi}$ are shown for the p_{T}-integrated bin and the corresponding numbers are reported in Table 6.2. The central values and the statistical uncertainties are obtained averaging the results for different signal and background shapes, while the systematic uncertainty is the sum in quadrature of the contribution associated to the signal extraction and input Monte Carlo shapes. It can be noticed that in both the helicity and Collins-Soper reference frames all the polarization parameters do no exhibit any significant deviation from zero, although for λ_θ the size of the uncertainties is rather large.

p_{T} (GeV/c)		Helicity	Collins-Soper
[0–15]	λ_θ	-0.053 ± 0.394 ± 0.093	0.398 ± 0.525 ± 0.177
	λ_ϕ	-0.090 ± 0.073 ± 0.020	-0.144 ± 0.086 ± 0.033
	$\lambda_{\theta\phi}$	-0.082 ± 0.099 ± 0.018	0.007 ± 0.111 ± 0.021

Table 6.2: Table of the Υ(1S) polarization parameters in the Helicity and Collins-Soper reference frames. The first error is the statistical uncertainty, while the second one is the systematic obtained as the sum in quadrature of the systematic uncertainties reported in Table 6.1.

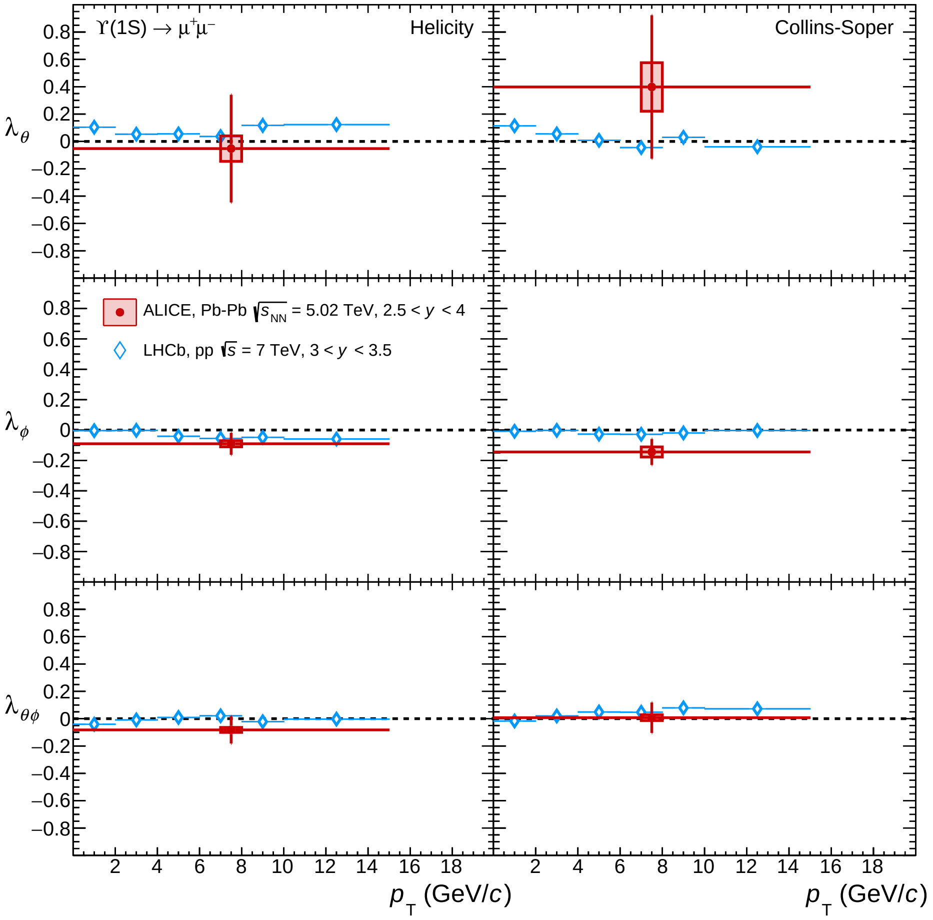

Figure 6.8: Inclusive Υ(1S) polarization parameters as a function of p_{T} for Pb–Pb collisions at $\sqrt{s_{\mathrm{NN}}} = 5.02$ TeV compared with results obtained in pp collisions by LHCb at $\sqrt{s} = 7$ TeV in the rapidity interval $3 < y < 3.5$ [163]. The error bars represent the total uncertainties for the pp results, while for Pb–Pb statistical and systematic uncertainties are plotted separately as a vertical bar and as a shaded box, respectively. In the left part of the plot the polarization parameters in the helicity reference frame are reported, in the right those for the Collins-Soper frame.

The values of λ_θ, λ_ϕ and $\lambda_{\theta\phi}$ are in agreement with the LHCb measurement in proton-proton collisions [163], where no sizable polarization was observed in similar kinematic region. Future measurements foreseen for Run 3 and Run 4 at the LHC, with an increase of the integrated luminosity of a factor ∼10 [206], should provide the precision necessary to perform a more significant comparison with other collision systems, benefiting also from the relatively high signal-to-background ratio in the Υ(1S) mass range.

Chapter 7

Conclusions

In this thesis the first measurements of the J/ψ and Υ(1S) polarization in heavy-ion collisions at the LHC energies were presented. These results were obtained making use of the Pb–Pb data sample collected by the ALICE experiment in 2015 and 2018 at $\sqrt{s_{\mathrm{NN}}} = 5.02$ TeV and the analyses were performed in the dimuon decay channel at forward rapidity ($2.5 < y < 4$). This observable, corresponding to the particle spin alignment with respect to a chosen axis, is evaluated through the extraction of the polarization parameters λ_θ, λ_ϕ and $\lambda_{\theta\phi}$, which quantify the anisotropies in the angular distributions of the decay products and are obtained in the helicity and Collins-Soper reference frames.

The J/ψ polarization parameters were extracted as a function of the transverse momentum in three p_{T} bins: $2 < p_{\mathrm{T}} < 4$, $4 < p_{\mathrm{T}} < 6$ and $6 < p_{\mathrm{T}} < 10$ GeV/c. In both reference frames λ_θ, λ_ϕ and $\lambda_{\theta\phi}$ exhibit at maximum slight deviations with respect to zero, with a mild transverse and longitudinal polarization in the helicity and Collins-Soper reference frames respectively, both with a significance of $\sim$2.1 standard deviations. Moreover the frame invariant parameter $\tilde{\lambda}$ was evaluated and found to be compatible within the uncertainties between the reference frames. These results were compared with ALICE measurements in pp collisions at $\sqrt{s} = 8$ TeV [196] and they were found to be compatible within uncertainties. A significant discrepancy ($\sim 3.3\sigma$) was observed in the helicity reference frame when comparing with the more accurate LHCb measurement at $\sqrt{s} = 7$ TeV in pp collisions [159], which showed a significant longitudinal polarization at low-p_{T} ($\lambda_\theta^{\mathrm{HE}} = -0.145 \pm 0.027$). Albeit the ALICE result in Pb–Pb was obtained for inclusive J/ψ production while the LHCb one for prompt only, the contribution from B-hadrons decay is expected to be negligible in the studied kinematic region, therefore this difference could be an effect associated to the different mechanisms occurring in large collisions systems. A measurement of J/ψ

polarization exploiting the large pp data sample collected by the ALICE experiment at $\sqrt{s} = 13$ TeV could help to sharpen the conclusions on the possible difference between polarization in pp and Pb–Pb collisions.

The J/ψ polarization parameters were also extracted as a function of the collision centrality, for $2 < p_{\mathrm{T}} < 6$ GeV/c and in four centrality classes: 0–20, 20–40, 40–60 and 60–90%. In both the helicity and Collins-Soper reference frames, λ_θ, λ_ϕ and $\lambda_{\theta\phi}$ did not exhibit strong deviation with respect to zero, with a maximum significance lower than two standard deviations. The slightly positive and negative λ_θ values in the helicity and Collins-Soper reference frames were consistent with the p_{T}-differential results, while for all the polarization parameters no strong centrality dependence was observed.

Since polarization is a very sensitive and versatile observable, it could be used to study a wide range of mechanisms. In particular, the possible effect on J/ψ polarization due to the formation of an intense magnetic field in heavy-ion collisions was discussed, presenting a possible analysis strategy. Even if this work is at a early stage, it appears to be promising, deserving more studies in the future.

The Υ(1S) polarization parameter were extracted in the helicity and Collins-Soper reference frames for $p_{\mathrm{T}} < 15$ GeV/c. λ_θ, λ_ϕ and $\lambda_{\theta\phi}$ were found to be compatible with zero within the uncertainties. This result is consistent with the measurements performed by LHCb in pp collisions in a similar kinematic region at $\sqrt{s} = 7$ and 8 TeV [163], even if the large statistical uncertainties prevent from drawing a strong conclusion.

The results presented in this thesis represent a first step in the exploration of quarkonium polarization in heavy-ion collisions. The good precision achieved by the J/ψ measurements provides, on one side, a further observable to explore the properties of large collision systems, while on the other a new challenge for the theoretical models. For the Υ(1S) polarization, the measurement is still limited by the large uncertainties, nevertheless the LHC Run 3 and 4 will provide enough statistics to achieve a more precise result.

Appendices

Appendix A

Study of $\psi(2S)$ production in p–Pb collisions at $\sqrt{s_{NN}} = 8.16$ TeV

The creation of the Quark-Gluon Plasma (QGP) in high-energy heavy-ion collisions is expected to modify the production rates of the various charmonium resonances by means of a suppression mechanism theorized for the first time by Matsui and Satz [66]. This effect is expected to increase with decreasing binding energy of the resonance, therefore the loosely bound states, as $\psi(2S)$ and χ_c, should disappear progressively when the color charge density and the temperature of the system are large enough. One of the key aspects is to disentangle the modification of the charmonium production due to the formation a strongly interacting medium from the one induced by "cold" nuclear effects. This kind of information can be accessed studying charmonium production in proton-nucleus collisions, where the energy density is expected to be lower than the threshold for the formation of a deconfined medium.

In this Appendix the analysis of the $\psi(2S)$ production in p–Pb collisions as a function of transverse momentum, rapidity and centrality will be illustrated. The result will be compared with experimental measurements for J/ψ and with theoretical predictions. The content of this part is collected into two papers, "*Measurement of nuclear effects on* $\psi(2S)$ *production in p–Pb collisions at* $\sqrt{s_{NN}} = 8.16$ *TeV*" [2] and "*Centrality dependence of* J/ψ *and* $\psi(2S)$ *production and nuclear modification in p–Pb collisions at* $\sqrt{s_{NN}} = 8.16$ *TeV*" [3].

A.1 Introduction

Cold Nuclear Matter (CNM) effects have been extensively investigated at the LHC in p–Pb collisions, with a particular focus on charmonia. The ALICE [241] and LHCb [242] collaborations published the nuclear modification factor ($R_{\rm pA}$) for J/ψ at $\sqrt{s_{\rm NN}} = 5.02$ TeV, observing a significant suppression at forward rapidity, which becomes weaker and than disappears for backward y. From a theoretical point of view this is explained with the *nuclear shadowing* [244, 245], which indicates the modification of the parton distribution function for the nucleon when it is bound inside the nucleus, with respect to when it is free. Moreover also models which implements coherent energy loss [246] in a cold nuclear medium are in fair agreement with data.

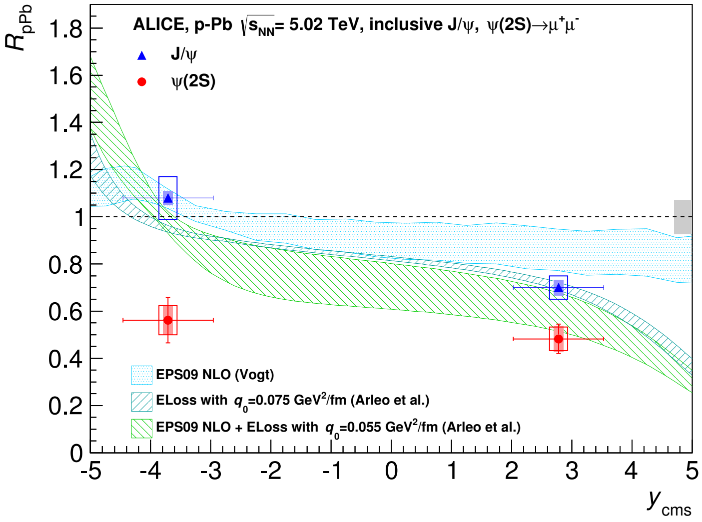

Figure A.1: J/ψ and ψ(2S) nuclear modification factor as function of rapidity measured by the ALICE collaboration in p–Pb collisions at $\sqrt{s_{\rm NN}} = 5.02$ TeV [243]. The results are compared with theoretical models including shadowing and energy loss.

Comparing these models with the ψ(2S) nuclear modification factor [243], surprisingly a larger suppression is observed with respect to J/ψ, in particular at backward rapidity, as shown in Fig. A.1. This was unexpected because the Cold Nuclear Matter effects previously mentioned are related to the heavy-quark hard production, therefore they were supposed to be similar for J/ψ and ψ(2S) .
Among the various mechanisms which could explain the additional suppression for the ψ(2S) , the dissociation of the $c\bar{c}$ pair due to the interaction with the particles produced

in the collisions, namely *comovers* [119], appears to be one of the best candidates. Even if the partonic or hadronic nature of comovers is still under debate, it is rather clear that final state effects are necessary to explain the observed ψ(2S) suppression, which is related to its lower binding energy with respect to J/ψ .

State	J/ψ	$\chi_{\rm c}$	ψ(2S)
m(GeV/c^2)	3.10	3.53	3.68
ΔE (GeV)	0.64	0.20	0.05

Table A.1: Mass (m) and binding energy (ΔE) for some of the charmonium states [128].

The results presented in this appendix are proposed to shed more light on this still open question, exploiting the p–Pb data sample collected by the ALICE experiment at the highest center-of-mass energy.

A.2 Analysis strategy description

The modification of ψ(2S) production in heavy-ion collisions is quantified by means of the *nuclear modification factor*, calculated as:

$$R^{\psi(2S)}_{\rm pPb}(p_{\rm T}, y_{\rm cms}) = \frac{{\rm d}^2\sigma^{\psi(2S)}_{\rm pPb}/{\rm d}p_{\rm T}{\rm d}y_{\rm cms}}{{\rm A_{Pb}}\cdot {\rm d}^2\sigma^{\psi(2S)}_{\rm pp}/{\rm dp_T dy_{cms}}} \tag{A.1}$$

where $\sigma_{\rm pp}$ and $\sigma_{\rm pPb}$ are the ψ(2S) double-differential cross sections in proton-proton and proton-lead collisions respectively, while $\rm A_{Pb}$ is the mass number of the lead nucleus ($\rm A_{Pb} = 208$). The nuclear modification factor is particularly useful for the comparison with theoretical predictions and a precise measurement of this quantity allows to discriminate among many models describing quarkonium production in heavy-ion collisions. Moreover also cross sections and their ratios are evaluated.

In the presented analysis there are three main ingredients for the evaluation of these quantities:

1. *raw yield*: the ψ(2S) raw yield is extracted fitting the $\mu^+\mu^-$ invariant mass distribution with a combination of signal and background functions

2. *acceptance-times-efficiency*: the $\psi(2S)$ raw yield needs to be corrected with an acceptance-times-efficiency evaluated in a Monte-Carlo simulation, in order to account for the geometrical coverage and the detector inefficiencies.

3. *reference cross section*: the $\psi(2S)$ production cross section in proton-nucleus collisions is compared with the so called "pp reference" cross section, which is evaluated at the same center-of-mass energy and in the same kinematic region as the p–Pb one.

A.3 Data sample and event selection

Data used for this analysis have been taken with two different beam configurations, obtained by inverting the sense of the orbits of two colliding beams. In particular the ranges $2.03 < y_{\rm cms} < 3.53$ and $-4.46 < y_{\rm cms} < -2.96$ are accessible, where positive rapidities correspond to the proton going towards the Muon Spectrometer, while negative to the Pb-going one (in the following these two configurations are defined as p–Pb and Pb–p respectively). Data were collected at the center of mass energy of 8.16 TeV, in November-December 2016. In Table A.2 general information about data samples is reported. The p–Pb and Pb–p periods are defined as LHC16r and LHC16s respectively, and correspond to a total integrated luminosity of $\mathcal{L}_{\rm int} \sim 20.6$ nb^{-1}.

Year	System	$\sqrt{s_{\rm NN}}$ (TeV)	Period	Runs	CMUL7 triggers
2016	p–Pb	8.16	LHC16r	57	2.5×10^7
2016	Pb–p	8.16	LHC16s	80	7.2×10^7

Table A.2: Summary of the run statistics corresponding to the p–Pb and Pb–p data taking periods with particular focus on the number of CMUL7-B-NOPF-MUFAST triggers.

Analogously to the J/ψ polarization analysis described in Chapter 5, events are selected according to the dimon trigger (CMUL7-B-NOPF-MUFAST), configured with a single muon threshold of $p_{\rm T} > 0.5$ GeV/c. The dimun sample is obtained applying a set of cuts at the single track level, which is a standard for most quarkonium analyses:

- both muon tracks in the tracking chambers must match a track in the trigger system
- tracks are selected in the pseudo-rapidity range $-4 < \eta_\mu < -2.5$ in order to reject tracks at the edge of the detector

- the track's transverse radius at the end of the front absorber is in the range $17.6 \leq R_{abs} \leq 89.5$ cm, removing tracks passing through its thicker part
- the reconstructed muon tracks match the low-$p_{\rm T}$ trigger threshold of 0.5 GeV/c. This cut reduces the contributions from hadrons escaped from the front absorber and low-$p_{\rm T}$ muons coming from kaon and pion decays

In addition to the single track cuts, each dimuon candidate is selected in the rapidity range $2.5 < y_{\mu\mu} < 4$ and with a total electric charge equal to zero.

A.4 Signal extraction

The ψ(2S) raw yield is extracted fitting the dimuon invariant mass spectrum with a combination of signal and background functions. Since this estimation is crucial for the calculation of the nuclear modification factor, normally the signal extraction is performed varying the functions and the parameters of the fit:

- signal shape: this function has to describe both the ψ(2S) and J/ψ peaks. For this analysis a *extended Crystal Ball* (CB2) and a *NA60* function are used (the definition of the signal functions is reported in Section 5.3).
- background shape: this function has to describe the background of the invariant mass distribution. For this analysis a *Variable Width Gaussian* (VWG) and the product of a fourth degree polynomial times an exponential (Pol4Exp) have been used (the definition of the background functions is reported in Section 5.3).
- fitting ranges: for each combination of background and signal function the fit is performed in two mass ranges (in this case $2.2 < m_{\mu\mu} < 4.5$ GeV/c^2 and $2 < m_{\mu\mu} < 5$ GeV/c^2) in order to check the stability of the fit.
- signal function tails : the tails of the signal function are not free parameters of the fit and they are normally fixed fitting J/ψ Monte-Carlo spectra or very large data samples.

The evaluation of the ψ(2S) raw yield is sensitive to the choice of the signal function tails and for this reasons the fit to the invariant mass spectrum is performed testing different sets of these parameters:

- tails tuned on J/ψ and ψ(2S) Monte-Carlo invariant mass spectrum integrated over $p_{\rm T}$ and y in p–Pb and Pb–p collisions at $\sqrt{s_{\rm NN}} = 8.16$ TeV
- tails tuned in the fits to the invariant mass spectra integrated over $p_{\rm T}$ and y in p–Pb and Pb–p collisions at $\sqrt{s_{\rm NN}} = 8.16$ TeV
- tails tuned in the fit to the invariant mass spectrum integrated over $p_{\rm T}$ and y in proton-proton collisions at $\sqrt{s} = 8$ TeV

As shown in Fig. A.2, the various sets of tail parameters exhibit a slightly different behavior, in particular for the Monte-Carlo ones the signal shape is wider. This feature will be reflected in the ψ(2S) raw yield, which will be larger for this specific set of parameters.

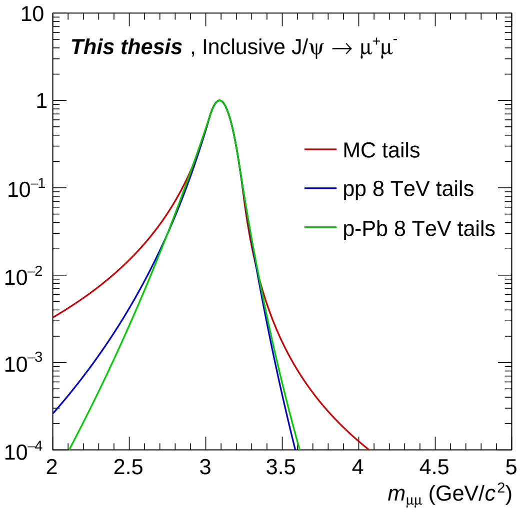

Figure A.2: J/ψ signal function (CB2) for different choices of tail parameters.

Given the relatively low signal-to-background ratio, the ψ(2S) mass and width parameters are not kept free in the fit, but they are bound to the J/ψ ones according the equations:

$$m_{\psi(2{\rm S})} = m^{\rm FIT}_{{\rm J}/\psi} + \Delta m^{\rm PDG} \tag{A.2}$$

$$\sigma_{\psi(2{\rm S})} = \sigma^{\rm FIT}_{{\rm J}/\psi} \cdot \frac{\sigma^{\rm MC}_{\psi(2{\rm S})}}{\sigma^{\rm MC}_{{\rm J}/\psi}} \tag{A.3}$$

as already detailed in Section 5.3. The correction factor $\sigma^{\mathrm{MC}}_{\psi(2\mathrm{S})}/\sigma^{\mathrm{MC}}_{\mathrm{J}/\psi}$ is extracted fitting the J/ψ and $\psi(2\mathrm{S})$ reconstructed mass spectra in the Monte-Carlo and performing a study of their ratio as a function of rapidity and transverse momentum. As shown in Fig. A.3, this quantity is found to be flat for both the variables and $a \sim 1.05$. In parallel the ratio is also checked in experimental data, in particular using the data sample collected in proton-proton collisions at $\sqrt{s} = 13$ TeV [92]. In this case the ratio is:

$$\sigma_{\psi(2\mathrm{S})}/\sigma_{\mathrm{J}/\psi}\Big|_{\mathrm{pp}\ \sqrt{s}=13\ \mathrm{TeV}} = 1.046 \pm 0.056 \tag{A.4}$$

which is compatible with the Monte-Carlo one within the uncertainty, amounting to ∼ 5%.

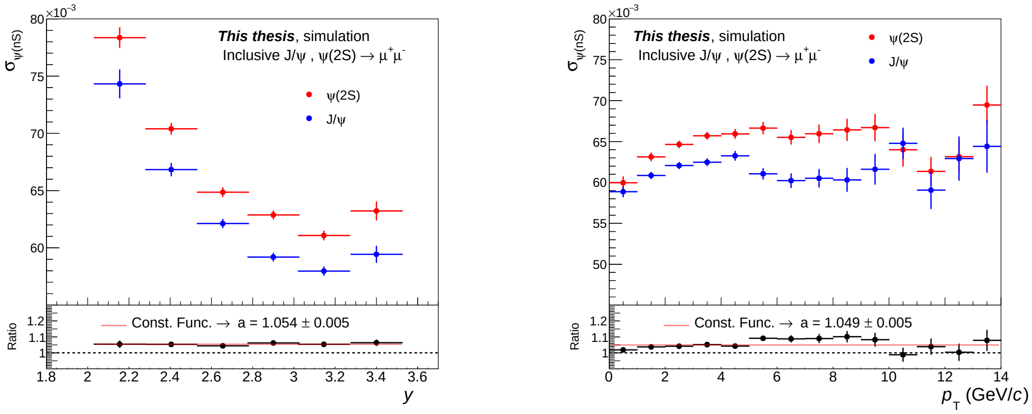

Figure A.3: Comparison between the J/ψ and $\psi(2\mathrm{S})$ width extracted from the Monte-Carlo as a function of rapidity (left panel) and transverse momentum (right panel). In the bottom part their ratio is shown and fitted with a constant function.

In the left panels of Fig. A.4 the fits to the dimuon invariant mass distributions corresponding to the forward (top) and backward (bottom) rapidity regions are shown. The different signal and background functions together with the variation of the fit range and the set of tail parameters, provide an overall number of 16 tests, as shown in the right panels of Fig. A.4. The $\psi(2\mathrm{S})$ and J/ψ raw yields and their statistical uncertainties are computed as the average of all these results, while their root-mean-square is taken as the systematic uncertainty on the signal extraction.
A further 5% systematic uncertainty is added to take into account the uncertainty on the ratio $\sigma_{\psi(2\mathrm{S})}/\sigma_{\mathrm{J}/\psi}$ in Eq. A.4. The $\psi(2\mathrm{S})$ raw yield for $p_{\mathrm{T}} < 12$ GeV/c and corresponding to the forward and the backward rapidity regions is reported in Table A.3.

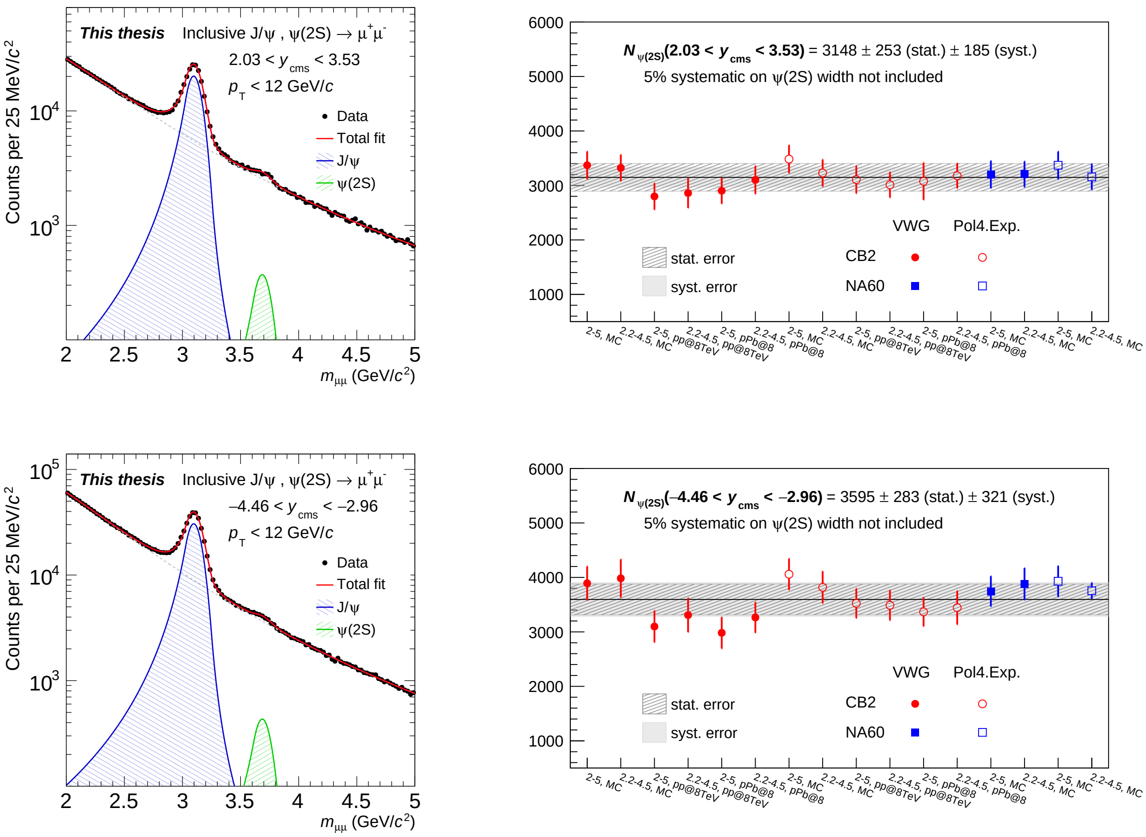

Figure A.4: Left panel: fit to the dimuon invariant mass spectrum at forward (top) and backward (bottom) rapidity. Right panel: $\psi(2S)$ raw yeld as a function of the test.

	$2.03 < y < 3.53$	$-4.46 < y < -2.93$
$N_{\psi(2S)}$	$3148 \pm 253 \pm 243$	$3595 \pm 283 \pm 368$

Table A.3: $\psi(2S)$ raw yield evaluated in the forward and backward rapidity regions. The first and the second uncertainties are the statistical and systematic respectively.

In the analysis as a function of transverse momentum and rapidity [2] the signal extraction is performed for $p_{\rm T} < 12$ GeV/c in 5 $p_{\rm T}$ bins, with the $\psi(2S)$ raw yield varying from $\sim$760 to $\sim$150 counts and from $\sim$1300 to $\sim$130 in the p–Pb and Pb–p periods respectively. Similarly the differential yields as a function of rapidity are extracted in two sub-ranges for $2.03 < y < 3.53$ and $-4.46 < y < -2.93$. In Fig. A.5 the $\psi(2S)$ yields as a function of the transverse momentum and rapidity are compared with the J/ψ ones, scaling the results to improve visibility.

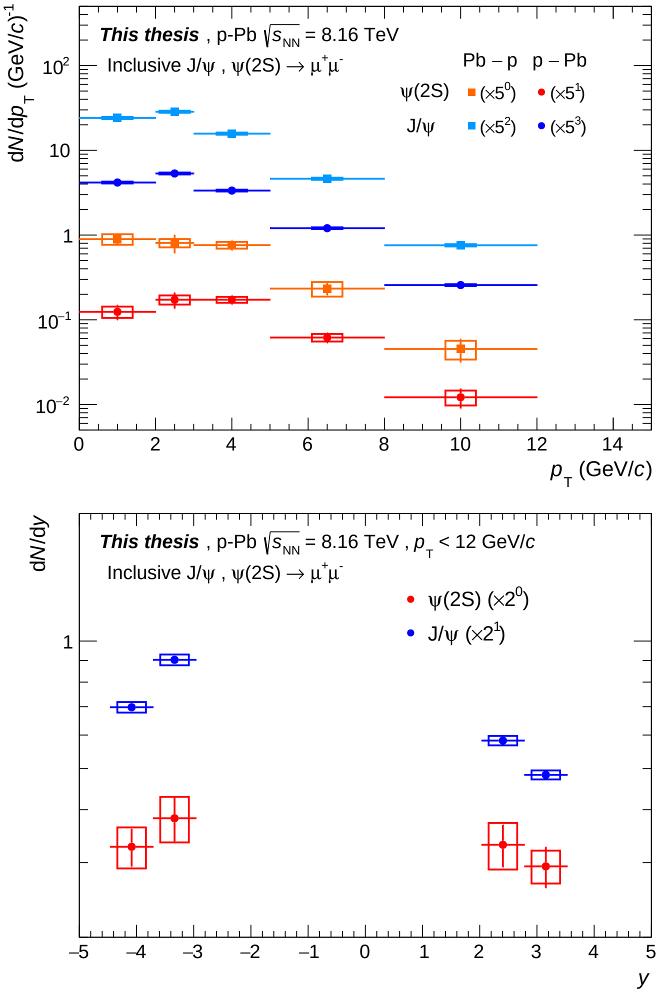

Figure A.5: Normalized J/ψ and $\psi(2S)$ raw yields as a function of the transverse momentum (top) and rapidity (bottom). Results are scaled for better visibility.

In the analysis as a function of centrality [3] the signal extraction is performed for $p_{\mathrm{T}} < 20$ GeV/c in 6 centrality classes, from 2 to 90%. The 0–2% range is excluded since Monte-Carlo simulations reproducing LHC running conditions have shown that a residual pile-up may be present in most central events. On the other hand, the 90–100% centrality interval is also excluded since the dimuon trigger may be affected by residual background contamination. In Fig. A.6 the ψ(2S) and J/ψ raw yields are shown as a function of the collision centrality in the forward and backward rapidity ranges. It can be noticed that the number of ψ(2S) decrease rapidly from central to peripheral collisions, passing from ∼520 to ∼160 and from ∼640 to ∼100 in p–Pb and Pb–p collisions respectively.

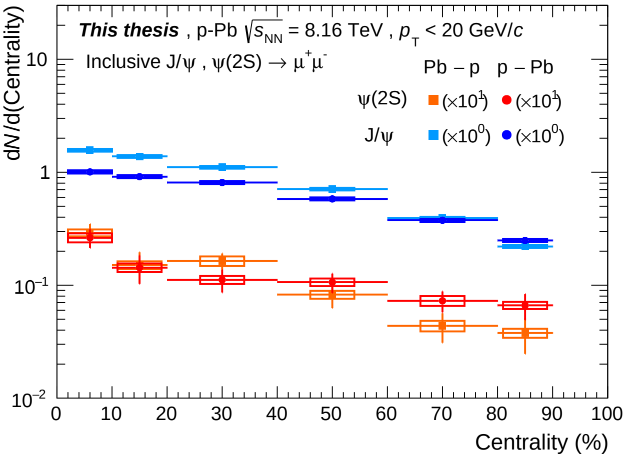

Figure A.6: Normalized J/ψ and ψ(2S) raw yields as a function of centrality. Results are scaled for better visibility.

A.5 Acceptance-times-efficiency evaluation

The product of the geometrical acceptance and the reconstruction efficiency is evaluated in a Monte-Carlo simulation, following the same procedure as detailed in Section 5.3.1. The input p_{T} and y shapes used in the generation of the ψ(2S) sample are tuned on data by means of an iterative procedure. In particular, at the step zero (*iteration 0*) the ψ(2S) is generated with the same parametrization as the J/ψ one. In the following iteration (*iteration 1*) the input shapes are obtained from the fit of the corrected ψ(2S) transverse momentum and rapidity distributions, whose evolution can be seen in Fig. A.7.

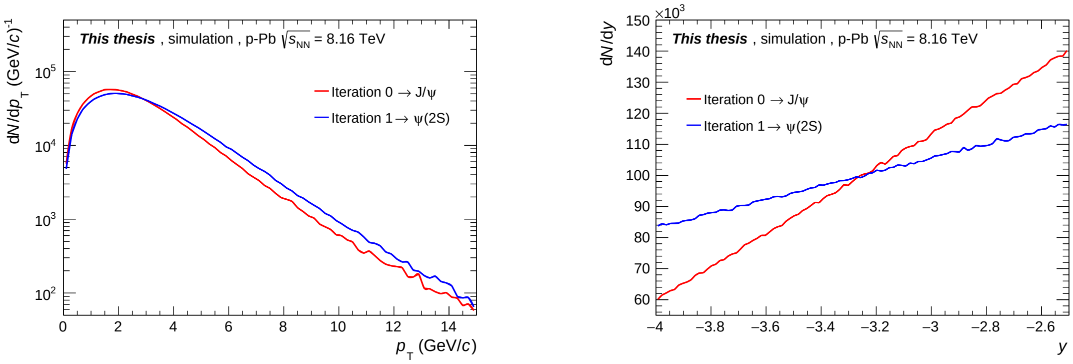

Figure A.7: $p_{\rm T}$ and y input shapes used for the different iteration in the Monte-Carlo.

In Fig. A.8 the acceptance-times-efficiency is shown as a function of the transverse momentum together with the integrated result (dotted line) in the two rapidity regions under study. The sensitivity of $A \times \varepsilon$ with respect to the adopted input shapes will be evaluated by including a corresponding systematic uncertainty on the final results (cross sections and $R_{\rm pA}$).

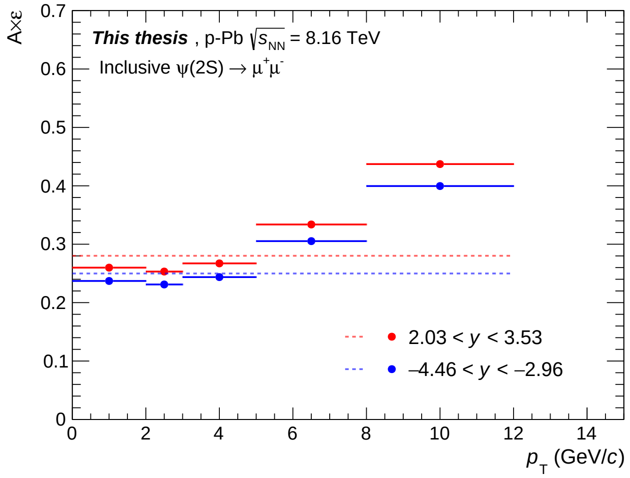

Figure A.8: Acceptance-times-efficiency as a function of the transverse momentum. The dashed lines represent the $A \times \varepsilon$ integrated over $p_{\rm T}$ and y.

A.6 The proton-proton reference cross section

The proton-proton reference cross section is one of the ingredients in the evaluation of the nuclear modification factor. As reported in Eq. A.1, the inverse of the ratio among this quantity, multiplied by the mass number $\mathrm{A_{Pb}}$, and the production cross section in proton-nucleus collisions represents a important observable which allows to investigate nuclear effects and to compare data with theoretical predictions. For this purpose the pp reference has to be evaluated at the same center-of-mass energy and in the same $p_{\rm T}$ and y ranges as the p–Pb one. Since this measurement was not directly performed by the ALICE experiment, the $\psi(2S)$ reference can be evaluated multiplying the J/ψ cross section by the corresponding ratio $\psi(2S)/\mathrm{J}/\psi$:

$$\sigma_{\psi(2S)}(p_{\rm T}, y)\Big|^{\rm Interp.}_{\sqrt{s}=8.16\rm TeV} = \sigma_{\mathrm{J}/\psi}(p_{\rm T}, y)\Big|_{\sqrt{s}=8.16\rm TeV} \times \left[\frac{\sigma_{\psi(2S)}(p_{\rm T}, y)}{\sigma_{\mathrm{J}/\psi}(p_{\rm T}, y)}\right]^{\rm Interp.}_{\sqrt{s}=8.16\rm TeV} . \tag{A.5}$$

where $\sigma_{\mathrm{J}/\psi}$ is the J/ψ cross section evaluated at $\sqrt{s}$ = 8.16 TeV [249], while $\sigma_{\psi(2S)}/\sigma_{\mathrm{J}/\psi}$ is obtained via the interpolation of the published results at different $\sqrt{s}$ values [94, 247, 92].

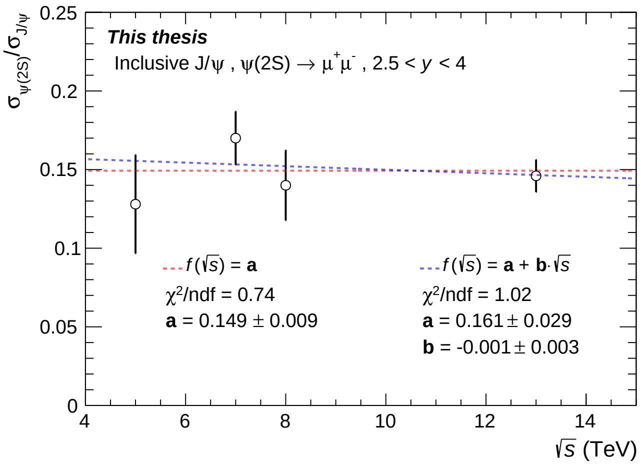

Figure A.9: Fit to the ratio $\sigma_{\psi(2S)}/\sigma_{\mathrm{J}/\psi}$ as a function of the center-of-mass energy with a linear and a constant function. Data points correspond to the results published by the ALICE experiment at $\sqrt{s}$ = 5, 7, 8 and 13 TeV [94, 247, 92].

Since it has been observed that the ratio $\psi(2S)/\mathrm{J}/\psi$ exhibits a negligible center-of-mass energy dependence, the interpolation can be performed with a constant function, as shown in Fig. A.9. Alternatively, as a check, a first order polynomial function is used in the fit, and the angular coefficient (b) is found to be compatible with zero within one standard deviation. A constant function is then used in the interpolation (see the legend in Fig.A.9).

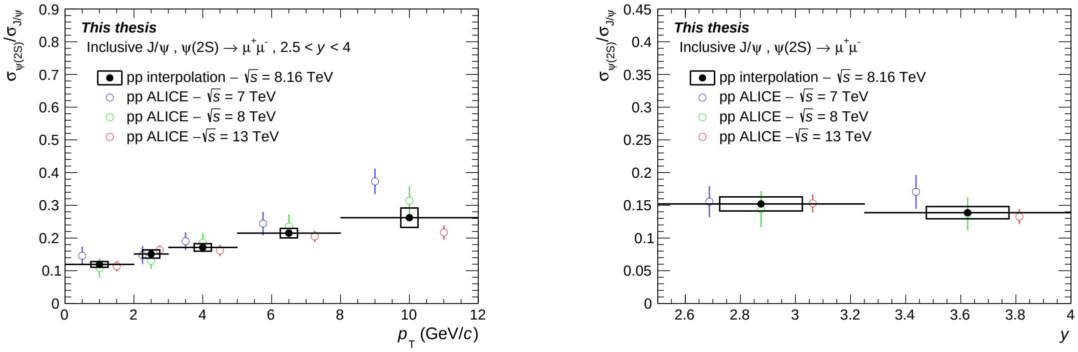

Figure A.10: Comparison between $\sigma_{\psi(2S)}/\sigma_{J/\psi}$ interpolated at $\sqrt{s} = 8.16$ TeV and the ratio measured by the ALICE experiment at $\sqrt{s} = 7$, 8 and 13 TeV as a function of p_T and y [94, 247, 92]. The empty box represent the error on the fit.

The same procedure is performed as a function of the transverse momentum and rapidity and the ratio $\psi(2S)/J/\psi$ extrapolated at $\sqrt{s} = 8.16$ TeV is shown in Fig. A.10. Comparing these results with the experimental measurements at different center-of-mass energies $\sqrt{s} = 7$, 8 and 13 TeV, it can be seen the size of the uncertainty on the interpolated values, which corresponds to the error on the fit parameter for a constant function, is smaller when compared with the results at $\sqrt{s} = 8$ TeV. This is due to the inclusion in the interpolation procedure of the measurement at $\sqrt{s} = 13$ TeV, the most precise result available in pp collisions. Moreover, it should be also noted that the rapidity range in pp collisions ($2.5 < y < 4$) is different from those in p–Pb ($2.03 < y < 3.53$) and Pb–p ($-4.46 < y < -2.96$), an aspect which deserves to be investigated in more detail. This can be done considering the J/ψ cross section in proton-proton collisions at $\sqrt{s} = 8$ TeV, whose width and mean value can be obtained fitting data with a Gaussian function. The expected $\psi(2S)$ distribution can be derived from the J/ψ one via the following transformation:

$$y^{\rm Max}_{\psi(2S)}/y^{\rm Max}_{J/\psi} = \log(\frac{\sqrt{s}}{m_{\psi(2S)}})\Big/\log(\frac{\sqrt{s}}{m_{J/\psi}}) \tag{A.6}$$

$$\sigma_{\psi(2S)} = \sigma^{\rm Fit}_{J/\psi} \cdot \left(y^{\rm Max}_{\psi(2S)}/y^{\rm Max}_{J/\psi}\right) \tag{A.7}$$

where y^{Max} is the maximum kinetically allowed rapidity for a certain particle and it depends on the resonance mass and on the center-of-mass energy of the collision. As shown in Fig. A.11 the J/ψ and the expected $\psi(2\mathrm{S})$ cross sections exhibit a slight difference for large y values, with a maximum discrepancy which ranges around ∼5% in the rapidity region corresponding to Pb–p collisions.

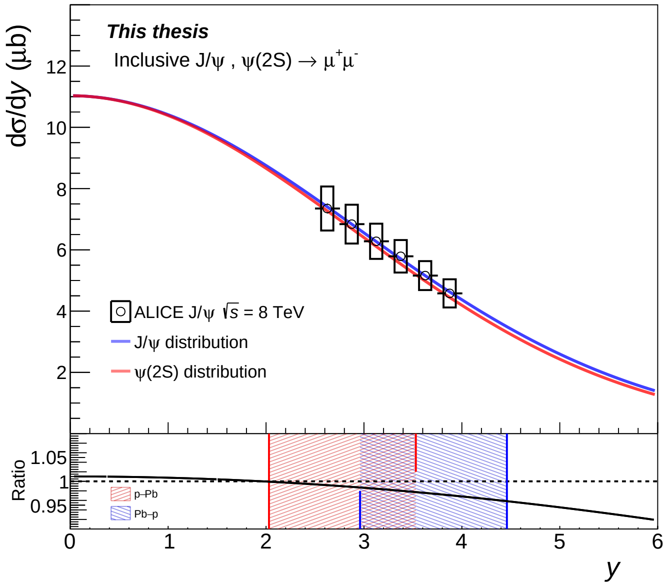

Figure A.11: Top panel: J/ψ and $\psi(2\mathrm{S})$ cross sections as function of the rapidity. Bottom panel: ratio of the J/ψ and $\psi(2\mathrm{S})$ cross sections. The p–Pb and Pb–p rapidity ranges are identified in red and blue respectively.

In order to quantify the effect of the different rapidity distributions for $\psi(2\mathrm{S})$ and J/ψ , the ratio of the integrals of the two distributions is computed in the p–Pb and Pb–p rapidity ranges and then it is normalized to the ratio of the same integral in the pp rapidity region:

$$f = (\psi(2S)/J/\psi)_{a<y<b} = \frac{\int_a^b (e^{\frac{(x-\mu)^2}{2\sigma}})_{\psi(2\mathrm{S})} \Big/ \int_a^b (e^{\frac{(x-\mu)^2}{2\sigma}})_{\mathrm{J}/\psi}}{\int_{2.5}^{4.0} (e^{\frac{(x-\mu)^2}{2\sigma}})_{\psi(2\mathrm{S})} \Big/ \int_{2.5}^{4.0} (e^{\frac{(x-\mu)^2}{2\sigma}})_{\mathrm{J}/\psi}} \cdot \left(\frac{\sigma_{\psi(2\mathrm{S})}}{\sigma_{\mathrm{J}/\psi}}\right)^{\mathrm{Interp.}}_{2.5-4.0} \tag{A.8}$$

where a and b correspond to the p–Pb ($2.03 < y < 3.53$) and Pb–p ($-4.46 < y < -2.96$) rapidity ranges.

If the ratio as a function of rapidity were constant then it would be equal to:

$$g = (\psi(2S)/J/\psi)_{2.5<y<4.0} = \left(\frac{\sigma_{\psi(2S)}}{\sigma_{J/\psi}}\right)^{\text{Interp.}}_{2.5-4.0} \tag{A.9}$$

The relative difference between a constant and a rapidity dependent ratio is:

$$\left(\frac{f-g}{g}\right)_{2.03<y<3.53} = 1.007 - 1 = +0.07 \sim 1\% \tag{A.10}$$

$$\left(\frac{f-g}{g}\right)_{2.96<y<4.46} = 0.992 - 1 = -0.08 \sim 1\% \tag{A.11}$$

showing that the contribution of a different y-dependence for J/ψ and $\psi(2S)$ is smaller than 1% both in p–Pb and Pb–p. This contribution will be added as a systematic uncertainty on the ratio of the reference cross sections.

The flatness of the $\psi(2S)$/J/ψ ratio as a function of the center-of-mass energy can be further tested by comparing the interpolated results with the predictions of NRQCD+CGC calculations [93, 91] and they are found to be compatible.

A.7 Systematic uncertainties

This section is dedicated to the description of the main sources of systematic uncertainties taken into account in this analysis.

Systematic uncertainty associated to the signal extraction

The systematic uncertainty on the signal extraction is obtained considering the results of several fits of the invariant mass spectra, where various shapes are used to describe the $\psi(2S)$ peak and the background. The estimate is performed changing the fitting ranges and the tail parameters, tuning them on data or on the spectra from Monte-Carlo simulations and the systematic uncertainty is then defined as the root-mean-square of the yields from all the tests. An additional 5% is included to take into account the uncertainty on the correction factor used to connect the J/ψ to the $\psi(2S)$ width (for more details see Section A.4). In the analysis as a function of transverse momentum and rapidity the total systematic uncertainty is found to vary from ∼8 to ∼20% and from ∼9 to ∼25% for p–Pb and Pb–p respectively. For the $\psi(2S)$ study in different centrality classes the systematic uncertainty ranges between ∼7.6 and ∼12.8% at forward rapidity and between ∼7.1 and ∼15.9% at backward rapidity.

Systematic uncertainty associated to the trigger efficiency

The systematic uncertainty related to the trigger efficiency is characterized by two components:

- the intrinsic trigger efficiency which is determined taking into account the uncertainties on the trigger chambers efficiencies measured in data and then applied to Monte-Carlo simulations
- the response of the trigger algorithm, which is determined evaluating the single muon response function. The latter is calculated as the fraction of muons passing the programmable p_T threshold and the systematic uncertainty is evaluated as the relative difference among the trigger response function in data and in the Monte-Carlo.

The overall systematic uncertainty amounts to 2.6% and 3.1% at backward and forward rapidity respectively. It does not exhibit a dependence on the collision centrality, and it ranges between ∼1% and ∼6% as a function of transverse momentum and rapidity.

Systematic uncertainty associated to the tracking efficiency

The tracking algorithm used by the ALICE experiment does not require that all the chambers have fired to reconstruct a track. This redundancy can be used to evaluate the overall tracking efficiency directly from data. The systematic uncertainty is evaluated as the discrepancy among the tracking efficiency obtained in data and in the Monte-Carlo simulation, where the status of each chamber is accurately described, and it is found to be 1% and 2% for p–Pb and Pb–p collisions respectively.

Systematic uncertainty associated to the matching efficiency

The systematic uncertainty on the matching efficiency between the tracking and the trigger tracks is 1% for both forward and backward rapidities. This quantity is given by the differences observed between experimental data and simulations performed applying different cuts on the matching χ^2 between the track reconstructed in the tracking and in the trigger chambers.

Systematic uncertainty associated to the pp reference

As discussed in Section A.6 the systematic uncertainty related to the proton-proton reference includes different contributions. The first one is the error associated to the interpolation of the ratio $\psi(2S)/J/\psi$ which depends on transverse momentum and rapidity and ranges between ∼7 and ∼12%. An additional 1% is included to take into account the different rapidity coverage between proton-proton ($2.5 < y < 4$) and proton-nucleus ($2.03 < y < 3.53$ and $-4.46 < y < 2.96$) collisions. Finally a further 1% is added to account for a possible non-flat $\psi(2S)/J/\psi$ ratio as a function of the center-of-mass energy. The $\psi(2S)$ proton-proton reference cross section is obtained multiplying the ratio $\psi(2S)/J/\psi$ by the J/ψ cross section, propagating the corresponding uncertainties. In particular this last contribution amounts to ∼7% and it is the same for p–Pb and Pb–p collisions.

Systematic uncertainty associated to the input Monte-Carlo input shapes

The estimation of the acceptance-times-efficiency depends on the $p_{\rm T}$ and y distributions used as input shapes in the Monte-Carlo simulation. The sensitivity of the results to this choice is evaluated comparing the $A \times \varepsilon$ obtained with two sets of Monte-Carlo simulations, performed with the generated J/ψ and $\psi(2S)$ input shapes. The relative difference among the two acceptance-times-efficiencies is taken as the systematic uncertainty and it corresponds to 3 and 1.5% for p–Pb and Pb–p respectively. As a function of $p_{\rm T}$ and y it is found to range between 0.3 and 4%.

Summary of the systematic uncertainties

In Table A.4 the summary of the main sources of systematic uncertainties is provided in percentage, separating the results of the $p_{\rm T}$ and y analysis from those of the $\psi(2S)$ study as a function of centrality. A further contribution associated to the integrated luminosity determination is reported, providing separately the correlated and uncorrelated contributions as a function of $p_{\rm T}$, y and centrality.

source	$2.03 < y_{\rm cms} < 3.53$		$-4.46 < y_{\rm cms} < -2.96$	
	$p_{\rm T}, y$	centr.	$p_{\rm T}, y$	centr.
signal extraction	8.0–20.0	7.6–12.8	9.1–24.9	7.1–15.9
trigger efficiency	2.6 (1.0–5.0)	2.6	3.1 (1.0–6.0)	3.1
tracking efficiency	1.0		2.0	
matching efficiency	1.0		1.0	
MC input	3 (0.4–4.0)	3 (2.5–2.7)	1.5 (0.1–4.4)	1.5 (1.6–1.7)
pp reference (corr.)	7.1		7.1	
pp reference (uncorr.)	6.3 (7.0–11.8)	6.3	6.5 (7.2–11.9)	6.5
$\mathcal{L}_{\rm int}^{\rm pPb}$ (corr.)	0.5		0.7	
$\mathcal{L}_{\rm int}^{\rm pPb}$ (uncorr.)	2.1		2.2	

Table A.4: Systematic uncertainties in percentage on the ψ(2S) shown separately for the p–Pb and Pb–p configurations and for the $p_{\rm T}, y$ and centrality analyses. When a single value is quoted, it refers to quantities that have no $p_{\rm T}$, y and centrality dependence. In the other cases, the number outside parentheses is for integrated quantities, while the ranges in parentheses indicate the variation of the systematic uncertainties in the $p_{\rm T}$, y and centrality intervals.

A.8 Results

In this section the results of the ψ(2S) analysis as a function of transverse momentum, rapidity and centrality will be presented, focusing on the cross section, single and double ratio of cross sections and the nuclear modification factor.

A.8.1 ψ(2S) cross section

The inclusive ψ(2S) cross section times the branching ratio is computed as:

$$\mathrm{B.R.}_{\psi(2S)\rightarrow\mu^+\mu^-} \cdot \frac{\mathrm{d}^2\sigma_{\rm pPb}^{\psi(2S)}}{\mathrm{d}p_{\rm T}\mathrm{d}y} = \frac{N_{\psi(2S)}^{\rm corr}(p_{\rm T}, y)}{\mathcal{L}_{\rm int}\cdot\Delta p_{\rm T}\Delta y} \tag{A.12}$$

where $N_{\psi(2S)}^{\rm corr}(p_{\rm T}, y)$ is the ψ(2S) raw yield $A\times\varepsilon$ corrected, $\mathcal{L}_{\rm int}$ is the integrated luminosity and Δy, $\Delta p_{\rm T}$ are the transverse momentum and rapidity intervals considered in the analysis. The result is not corrected for the branching ratio to muon pairs in order to not introduce the associated systematic uncertainty, which amounts to ∼8% [5]. The inclusive $\psi(2S)$ production cross sections integrated over $p_{\rm T} < 12$ GeV/c, corresponding to the forward and backward rapidity regions, are:

$$\mathrm{B.R.}_{\psi(2S)\rightarrow\mu^+\mu^-} \cdot \sigma^{\psi(2S)}_{\rm pPb}(2.03 < y_{\rm cms} < 3.53) = 1.337 \pm 0.108 \pm 0.121 \pm 0.007\,\mu\mathrm{b}$$
$$\mathrm{B.R.}_{\psi(2S)\rightarrow\mu^+\mu^-} \cdot \sigma^{\psi(2S)}_{\rm Pbp}(-4.46 < y_{\rm cms} < -2.96) = 1.124 \pm 0.089 \pm 0.126 \pm 0.008\,\mu\mathrm{b}$$

where the first uncertainty is statistical, while the second and the third are the uncorrelated and correlated systematic uncertainties respectively.

The cross section is also evaluated in four rapidity intervals and in five $p_{\rm T}$ bins, as shown in Figs. A.12 and A.13. In addition to the data points, the proton-proton reference obtained via the interpolation procedure described in Section A.6 and multiplied by the mass number $\mathrm{A}_{\rm Pb}$ is also shown as a gray band in all the figures. Furthermore it should be noticed that the reported results include both the prompt component and the contribution from b-hadron decays. The latter was studied in the same collision system and in a similar rapidity region by LHCb at $\sqrt{s_{\rm NN}} = 5.02$ TeV [250] and it is found to correspond to the 20–30% of the inclusive cross section, with a clear $p_{\rm T}$-dependence.

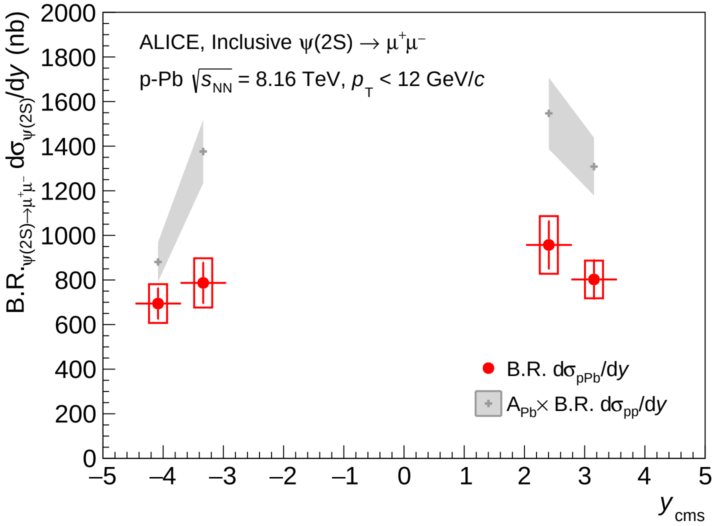

Figure A.12: The differential cross section times branching ratio $\mathrm{B.R.}_{\psi(2S)\rightarrow\mu^+\mu^-} \mathrm{d}\sigma^{\psi(2S)}/\mathrm{d}y$ for $p_{\rm T} < 12$ GeV/c. The error bars represent the statistical uncertainties, while the boxes correspond to total systematic uncertainties. The grey bands correspond to the reference pp cross section scaled by $\mathrm{A}_{\rm Pb}$.

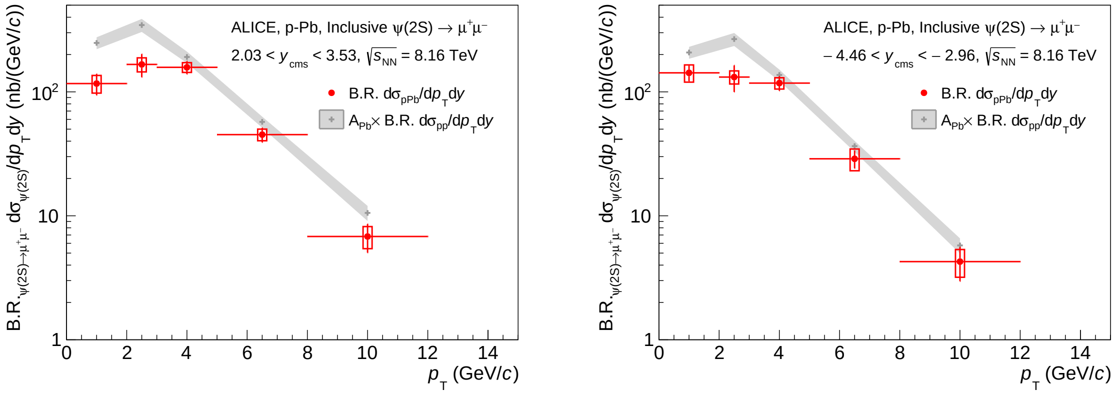

Figure A.13: The differential cross sections $\text{B.R.}_{\psi(2\text{S})\rightarrow\mu^+\mu^-}\text{d}^2\sigma^{\psi(2\text{S})}/\text{d}p_{\rm T}\text{d}y$ for p–Pb (left panel) and Pb–p (right panel) collisions at $\sqrt{s_{\rm NN}} = 8.16$ TeV. The error bars represent the statistical uncertainties, while the boxes correspond to total systematic uncertainties. The grey bands correspond to the reference pp cross section scaled by A_{Pb}.

A.8.2 Ratio $(\sigma_{\psi(2\text{S})}/\sigma_{\text{J}/\psi})_{\text{pPb}}$

The ratio between ψ(2S) and J/ψ cross sections, also called shortly as the *single ratio*, represents an interesting quantity to compare the production cross sections for the two resonances and is computed as:

$$\frac{\text{B.R.}_{\psi(2\text{S})\rightarrow\mu^+\mu^-}\cdot\sigma^{\psi(2\text{S})}_{\text{pPb}}}{\text{B.R.}_{\text{J}/\psi\rightarrow\mu^+\mu^-}\cdot\sigma^{\text{J}/\psi}_{\text{pPb}}} = \frac{N_{\psi(2\text{S})}}{A\times\varepsilon_{\psi(2\text{S})}}\cdot\frac{A\times\varepsilon_{\text{J}/\psi}}{N_{\text{J}/\psi}} \tag{A.13}$$

One of its main advantages is that some of the systematic uncertainties which are in common between ψ(2S) and J/ψ cancel out in the ratio and only those associated to the signal extraction and to the Monte-Carlo input shapes survive. In Fig. A.14 the single ratio integrated over $p_{\rm T} < 12$ GeV/c is shown as a function of rapidity. This result is compared with the measurement performed at $\sqrt{s_{\rm NN}} = 5.02$ TeV corresponding to $p_{\rm T} < 8$ GeV/c [243] and with the ratio ψ(2S)/J/ψ obtained with the interpolation procedure in proton-proton collisions.

The single ratios measured as function of y in p–Pb collisions at $\sqrt{s_{\rm NN}} = 5.02$ and 8.16 TeV agree within the uncertainties, which is an indication of a weak center-of-mass energy dependence of this quantity. Furthermore it should be noticed that the ratio at backward rapidity is significantly lower than the pp one, while at forward they are compatible within the uncertainties. A similar effect can be observed in Fig. A.15, where the single ratio obtained in p–Pb collisions is compared with the pp one as a function of the transverse momentum.

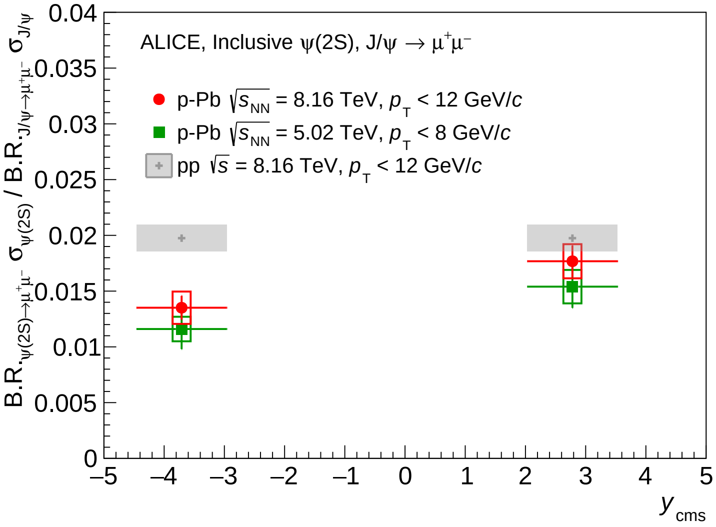

Figure A.14: The ratio $\mathrm{B.R.}_{\psi(2S)\to\mu^+\mu^-}\sigma^{\psi(2S)}/\mathrm{B.R.}_{J/\psi\to\mu^+\mu^-}\sigma^{J/\psi}$ as a function of y for p–Pb collisions at $\sqrt{s_{NN}} = 8.16$ and 5.02 TeV [243], compared with the corresponding pp quantity, shown as a grey band and obtained via an interpolation of results at $\sqrt{s} = 5$, 7, 8 and 13 TeV [92]. The error bars represent the statistical uncertainties, while the boxes correspond to uncorrelated systematic uncertainties.

In Fig. A.16 the ratio $\psi(2S)/J/\psi$ obtained at $\sqrt{s_{NN}} = 8.16$ TeV is shown as a function of the number of collisions, separately for forward and backward rapidities. The results are compared with the same quantity in p–Pb collisions at $\sqrt{s_{NN}} = 5.02$ TeV [251]. The pp value is also indicated as a line in the plot [94]. Also in this case the dependence on the center-of-mass energy is not visible. Secondly the ratio is smaller that the pp one in both the rapidity ranges under study, with the exception of the most central and peripheral collisions. Given the current experimental uncertainties it is not possible to extract a clear trend of the ratio $\psi(2S)/J/\psi$ as a function of centrality, nevertheless the $\psi(2S)$ is clearly more suppressed than J/ψ at backward rapidity, in agreement with what has been observed as function of p_T and y.

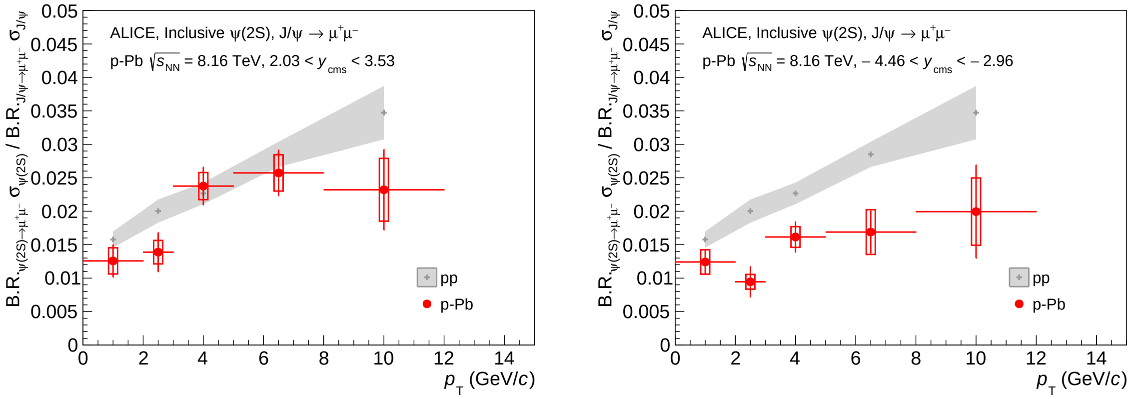

Figure A.15: The ratio $\mathrm{B.R.}_{\psi(2S)\rightarrow\mu^+\mu^-}\sigma^{\psi(2S)}/\mathrm{B.R.}_{J/\psi\rightarrow\mu^+\mu^-}\sigma^{J/\psi}$ as a function of $p_{\rm T}$, for p–Pb collisions at $\sqrt{s_{\rm NN}} = 8.16$ TeV, compared with the corresponding pp quantity, shown as a grey band and obtained via an interpolation of results at $\sqrt{s} = 7$, 8 and 13 TeV [92]. The error bars represent the statistical uncertainties, while the boxes correspond to uncorrelated systematic uncertainties.

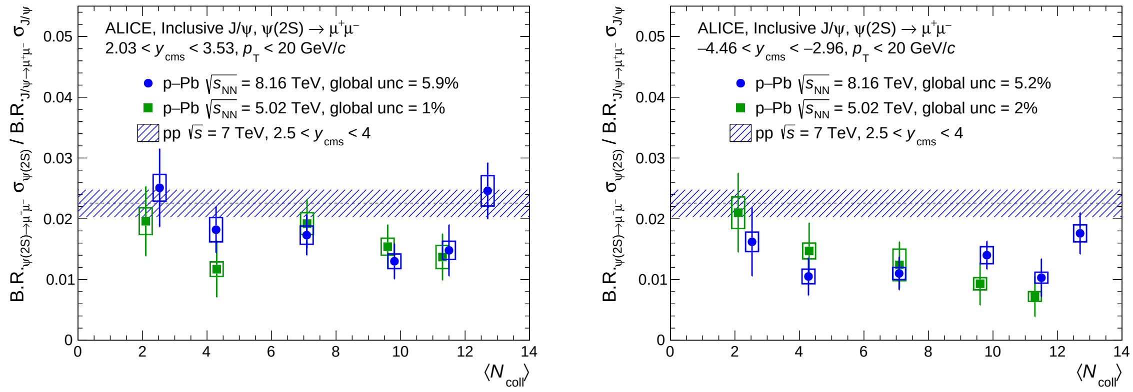

Figure A.16: $\mathrm{B.R.}_{\psi(2S)\rightarrow\mu^+\mu^-}\sigma_{\psi(2S)}/\mathrm{B.R.}_{J/\psi\rightarrow\mu^+\mu^-}\sigma_{J/\psi}$ as a function of $\langle N_{\rm coll}\rangle$ at backward (left) and forward (right) rapidity compared with the measurement in pp collisions at $\sqrt{s} = 7$ TeV [94] (line with the band representing the total uncertainty), and to the results at $\sqrt{s_{\rm NN}} = 5.02$ TeV [251]. Vertical error bars represent the statistical uncertainties, while the open boxes correspond to the systematic uncertainties.

A.8.3 Ratio $(\sigma_{\psi(2\mathrm{S})}/\sigma_{\mathrm{J}/\psi})_{\mathrm{pPb}}/(\sigma_{\psi(2\mathrm{S})}/\sigma_{\mathrm{J}/\psi})_{\mathrm{pp}}$

The so-called *double ratio* allows to compare the relative suppression of the $\psi(2\mathrm{S})$ with respect to the J/ψ in different colliding systems and is computed as:

$$\left(\frac{\sigma_{\psi(2\mathrm{S})}}{\sigma_{\mathrm{J}/\psi}}\right)_{\mathrm{pPb}}\Bigg/\left(\frac{\sigma_{\psi(2\mathrm{S})}}{\sigma_{\mathrm{J}/\psi}}\right)_{\mathrm{pp}} = \left(\frac{N^{\mathrm{corr}}_{\psi(2\mathrm{S})}}{N^{\mathrm{corr}}_{\mathrm{J}/\psi}}\right)_{\mathrm{pPb}} \cdot \left(\frac{\mathrm{B.R.}_{\mathrm{J}/\psi\to\mu^+\mu^-}\cdot\sigma_{\mathrm{J}/\psi}}{\mathrm{B.R.}_{\psi(2\mathrm{S})\to\mu^+\mu^-}\cdot\sigma_{\psi(2\mathrm{S})}}\right)_{\mathrm{pp}} \tag{A.14}$$

where N^{corr} is the raw yield corrected by $A\times\varepsilon$, while the ratio $\psi(2\mathrm{S})/\mathrm{J}/\psi$ in proton-proton collisions is the one obtained via the interpolation procedure. Similarly to the single ratio, one of the advantages of this observable is that some of the systematic uncertainties which are shared among $\psi(2\mathrm{S})$ and J/ψ cancel out, as those related to the trigger efficiency, tracking and matching. In Fig. A.17 the double ratio obtained at $\sqrt{s_{\mathrm{NN}}} = 8.16$ TeV is compared with the one at $\sqrt{s_{\mathrm{NN}}} = 5.02$ TeV. The measurement also confirms as expected the larger suppression for $\psi(2\mathrm{S})$ at backward rapidity.

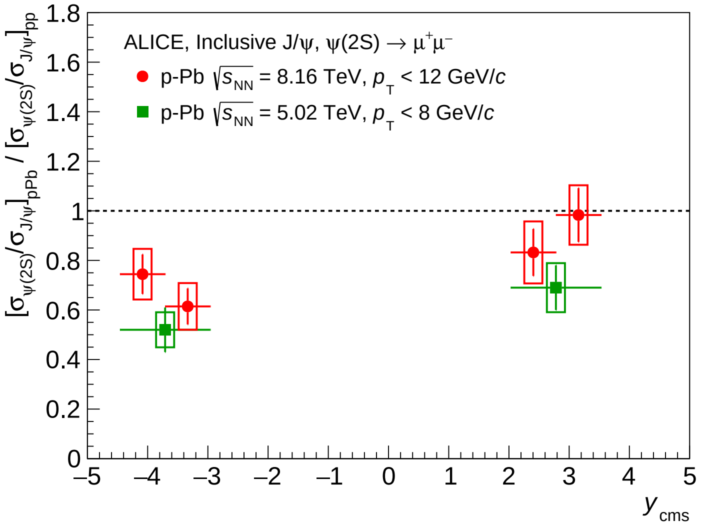

Figure A.17: Double ratio of $\psi(2\mathrm{S})$ and J/ψ cross sections in p–Pb and pp collisions as a function of rapidity, at $\sqrt{s_{\mathrm{NN}}} = 8.16$ TeV, compared with the corresponding results at $\sqrt{s_{\mathrm{NN}}} = 5.02$ TeV [243]. The error bars represent the statistical uncertainties, while the boxes correspond to uncorrelated systematic uncertainties.

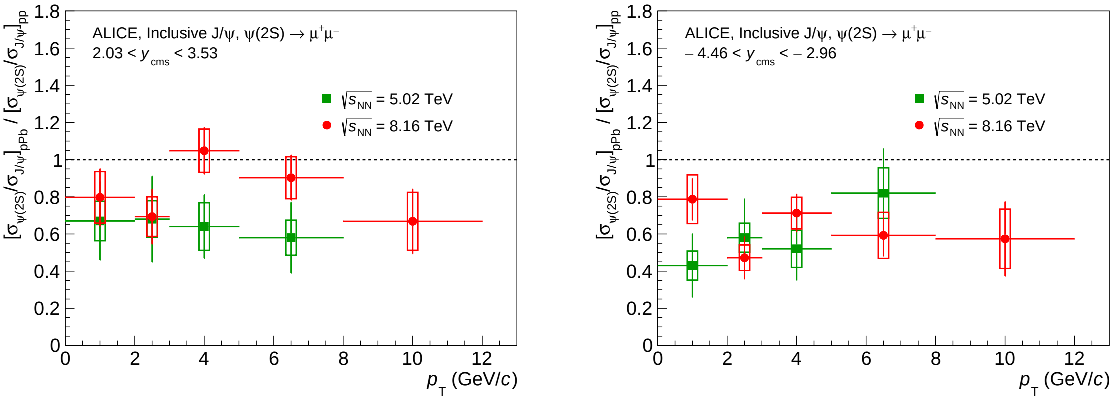

Figure A.18: Double ratio of $\psi(2S)$ and J/ψ cross sections in p–Pb and pp collisions as a function of transverse momentum, at forward (left) and backward (right) rapidity at $\sqrt{s_{\rm NN}} = 8.16$ TeV, compared with the corresponding results at $\sqrt{s_{\rm NN}} = 5.02$ TeV [243]. The error bars represent the statistical uncertainties, while the boxes correspond to uncorrelated systematic uncertainties.

In Fig. A.18 the double ratio is shown as a function of the transverse momentum for p–Pb and Pb–p collisions at $\sqrt{s_{\rm NN}} = 8.16$ and 5.02 TeV. The $p_{\rm T}$-dependence does not indicate a clear trend, while the results at the two energies are in fair agreement.

Finally the double ratio is evaluated as a function of the mean number of collisions and it is shown in Fig. A.19, separating the results for forward and backward rapidities. This result confirms the weak energy dependence of the double ratio. The measurements are also compared with the calculations from a comover model [119]. In this model $\psi(2S)$ and J/ψ can be dissociated interacting with "comoving particles" which are produced in the same rapidity region. The partonic or hadronic nature of *comovers* is not defined in the model. For these specific calculations the resonance dissociation is determined by the interaction cross section among comovers and the charmonium resonance, which is fixed from lower-energy experiments. This comparison with the double ratio is particularly appropriate, since its main source of uncertainty is due to the nuclear PDF parametrization, which cancels out in the ratio because it is strongly correlated between J/ψ and $\psi(2S)$. In Fig. A.19 data are shown to be in good agreement with theoretical predictions. A slight decrease of the double ratio with increasing $\sqrt{s_{\rm NN}}$, due to the corresponding increase of the comover density, is foreseen, but the effect is quite small and cannot be verified experimentally.

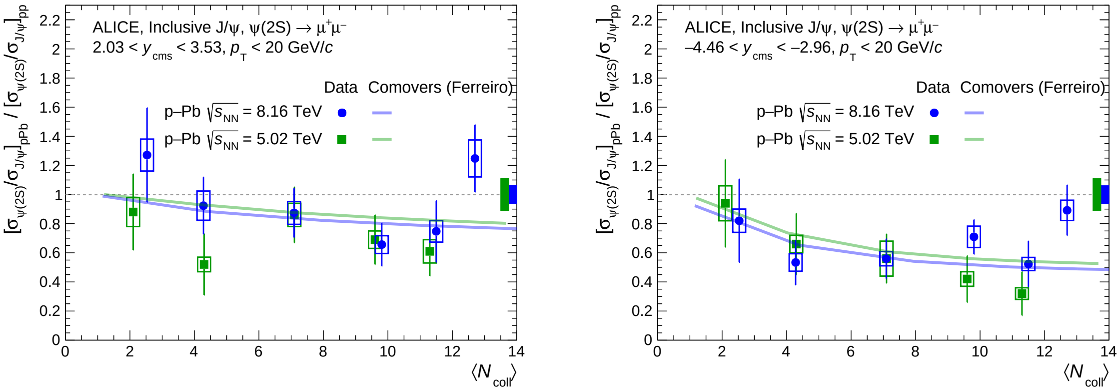

Figure A.19: Double ratio as a function of $\langle N_{\rm coll}\rangle$ at backward (left) and forward (right) rapidity compared with the one at $\sqrt{s_{\rm NN}} = 5.02$ TeV [252]. The vertical error bars represent the statistical uncertainties and the open boxes around the data points the uncorrelated systematic uncertainties. The boxes around unity represent the correlated systematic uncertainty and correspond to the uncertainty on the ratio $\psi(2S)/J/\psi$ in pp collisions. Experimental points are compared with the theoretical predictions of the comovers model at $\sqrt{s_{\rm NN}} = 5.02$ TeV (green line [119]) and $\sqrt{s_{\rm NN}} = 8.16$ TeV (blue line [253],[117]).

A.8.4 Nuclear modification factor

The $\psi(2S)$ *nuclear modification factor* is computed as:

$$R^{\psi(2S)}_{\rm pPb} = \frac{N^{\rm corr}_{\psi(2S)}}{\langle T_{\rm pPb}\rangle \cdot N_{\rm MB} \cdot {\rm B.R.}_{\psi(2S)\to\mu^+\mu^-} \cdot \sigma^{\psi(2S)}_{\rm pp}}, \tag{A.15}$$

where $\langle T_{\rm pPb}\rangle$ is the average nuclear thickness function and $N_{\rm MB}$ is the number of minimum bias events. The latter quantity is obtained multiplying the number of dimuon triggers (CMUL7) by a normalization factor ($\rm F_{norm}$) which corresponds to the inverse of the probability of producing a dimuon in a MB event. The numerical values for the region $p_{\rm T} < 12$ GeV/c, are:

$$R^{\psi(2S)}_{\rm pPb}(2.03 < y_{\rm cms} < 3.53) = 0.628 \pm 0.050 \pm 0.069 \pm 0.045$$
$$R^{\psi(2S)}_{\rm Pbp}(-4.46 < y_{\rm cms} < -2.96) = 0.684 \pm 0.054 \pm 0.088 \pm 0.049$$

where the first uncertainty is statistical, while the second and the third are the the uncorrelated and correlated systematic uncertainty respectively.

In Fig. A.20 the $\psi(2S)$ nuclear modification factor is shown as a function of rapidity. In both the forward and backward rapidity regions the R_{pA} is lower than unity and the $\psi(2S)$ suppression reaches 30–40%. It is important to notice that if compared with the J/ψ, the $\psi(2S)$ R_{pA} is compatible at forward rapidity, while at backward it is significantly smaller. The results are compared with theoretical calculation based on the CGC approach [121, 117], on coherent energy loss [116, 117] and on nuclear shadowing, implemented with different parameterizations (EPS09NLO [122], nCTEQ15 [124]). All these theoretical predictions are based on *initial state effects* and are expected to influence in a similar way the two resonances. Nevertheless, even if they are able to describe properly the J/ψ behavior, they fail with the $\psi(2S)$ at backward rapidity. For this reason the impact of *final state effects* should be taken into account. In CGC + ICEM [120] the break-up of the charmonium resonance occurs already at a partonic level via soft color exchanges with the hadronizing $c\bar{c}$ pair. The model calculation is available only at forward rapidity since they are performed within the framework of the Color Glass Condensate effective theory, which is applicable only for low Bjorken-x values, corresponding to the forward rapidity region.

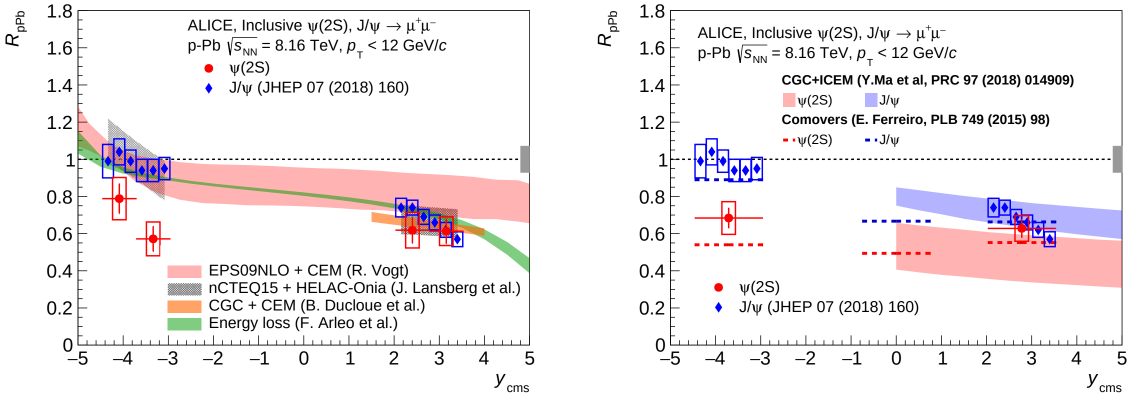

Figure A.20: The y-dependence of R_{pPb} for $\psi(2S)$ and J/ψ [249] in p–Pb collisions at $\sqrt{s_{NN}} = 8.16$ TeV. The box around $R_{pPb} = 1$ to correlated systematic uncertainties. The results are compared with models including initial-state effects [121, 117, 118] and coherent energy loss [116, 117] (left panel), and to models which also implement final-state effects [120, 119] (right panel).

In Fig. A.20 the comovers model [119] results are also shown. In the model the charmonium dissociation is due to the interaction with soft particles, which affect more strongly the $\psi(2S)$ than the J/ψ , given its larger size. This effect is proportional to the density of comovers, therefore is more significant in central collisions in the nucleus-going direction.

Both models are in fair agreement with data, in particular it is clear that including final state effects it is possible to reproduce the different suppression for $\psi(2S)$ and J/ψ .
In Fig. A.21 the $\psi(2S)$ nuclear modification factor at $\sqrt{s_{NN}} = 8.16$ and 5.02 TeV is shown together with models implementing final state effects. The results at the two energies are compatible within the uncertainties and with the theoretical predictions, even if the size of the uncertainties does not allow to be sensitive to the larger suppression predicted at higher center-of-mass energies.

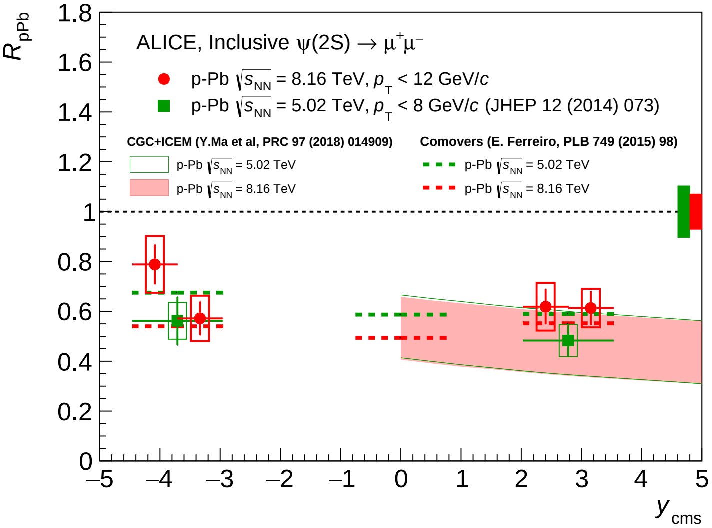

Figure A.21: Comparison of the rapidity dependence of R_{pPb} for $\psi(2S)$ in p–Pb collisions at $\sqrt{s_{NN}} = 8.16$ and 5.02 TeV [243]. The error bars represent the statistical uncertainties, while the boxes correspond to uncorrelated systematic uncertainties and the boxes at $R_{pPb} = 1$ to correlated systematic uncertainties, separately shown for the two energies. The results are also compared with theoretical models that include final-state effects [120, 119].

The p_T-dependence of the nuclear modification factor is also investigated, as shown in Fig. A.22. It can be noticed that at forward rapidity the $\psi(2S)$ suppression is compatible with the J/ψ one and with the prediction of CGC+ICEM model [120]. In the backward rapidity region the $\psi(2S)$ R_{pA} is systematically lower than the J/ψ one. The large size of the statistical and systematic uncertainties does not allow to identify a clear trend for the nuclear modification factor as a function of the transverse momentum.

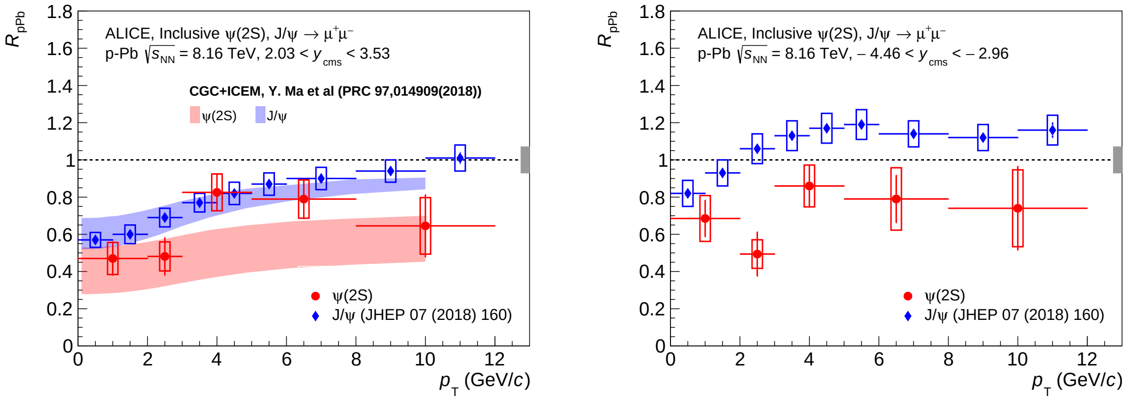

Figure A.22: The p_{T}-dependence of R_{pPb} for $\psi(2S)$ and J/ψ at forward (left) and backward (right) rapidity in p–Pb collisions, at $\sqrt{s_{\mathrm{NN}}} = 8.16$ TeV. The error bars represent the statistical uncertainties, while the boxes correspond to uncorrelated systematic uncertainties and the box at $R_{\mathrm{pPb}} = 1$ to correlated systematic uncertainties. The comparison with the results of a CGC-based model [120], which implements final-state effects, is also shown.

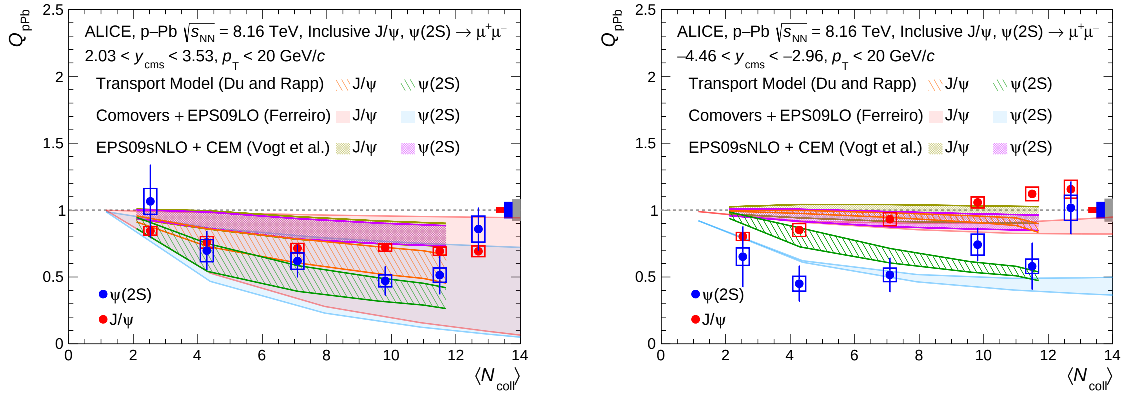

Figure A.23: Inclusive $\psi(2S)$ Q_{pPb} as a function of $\langle N_{\mathrm{coll}}\rangle$ at backward (left) and forward (right) rapidity compared to J/ψ Q_{pPb} and with the theoretical models. Vertical error bars represent the statistical uncertainties, while the open boxes around the data points correspond to the uncorrelated systematic uncertainties. The red and blue boxes around unity represent the correlated systematic uncertainty specific to the J/ψ and $\psi(2S)$, respectively. The grey box corresponds to the common systematic uncertainty correlated over $\langle N_{\mathrm{coll}}\rangle$.

The nuclear modification factor is also studied as a function of the mean number of collisions, as shown in Fig. A.23. The notation Q_{pA} is used instead of the standard R_{pA} in order to indicate the possible bias due to the loose correlation among the collision geometry and the centrality estimator [254]. The results are compared with EPS09s NLO + CEM calculations [255], which implement initial state effects and provides similar values for $\psi(2S)$ and J/ψ , failing in the description of the first. Even if compatible within the uncertainties, the J/ψ nuclear modification factor exhibits a different behavior as function of centrality with respect to the theoretical predictions at backward rapidity. On the other hand the comovers model [119] is able to describe qualitatively the different suppression for $\psi(2S)$ and J/ψ, even if the large uncertainties do not allow to draw a firm conclusion at forward rapidity. In the transport model [136], which exhibits a fair agreement with experimental data, the larger $\psi(2S)$ suppression is caused by its dissociation inside the short-living QGP and hadron resonance gas phases. From all these it is clear that a detailed description of the $\psi(2S)$ behavior needs the inclusion of final state effects, whose nature is still under debate.

A.9 Conclusions

The $\psi(2S)$ production has been studied in proton-nucleus collisions at $\sqrt{s_{NN}} = 8.16$ TeV as a function of rapidity, transverse momentum and centrality. The collected data sample allowed to improve the precision of the measurements with respect to the results obtained at $\sqrt{s_{NN}} = 5.02$ TeV [243], adopting a narrower binning and reaching higher p_T range.
The nuclear modification factor indicates a $\psi(2S)$ suppression of the order of 30–40%, similar at backward and forward rapidity. If compared with J/ψ , the $\psi(2S)$ suppression is stronger in the Pb-going direction, while for the p-going one the two results agree within the uncertainties. No clear dependence on the collision energy has been observed.
The comparison with theoretical models indicates that final state effects are crucial in the description of the $\psi(2S)$ and J/ψ behaviors. In fact initial states effects, as parton shadowing and energy loss, should affect similarly the two states, nevertheless these predictions are not confirmed by experimental measurements. On the other hand the inclusion of final state interaction with comoving particles improves the agreement among data and theory, even if the size of the uncertainties on the model calculations limits for the moment a complete understanding of all the mechanisms at play.
Future theory developments in the determination of the comover's nature and a parallel improvement in the precision of the experimental measurements expected in Run 3 and Run 4 of the LHC, will likely extend our understanding of these effects.

Appendix B

Polarization parameters extraction

B.1 J/ψ polarization as a function of p_{T}

In the following some of the fits to the J/ψ corrected angular distributions are reported as a function of p_{T}. The corresponding J/ψ yield has been extracted fitting the dimuon invariant mass distribution with the extended Crystal Ball (CB2) for the signal and a Variable Width Gaussian (VWG) for the background.

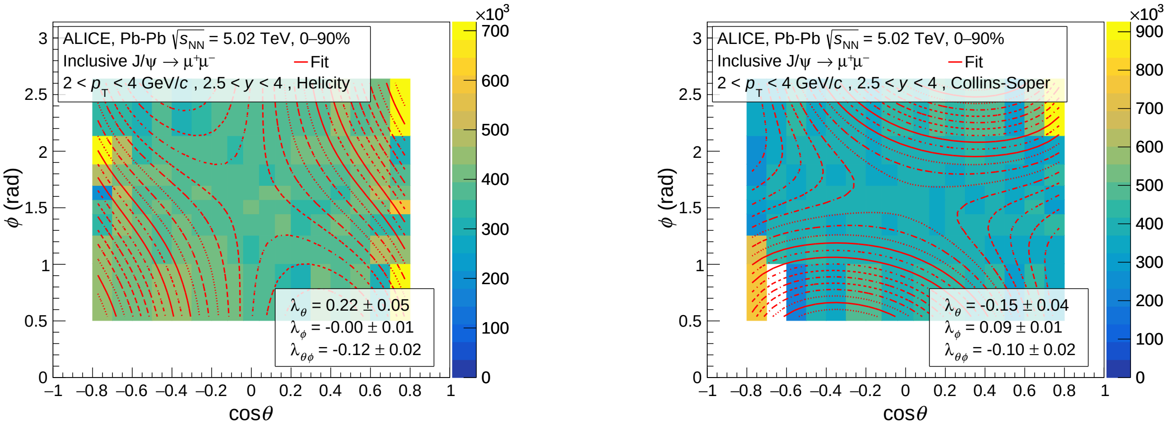

Figure B.1: Fit to the J/ψ angular distribution $A \times \varepsilon$-corrected in the helicity (left panel) and Collins-Soper (right panel) reference frames and corresponding to $2 < p_{\mathrm{T}} < 4$ GeV/c.

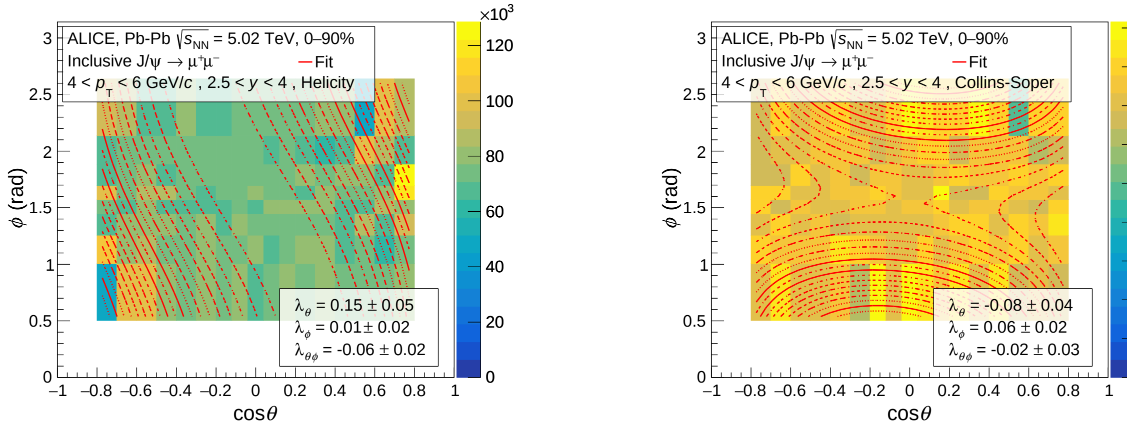

Figure B.2: Fit to the J/ψ angular distribution $A \times \varepsilon$-corrected in the helicity (left panel) and Collins-Soper (right panel) reference frames and corresponding to $4 < p_{\mathrm{T}} < 6$ GeV/c.

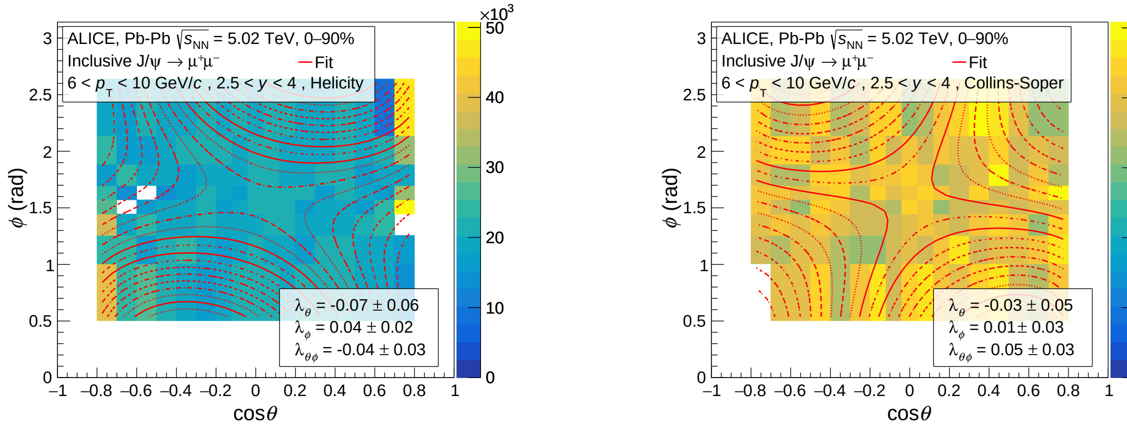

Figure B.3: Fit to the J/ψ angular distribution $A \times \varepsilon$-corrected in the helicity (left panel) and Collins-Soper (right panel) reference frames and corresponding to $6 < p_{\mathrm{T}} < 10$ GeV/c.

B.2 J/ψ polarization as a function of centrality

In the following some of the fits to the J/ψ corrected angular distributions are reported as a function of centrality. The corresponding J/ψ yield has been extracted fitting the dimuon invariant mass distribution with the extended Crystal Ball (CB2) for the signal and a Variable Width Gaussian (VWG) for the background.

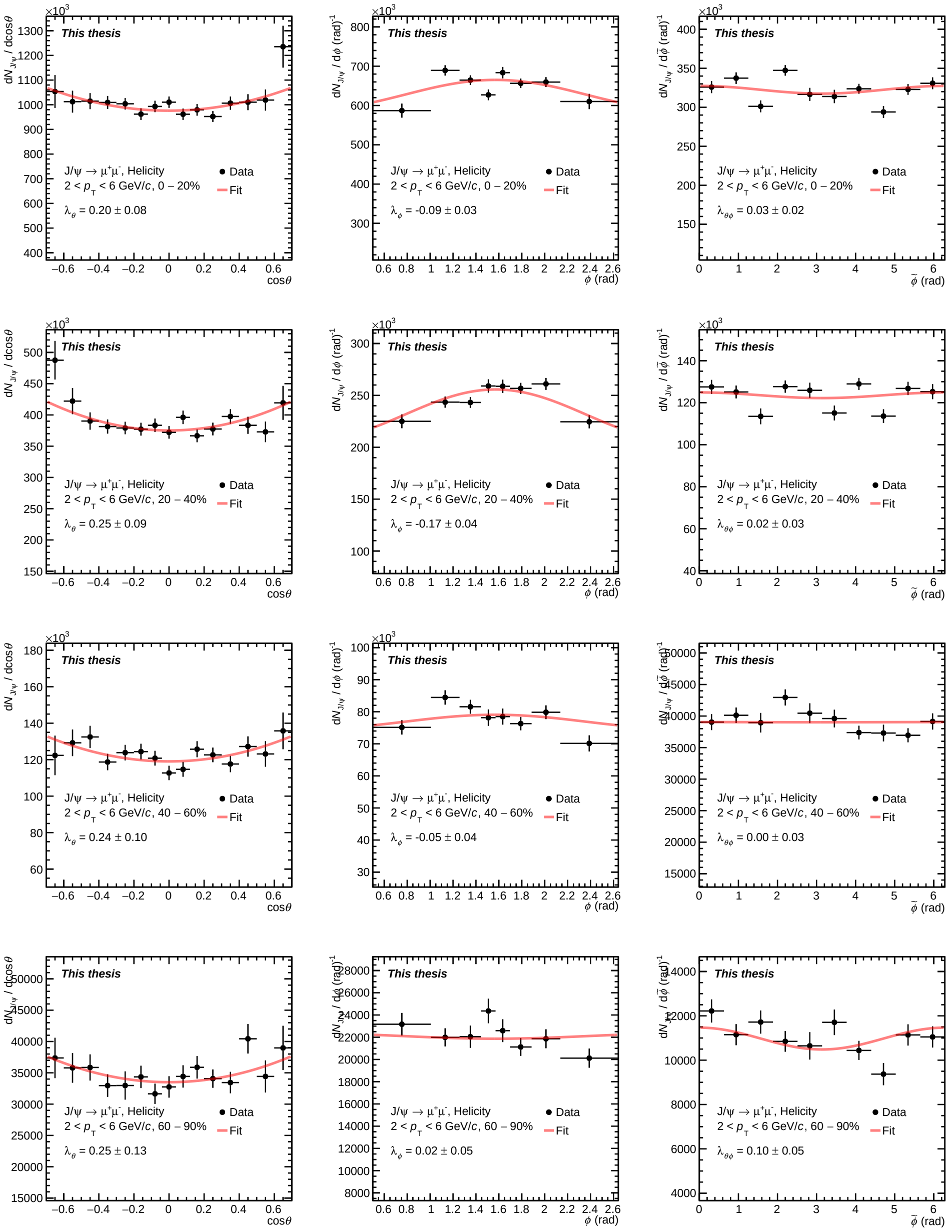

Figure B.4: Fit to the J/ψ angular distributions $A \times \varepsilon$-corrected in the helicity reference frame in four different centrality classes: 0–20, 20–40, 40–60 and 60–90%.

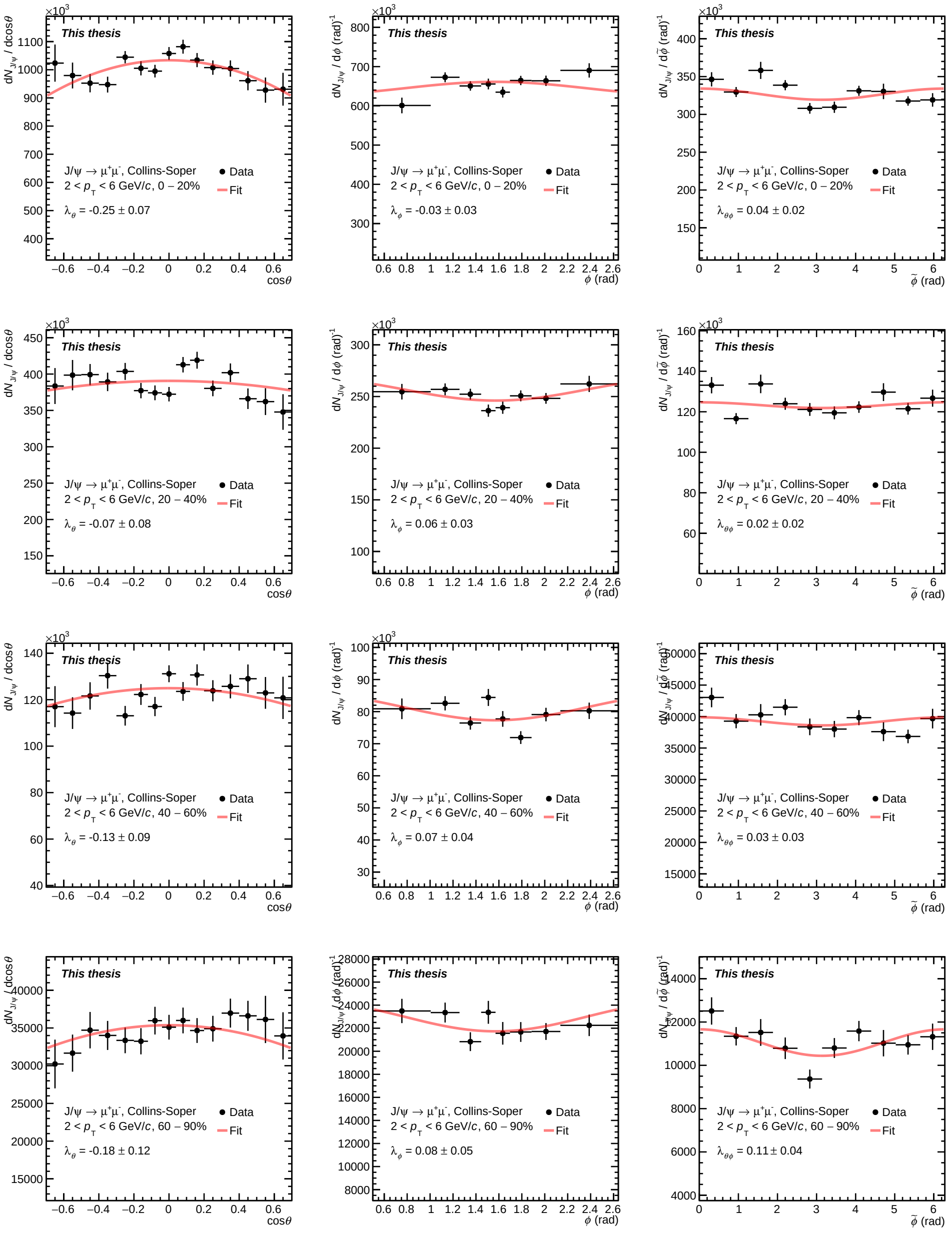

Figure B.5: Fit to the J/ψ angular distributions $A \times \varepsilon$-corrected in the Collins-Soper reference frame in four different centrality classes: 0–20, 20–40, 40–60 and 60–90%.

Appendix C

Centrality determination in ALICE

In heavy-ion collisions the impact parameter vector b connects the center of the colliding nuclei and lays on the plane perpendicular to the beam direction. Since it cannot be directly measured, the geometry of the collision can be evaluated in terms of *centrality*. The latter is directly related to the impact parameter, in particular collisions with small impact parameter are defined as central, while for large values of b they are denoted as peripheral. From an experimental point of view the centrality can be estimated through the charged-particles multiplicity (N_{ch}) and the energy carried by the particles traveling along the beam direction, measured in ALICE by the V0 detector and by the Zero Degree Calorimeter (ZDC) respectively. The connection among these two quantities and the impact parameter is provided by the Glauber model [22]. This model, in which nucleus-nucleus collisions are treated as a sequence of binary nucleon-nucleon interactions, provides a quantitative expression to compute the number of participants (N_{part}) and the number of binary collisions (N_{coll}). In principle, centrality can be expressed in terms of b as a percentile of the hadronic interaction cross section σ_{AA}:

$$c(b) \approx \int_0^{b_0} \frac{\mathrm{d}\sigma}{\mathrm{d}b'}\mathrm{d}b' \Bigg/ \int_0^{\infty} \frac{\mathrm{d}\sigma}{\mathrm{d}b'}\mathrm{d}b' = \frac{1}{\sigma_{\mathrm{AA}}} \int_0^{b_0} \frac{\mathrm{d}\sigma}{\mathrm{d}b'}\mathrm{d}b' \tag{C.1}$$

This expression can be rewritten in terms of particle multiplicity (N_{ch}) and energy deposited in the ZDC (E_{ZDC}) above a given threshold, assuming their monotonic behavior with the overlap volume:

$$c \approx \frac{1}{\sigma_{\mathrm{AA}}} \int_{N_{\mathrm{ch}}^{THR}}^{\infty} \frac{\mathrm{d}\sigma}{\mathrm{d}N_{\mathrm{ch}}'}\mathrm{d}N_{\mathrm{ch}}' \approx \frac{1}{\sigma_{\mathrm{AA}}} \int_0^{E_{\mathrm{ZDC}}^{THR}} \frac{\mathrm{d}\sigma}{\mathrm{d}E_{\mathrm{ZDC}}'}\mathrm{d}E_{\mathrm{ZDC}}' \tag{C.2}$$

For the ZDC this assumption holds up to $c \lesssim 50\%$. This happens because the nuclear fragments, with a charge-over-mass ratio similar to the beam, continue to travel along the beam pipe and are not detected by the ZDC. This effect is mainly observed in peripheral collisions and in order to cope with it the ZDC information is correlated with the one of the two electromagnetic calorimeters (ZEM).

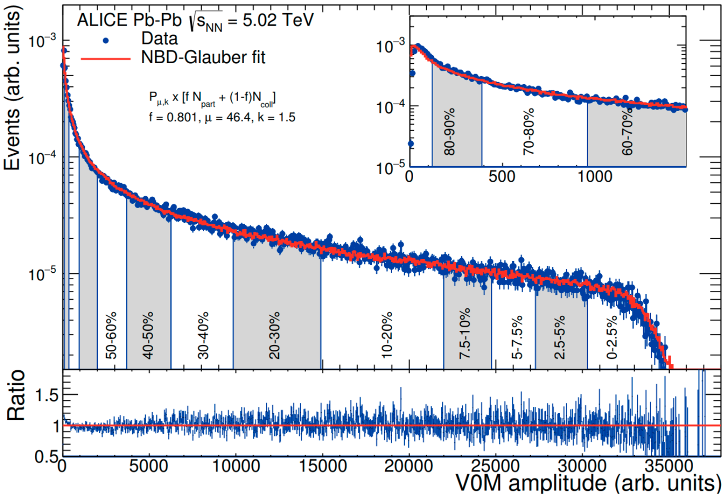

Figure C.1: Distribution of the sum of amplitudes in the V0 scintillators for Pb–Pb collisions at $\sqrt{s_{\rm NN}} = 5.02$ TeV [238]. The distribution is fitted with the NBD-Glauber fit shown as a line. The insert shows a zoom of the most peripheral region.

In Fig. C.1 the V0 signal amplitude is shown for Pb–Pb collisions at $\sqrt{s_{\rm NN}} = 5.02$ TeV [238]. The experimental multiplicity distribution is reproduced coupling the Glauber Monte Carlo to a model for particle production, based on negative binomial distribution (NBD):

$$P_{\mu,k}(n) = \frac{\Gamma(n+k)}{\Gamma(n+1)\Gamma(k)} \cdot \frac{(\mu/k)^n}{(\mu/k+1)^n} \tag{C.3}$$

where μ is the mean multiplicity per emitting source (namely *ancestor*) and k controls the width. This distribution provides the probability to measure n hits per emitting source and it is sampled $N_{\rm ancestors}$ times to reproduce the average V0 simulated amplitude for a certain event. Since it can be assumed that $N_{\rm ancestors} = f \cdot N_{\rm part} + (1-f) \cdot N_{\rm coll}$, after having performed a χ^2 fit to evaluate the best parametrization for μ, k and f, the mean number of participants $\langle N_{\rm part} \rangle$ and collisions $\langle N_{\rm coll} \rangle$ is obtained.

Acknowledgements

These three years have been an amazing experience, enriched by all the human aspects which make unique the life of a physicist.
First of all I would like to thank Enrico Scomparin and Roberta Arnaldi, for all their support since the very beginning of my work as a researcher. Their suggestions, together with the continuous and fruitful discussions, have represented one of the key points to overcome all the difficulties I encountered to complete the work presented in this thesis. A special acknowledgment to Livio Bianchi, who introduced me to the complex world of polarization and for the ideas of new applications of this interesting (and sometimes mysterious) observable.
I would like to thank all the ALICE group in Torino, in particular Gabriele Fronzé, Biswarup Paul and Antonio Bianchi. I thank all the colleagues I met during my year at CERN as cooperation associate, especially Mattia Faggin, who shared with me all the unexpected events of this 2020.
I want to thank all the members of the PWG DQ, for the discussions and the constructive questions which helped me to improve my expertise in many aspects of quarkonium studies.

I would like to dedicate a special thank to all my friends, Riccardo, Nicoló, Lorenzo, Silvia, Silvia and Alessandra, who make me think that being happy is a matter of people we decide to share our path with.
I want to thank my family for everything and for believing in me probably more than I have ever believed in myself.
Finally the most important thank to my Michela, the reason why I know how to save a life and the person I dedicate all this thesis.

References

[1] S. Acharya *et al.*, “First measurement of quarkonium polarization in nuclear collisions at the LHC,” 5 2020.

[2] S. Acharya *et al.*, “Measurement of nuclear effects on $\psi(2S)$ production in p-Pb collisions at $\sqrt{s_{\mathrm{NN}}} = 8.16$ TeV,” *JHEP*, vol. 07, p. 237, 2020.

[3] S. Acharya *et al.*, “Centrality dependence of J/ψ and $\psi(2S)$ production and nuclear modification in p-Pb collisions at $\sqrt{s_{\mathrm{NN}}} = 8.16$ TeV,” 8 2020.

[4] A. Pich, “The Standard Model of Electroweak Interactions. The Standard model of electroweak interactions,” pp. 1–49. 50 p, Jun 2007.

[5] Patrignani. et al., “Review of Particle Physics, 2016-2017,” *Chin. Phys. C*, vol. 40, no. 10, p. 100001. 1808 p, 2016.

[6] P. Huovinen and P. Petreczky, “QCD Equation of State and Hadron Resonance Gas,” *Nucl. Phys. A*, vol. 837, pp. 26–53, 2010.

[7] F. Karsch and E. Laermann, “Thermodynamics and in medium hadron properties from lattice QCD,” pp. 1–59, 5 2003.

[8] M. G. Alford, A. Schmitt, K. Rajagopal, and T. Schfer, “Color superconductivity in dense quark matter,” *Rev. Mod. Phys.*, vol. 80, pp. 1455–1515, 2008.

[9] A. Chodos, R. L. Jaffe, K. Johnson, C. B. Thorn, and V. F. Weisskopf, “New extended model of hadrons,” *Phys. Rev. D*, vol. 9, pp. 3471–3495, Jun 1974.

[10] R. S. Bhalerao, “Relativistic heavy-ion collisions,” pp. 219–239. 21 p, Apr 2014. Comments: Updated version of the lectures given at the First Asia-Europe-Pacific School of High-Energy Physics, Fukuoka, Japan, 14-27 October 2012. Published as a

CERN Yellow Report (CERN-2014-001) and KEK report (KEK-Proceedings-2013-8), K. Kawagoe and M. Mulders (eds.), 2014, p. 219. Total 21 pages.

[11] F. Karsch, K. Redlich, and A. Tawfik, "Hadron resonance mass spectrum and lattice QCD thermodynamics," *Eur. Phys. J. C*, vol. 29, pp. 549–556, 2003.

[12] A. Bazavov *et al.*, "Equation of state in (2+1)-flavor QCD," *Phys. Rev. D*, vol. 90, p. 094503, 2014.

[13] A. Bazavov *et al.*, "The chiral and deconfinement aspects of the QCD transition," *Phys. Rev. D*, vol. 85, p. 054503, 2012.

[14] J. Bjorken, "Highly Relativistic Nucleus-Nucleus Collisions: The Central Rapidity Region," *Phys. Rev. D*, vol. 27, pp. 140–151, 1983.

[15] R. Sahoo, A. N. Mishra, N. K. Behera, and B. K. Nandi, "Charged Particle, Photon Multiplicity, and Transverse Energy Production in High-Energy Heavy-Ion Collisions," *Adv. High Energy Phys.*, vol. 2015, p. 612390, 2015. [Erratum: Adv.High Energy Phys. 2017, 4517153 (2017)].

[16] P. Braun-Munzinger and B. Dönigus, "Loosely-bound objects produced in nuclear collisions at the LHC," *Nucl. Phys. A*, vol. 987, pp. 144–201, 2019.

[17] C. Gale, S. Jeon, and B. Schenke, "Hydrodynamic Modeling of Heavy-Ion Collisions," *Int. J. Mod. Phys. A*, vol. 28, p. 1340011, 2013.

[18] D. Tlusty, "The RHIC Beam Energy Scan Phase II: Physics and Upgrades," in *13th Conference on the Intersections of Particle and Nuclear Physics*, 10 2018.

[19] J. M. Heuser, "The Compressed Baryonic Matter Experiment at FAIR: Progress with feasibility studies and detector developments," *Nucl. Phys. A*, vol. 830, pp. 563C–566C, 2009.

[20] L. Turko, "NA61/SHINE Experiment—Program beyond 2020," *Particles*, vol. 1, no. 1, pp. 296–304, 2018.

[21] T. Dahms, E. Scomparin, and G. Usai, "Expression of Interest for a new experiment at the CERN SPS: NA60+," Tech. Rep. CERN-SPSC-2019-017. SPSC-EOI-019, CERN, Geneva, May 2019.

[22] M. L. Miller, K. Reygers, S. J. Sanders, and P. Steinberg, "Glauber modeling in high energy nuclear collisions," *Ann. Rev. Nucl. Part. Sci.*, vol. 57, pp. 205–243, 2007.

[23] S. Adler *et al.*, "Centrality dependence of direct photon production in s(NN)**(1/ 2) = 200-GeV Au + Au collisions," *Phys. Rev. Lett.*, vol. 94, p. 232301, 2005.

[24] G. Aad *et al.*, "Centrality, rapidity and transverse momentum dependence of isolated prompt photon production in lead-lead collisions at $\sqrt{s_{\mathrm{NN}}} = 2.76$ TeV measured with the ATLAS detector," *Phys. Rev. C*, vol. 93, no. 3, p. 034914, 2016.

[25] S. Chatrchyan *et al.*, "Measurement of isolated photon production in *pp* and PbPb collisions at $\sqrt{s_{NN}} = 2.76$ TeV," *Phys. Lett. B*, vol. 710, pp. 256–277, 2012.

[26] A. Adare *et al.*, "Centrality dependence of low-momentum direct-photon production in Au+Au collisions at $\sqrt{s_{_{NN}}} = 200$ GeV," *Phys. Rev. C*, vol. 91, no. 6, p. 064904, 2015.

[27] J. Adam *et al.*, "Direct photon production in Pb-Pb collisions at $\sqrt{s_{\mathrm{NN}}} = 2.76$ TeV," *Phys. Lett. B*, vol. 754, pp. 235–248, 2016.

[28] D. G. d'Enterria and D. Peressounko, "Probing the QCD equation of state with thermal photons in nucleus-nucleus collisions at RHIC," *Eur. Phys. J. C*, vol. 46, pp. 451–464, 2006.

[29] S. Afanasiev *et al.*, "Measurement of Direct Photons in Au+Au Collisions at $\sqrt{s_{NN}} =$ 200 GeV," *Phys. Rev. Lett.*, vol. 109, p. 152302, 2012.

[30] B. Abelev *et al.*, "Systematic Measurements of Identified Particle Spectra in pp, d^{+} Au and Au+Au Collisions from STAR," *Phys. Rev. C*, vol. 79, p. 034909, 2009.

[31] S. Adler *et al.*, "Identified charged particle spectra and yields in Au+Au collisions at S(NN)**1/2 = 200-GeV," *Phys. Rev. C*, vol. 69, p. 034909, 2004.

[32] B. Abelev *et al.*, "Pion, Kaon, and Proton Production in Central Pb–Pb Collisions at $\sqrt{s_{NN}} = 2.76$ TeV," *Phys. Rev. Lett.*, vol. 109, p. 252301, 2012.

[33] B. Abelev *et al.*, "Strange particle production in p+p collisions at s**(1/2) = 200-GeV," *Phys. Rev. C*, vol. 75, p. 064901, 2007.

[34] B. Abelev *et al.*, "Centrality dependence of π, K, p production in Pb-Pb collisions at $\sqrt{s_{NN}} = 2.76$ TeV," *Phys. Rev. C*, vol. 88, p. 044910, 2013.

[35] E. Schnedermann, J. Sollfrank, and U. W. Heinz, "Thermal phenomenology of hadrons from 200-A/GeV S+S collisions," *Phys. Rev. C*, vol. 48, pp. 2462–2475, 1993.

[36] R. Snellings, “Elliptic Flow: A Brief Review,” *New J. Phys.*, vol. 13, p. 055008, 2011.

[37] S. Acharya *et al.*, “Anisotropic flow of identified particles in Pb-Pb collisions at $\sqrt{s}_{\mathrm{NN}} = 5.02$ TeV,” *JHEP*, vol. 09, p. 006, 2018.

[38] P. Koch, B. Muller, and J. Rafelski, “Strangeness in Relativistic Heavy Ion Collisions,” *Phys. Rept.*, vol. 142, pp. 167–262, 1986.

[39] F. Antinori *et al.*, “Energy dependence of hyperon production in nucleus nucleus collisions at SPS,” *Phys. Lett. B*, vol. 595, pp. 68–74, 2004.

[40] J. Cleymans, I. Kraus, H. Oeschler, K. Redlich, and S. Wheaton, “Statistical model predictions for particle ratios at s(NN)**(1/2) = 5.5-TeV,” *Phys. Rev. C*, vol. 74, p. 034903, 2006.

[41] F. Becattini and G. Pettini, “Strange quark production in a statistical effective model,” *Phys. Rev. C*, vol. 67, p. 015205, 2003.

[42] T. Sjostrand, S. Mrenna, and P. Z. Skands, “A Brief Introduction to PYTHIA 8.1,” *Comput. Phys. Commun.*, vol. 178, pp. 852–867, 2008.

[43] T. Pierog, I. Karpenko, J. Katzy, E. Yatsenko, and K. Werner, “EPOS LHC: Test of collective hadronization with data measured at the CERN Large Hadron Collider,” *Phys. Rev. C*, vol. 92, no. 3, p. 034906, 2015.

[44] C. Bierlich and J. R. Christiansen, “Effects of color reconnection on hadron flavor observables,” *Phys. Rev. D*, vol. 92, no. 9, p. 094010, 2015.

[45] J. Adam *et al.*, “Enhanced production of multi-strange hadrons in high-multiplicity proton-proton collisions,” *Nature Phys.*, vol. 13, pp. 535–539, 2017.

[46] M. Pluemer, M. Gyulassy, and X. Wang, “Jet quenching and monojet rates in ultrarelativistic nucleus nucleus collisions,” *Nucl. Phys. A*, vol. 590, pp. 511C–514C, 1995.

[47] R. Baier, Y. L. Dokshitzer, S. Peigne, and D. Schiff, “Induced gluon radiation in a QCD medium,” *Phys. Lett. B*, vol. 345, pp. 277–286, 1995.

[48] J. Adams *et al.*, “Evidence from d + Au measurements for final state suppression of high p(T) hadrons in Au+Au collisions at RHIC,” *Phys. Rev. Lett.*, vol. 91, p. 072304, 2003.

[49] S. Acharya *et al.*, "Measurements of inclusive jet spectra in pp and central Pb-Pb collisions at $\sqrt{s_{\mathrm{NN}}} = 5.02$ TeV," *Phys. Rev. C*, vol. 101, no. 3, p. 034911, 2020.

[50] G. Aad and oters, "Measurements of the nuclear modification factor for jets in Pb+Pb collisions at $\sqrt{s_{\mathrm{NN}}} = 2.76$ TeV with the atlas detector," *Phys. Rev. Lett.*, vol. 114, p. 072302, Feb 2015.

[51] M. Aaboud *et al.*, "Measurement of the nuclear modification factor for inclusive jets in Pb+Pb collisions at $\sqrt{s_{\mathrm{NN}}} = 5.02$ TeV with the ATLAS detector," *Phys. Lett. B*, vol. 790, pp. 108–128, 2019.

[52] V. Khachatryan *et al.*, "Measurement of inclusive jet cross sections in *pp* and pbpb collisions at $\sqrt{s_{\mathrm{NN}}} = 2.76$ tev," *Phys. Rev. C*, vol. 96, p. 015202, Jul 2017.

[53] A. Andronic *et al.*, "Heavy-flavour and quarkonium production in the LHC era: from proton–proton to heavy-ion collisions," *Eur. Phys. J. C*, vol. 76, no. 3, p. 107, 2016.

[54] F.-M. Liu and S.-X. Liu, "Quark-gluon plasma formation time and direct photons from heavy ion collisions," *Phys. Rev. C*, vol. 89, no. 3, p. 034906, 2014.

[55] V. Greco, C. Ko, and R. Rapp, "Quark coalescence for charmed mesons in ultrarelativistic heavy ion collisions," *Phys. Lett. B*, vol. 595, pp. 202–208, 2004.

[56] J. C. Collins, D. E. Soper, and G. F. Sterman, *Factorization of Hard Processes in QCD*, vol. 5, pp. 1–91. 1989.

[57] S. Acharya *et al.*, "Measurement of D^0, D^+, D^{*+} and D_s^+ production in Pb-Pb collisions at $\sqrt{s_{\mathrm{NN}}} = 5.02$ TeV," *JHEP*, vol. 10, p. 174, 2018.

[58] M. He, R. J. Fries, and R. Rapp, "Heavy Flavor at the Large Hadron Collider in a Strong Coupling Approach," *Phys. Lett. B*, vol. 735, pp. 445–450, 2014.

[59] J. Uphoff, O. Fochler, Z. Xu, and C. Greiner, "Elastic and radiative heavy quark interactions in ultra-relativistic heavy-ion collisions," *J. Phys. G*, vol. 42, no. 11, p. 115106, 2015.

[60] S. Cao, T. Luo, G.-Y. Qin, and X.-N. Wang, "Heavy and light flavor jet quenching at RHIC and LHC energies," *Phys. Lett. B*, vol. 777, pp. 255–259, 2018.

[61] A. Beraudo, A. De Pace, M. Monteno, M. Nardi, and F. Prino, "Heavy flavors in heavy-ion collisions: quenching, flow and correlations," *Eur. Phys. J. C*, vol. 75, no. 3, p. 121, 2015.

[62] M. Nahrgang, J. Aichelin, P. B. Gossiaux, and K. Werner, “Influence of hadronic bound states above T_c on heavy-quark observables in Pb + Pb collisions at at the CERN Large Hadron Collider,” *Phys. Rev. C*, vol. 89, no. 1, p. 014905, 2014.

[63] T. Song, H. Berrehrah, D. Cabrera, W. Cassing, and E. Bratkovskaya, “Charm production in Pb + Pb collisions at energies available at the CERN Large Hadron Collider,” *Phys. Rev. C*, vol. 93, no. 3, p. 034906, 2016.

[64] A. M. Sirunyan *et al.*, “Studies of Beauty Suppression via Nonprompt D^0 Mesons in Pb-Pb Collisions at $Q^2 = 4$ GeV^2,” *Phys. Rev. Lett.*, vol. 123, no. 2, p. 022001, 2019.

[65] N. Zardoshti, “First Direct Observation of the Dead-Cone Effect,” *Nucl. Phys. A*, vol. 1005, p. 121905, 2021.

[66] T. Matsui and H. Satz, “J/ψ Suppression by Quark-Gluon Plasma Formation,” *Phys. Lett. B*, vol. 178, pp. 416–422, 1986.

[67] J. Adam *et al.*, “J/ψ suppression at forward rapidity in Pb-Pb collisions at $\sqrt{\mathbf{s}_{\mathrm{NN}}} = \mathbf{5.02}$ TeV,” *Phys. Lett. B*, vol. 766, pp. 212–224, 2017.

[68] A. M. Sirunyan *et al.*, “Measurement of nuclear modification factors of Υ(1S), Υ(2S), and Υ(3S) mesons in PbPb collisions at $\sqrt{s_{_{\mathrm{NN}}}} = 5.02$ TeV,” *Phys. Lett. B*, vol. 790, pp. 270–293, 2019.

[69] J. Aubert *et al.*, “Experimental Observation of a Heavy Particle J,” *Phys. Rev. Lett.*, vol. 33, pp. 1404–1406, 1974.

[70] J. Augustin *et al.*, “Discovery of a Narrow Resonance in e^+e^- Annihilation,” *Phys. Rev. Lett.*, vol. 33, pp. 1406–1408, 1974.

[71] J. Bjorken and S. Glashow, “Elementary Particles and SU(4),” *Phys. Lett.*, vol. 11, pp. 255–257, 1964.

[72] S. Glashow, J. Iliopoulos, and L. Maiani, “Weak Interactions with Lepton-Hadron Symmetry,” *Phys. Rev. D*, vol. 2, pp. 1285–1292, 1970.

[73] S. W. Herb *et al.*, “Observation of a dimuon resonance at 9.5 gev in 400-gev proton-nucleus collisions,” *Phys. Rev. Lett.*, vol. 39, pp. 252–255, Aug 1977.

[74] W. R. Innes *et al.*, “Observation of structure in the Υ region,” *Phys. Rev. Lett.*, vol. 39, pp. 1240–1242, Nov 1977.

[75] K. Ueno *et al.*, "Evidence for the Υ" and a search for new narrow resonances," *Phys. Rev. Lett.*, vol. 42, pp. 486–489, Feb 1979.

[76] F. Abe *et al.*, "Evidence for top quark production in p$\bar{p}$ collisions at $\sqrt{\mathrm{s}}$ =1.8 tev," *Phys. Rev. D*, vol. 50, pp. 2966–3026, Sep 1994.

[77] F. Abe *et al.*, "Measurement of B hadron lifetimes using J/ψ final states at CDF," *Phys. Rev. D*, vol. 57, pp. 5382–5401, 1998.

[78] B. Abelev *et al.*, "Measurement of prompt J/ψ and beauty hadron production cross sections at mid-rapidity in pp collisions at $\sqrt{s} = 7$ TeV," *JHEP*, vol. 11, p. 065, 2012.

[79] G. Aad *et al.*, "Measurement of the differential cross-sections of inclusive, prompt and non-prompt J/ψ production in proton-proton collisions at $\sqrt{s} = 7$ TeV," *Nucl. Phys. B*, vol. 850, pp. 387–444, 2011.

[80] S. Chatrchyan *et al.*, "J/ψ and $\psi(2S)$ production in pp collisions at $\sqrt{s} = 7$ TeV," *JHEP*, vol. 02, p. 011, 2012.

[81] R. Aaij *et al.*, "Measurement of the ratio of prompt χ_c to J/ψ production in pp collisions at $\sqrt{s} = 7$ TeV," *Phys. Lett. B*, vol. 718, pp. 431–440, 2012.

[82] R. Aaij *et al.*, "Measurement of the fraction of $\Upsilon(1S)$ originating from $\chi_b(1P)$ decays in pp collisions at $\sqrt{s} = 7$ TeV," *JHEP*, vol. 11, p. 031, 2012.

[83] R. Aaij *et al.*, "Measurement of $\psi(2S)$ production cross-sections in proton-proton collisions at $\sqrt{s} = 7$ and 13 TeV," *Eur. Phys. J.*, vol. C80, no. 3, p. 185, 2020.

[84] R. Aaij *et al.*, "Measurement of Υ production in pp collisions at $\sqrt{s}$= 13 TeV," *JHEP*, vol. 07, p. 134, 2018. [Erratum: JHEP 05, 076 (2019)].

[85] E. Braaten, "Introduction to the NRQCD factorization approach to heavy quarkonium," in *3rd International Workshop on Particle Physics Phenomenology*, 11 1996.

[86] F. Abe *et al.*, "J/ψ and $\psi(2S)$ production in $p\overline{p}$ collisions at $\sqrt{s} = 1.8$TeV," *Phys. Rev. Lett.*, vol. 79, pp. 572–577, Jul 1997.

[87] J. Campbell, F. Maltoni, and F. Tramontano, "Qcd corrections to j/ψ and Υ production at hadron colliders," *Phys. Rev. Lett.*, vol. 98, p. 252002, Jun 2007.

[88] G. T. Bodwin, E. Braaten, and G. Lepage, "Rigorous QCD analysis of inclusive annihilation and production of heavy quarkonium," *Phys. Rev. D*, vol. 51, pp. 1125–1171, 1995. [Erratum: Phys.Rev.D 55, 5853 (1997)].

[89] M. Butenschoen and B. A. Kniehl, "Next-to-leading-order tests of NRQCD factorization with J/ψ yield and polarization," *Mod. Phys. Lett. A*, vol. 28, p. 1350027, 2013.

[90] J. Lansberg, "On the mechanisms of heavy-quarkonium hadroproduction," *Eur. Phys. J. C*, vol. 61, pp. 693–703, 2009.

[91] Y.-Q. Ma and R. Venugopalan, "Comprehensive Description of J/ψ Production in Proton-Proton Collisions at Collider Energies," *Phys. Rev. Lett.*, vol. 113, no. 19, p. 192301, 2014.

[92] S. Acharya *et al.*, "Energy dependence of forward-rapidity J/ψ and ψ(2S) production in pp collisions at the LHC," *Eur. Phys. J. C*, vol. 77, no. 6, p. 392, 2017.

[93] Y.-Q. Ma, K. Wang, and K.-T. Chao, "$J/\psi(\psi')$ production at the Tevatron and LHC at $\mathcal{O}(\alpha_s^4 v^4)$ in nonrelativistic QCD," *Phys. Rev. Lett.*, vol. 106, p. 042002, 2011.

[94] B. B. Abelev *et al.*, "Measurement of quarkonium production at forward rapidity in *pp* collisions at $\sqrt{s} = 7$ TeV," *Eur. Phys. J. C*, vol. 74, no. 8, p. 2974, 2014.

[95] R. Aaij *et al.*, "Measurement of J/ψ production in *pp* collisions at $\sqrt{s} = 7$ TeV," *Eur. Phys. J. C*, vol. 71, p. 1645, 2011.

[96] V. Khachatryan *et al.*, "Measurement of J/ψ and ψ(2S) Prompt Double-Differential Cross Sections in pp Collisions at $\sqrt{s}$=7 TeV," *Phys. Rev. Lett.*, vol. 114, no. 19, p. 191802, 2015.

[97] V. Khachatryan *et al.*, "Prompt and Non-Prompt J/ψ Production in *pp* Collisions at $\sqrt{s} = 7$ TeV," *Eur. Phys. J. C*, vol. 71, p. 1575, 2011.

[98] A. Sirunyan *et al.*, "Measurement of quarkonium production cross sections in pp collisions at $\sqrt{s} = 13$ TeV," *Phys. Lett. B*, vol. 780, pp. 251–272, 2018.

[99] V. Khachatryan *et al.*, "Measurement of Prompt J/ψ Pair Production in pp Collisions at $\sqrt{s} = 7$ Tev," *JHEP*, vol. 09, p. 094, 2014.

[100] V. Khachatryan *et al.*, "Observation of Υ(1S) pair production in proton-proton collisions at $\sqrt{s} = 8$ TeV," *JHEP*, vol. 05, p. 013, 2017.

[101] A. M. Sirunyan *et al.*, "Study of J/ψ meson production inside jets in pp collisions at $\sqrt{s} = 8$ TeV," *Phys. Lett. B*, vol. 804, p. 135409, 2020.

[102] “Dimuon spectrum 2016,” Aug 2016.

[103] M. Baumgart, A. K. Leibovich, T. Mehen, and I. Z. Rothstein, “Probing Quarkonium Production Mechanisms with Jet Substructure,” *JHEP*, vol. 11, p. 003, 2014.

[104] R. Aaij *et al.*, “Measurement of forward J/ψ production cross-sections in pp collisions at $\sqrt{s} = 13$ TeV,” *JHEP*, vol. 10, p. 172, 2015. [Erratum: JHEP 05, 063 (2017)].

[105] G. Aad *et al.*, “Measurement of the differential cross-sections of prompt and non-prompt production of J/ψ and $\psi(2\mathrm{S})$ in pp collisions at $\sqrt{s} = 7$ and 8 TeV with the ATLAS detector,” *Eur. Phys. J. C*, vol. 76, no. 5, p. 283, 2016.

[106] P. Artoisenet, J. M. Campbell, J. Lansberg, F. Maltoni, and F. Tramontano, “Υ Production at Fermilab Tevatron and LHC Energies,” *Phys. Rev. Lett.*, vol. 101, p. 152001, 2008.

[107] J. Amundson, O. J. Eboli, E. Gregores, and F. Halzen, “Colorless states in perturbative QCD: Charmonium and rapidity gaps,” *Phys. Lett. B*, vol. 372, pp. 127–132, 1996.

[108] G. Aad *et al.*, “Measurement of the $\Upsilon(1\mathrm{S})$ production cross-section in pp collisions at $\sqrt{s} = 7$ TeV in ATLAS,” *Phys. Lett. B*, vol. 705, pp. 9–27, 2011.

[109] G. Aad *et al.*, “Measurement of Upsilon production in 7 TeV pp collisions at ATLAS,” *Phys. Rev. D*, vol. 87, no. 5, p. 052004, 2013.

[110] G. Aad *et al.*, “Measurement of χ_{c1} and χ_{c2} production with $\sqrt{s} = 7$ TeV pp collisions at ATLAS,” *JHEP*, vol. 07, p. 154, 2014.

[111] W. Cassing and E. Bratkovskaya, “Production and absorption of c anti-c pairs in nuclear collisions at SPS energies,” *Nucl. Phys. A*, vol. 623, pp. 570–590, 1997.

[112] N. Armesto, “Nuclear shadowing,” *J. Phys. G*, vol. 32, pp. R367–R394, 2006.

[113] G. Altarelli and G. Parisi, “Asymptotic Freedom in Parton Language,” *Nucl. Phys. B*, vol. 126, pp. 298–318, 1977.

[114] D. de Florian and R. Sassot, “Nuclear parton distributions at next to leading order,” *Phys. Rev. D*, vol. 69, p. 074028, Apr 2004.

[115] F. Gelis, E. Iancu, J. Jalilian-Marian, and R. Venugopalan, “The Color Glass Condensate,” *Ann. Rev. Nucl. Part. Sci.*, vol. 60, pp. 463–489, 2010.

[116] F. Arleo and S. Peign, “Quarkonium suppression in heavy-ion collisions from coherent energy loss in cold nuclear matter,” *JHEP*, vol. 10, p. 073, 2014.

[117] J. L. Albacete *et al.*, “Predictions for Cold Nuclear Matter Effects in p+Pb Collisions at $\sqrt{s_{NN}} = 8.16$ TeV,” *Nucl. Phys. A*, vol. 972, pp. 18–85, 2018.

[118] A. Kusina, J.-P. Lansberg, I. Schienbein, and H.-S. Shao, “Gluon Shadowing in Heavy-Flavor Production at the LHC,” *Phys. Rev. Lett.*, vol. 121, no. 5, p. 052004, 2018.

[119] E. Ferreiro, “Excited charmonium suppression in proton–nucleus collisions as a consequence of comovers,” *Phys. Lett. B*, vol. 749, pp. 98–103, 2015.

[120] Y.-Q. Ma, R. Venugopalan, K. Watanabe, and H.-F. Zhang, “$\psi(2S)$ versus J/ψ suppression in proton-nucleus collisions from factorization violating soft color exchanges,” *Phys. Rev. C*, vol. 97, no. 1, p. 014909, 2018.

[121] B. Duclou, T. Lappi, and H. Mntysaari, “Forward J/ψ production at high energy: centrality dependence and mean transverse momentum,” *Phys. Rev. D*, vol. 94, no. 7, p. 074031, 2016.

[122] K. Eskola, H. Paukkunen, and C. Salgado, “EPS09: A New Generation of NLO and LO Nuclear Parton Distribution Functions,” *JHEP*, vol. 04, p. 065, 2009.

[123] K. J. Eskola, P. Paakkinen, H. Paukkunen, and C. A. Salgado, “EPPS16: Nuclear parton distributions with LHC data,” *Eur. Phys. J. C*, vol. 77, no. 3, p. 163, 2017.

[124] K. Kovarik *et al.*, “nCTEQ15 - Global analysis of nuclear parton distributions with uncertainties in the CTEQ framework,” *Phys. Rev. D*, vol. 93, no. 8, p. 085037, 2016.

[125] E. G. Ferreiro and J.-P. Lansberg, “Is bottomonium suppression in proton-nucleus and nucleus-nucleus collisions at LHC energies due to the same effects?,” *JHEP*, vol. 10, p. 094, 2018. [Erratum: JHEP 03, 063 (2019)].

[126] S. Acharya *et al.*, “Υ production in p–Pb collisions at $\sqrt{s_{NN}}$=8.16 TeV,” *Phys. Lett. B*, vol. 806, p. 135486, 2020.

[127] R. Aaij *et al.*, “Study of Υ production in pPb collisions at $\sqrt{s_{NN}} = 8.16$ TeV,” *JHEP*, vol. 11, p. 194, 2018. [Erratum: JHEP 02, 093 (2020)].

[128] H. Satz, “Charm and beauty in a hot environment,” in *Sense of Beauty in Physics: Miniconference in Honor of Adriano Di Giacomo on his 70th Birthday*, 2 2006.

[129] Y. Burnier, O. Kaczmarek, and A. Rothkopf, “Quarkonium at finite temperature: Towards realistic phenomenology from first principles,” *JHEP*, vol. 12, p. 101, 2015.

[130] B. Abelev *et al.*, “J/ψ suppression at forward rapidity in Pb-Pb collisions at $\sqrt{s_{NN}} =$ 2.76 TeV,” *Phys. Rev. Lett.*, vol. 109, p. 072301, 2012.

[131] J. Adam *et al.*, “Differential studies of inclusive J/ψ and ψ(2S) production at forward rapidity in Pb-Pb collisions at $\sqrt{s_{\mathrm{NN}}} = 2.76$ TeV,” *JHEP*, vol. 05, p. 179, 2016.

[132] A. Adare *et al.*, “J/ψ suppression at forward rapidity in Au+Au collisions at $\sqrt{s_{NN}} =$ 200 GeV,” *Phys. Rev. C*, vol. 84, p. 054912, 2011.

[133] X. Zhao and R. Rapp, “Medium Modifications and Production of Charmonia at LHC,” *Nucl. Phys. A*, vol. 859, pp. 114–125, 2011.

[134] K. Zhou, N. Xu, Z. Xu, and P. Zhuang, “Medium effects on charmonium production at ultrarelativistic energies available at the CERN Large Hadron Collider,” *Phys. Rev. C*, vol. 89, no. 5, p. 054911, 2014.

[135] P. Braun-Munzinger and J. Stachel, “(Non)thermal aspects of charmonium production and a new look at J / psi suppression,” *Phys. Lett. B*, vol. 490, pp. 196–202, 2000.

[136] X. Du and R. Rapp, “Sequential Regeneration of Charmonia in Heavy-Ion Collisions,” *Nucl. Phys. A*, vol. 943, pp. 147–158, 2015.

[137] S. Acharya *et al.*, “J/ψ elliptic and triangular flow in Pb-Pb collisions at $\sqrt{s_{\mathrm{NN}}} =$ 5.02 TeV,” 5 2020.

[138] S. Acharya *et al.*, “Measurement of Υ(1S) elliptic flow at forward rapidity in Pb-Pb collisions at $\sqrt{s_{\mathrm{NN}}} = 5.02$ TeV,” *Phys. Rev. Lett.*, vol. 123, no. 19, p. 192301, 2019.

[139] Y.-Q. Ma, T. Stebel, and R. Venugopalan, “J/ψ polarization in the CGC+NRQCD approach,” *JHEP*, vol. 12, p. 057, 2018.

[140] P. Faccioli, C. Lourenco, J. Seixas, and H. K. Wohri, “Towards the experimental clarification of quarkonium polarization,” *Eur. Phys. J. C*, vol. 69, pp. 657–673, 2010.

[141] D. Brink and G. Stachler, *Angular momentum*, Clarendon Press. 1993.

[142] J. C. Collins and D. E. Soper, “Angular Distribution of Dileptons in High-Energy Hadron Collisions,” *Phys. Rev. D*, vol. 16, p. 2219, 1977.

[143] K. Gottfried and J. D. Jackson, “On the connection between production mechanism and decay of resonances at high energies,” *Nuovo Cimento*, vol. 33, no. CERN-TH-397, pp. 309–330, 1964.

[144] A. Abulencia *et al.*, “Polarization of J/ψ and $\psi(2S)$ Mesons Produced in $p\overline{p}$ Collisions at $\sqrt{s} = 1.96$-TeV,” *Phys. Rev. Lett.*, vol. 99, p. 132001, 2007.

[145] E. Braaten, B. A. Kniehl, and J. Lee, “Polarization of prompt J/ψ at the fermilab tevatron,” *Phys. Rev. D*, vol. 62, p. 094005, Sep 2000.

[146] S. P. Baranov, “Highlights from the k_T-factorization approach on the quarkonium production puzzles,” *Phys. Rev. D*, vol. 66, p. 114003, Dec 2002.

[147] T. Affolder *et al.*, “Measurement of J/ψ and $\psi(2S)$ polarization in $p\overline{p}$ collisions at $\sqrt{s} = 1.8$ TeV,” *Phys. Rev. Lett.*, vol. 85, pp. 2886–2891, 2000.

[148] Abazov *et al.*, “Measurement of the polarization of the $\Upsilon(1s)$ and $\Upsilon(2s)$ states in $p\overline{p}$ collisions at $\sqrt{s} = 1.96$ TeV,” *Phys. Rev. Lett.*, vol. 101, p. 182004, Oct 2008.

[149] Acosta *et al.*, “Υ production and polarization in $p\overline{p}$ collisions at $\sqrt{s} = 1.8$TeV,” *Phys. Rev. Lett.*, vol. 88, p. 161802, Apr 2002.

[150] E. Braaten and J. Lee, “Polarization of Υ_{nS} at the Tevatron,” *Phys. Rev. D*, vol. 63, p. 071501, 2001.

[151] A. Adare *et al.*, “Transverse momentum dependence of J/ψ polarization at midrapidity in $p + p$ collisions at $\sqrt{s} = 200$ GeV,” *Phys. Rev. D*, vol. 82, p. 012001, Jul 2010.

[152] U. Acharya *et al.*, “Polarization and cross section of midrapidity J/ψ production in proton-proton collisions at $\sqrt{s} = 510$ GeV,” 5 2020.

[153] J. Adam *et al.*, “Measurement of inclusive J/ψ polarization in $p + p$ collisions at $\sqrt{s}$ =200 GeV by the STAR experiment,” *Phys. Rev. D*, vol. 102, no. 9, p. 092009, 2020.

[154] V. Cheung and R. Vogt, “Production and polarization of prompt J/ψ in the improved color evaporation model using the k_T-factorization approach,” *Phys. Rev. D*, vol. 98, p. 114029, Dec 2018.

[155] B. Gong, L.-P. Wan, J.-X. Wang, and H.-F. Zhang, "Polarization for Prompt J/ψ and ψ(2s) Production at the Tevatron and LHC," *Phys. Rev. Lett.*, vol. 110, no. 4, p. 042002, 2013.

[156] H.-F. Zhang, Z. Sun, W.-L. Sang, and R. Li, "Impact of η_c hadroproduction data on charmonium production and polarization within the nonrelativistic qcd framework," *Phys. Rev. Lett.*, vol. 114, p. 092006, Mar 2015.

[157] B. Abelev *et al.*, "J/ψ polarization in *pp* collisions at $\sqrt{s} = 7$ TeV," *Phys. Rev. Lett.*, vol. 108, p. 082001, 2012.

[158] M. Butenschoen and B. A. Kniehl, "J/psi polarization at Tevatron and LHC: Nonrelativistic-QCD factorization at the crossroads," *Phys. Rev. Lett.*, vol. 108, p. 172002, 2012.

[159] R. Aaij *et al.*, "Measurement of J/ψ polarization in *pp* collisions at $\sqrt{s} = 7$ TeV," *Eur. Phys. J. C*, vol. 73, no. 11, p. 2631, 2013.

[160] K.-T. Chao, Y.-Q. Ma, H.-S. Shao, K. Wang, and Y.-J. Zhang, "j/ψ polarization at hadron colliders in nonrelativistic qcd," *Phys. Rev. Lett.*, vol. 108, p. 242004, Jun 2012.

[161] S. Chatrchyan *et al.*, "Measurement of the Prompt J/ψ and ψ(2S) Polarizations in *pp* Collisions at $\sqrt{s} = 7$ TeV," *Phys. Lett. B*, vol. 727, pp. 381–402, 2013.

[162] S. Chatrchyan *et al.*, "Measurement of the $Y(1S), Y(2S)$ and $Y(3S)$ Polarizations in *pp* Collisions at $\sqrt{s} = 7$ TeV," *Phys. Rev. Lett.*, vol. 110, no. 8, p. 081802, 2013.

[163] R. Aaij *et al.*, "Measurement of the Υ polarizations in *pp* collisions at $\sqrt{s} = 7$ and 8 TeV," *JHEP*, vol. 12, p. 110, 2017.

[164] B. Ioffe and D. Kharzeev, "Quarkonium polarization in heavy ion collisions as a possible signature of the quark gluon plasma," *Phys. Rev. C*, vol. 68, p. 061902, 2003.

[165] I. Abt *et al.*, "Angular distributions of leptons from J/ψ ' s produced in 920 GeV fixed-target proton-nucleus collisions," *Eur. Phys. J. C*, vol. 60, pp. 517–524, 2009.

[166] R. Arnaldi, "J/psi production in p-A and A-A collisions at fixed target experiments," *Nucl. Phys. A*, vol. 830, pp. 345C–352C, 2009.

[167] D. E. Kharzeev, L. D. McLerran, and H. J. Warringa, "The Effects of topological charge change in heavy ion collisions: 'Event by event P and CP violation'," *Nucl. Phys. A*, vol. 803, pp. 227–253, 2008.

[168] D. E. Kharzeev, "The Chiral Magnetic Effect and Anomaly-Induced Transport," *Prog. Part. Nucl. Phys.*, vol. 75, pp. 133–151, 2014.

[169] V. Khachatryan *et al.*, "Observation of charge-dependent azimuthal correlations in p-Pb collisions and its implication for the search for the chiral magnetic effect," *Phys. Rev. Lett.*, vol. 118, no. 12, p. 122301, 2017.

[170] B. Abelev *et al.*, "Charge separation relative to the reaction plane in Pb-Pb collisions at $\sqrt{s_{NN}} = 2.76$ TeV," *Phys. Rev. Lett.*, vol. 110, no. 1, p. 012301, 2013.

[171] B. Abelev *et al.*, "Azimuthal Charged-Particle Correlations and Possible Local Strong Parity Violation," *Phys. Rev. Lett.*, vol. 103, p. 251601, 2009.

[172] S. Acharya *et al.*, "Probing the effects of strong electromagnetic fields with charge-dependent directed flow in Pb-Pb collisions at the LHC," *Phys. Rev. Lett.*, vol. 125, no. 2, p. 022301, 2020.

[173] F. Becattini, F. Piccinini, and J. Rizzo, "Angular momentum conservation in heavy ion collisions at very high energy," *Phys. Rev. C*, vol. 77, p. 024906, 2008.

[174] Y.-G. Yang, R.-H. Fang, Q. Wang, and X.-N. Wang, "Quark coalescence model for polarized vector mesons and baryons," *Phys. Rev. C*, vol. 97, no. 3, p. 034917, 2018.

[175] S. Acharya *et al.*, "Evidence of Spin-Orbital Angular Momentum Interactions in Relativistic Heavy-Ion Collisions," *Phys. Rev. Lett.*, vol. 125, no. 1, p. 012301, 2020.

[176] D. Colella, "ALICE ITS: the Run 1 to Run 2 transition and recent operational experience," *PoS*, vol. VERTEX2015, p. 003, 2015.

[177] A. Rashevsky *et al.*, "Characteristics of the ALICE silicon drift detector," *Nucl. Instrum. Meth. A*, vol. 461, pp. 133–138, 2001.

[178] M. Germain *et al.*, "Irradiation of a silicon-strip detector for the ALICE experiment at LHC," *Nucl. Instrum. Meth. A*, vol. 482, pp. 634–643, 2002.

[179] A. P. De Haas, C. J. Oskamp, A. Van den Brink, P. G. Kuijer, V. N. Borshchov, S. K. Kiprich, and V. M. Ruzhitsky, "Very low mass microcables for the ALICE silicon strip detector. Very Low-Mass Microcables for the ALICE SSD Detector," p. 4 p, May 1999.

[180] G. Dellacasa *et al.*, *ALICE time projection chamber: Technical Design Report.* Technical Design Report ALICE,CERN-LHCC-2000-001, Geneva: CERN, 2000.

[181] T. A. Collaboration, "The ALICE experiment at the CERN LHC," *Journal of Instrumentation*, vol. 3, pp. S08002–S08002, aug 2008.

[182] P. Cortese, *ALICE transition-radiation detector: Technical Design Report.* Technical Design Report ALICE, CERN-LHCC-2001-021, Geneva: CERN, 2001.

[183] *ALICE Time-Of-Flight system (TOF): Technical Design Report.* Technical Design Report ALICE, CERN-LHCC-2000-012, Geneva: CERN, 2000.

[184] E. Cerron Zeballos, I. Crotty, D. Hatzifotiadou, J. Lamas Valverde, S. Neupane, M. Williams, and A. Zichichi, "A New type of resistive plate chamber: The Multigap RPC," *Nucl. Instrum. Meth. A*, vol. 374, pp. 132–136, 1996.

[185] F. Piuz, W. Klempt, L. Leistam, J. De Groot, and J. Schkraft, *ALICE high-momentum particle identification: Technical Design Report.* Technical Design Report ALICE, Geneva: CERN, 1998.

[186] V. I. Man'ko, W. Klempt, L. Leistam, J. De Groot, and J. Schkraft, *ALICE Photon Spectrometer (PHOS): Technical Design Report.* Technical Design Report ALICE, CERN-LHCC-99-004, Geneva: CERN, 1999.

[187] T. Cormier, C. W. Fabjan, L. Riccati, and H. de Groot, "ALICE electromagnetic calorimeter: addendum to the ALICE technical proposal," Tech. Rep. CERN-LHCC-2006-014, CERN, Geneva, Mar 2006.

[188] P. Crochet and P. Braun-Munzinger, "Investigation of background subtraction techniques for high mass dilepton physics," *Nucl. Instrum. Meth. A*, vol. 484, pp. 564–572, 2002.

[189] P. Cortese *et al.*, *ALICE forward detectors: FMD, TO and VO: Technical Design Report.* Technical Design Report ALICE, CERN-LHCC-2004-025, Geneva: CERN, 2004. Submitted on 10 Sep 2004.

[190] B. B. Abelev *et al.*, "Performance of the ALICE Experiment at the CERN LHC," *Int. J. Mod. Phys. A*, vol. 29, p. 1430044, 2014.

[191] A. I. Zinchenko and G. Chabratova, "A new approach to cluster finding and hit reconstruction in cathode pad chambers and its development for the forward muon

spectrometer of ALICE," *Nucl. Instrum. Methods Phys. Res., A*, vol. 502, pp. 778–780, 2003.

[192] E. Mathieson, "Cathode Charge Distributions in Multiwire Chambers. 4: Empirical Formula for Small Anode - Cathode Separation," *Nucl. Instrum. Meth. A*, vol. 270, pp. 602–603, 1988.

[193] F. Bossu, M. Gagliardi, and M. Marchisone, "Performance of the RPC-based ALICE muon trigger system at the LHC," *PoS*, vol. RPC2012, p. 059, 2012.

[194] "Quarkonium signal extraction in ALICE," ALICE-PUBLIC-2015-006, Oct 2015.

[195] R. Shahoyan, "J/ψ and ψ' production in 450 GeV pA interactions and its dependence on the rapidity and x_F," 2001. Presented on 2001.

[196] S. Acharya *et al.*, "Measurement of the inclusive J/ ψ polarization at forward rapidity in pp collisions at $\mathbf{\sqrt{s} = 8}$ TeV," *Eur. Phys. J. C*, vol. 78, no. 7, p. 562, 2018.

[197] B. Abelev *et al.*, "Centrality determination of pb-pb collisions at $\sqrt{s_{NN}} = 2.76$ tev with alice," *Phys. Rev. C*, vol. 88, p. 044909, Oct 2013.

[198] I. Antcheva *et al.*, "ROOT: A C++ framework for petabyte data storage, statistical analysis and visualization," *Comput. Phys. Commun.*, vol. 180, pp. 2499–2512, 2009.

[199] S. Acharya *et al.*, "Studies of J/ψ production at forward rapidity in Pb-Pb collisions at $\sqrt{s_{\rm NN}} = 5.02$ TeV," *JHEP*, vol. 02, p. 041, 2020.

[200] A. M. Poskanzer and S. Voloshin, "Methods for analyzing anisotropic flow in relativistic nuclear collisions," *Phys. Rev. C*, vol. 58, pp. 1671–1678, 1998.

[201] S. Acharya *et al.*, "Global polarization of $\Lambda\bar{\Lambda}$ hyperons in Pb-Pb collisions at $\sqrt{s_{NN}}$ = 2.76 and 5.02 TeV," *Phys. Rev. C*, vol. 101, no. 4, p. 044611, 2020.

[202] T. Aaltonen *et al.*, "Measurements of Angular Distributions of Muons From Υ Meson Decays in $p\bar{p}$ Collisions at $\sqrt{s} = 1.96$ TeV," *Phys. Rev. Lett.*, vol. 108, p. 151802, 2012.

[203] V. Abazov *et al.*, "Measurement of the polarization of the v_{1S} and v_{2S} states in $p\bar{p}$ collisions at $\sqrt{s} = 1.96$-TeV," *Phys. Rev. Lett.*, vol. 101, p. 182004, 2008.

[204] B. Gong, L.-P. Wan, J.-X. Wang, and H.-F. Zhang, "Complete next-to-leading-order study on the yield and polarization of $\Upsilon(1S, 2S, 3S)$ at the Tevatron and LHC," *Phys. Rev. Lett.*, vol. 112, no. 3, p. 032001, 2014.

[205] S. Acharya *et al.*, "Υ suppression at forward rapidity in Pb-Pb collisions at $\sqrt{s_{\mathrm{NN}}} =$ 5.02 TeV," *Phys. Lett. B*, vol. 790, pp. 89–101, 2019.

[206] Z. Citron *et al.*, "Report from Working Group 5: Future physics opportunities for high-density QCD at the LHC with heavy-ion and proton beams," *CERN Yellow Rep. Monogr.*, vol. 7, pp. 1159–1410, 2019.

[207] U. W. Heinz, "Concepts of heavy ion physics," in *2nd CERN-CLAF School of High Energy Physics*, pp. 165–238, 7 2004.

[208] O. Philipsen, "Lattice QCD at finite temperature and density," *Eur. Phys. J. ST*, vol. 152, pp. 29–60, 2007.

[209] B. Andersson, G. Gustafson, and B. Soderberg, "A General Model for Jet Fragmentation," *Z. Phys. C*, vol. 20, p. 317, 1983.

[210] J. Cronin, H. J. Frisch, M. Shochet, J. Boymond, R. Mermod, P. Piroue, and R. L. Sumner, "Production of hadrons with large transverse momentum at 200, 300, and 400 GeV," *Phys. Rev. D*, vol. 11, pp. 3105–3123, 1975.

[211] G. Goldhaber *et al.*, "Observation in e^+e^- annihilation of a narrow state at 1865 mev/c^2 decaying to $k\pi$ and $k\pi\pi\pi$," *Phys. Rev. Lett.*, vol. 37, pp. 255–259, Aug 1976.

[212] B. Knapp *et al.*, "Observation of a Narrow anti-Baryon State at 2.26-GeV/c**2," *Phys. Rev. Lett.*, vol. 37, p. 882, 1976.

[213] C. Bebek *et al.*, "Evidence for new-flavor production at the $\Upsilon(4s)$," *Phys. Rev. Lett.*, vol. 46, pp. 84–87, Jan 1981.

[214] M. Basile *et al.*, "Evidence for a New Particle With Naked 'Beauty' and for Its Associated Production in High-energy (p p) Interactions," *Lett. Nuovo Cim.*, vol. 31, p. 97, 1981.

[215] C. Patrignani *et al.*, "Review of Particle Physics," *Chin. Phys. C*, vol. 40, no. 10, p. 100001, 2016.

[216] S. Okubo, "Phi meson and unitary symmetry model," *Phys. Lett.*, vol. 5, pp. 165–168, 1963.

[217] G. Zweig, *An SU(3) model for strong interaction symmetry and its breaking*, pp. 22–101. 2 1964.

[218] J. Iizuka, “Systematics and phenomenology of meson family,” *Prog. Theor. Phys. Suppl.*, vol. 37, pp. 21–34, 1966.

[219] R. Gupta, “Introduction to lattice QCD: Course,” in *Les Houches Summer School in Theoretical Physics, Session 68: Probing the Standard Model of Particle Interactions*, pp. 83–219, 7 1997.

[220] M. Ryskin, R. Roberts, A. D. Martin, and E. Levin, “Diffractive J / psi photoproduction as a probe of the gluon density,” *Z. Phys. C*, vol. 76, pp. 231–239, 1997.

[221] B. Abelev *et al.*, “Coherent J/ψ photoproduction in ultra-peripheral Pb-Pb collisions at $\sqrt{s_{NN}} = 2.76$ TeV,” *Phys. Lett. B*, vol. 718, pp. 1273–1283, 2013.

[222] F. Abe *et al.*, “Production of J/ψ mesons from χ_c meson decays in $p\overline{p}$ collisions at $\sqrt{s} = 1.8$TeV,” *Phys. Rev. Lett.*, vol. 79, pp. 578–583, Jul 1997.

[223] M. Cacciari, S. Frixione, N. Houdeau, M. L. Mangano, P. Nason, and G. Ridolfi, “Theoretical predictions for charm and bottom production at the LHC,” *JHEP*, vol. 10, p. 137, 2012.

[224] H. Han, Y.-Q. Ma, C. Meng, H.-S. Shao, Y.-J. Zhang, and K.-T. Chao, “$\Upsilon(nS)$ and $\chi_b(nP)$ production at hadron colliders in nonrelativistic QCD,” *Phys. Rev. D*, vol. 94, no. 1, p. 014028, 2016.

[225] P. Braun-Munzinger and J. Stachel, “The quest for the quark-gluon plasma,” *Nature*, vol. 448, pp. 302–309, 2007.

[226] A. M. Sirunyan *et al.*, “Measurement of the azimuthal anisotropy of Υ(1S) and Υ(2S) mesons in PbPb collisions at $\sqrt{s_{\mathrm{NN}}} = 5.02$ TeV,” 6 2020.

[227] E. L. Berger, “THE EMC EFFECT,” *AIP Conf. Proc.*, vol. 150, pp. 165–184, 1986.

[228] F. Arleo, “Quenching of Hadron Spectra in Heavy Ion Collisions at the LHC,” *Phys. Rev. Lett.*, vol. 119, no. 6, p. 062302, 2017.

[229] M. Spousta, “On similarity of jet quenching and charmonia suppression,” *Phys. Lett. B*, vol. 767, pp. 10–15, 2017.

[230] A. M. Sirunyan *et al.*, “Observation of prompt J/ψ meson elliptic flow in high-multiplicity pPb collisions at $\sqrt{s_{\mathrm{NN}}} = 8.16$ TeV,” *Phys. Lett. B*, vol. 791, pp. 172–194, 2019.

[231] C. Zhang, C. Marquet, G.-Y. Qin, S.-Y. Wei, and B.-W. Xiao, “Elliptic Flow of Heavy Quarkonia in pA Collisions,” *Phys. Rev. Lett.*, vol. 122, no. 17, p. 172302, 2019.

[232] E. Braaten, S. Fleming, and A. K. Leibovich, “Nonrelativistic qcd analysis of bottomonium production at the fermilab tevatron,” *Phys. Rev. D*, vol. 63, p. 094006, Mar 2001.

[233] J. R. Andersen *et al.*, “Small x phenomenology: Summary and status,” *Eur. Phys. J. C*, vol. 35, pp. 67–98, 2004.

[234] L. Adamczyk *et al.*, “J/ψ polarization in p+p collisions at $\sqrt{s} = 200$ GeV in STAR,” *Phys. Lett. B*, vol. 739, pp. 180–188, 2014.

[235] J. Lansberg, “QCD corrections to J/psi polarisation in pp collisions at RHIC,” *Phys. Lett. B*, vol. 695, pp. 149–156, 2011.

[236] H. S. Chung, C. Yu, S. Kim, and J. Lee, “Polarization of prompt j/ψ in proton-proton collisions at rhic,” *Phys. Rev. D*, vol. 81, p. 014020, Jan 2010.

[237] T. H. Chang, , *et al.*, “j/ψ polarization in 800-gev $p-$Cu interactions,” *Phys. Rev. Lett.*, vol. 91, p. 211801, Nov 2003.

[238] “Centrality determination in heavy ion collisions,” ALICE-PUBLIC-2018-011, Aug 2018.

[239] X. Zhang, “Study of Heavy Flavours from Muons Measured with the ALICE Detector in Proton-Proton and Heavy-Ion Collisions at the CERN-LHC,” 2012. CERN-THESIS-2012-325

[240] S. Acharya *et al.*, “Coherent J/ψ photoproduction at forward rapidity in ultra-peripheral Pb-Pb collisions at $\sqrt{s_{\rm NN}} = 5.02$ TeV,” *Phys. Lett. B*, vol. 798, p. 134926, 2019.

[241] B. B. Abelev *et al.*, “J/ψ production and nuclear effects in p-Pb collisions at $\sqrt{S_{NN}}$ = 5.02 TeV,” *JHEP*, vol. 02, p. 073, 2014.

[242] R. Aaij *et al.*, “Study of J/ψ production and cold nuclear matter effects in pPb collisions at $\sqrt{s_{NN}} = 5$ TeV,” *JHEP*, vol. 02, p. 072, 2014.

[243] B. B. Abelev *et al.*, “Suppression of ψ(2S) production in p-Pb collisions at $\sqrt{s_{\rm NN}} =$ 5.02 TeV,” *JHEP*, vol. 12, p. 073, 2014.

[244] J. Albacete *et al.*, "Predictions for p+Pb Collisions at sqrt s_NN = 5 TeV," *Int. J. Mod. Phys. E*, vol. 22, p. 1330007, 2013.

[245] J.-P. Lansberg and H.-S. Shao, "Towards an automated tool to evaluate the impact of the nuclear modification of the gluon density on quarkonium, D and B meson production in proton–nucleus collisions," *Eur. Phys. J. C*, vol. 77, no. 1, p. 1, 2017.

[246] F. Arleo, R. Kolevatov, S. Peigné, and M. Rustamova, "Centrality and pT dependence of J/psi suppression in proton-nucleus collisions from parton energy loss," *JHEP*, vol. 05, p. 155, 2013.

[247] J. Adam *et al.*, "Inclusive quarkonium production at forward rapidity in pp collisions at $\sqrt{s} = 8$ TeV," *Eur. Phys. J. C*, vol. 76, no. 4, p. 184, 2016.

[248] "Quarkonium projections in p-Pb collisions for Run 3 and Run 4," ALICE-PUBLIC-2020-008, Oct 2020.

[249] S. Acharya *et al.*, "Inclusive J/ψ production at forward and backward rapidity in p-Pb collisions at $\sqrt{s_{\mathrm{NN}}} = 8.16$ TeV," *JHEP*, vol. 07, p. 160, 2018.

[250] R. Aaij *et al.*, "Study of $\psi(2S)$ production and cold nuclear matter effects in pPb collisions at $\sqrt{s_{NN}} = 5$ TeV," *JHEP*, vol. 03, p. 133, 2016.

[251] J. Adam *et al.*, "Centrality dependence of ψ(2S) suppression in p-Pb collisions at $\sqrt{s_{\mathrm{NN}}} = 5.02$ TeV," *JHEP*, vol. 06, p. 050, 2016.

[252] J. Adam *et al.*, "Centrality dependence of inclusive J/ψ production in p-Pb collisions at $\sqrt{s_{\mathrm{NN}}} = 5.02$ TeV," *JHEP*, vol. 11, p. 127, 2015.

[253] J. L. Albacete *et al.*, "Predictions for p+Pb Collisions at $\sqrt{s_{NN}} = 5$ TeV: Comparison with Data," *Int. J. Mod. Phys. E*, vol. 25, no. 9, p. 1630005, 2016.

[254] J. Adam *et al.*, "Centrality dependence of particle production in p-Pb collisions at $\sqrt{s_{\mathrm{NN}}}= 5.02$ TeV," *Phys. Rev. C*, vol. 91, no. 6, p. 064905, 2015.

[255] D. McGlinchey, A. Frawley, and R. Vogt, "Impact parameter dependence of the nuclear modification of J/ψ production in d+Au collisions at $\sqrt{S_{NN}} = 200$ GeV," *Phys. Rev. C*, vol. 87, no. 5, p. 054910, 2013.

[256] A. M. Sirunyan *et al.*, "Constraints on the χ_{c1} versus χ_{c2} Polarizations in Proton-Proton Collisions at $\sqrt{s} = 8$ TeV," *Phys. Rev. Lett.*, vol. 124, no. 16, p. 162002, 2020.